NOVEL TOOLS FOR PRACTICAL CO-OPTIMIZATION AND GUIDANCE OF SPACE MISSIONS

A Dissertation

by

VISHALA

Submitted to the Graduate and Professional School of
Texas A&M University
in partial fulfillment of the requirements for the degree of
DOCTOR OF PHILOSOPHY

Chair of Committee,	John L. Junkins
Committee Members,	Manoranjan Majji
	Srinivas R. Vadali
	Shankar Bhattacharya
Head of Department,	Ivett Levya

May 2022

Major Subject: Aerospace Engineering

ABSTRACT

Electric propulsion is defining the space travel of this era with its more payload to fuel efficiency and ability to result in robust deep space missions. Moreover, the complex sub-systems of these low thrust engines (like DAWN's NSTAR, NEXT, Psyche's SPT-140) provide unprecedented system-level challenges for co-optimization of trajectory and spacecraft for a holistic optimized mission. This work describes novel extensions of classical indirect methods to optimize such systems involving inequality constraints, discontinuities in states and controls and abrupt time triggered events. Furthermore, innovative methods are introduced that enable multiple preliminary trade-off aspects like mission objectives, propulsion constraints, solar power sub-systems and parameters, trajectory design and operational constraints. These challenges are addressed by an ingenious inclusion of spacecraft system level optimization in the preliminary mission design phase. The result is an indirect multi-disciplinary optimization (MDO) family of methods for missions. The approach is a fusion of invariant embedding, and mixed integer nonlinear programming with calculus of variation that very significantly expands the current class of trajectory optimization problems solvable by classical methods. The algorithms enjoy local optimality guaranteed by indirect methods though hybrid methods are employed to find the global optimal when multiple local optimal solutions are suspected. For autonomous guidance, there are many considerations like error in dynamics, bias in the sensors, actuator errors, sudden actuator failure, science operation constraints, and orbit determination requirements, that are required to be accommodated. This work introduces an original stochastic, covariance constrained guidance approach for tracking with associated contingencies for space missions. The designed algorithm achieves a desired time varying error covariance bound relative to tracking the optimized nominal trajectory by adaptively tuning a feedback controller. This contribution is anticipated to be the initiating step towards an autonomous guidance approach that enables cooperative autonomy, reliability and precision of future missions. The presented methods yield breakthrough recipes for system-level optimization involving realistic discrete operational constraints/events/multi-mode actuators with an attribute

of real-time re-planning capability. The optimization approach while demonstrated on aerospace dynamical systems has a wide applicability.

DEDICATION

To the two Doctor Superwomen in my family (my mother and sister) !

ACKNOWLEDGMENTS

I am forever indebted to my adviser, Dr. Junkins for sharing his treasure of wisdom and knowledge that can be better labelled as life hacks than just engineering tools. He has invested so much time in my development, oftentimes in the form of cultural anecdotes during *story time with Junkins* which made my PhD journey more rich and wholesome. Dr. Junkins is a visionary who has an extraordinary passion that infects you. He guides you but helps you think for yourself at the same time. He is the biggest cheerleader for every touchdown you make and has a way of correcting you such that you still can feel the warmth and care he bears for you. I am grateful beyond words to have such a Ph.D. adviser. I am also grateful to my committee members Dr. Manoranjan Majji, Dr. Srinivas Vadali, and Dr. Shankar Bhattacharyya for their time, guidance and appreciation for my research work.

Additionally, I have been fortunate to find friendship in my mentors Ehsan Taheri and Robyn Woollands. I owe my smooth transition from the field of robotics into trajectory optimization and optimal control to Dr. Taheri. His constant suggestions of different technical papers, new software tools and even hardware technologies helped me to stay updated with the developments in the field. His faith in my abilities and research acumen lifted my spirits at multiple low moments during my PhD journey and reinforced my self-confidence. Robyn has always acted as a guiding angel where she personally kept track of my life events to step in to give the best life/career advice whenever needed. Both Dr. Taheri and Dr. Woollands have guided and encouraged me since the beginning of my PhD and I believe, will be sources of life-long camaraderie.

My parents always motivated me to value education and pushed me towards attaining excellence. I have inherited from them not only the mental strength to be persistent amidst challenges but also the discipline and dedication to consistently put forward one step at a time for any task. My elder brother and sister have always been a constant source of strength right from my childhood and have played a key role in shaping who I am today. You are as strong as your best support system, is something I realized to be true more than a few times during my graduate studies. I

could not have been successful without the unwavering confidence, support and love of my best friend, Hari and my personal cheer squad consisting of Matthias, Amogh, Shruthi and Hrishi. The amount of pride and happiness I saw in their eyes for every little achievement in my life made it even more precious and fulfilling.

On a lighter note, I owe my Saturday group (SNL) consisting of Raman, Utkarsh and Atanu for the various fun-filled activities, life-questioning discussions and the various camping trips. The list is incomplete without the mention of a cohorts of friends I have made in these many years like Darpit, Dwarkanath, Akshay, Kaushik, Dipanajan, Niladri ; to name a few. I would also like to thank my office mates Sandeep, Joe and Patrick for their company, discussions and for bearing with my long presentations. Speaking of the office folks, Amanda has been most helpful in making each of our lives so much easier with her excellent, efficient, and ever-present administrative support. On a personal front, she also fulfilled the role of the much needed woman support on the floor whenever I needed one.

At last, I would like to thank every conference organizer and attendee, journal reviewers, and researchers in my field who provided me the opportunity to learn, grow and get inspired. Every conference that I have attended left me with a storm of ideas and overwhelming desire to keep experimenting and researching.

CONTRIBUTORS AND FUNDING SOURCES

Contributors

This work was supported by a dissertation committee consisting of Professors John Junkins (adviser), Manoranjan Majji, Srinivas Rao Vadali of the Department of Aerospace Engineering and Professor Shankar Bhattacharya of the Department of Electrical & Computer Engineering.

All the work conducted for the dissertation was completed by the student independently.

Funding Sources

Graduate study was supported by Jet Propulsion Laboratory, California Institute of Technology, under contract with the National Aeronautics and Space Administration (R.19.023.132), and support from Air Force Research Laboratory (AFRL)/AFOSR, Sandia Laboratory and NASA JPL Grace Follow-On Mission Team.

NOMENCLATURE

I_{sp}	specific impulse of the engine, seconds
$\boldsymbol{r}_{\text{sc}}$	position vector of the spacecraft relative to the sun
$\boldsymbol{v}_{\text{sc}}$	velocity vector of the spacecraft relative to the sun
$\boldsymbol{r}_{\text{planet}}$	position vector of the gravity assist planet
$\boldsymbol{v}_{\text{planet}}$	velocity vector of the gravity assist planet
$\boldsymbol{v}_{\infty}^{-}$	hyperbolic excess velocity vector with respect to the planet prior to gravity assist
$\boldsymbol{v}_{\infty}^{+}$	hyperbolic excess velocity vector with respect to the planet post gravity assist
μ_p	gravitational parameter of the flyby planet
r_p	periapsis radius of the flyby hyperbola
t_0	launch time or intial time
t_f	final time
Δt_i	time of flight of the i^{th} trajectory leg
v_{∞_L}	magnitude of launch hyperbolic excess velocity
n_p	number of planetary flybys during the mission
AU	astronomical unit
TU	time unit ($\frac{1}{2\pi}$ of the year)
P_{BL}	nominal beginning of life power generated by the solar arrays at launch at 1 AU (kW)
P_{SA}	power generated by the solar arrays
r	radial distance of the spacecraft from the sun in AU.
t	time elapsed since launch in years
P_{max}	maximum allowable power for the PPU

P_{min}	minimum operational power for the PPU
PPU	Power Processing Unit
PL	power required for the sustenance of essential spacecraft systems
P_{av}	power available for thrusting
p, f, g, h, k, l	modified equinoctial elements
$\boldsymbol{x}$	state vector associated with modified equinoctial elements
$\lambda_p, \lambda_f, \lambda_g, \lambda_h, \lambda_k, \lambda_l$	costates associated with modified equinoctial elements
T	Thrust, Newton
m	instantaneous mass of the spacecraft (kg)
a_r	radial component of the acceleration
a_t	transversal component of the acceleration
a_n	normal component of the acceleration
$\boldsymbol{A}$	$\in R^{6\times 1}$ denotes the unforced vector part of the dynamics
$\mathbb{B}$	$\in R^{6\times 3}$ denotes the control influence matrix for the dynamics
$\dot{m}$	propellant consumption rate (kg/sec)
$\boldsymbol{x}_0$	states at initial time
$\tilde{\boldsymbol{x}}_d$	desired states at final time
m_0	mass of the spacecraft at initial time
c	exhaust velocity of the engine
c_{min}	minimum admissible exhaust velocity
c_{max}	maximum admissible exhaust velocity
c_{op}	optimal exhaust velocity
$\tilde{c}$	effective optimal exhaust velocity
g_0	Earth's gravitational acceleration at the equator
$\boldsymbol{P}_{\text{sel}}, \dot{\boldsymbol{m}}_{\text{sel}}, \boldsymbol{T}_{\text{sel}}, \boldsymbol{I}_{\text{sp}_{\text{sel}}}$	vectors with each element representing the operating power, mass flow rate, thrust

	and I_{sp} for every operating mode of the engine respectively
T_{av}	operating thrust at every time, Newton
T_{min}	minimum operating thrust as per the available operating modes in the throttle table, Newton
T_{max}	maximum operating thrust as per the available operating modes in the table, Newton
T_{peak}	maximum thrust operated in the mission, Newton
$I_{\text{sp}_{\text{avg}}}$	average I_{sp} in the mission
m_f	final mass of the spacecraft, kg
g_p	condition to determine if power for thrusting is less or equal to the P_{max}
N_m	number of selected modes
$\boldsymbol{P_w}$	smooth function (using HTS) of $P_{\text{av}} - \boldsymbol{P}_{\text{sel}}$
$\boldsymbol{S_\delta}$	smooth function (using HTS) to determine the throttle input of the engine for every mode
$\boldsymbol{S_L}$	smooth function for combined power and throttle input criteria as per very mode
$\boldsymbol{S_H}$	vector representing Hamiltonian associated with each mode
$\boldsymbol{S_m}$	vector with elements representing the combined evaluation of criteria of power, throttle input and Hamiltonian for every mode
$\boldsymbol{\eta_m}$	smooth representation of the optimal contribution of each mode towards engine operation
δ_b	$\in [0, 1]$, throttle input decided as per the optimality criterion
δ_f	$\in [0, 1]$, enforces forced coast arcs at any time for any duration
δ_k	$\in [0, 1]$, throttle input ensuring no operation when $P_{\text{av}} < P_{\text{min}}$
$\hat{\boldsymbol{\alpha}}$	thrust steering unit vector
η_d	duty cycle
σ	time degradation factor of the solar arrays
δ	$\in [0, 1]$, engine throttling input
δ^*	$\in [0, 1]$, optimal engine throttling input

η	thruster efficiency
$\rho_p, \rho_c, \rho_b, \rho_f, \rho_k, \rho_m$	homotopy parameters to enforce various discontinuous events
χ	activation functions

TABLE OF CONTENTS

Page

ABSTRACT ii

DEDICATION iv

ACKNOWLEDGMENTS v

CONTRIBUTORS AND FUNDING SOURCES vii

NOMENCLATURE viii

TABLE OF CONTENTS xii

LIST OF FIGURES xv

LIST OF TABLES xxi

1. INTRODUCTION AND LITERATURE REVIEW 1

    1.1 Summary 11

2. **Orbit Transfers** 13

    2.1 Preliminaries 14
        2.1.1 Dynamics 14
        2.1.2 Coordinate System 15
            2.1.2.1 Cartesian 16
            2.1.2.2 Modified Equinoctial Elements (MEEs) 17
        2.1.3 Optimal Control Problem 18
            2.1.3.1 Indirect Optimization 19
            2.1.3.2 Numerical Continuation 21
            2.1.3.3 Analytical Sensitivities 25
    2.2 Fast Impulsive maneuvers 28
        2.2.1 Control Sweep (CS step) 31
            2.2.1.1 $c_{\max}$ method 31
            2.2.1.2 $a_{\max}$ method 36
        2.2.2 Primer Vector Theory (PVT) step 38
            2.2.2.1 Extraction of Impulses 39
        2.2.3 Impulsive verification 39
        2.2.4 Numerical Example 41
            2.2.4.1 Earth to Mars (E2M) 41

2.2.4.2 Earth to Dionysus (E2D) 44
2.2.4.3 GTO to L1 (GTO2L1) 50
2.3 Low Thrust Transfer with Inequality Constraints 55
2.3.1 Rendezvous Problem Formulation 58
2.3.2 Eclipse Modelling 60
2.3.3 Warm-up Time Model 61
2.3.4 Numerical Simulation 66
2.3.5 Results 67
2.4 Gravity Assist Maneuvers 74
2.4.1 Gravity Assist Formulation 75
2.4.2 Inner Solver 80
2.4.3 Hybrid Optimization Formulation 80
2.4.4 Numerical Example 85
2.4.4.1 Earth-Venus-Mars (EVM) Problem 86
2.4.4.2 Post-analysis of EVM test case 88
2.4.4.3 Thrust Continuation 90

3. **Optimization of Propulsion System and other Spacecraft Sub-systems Selections in Interplanetary Mission Design** 95

3.1 Payload Optimization 95
3.1.1 Power Modelling of Variable-I_{sp} SEP Engines 98
3.1.2 Invariant Embedding 101
3.1.3 Indirect OCP 102
3.1.4 Numerical Example Cases 106
3.1.4.1 Earth to Dionysus Problem 1-3 (EDP1-EDP3) 113
3.1.4.2 Earth to Dionysus Problem 4 (EDP4) 116
3.2 Fuel-Optimization with Ion-Gridded Engines 121
3.2.1 Power Modelling 122
3.2.2 Optimal Control Problem Formulation 123
3.2.2.1 Modelling of VIVT Engines 124
3.2.2.2 Polynomial-Based Modelling of Thruster's Performance 125
3.2.2.3 Multi-Mode Performance Modeling 129
3.2.3 Results 134
3.2.3.1 PF1: VIVT Modelling 137
3.2.3.2 PF2: Polynomial-Based Modelling 140
3.2.3.3 PF3: Multi-Mode Modelling 141
3.3 Discrete Modes Multi-disciplinary Design Optimization 147
3.3.1 Problem Formulation 148
3.3.2 Maximum-Payload-Mass Optimal Control Problem 150
3.3.3 Mode Optimization with Discrete Modes 151
3.3.4 Optimal Mode-Pruning Algorithm 152
3.3.5 Results 154

4. **Guidance & Control** 169

4.1 Covariance Control 169
4.1.1 Bounded Output Covariance Assignment 170
4.1.1.1 Notation 170
4.1.1.2 System Definition 170
4.1.1.3 Problem Statement 171
4.1.2 Main Result and Algorithm 171
4.1.2.1 Remark: Relation with LQR 175
4.1.2.2 CAWS : Covariance Assignment via Weight Selection Algorithm . 175
4.1.3 Example Application 177
4.1.3.1 Attitude maneuver 177
4.1.3.2 Interplanetary maneuver 181
4.1.4 Numerical Results 181
4.1.4.1 Attitude maneuver 181
4.1.4.2 Interplanetary maneuver 189

5. Conclusions & Future Work 197

REFERENCES 199

LIST OF FIGURES

FIGURE Page

2.1 Propulsion Systems 15

2.2 Demonstration of the HTS method for approximating a sign function for different value of ρ 23

2.3 Algorithm flow chart. 30

2.4 Thrust profile and I_{sp} vs. time for the E2M problem (unconstrained VIVT formulation). 42

2.5 Thrust profile and I_{sp} for the E2M problem with $I_{sp,max} = 1500s$..... 42

2.6 Thrust profile and I_{sp} for the E2M problem with $I_{sp,max} = 800s$. 42

2.7 Thrust and switching function of approximate low-thrust impulsive trajectory (top) and norm of the primer vector associated with the optimal impulsive trajectory (bottom) for the E2M problem..... 43

2.8 Minimum-ΔV, three-impulse trajectory for the E2M problem with red arrows indicating impulses. 44

2.9 Continuation trend for Δv_{total} vs a_{max} for the E2D problem..... 45

2.10 Thrust profile with the switching function for the E2D problem with $a_{max} = 1.0 \times 10^{-3}$ m/s^2. 46

2.11 Primer vector magnitude vs. time for the E2D problem with $N_{rev} = 5$..... 46

2.12 Minimum-ΔV, six-impulse trajectory for the E2D problem..... 47

2.13 Maximum acceleration sweep switch surface for Earth to Dionysus maneuver..... 48

2.14 Maximum thrust sweep switch surface for Earth to Dionysus maneuver..... 48

2.15 2D slice of acceleration (top) an thrust (bottom) switch surfaces (S=0 contours)..... 49

2.16 Optimal thrust and switching function profiles for the GTO2L1 problem using unconstrained I_{sp} in c_{max} method. 51

2.17 ΔV, departure time and number of impulses are plotted against the sweeping parameter $a_{\max}$ for the optimal approximate impulsive trajectory for the GTO2L1 problem. 51

2.18 Optimal approximate impulsive trajectory for the GTO2L1 problem. 52

2.19 Acceleration and switching function profile for the GTO2L1 problem for $a_{\max} = 7.5e^{-3}m/s^2$ 53

2.20 Δv distribution for the optimal approximate impulsive trajectory for the GTO2L1 problem plotted on a log scale against time of impulses. 53

2.21 Schematic for a time explicit control operational constraint. 60

2.22 Schematic for a time explicit control operational constraint of first kind. 62

2.23 Schematic for a time explicit control operational constraint. 62

2.24 Minimum time trajectory for the GTO to GEO maneuver with thrust history reflecting eclipse constraints. 69

2.25 Thrust profile for the GTO to GEO maneuver with coast arcs owing to eclipse and warm up constraints. 70

2.26 Trajectory for the GTO to GEO maneuver with thrust history, eclipse and warm up times indicated (XY view). 71

2.27 Trajectory for the GTO to GEO maneuver with thrust history, eclipse and warm up times indicated (YZ view). 71

2.28 Thrust profile for the GTO to GEO maneuver with coast arcs owing to eclipse and warm up constraints. 72

2.29 Schematics for a patched-conic fly-by maneuver. 75

2.30 Spherical formulation of $\boldsymbol{v}_{\infty}^{-}$. 77

2.31 Spherical angles used to orient $\mathbf{v}_{\infty}^{-}$. 77

2.32 Definition of B Plane for gravity-assist. 79

2.33 Impulsive gravity-assist transfer schematic. 81

2.34 Optimal trajectory for the EVM problem with the direction of thrust indicated by red arrows. 83

2.35 Optimal thrust history and switching profile for the EVM problem for $\rho = 10^{-6}$. 85

2.36 Extremal map for EVM impulsive and low-thrust solutions; $T_0 = 0.75N$ via a single PSO run with $\rho = 0.7$. 87

2.37 Cluster of the converged solutions vs. departure date corresponding to the best PSO initiated iterations of the hybrid solver for EVM, $T_0 = 0.75N$. 87

2.38 Cluster of the solutions vs time of flight corresponding to the best iterations of the hybrid solver for EVM, $T_0 = 0.75N$. 88

2.39 Comparison of transfer energy history obtained for the optimal solution from our tool, MALTO, EMTG. 89

2.40 Comparison of orbit transfer osculating inclination history for the optimal solution from this work, MALTO, EMTG and ZOSO with the same initial guess. 90

2.41 Comparison of optimal result obtained using MALTO, EMTG and ZOSO using the same initial guess. 91

2.42 Comparison of final mass obtained against varying nominal thrust using three different strategies. 92

2.43 Near-Optimal thrust profile for EVM for $T_0 = 0.222N$. 93

2.44 Contour plot of optimal switching surface. 94

3.1 Spacecraft payload and electric propulsion sub-system mass breakdown. 96

3.2 EDP1: Optimal trajectory with the direction of thrust indicated by red arrows for $\rho_b = \rho_p = 1.0 \times 10^{-4}$ and $\rho_c = 1.0 \times 10^{-5}$ 109

3.3 EDP1: Comparison of thrust profile for different test runs to determine the most fuel-optimal solution with fixed I_{sp} values. 110

3.4 EDP1: Variation in osculating true anomaly, thrust profile and acceleration (log scale) vs. time; $\rho_b = 1 \times 10^{-4}$, $\rho_p = 1 \times 10^{-4}$. 111

3.5 EDP2: Thrust profile, power activation constraint and switching function vs. time; SF and g_P are both normalized by 10000 for better visibility of thrust profile. 112

3.6 EDP2: osculating true anomaly, thrust profile and I_{sp} vs. time; $\rho_b = \rho_p = 1 \times 10^{-4}$ and $\rho_c = 1 \times 10^{-5}$ 112

3.7 EDP3: thrust profile, power activation constraint and power switching function vs. time; g_P is normalized by 10000 for better visibility of thrust profile. 114

3.8 EDP3: The osculating true anomaly, thrust profile, and I_{sp} vs. time; $\rho_b = \rho_p = 1.0 \times 10^{-4}$ and $\rho_c = 1.0 \times 10^{-5}$ 115

3.9 EDP4: Comparison of evolution of thruster efficiency for linear and quadratic modelling. 115

3.10 EDP4: Comparison of time history of optimal I_{sp} for constant, linear and quadratic modelling of thruster efficiency. 116

3.11 EDP4: The osculating true anomaly, thrust profile, and I_{sp} vs. time for linearly varying efficiency,η_l; $\rho_b = \rho_p = 1.0 \times 10^{-4}$ and $\rho_c = 1.0 \times 10^{-5}$ 117

3.12 EDP4: The osculating true anomaly, thrust profile, and I_{sp} vs. time for quadratically varying η_q; $\rho_b = \rho_p = 1.0 \times 10^{-4}$ and $\rho_c = 1.0 \times 10^{-5}$ 118

3.13 EDP5: The osculating true anomaly, thrust profile, and I_{sp} vs. time; $\rho_b = \rho_p = 1.0 \times 10^{-4}$ and $\rho_c = 1.0 \times 10^{-3}$ 119

3.14 The best fit curve for thrust vs. power taking into account both all modes and selected modes. Out of the 21 operation modes of SPT-140, 7 modes (pink circles) are selected. 126

3.15 The best-fit curve for mass flow rate vs. power taking for all and a few selected modes. Out of the 21 operation modes of SPT-140, 7 modes (pink circles) are selected. 127

3.16 The best fit curve (linear and quadratic) for thruster efficiency (η) vs. I_{sp} for all modes. Out of the 21 operation modes of SPT-140, 7 modes (pink circles) are some selected modes. 128

3.17 The optimal VIVT trajectory. Trajectories obtained using other propulsion modelling are graphically identical. 136

3.18 PF1: Time histories of the osculating true anomaly, thrust profile and specific impulse. 138

3.19 PF1: Thrust profile, power activation constraint and switching function vs. time; SF and g_P are both normalized by 10000 for better visibility of thrust profile. 138

3.20 PF2: Osculating true anomaly, thrust profile, and specific impulse vs. time. 139

3.21 PF3: Osculating true anomaly, thrust, and I_{sp} vs. time; the gaps in the I_{sp} profile at the time of coasting denote undefined values. 140

3.22 PF3: Plot of power differential function ($P_{av} - P_{sel}$) in kW corresponding to each mode vs. time. 141

3.23 PF3: Plot of switching function (SF) corresponding to each mode vs. time. 142

3.24 PF3: Plot of Hamiltonian corresponding to each mode vs. time. 143

3.25 PF3: Optimal thrust mode selection vs. time. 146

3.26 Payload and propulsion sub-system mass breakdown. 149

3.27 Comparison of All-Mode optimization (left block) to two-tier optimization (right block) 153

3.28 Three-dimensional view of the optimal trajectory for the most optimal solution. 155

3.29 Time histories of power differential (Pdiff) and SF for operating and non-operating (black) modes for $N_{\text{sel}} = N_{\text{tot}}$ case. 156

3.30 Profiles of the Hamiltonian for operating and non-operating (black) modes for $N_{\text{sel}} = N_{\text{tot}}$ case. 157

3.31 Time histories of thrust, SF and g_p for $N_{\text{sel}} = N_{\text{tot}}$ case. 157

3.32 Time history of the optimal selected modes for $N_{\text{sel}} = N_{\text{tot}}$ case. 159

3.33 Comparison of the time histories of the optimal selected modes for all pruned cases. 160

3.34 Variation of payload mass (m_u) against the number of operating modes. 162

4.1 Time history of the diagonal entries of the output covariance for all states using the $\boldsymbol{Q}_d$ matrix designed by CAWS. 182

4.2 Rate of elimination of time points that violate the covariance bound constraint during CAWS. 183

4.3 Diagonal entries for the designed $\boldsymbol{Q}_d$ matrix profile plotted against time-steps. 184

4.4 Time history of errors in CRPs and angular velocities plotted against time with the black lines (solid or dashed) denoting the set covariance bound for time varying $\boldsymbol{Q}$. . 185

4.5 Time history of controls for 100 sample trajectories for time varying $\boldsymbol{Q}$. 185

4.6 Time history of errors in CRPs and angular velocities plotted against time with the black lines (solid or dashed) denoting the prescribed covariance bound for constant $\boldsymbol{Q_c}$ case. 186

4.7 Time history of controls for 100 sample trajectories for constant $\boldsymbol{Q_c}$ case. 187

4.8 Comparison of standard deviation of feedback control history for designed $\boldsymbol{Q_d}$ and constant $\boldsymbol{Q_c}$ cases on linearized system and the non-linear Monte Carlo (MC) simulations. 188

4.9 Nominal fuel optimal trajectory from Earth to Mars with dashed lines displaying tracked trajectories. 189

4.10 Time history of the diagonal entries of the output covariance for all states using the $\boldsymbol{Q}_d$ matrix designed by CAWS. The dashed black lines here are the set covariance bounds on the individual states. 190

4.11 Rate of elimination of time points that violate the covariance bound constraint during CAWS..... 192

4.12 Diagonal entries for the designed $\boldsymbol{Q}_d$ matrix profile plotted against time-steps. Both figures are accompanied by a zoomed-in mini-plot to illustrate the fine variations in the profile at the initial time steps..... 192

4.13 Time history of errors in position and velocity plotted against time with the solid black lines denoting the set covariance bound for time varying $\boldsymbol{Q}$. The large difference between the scaling of the two plots is due to the normalization scheme adopted..... 193

4.14 Time history of controls for 100 sample trajectories for time varying $\boldsymbol{Q}$..... 194

4.15 Mass history as well as final mass values for the 100 sample trajectories are plotted for time varying $\boldsymbol{Q}$. The dashed black lines in the left figure denote the mass history for the nominal trajectory and the embedded top and bottom mini-plots are the zoomed-in versions of the first encountered thrust and coast arcs respectively. ... 195

LIST OF TABLES

TABLE Page

2.1 Comparison of the E2M Impulsive solutions. 43

2.2 Comparison of the approximate and optimal minimum-ΔV solutions for the E2D problem. 50

2.3 Coefficients for polynomial interpolation of Sun's position. 66

2.4 GTO-GEO maneuver boundary conditions 68

2.5 Spacecraft Parameters 68

2.6 Summary of results 72

2.7 Optimal Design Variables 82

2.8 Engine Specifications 84

2.9 EVM optimal result for the low-thrust transfer with $\rho = 1.0 \times 10^{-6}$ 84

3.1 Summary of different cases for the TPBVP 107

3.2 Spacecraft parameters; γ_1, γ_2 and a_{tk} are taken from [1] and P_{BL}, P_{max} and PL are adopted from [2]. 108

3.3 EPD1: Final mass for a range of I_{sp} values for a fixed-I_{sp} thruster. 113

3.4 Comparison of results of five cases (EDP1-5) for Earth-to-Dionysus problem. 118

3.5 Coefficients for polynomial interpolation of control variables for SPT-140. 125

3.6 Operation modes of the Hall-effect SPT-140 thruster [3]. 126

3.7 Summary of the control inputs and the form of SF for the three propulsion modelling approaches. 133

3.8 Spacecraft parameters used for the three test cases. 134

3.9 Design parameters for the E-M-P mission. 135

3.10 Design variables of the PSO with bounds and the final converged solution. 136

3.11 Selected Operation Modes of SPT-140 for E-M-P mission. 144

3.12 Comparison of results of the Earth-Mars-Pysche problem using VIVT, polynomial and optimal discrete modes propulsion models using an SPT-140 thruster. 145

3.13 Comparison of masses and P_{BL} for solutions with different number of modes. 161

3.14 Summary of Pdiff and SF for solutions with different number of modes: $N_{\text{sel}} = \{1, 2, 3, 4, 5\}$ 164

3.15 Thrust, SF, g_p, and Hamiltonian for solutions with different number of modes- $N_{\text{sel}} = \{1, 2, 3, 4, 5\}$ 166

4.1 Boundary conditions and parameters 182

4.2 Tracking parameters for interplanetary maneuver 191

1. INTRODUCTION AND LITERATURE REVIEW

Since the earliest days of discovery and experimentation, rockets have evolved from gunpowder devices to multi-staged rockets. Led by several pioneers like Tsiolkovosky, Goddard, Von Karman, Malina, and Oberth, the ambition of venturing deeper into space has been accomplished by an array of incrementally improving propulsion systems categorized broadly into class of chemical engines, electric engines and propellant-less engines like solar sails and electrodynamic tethers. Pioneers like Robert Goddard recognized early on that rocket hardware innovations must necessarily go hand in hand with enhanced active control and trajectory design. The current era is led by the technological advancements in solar electric propulsion (SEP) systems that have expanded the capability of spacecraft in many respects. These advancements are especially relevant for scientific exploration, robotic and re-supply missions. These enhanced spacecraft capabilities reflecting especially the advanced low thrust propulsion technology also induce the need for numerical enhancements in the field of trajectory optimization. With more complex engines that may involve optimization over both continuous and discrete design variables (e.g., operation mode and number of active engines), it has become evident that novel methods are needed to solve for fuel- or time-optimal trajectories. Remarkably these advancements, while aimed mainly at low thrust missions have turned out to be applicable to more general high thrust applications.

Trajectory optimization for these missions is most often addressed by two major approaches; solving by *direct* methods or *indirect* methods [4]. Direct methods are known to have better robustness with respect to the initial guess but the typically artistic parameterization may lead to a large number of variables and yet, a poor approximation of the extremal and for the case of moderate dimensionality of the parameterization [5]. Indirect methods, on the other hand, typically have excellent convergence properties when the initial guess is sufficiently near a solution, but the inherent sensitivities imply a small radius of convergence [6]. Additionally, indirect methods have historically proven difficult to generalize for higher fidelity models and atypical constraints involving inequalities, discontinuities, and path constraints. Even with the availability of fast modern com-

puting, direct methods, with respect to space mission applications, have retained their traditional adoption lead over the more rigorous indirect based methods [7]. In some broad sense, this dissertation is motivated by the recent progress in indirect optimization that promise to disrupt the state of practice. It will become clear in reading this dissertation that indirect methods are being rapidly matured and are indeed now capable of robust convergence, even for discontinuous controls and non-linear state and control variable inequality constraints.

In order to set up the trajectory optimization problem, every propulsion system must be modeled as an appropriate forcing function to formulate the dynamics of the rocket system. Two most popular propulsion systems are: 1) Chemical engines: Near impulsive short burn-time maneuvers 2) Electric engines: Low thrust long burn-time maneuvers. The thrusting capability of the chemical engines is frequently idealized and quantified in terms of perfect impulses that are equivalent to a dirac delta function and is approximately and practically realized as short duration finite burns. One evident exception is in the case of launch trajectories which are high thrust but are operated for a long duration and hence cannot be adequately approximated as impulsive. Impulsive maneuvers, however, have always held a special place within reachability analysis studies and preliminary design phases of space missions [8, 9] as well as uncertainty propagation analysis [10]. Especially, for chemical engines used for deep space orbit transfer, high thrust is usually applied with burn time very short compared to long coast arcs. Impulsive maneuvers also provide the theoretical limits for minimum-time and minimum-fuel extremals and are therefore used to do preliminary analysis and feasibility studies. The earliest efforts in finding the optimal impulsive solutions for orbit transfer were carried out by Lawden, culminating in Lawden's necessary conditions [11] followed by the works by Edelbaum [12, 13]. Traditional methods for finding minimum-ΔV trajectories use heuristics [14] and rely on parameter optimization and transcription methods that keep increasing the number, estimated times, directions, and magnitudes of the impulses. For trajectories that consist of N impulses, non-linear optimization over a $4N$ dimensional search space $(t_i, \Delta v_i, i = 1, 2...N)$ has to be performed. However, the search space is riddled with local extrema with no guaranteed unimodal performance hypersurface [15]. When N is a large two-digit number,

experience shows that the dual curse of non-linearity and high dimensionality can defeat even the best available non-linear programming algorithm.

Evolutionary methods have been used in many works [16, 17, 18] to attempt finding a global optimal, but the solutions are a result of heuristic bootstrapping approaches and an optimal solution is not guaranteed. A review of the trajectory optimization methods for solving minimum-fuel impulsive rendezvous problems is given in [19]. Historically, indirect methods have also been either too cumbersome to converge, leading to challenging optimization problems as the number of impulses grow into double digits, or have suffered from multiple closely located or non-unique solutions [15]. Recently, Taheri and Junkins [20] introduced the concept of *optimal switching surfaces* for indirect optimal minimal fuel trajectory and answered Edelbaum's question [12] with a surprising finding that *there does not always exist a unique optimal answer to Edelbaum's question.* However, their proposed methodology required information about maximum thrust magnitude, the specific impulse of the propulsion system as well as the mass of the spacecraft, which is necessary for constructing fuel- and time-optimal trajectories. In view of the computation time required to generate the results using the above method, a set of advancements are needed and are proposed in this work to facilitate and accelerate the numerical solution procedure by minimization of the integral of the acceleration norm. This approach does not need to specify mass, I_{sp} or more maximum thrust levels. This approach also allows the continuous version of Edelbaum's minimum impulse question to be addressed. It is also more intuitively comfortable that the infinite acceleration limiting case is the impulsive answer to Edelbaum's question.

Compared to chemical propulsion, electric propulsion provides higher specific impulse, an improved payload-to-mass ratio [21, 22] and low thrust that results in a longer time of flight. Importantly, chemical propulsion requires a significant fraction of the spacecraft dry mass to be devoted to plumbing and nozzle hardware, in contrast to electric propulsion with much lower propulsion system hardware mass. Nuclear Electric propulsion (NEP) engines are most typically modeled as constant thrust, constant specific impulse with a throttling function that shuts the thruster "on" or "off'. The optimum throttle function, in case of fuel-optimal solutions, give rise to a thrust profile

featuring a bang-off-bang structure that has been handled using a variety of smoothing techniques to aid convergence of gradient based solvers [4, 6]. SEP thruster delivers thrust as a function of specific impulse (I_{sp}), power available and the thruster efficiency [23, 24]. While a high-I_{sp} engine reduces the propellant mass, a high-thrust engine reduces the overall trip time. Therefore, a freedom to select thrust and I_{sp} can ideally be exploited to strike a trade-off between time of flight and fuel consumption for a given available power to the engine. Conceptual variable-I_{sp} engines are used to exploit this feature, driving the optimization to include I_{sp} as one of the optimization variables within some bounds for optimal management of available power.

In recent years, there has been significant studies aimed at uitilization of variable-I_{sp} thrusters for their reduced propellant consumption feature [25, 26, 27, 28]. Mengali et al. [29] solved the fuel-optimal rendezvous problem using bounded variable I_{sp} and variable thruster efficiency. Taheri et al. [30] introduced and demonstrated the application of a novel Composite Smooth Control (CSC) framework for solving trajectory optimization problems of spacecraft equipped with variable-I_{sp}, variable-thrust engines. They have also demonstrated the utility of the method for designing fuel-optimal trajectories for spacecraft equipped with multiple engines [31]. In actuality, virtually all currently available engines do not feature an infinite range of values of time variable I_{sp} as considered in variable I_{sp} engines, but only engines with a discrete countable number of operating modes are currently available as featured by gridded-ion engines. Following the successful applications in conducting deep-space missions like the Dawn mission [32], gridded-ion engines like NASA's Evolutionary Xenon Thruster (NEXT) and NASA Solar Electric Propulsion Technology Application Readiness (NSTAR), have assumed center stage for next generation deep space missions. In fact, NASA is set to utilize a fully electrically propelled spacecraft in its upcoming Psyche mission [33]. This mission will be the first to use only Hall-effect thrusters for propulsion with no chemical propellant on board, representing a benchmark and provides an opportunity to gain improved insights while demonstrating the reliability, cost-reductions and performance of Hall-effect thrusters for multi-year missions [34].

These gridded-ion engines usually consist of multiple discrete operating modes of electric

thrusters with specific performance metrics associated with each mode that enable a discrete multi-mode realization of overall control capability of the thruster. Precision mathematical models, from first principles, for these highly nonlinear multi-mode systems are not presently in a mature state of development. As a consequence, experimentally derived models represent the state of the art. These experimented models typically consist of a significant family of operational modes, frequently a double digit. Each of these local modes are characterized pre-flight in the laboratory and the location of these modes in the design space are such that they span the practical capability envelop of the specific engine. In principle, a few thousands of operation modes could possibly be realized through modulation of the current and voltage inputs [35]. Typically, only a handful of these modes, however, are considered practical for a particular mission, owing to the increased hardware requirements for operating more modes, increasing the overall complexity, and introducing the necessity of conducting an expensive systematic calibration of the characteristics of each modes. The frequently disjoint set of experimentally characterized modes, especially when there is a large number of them, may defy any heuristic idea of the resulting performance of the engine but rather are commonly specified as a discrete set of values, typically referred to as a "throttle table".

Polynomial approximations by means of interpolating discrete operation points of multi-mode engines have been historically utilized to approximately capture the aggregate performance of these engines. Despite the lack of guaranteed accuracy in capturing the macroscopic performance of disjoint multi-mode engines, polynomial approximations remain widely used for mission design, because smoothness of these models enhances reliable numerical convergence of gradient-based solvers. Polynomial approximation of multi-mode propulsion system modelling was first reported by Rayman and Williams [36] to investigate the capability of SEP systems. Mengali and Quarta [37] solved minimum-time rendezvous maneuvers using the discrete modes of the NEXT by an indirect approach. Knittel et al. [38] captured the multiple operation modes of the NEXT using improved polynomial approximations. Their work involved solving problems with gravity-assist maneuvers using a direct optimization method. Taheri et al [39] also attempted at solving

a fuel-optimal trajectory to rendezvous with comet 67P/Churyumov-Gerasimenko using the CSC framework. However, the results obtained by Taheri et al were sub-optimal.

Apart from regularizing the discrete modes of operation of propulsion systems, smoothing techniques are also employed to smooth discontinuities associated with state path inequality constraints[40] and all other inequality constraints [41] into an invariant embedding indirect optimization framework. Through judicious smooth approximation of all control switch discontinuities and inequality constraints, the discontinuous Pontryagin necessary conditions can be made the limiting case of smooth family of differential equations. These constraints may reflect either a certain science objective, or orbit determination requirements, or all other operational constraints. The key elements about these inequality constraints are their frequent dependence on osculating states [41] or predetermined time horizon [42] in the mission. However, there are discrete events and operational constraints that are chanced on specific states as well as being explicit functions of time. Typical mission inequality constraints embody a variety of scenarios such as thermal constraints in sun proximity missions, post eclipse warm-up time for engines, operational limitation of thrusters, radiation regulation, limitation on pointing to enable imaging to accommodate communications etc.

It is also frequently the case that some operational constraints play a critical role in establishing the feasibility of the mission. For instance, in order to regulate the duration of time spent in the eclipse or radiation absorbed in Van Allen belt, one can either explicitly choose net eclipse duration as an optimization objective or can formally introduce an upper bound constraint on the net duration depending on their significance in the mission. Obviously, imposing ad hoc decisions as constraints frequently leads to significant performance loss. The algorithm developed in this work provides a mathematically smooth framework to accommodate all inequality constraints scenarios while using an indirect optimization scheme. In the invariant embedding approach presented, as the homotopy parameter is swept towards zero, the switches approach instantaneous for all practical purposes, and the trajectory and controls approach high precision satisfaction of the underlying Pontryagin necessary conditions. When the smoothing parameter is large, the smooth

trajectory is much easier to optimize. As the homotopy parameter is swept smaller, the initially more challenging, near discontinuous trajectory and controls are now approached smoothly.

Most trajectory optimization methods revolve around minimizing fuel or time and not the primary science payload parameters which intrinsically involves optimization of launch vehicle, solar arrays, spacecraft subsystems etc. A *co-optimization* of vehicle and/or payload parameters however lead to a "more optimal" final payload trajectory which can be very different from the idealized minimum fuel solution, as shown by Arya et al [43]. Therefore, operational couplings that exist in spacecraft sub-systems present an opportunity to conduct simultaneous optimization of different sub-systems (or disciplines); this class of problems are more broadly known as multi-disciplinary optimization (MDO). While MDO has frequently been done in other settings, until recently MDO and indirect optimal control to design space missions, especially with non-linear inequality constraints including design of the optimal trajectory has not been done. For instance, in case of Solar Electric Propulsion (SEP) system, power is generated by solar arrays, which in turn is a function of distance of the spacecraft from the Sun, powers all subsystems as well as determines the performance of the thruster [33]. However, altering the size of the solar array changes the system mass and couples with many other sub-systems. The presence of power cross coupling between the several units of the spacecraft system as well as the optimal trajectory itself inspires generalization of the approach to accommodate optimization over both continuous and discrete design variables.

Until recent advances were made that significantly enhanced convergence of indirect optimal control, general co-optimization would not have likely led to practical algorithms. Rather heuristic experience based insights have been used to specify system design parameters that were held fixed during trajectory optimization. However, a few special cases with coupled subsystem and trajectory have been successful. Vavrina et al. [44] formulated a hybrid control algorithm to do joint optimization of spacecraft and trajectory for small body missions involving flybys. They used a combination of a genetic algorithm and Sims & Flanagan-based transcription [45] to solve for approximate low thrust fuel-optimal trajectories. Petukhov et al. [1] provided a framework for the joint optimization of the trajectory with the spacecraft parameters and systems.

When the inherent coupling is considered along with the discrete operating modes of the gridded-ion engine, the optimization problem becomes richer and beyond the scope of simple heuristic margins. Furthermore, when these generalizations in the context of indirect methods are considered, the resulting optimization methods portray breakthrough capabilities. The selection of the engine and more specifically the operating range and the specific number of operating modes play an integral role in the overall mission feasibility and optimization analysis and has a significant impact on the design of the optimal trajectory. However, the *optimal* trajectory and its design methodology should be flexible enough to accommodate practical consideration, allowing a variety of sub-optimal solutions to be explored and adopted if the analyst expects the approach to be used in actual missions. It will remain impossible to anticipate "everything" when designing an optimal trajectory, so in the end game of executing an actual mission, the trajectory design tools must accommodate exploration of neighboring solutions. For example, the use of a lesser number of operating modes not only reduces the complexity of the Power Processing Unit (PPU) but also reduces the number of mode switches, providing robustness towards execution failures. Therefore, it is beneficial to include such sub-optimal solutions as trade studies seamlessly in the trajectory optimization process for a coordination between the mission designer and propulsion engineer even at a preliminary stage of mission design and at subsequent time prior to launch. The availability of the optimal solution obviously allows one to assess the loss of optimality when considering various sub-optimal solutions.

With reference to the MDO literature [46, 47, 48], the overwhelming choice of optimization algorithms to solve such complex problems are direct methods. This drives the motivation of one of the segments of this dissertation that pushes the boundaries of traditional trajectory optimization [49, 50] by demonstrating a novel fusion of indirect methods, invariant embedding [51], and mixed integer nonlinear programming [52]. Maturation of indirect MDO trajectory design is believed to be of very significant importance to the field and is one major focus of this dissertation.

Although low-thrust trajectory design methods are conventionally implemented on deterministic system models, in actual spacecraft operations, the trajectories are perturbed by disturbances

including unmodeled external accelerations, guidance/navigation errors, propulsion system performance variations and missed thrust events [53] (i.e., coasting periods contingent on operational failures). For these reasons, a nominal trajectory, typically, is designed adopting a deterministic system assuming a sub-performing and approximated as constant specific impulse engine to implicitly provide actuation authority needed to accommodate "all reasonable" off-nominal errors and unforeseen failures. Due to the inability to model the exact discrete propulsion models in the dynamical model underlying the nominal trajectory, the approximated modelling of propulsion systems augments the mission uncertainty. To accommodate these irregularities and discrepancies, heuristic parameters in terms of duty cycle, margins and forced coasts are introduced that require robustness evaluation and additional tuning. These approaches in the current state of practice, require professional hand-tuning and are time consuming, while still leading to conservative margins [54]. Olympio and Yam [55] have suggested a non-heursitic surrogate-based method featuring a single engine failure. Additionally, Olympio [56] has also solved a two-stage stochastic programming problem while still handling only one temporary engine failure. Both the methods are not generally applicable to model multiple engine failures and the more general persistent disturbances.

One of the most important elements of such a stochastic guidance approach is the design of the tracking control. Among the closed loop techniques, Linear Quadratic Regulator (LQR) is the most common approach used to determine the feedback control required to closely follow the nominal with or without the given control upper bound. Other traditional techniques comprise of sliding mode control [57] that utilizes feedback linearization and an add-on term for uncertainty and robust control schemes like H_∞ control that provides spacecraft stability in the presence of disturbances by solving the Hamilton-Jacobi inequalities. Another class of controllers that have been shown to be robust to model errors and disturbances are based on adaptive control techniques [58]. Adaptive techniques [59] estimate the external torques by tracking a Lyapunov function and updating the selected model parameters in operation based on measured performances. Lyapunov based methods provide asymptotic stability characteristics with respect to tracking errors but not in learning the uncertain parameters. Some Lyapunov approaches have been developed for a fast computa-

tion of a feasible trajectory that can be designed to intermittently track the nominal. Additionally, approaches like Model Predictive Control (MPC) have risen to prominence owing to an increase in computing capabilities especially in the ability to solve online finite horizon optimization algorithms. The main advantage claimed for these last two approaches is their direct application using the high fidelity non-linear dynamical model, removing the requirement of linearization.

There has also been recent research in the area of covariance control, where its importance in conducting stochastic mission analysis was first recognized because it yields comparable accuracy to a Monte Carlo analysis with much less computational effort [60]. Linear covariance techniques have been presented as an efficient methodology to design and statistically analyze stability of the closed-loop systems and performance of the desired outputs [61, 62]. Concurrently, covariance analysis has also been used specifically for bounding the output and state covariance at the final time for both continuous and discrete-time systems [63, 64, 62]. These works were limited to bounding the steady-state covariance for only the linear time-invariant systems [63, 64, 65]. The covariance control problem has recently been studied with applications in space mission designs (powered descent guidance algorithm) and vehicle path planning [66, 67, 68]. These finite-horizon covariance steering problems have been explored in the presence of both convex and non-convex state constraints [69] which can also be formulated as chance constraints allowing the satisfaction of constraints with specified (high) probability [67, 70]. A solution for nonlinear dynamical systems was also recently proposed as an iterative covariance steering with convex state chance constraints [68]. In this work, a novel covariance based controller is introduced that mimics standard LQR implementation but assigns a 3D bounded space for the manifold of trajectories in the presence of disturbances. This approach is applied to departure motion to a deterministic nominal trajectory. The controller features self-adaptive control tuning parameters that are adapted to achieve the time varying output covariance (error tube) as defined per the mission objectives. The stochastic covariance constrained guidance approach is a novel contribution to the literature that is anticipated to be the first step towards an autonomous guidance approach that will enhance autonomy, reliability and precision of future missions.

1.1 Summary

With innovations in propulsion and material technology, we have entered an era involving long duration missions that are targeting science experiments revolving about some specific planets or asteroids in deep space. The advent of electric propulsion technology and its suitability for such multi-year, low-thrust missions has inspired this dissertation, focused on investigation of enhanced optimization techniques for designing the ensuing trajectories more efficiently. One of the primary objectives of this dissertation is to revisit indirect methods and recondition this approach with novel smoothing mechanisms to rigorously and more efficiently include various inequality constraints and through these innovations, re-enhance its domain of convergence to handle complex optimal control problems (OCPs) of multi-revolution trajectories. This method is a generalized invariant embedding approach that embeds the Pontryagin necessary conditions into a smooth family that can smoothly approach satisfaction of the exact necessary conditions with arbitrary precision.

The other objective is to incorporate the concept of spacecraft system level optimization into the preliminary mission design phase using indirect methods and thereby launch an MDO indirect family of methods for mission design. For a successful mission design, there are multiple preliminary aspects that are to be considered like mission objectives, propulsion constraints, solar power sub-systems and parameters, trajectory design and operational constraints. Such system optimization problems call for a multidisciplinary design approach where these coupled aspects provide an opportunity for simultaneous optimization of different sub-systems.

The introduced algorithms enjoy local optimality guaranteed by indirect methods though hybrid methods are employed to seek the global optimal when multiple local optimal solutions are suspected. The approach established in this work very significantly expands the class of trajectory optimization problems solvable by indirect methods by a novel fusion of indirect methods, invariant embedding, and mixed integer nonlinear programming. The novelty lies in not only delivering the most optimal thrust-modes for payload maximization but also in enabling sub-optimal trade studies by investing into a systematic mode-pruning strategy. This proposed framework provides the foundation for a practical tool-set needed for trajectory and sub-system design purposes with

designer defined number of operating modes. The last objective is to provide an advanced tracking algorithm by means of solving a novel covariance assignment problem to facilitate autonomous space travel amidst model uncertainties. Advancing indirect and hybrid optimization methods to accommodate a new lead of autonomy is the over-arching goal of this dissertation. To summarise, the contribution of the dissertation is developing advanced algorithms that allow pragmatic increments in the process of preliminary mission design while augmenting the capability to execute the final mission autonomously with a novel tracking algorithm. The methods introduced in this dissertation open the pathway for a more involved optimization that provides a breakthrough recipe for system optimization with discrete operational constraints/events. The methodology introduced is not limited to only aerospace systems and therefore, is expected to find applications to dynamical systems broadly. The dissertation is divided into three sections: a) Trajectory design b) System design and optimization c) Autonomous tracking control. Each section comprises multiple chapters with clearly defined contributions within every chapter. The key objectives/highlights are listed below:

1. Fast algorithm to find near-optimal multiple impulses maneuvers using a novel acceleration based method.

2. An indirect scheme is introduced that can include the discrete operational constraints that are explicit functions of time into the trajectory optimization.

3. Indirect methods are enhanced to enable a simultaneous optimization of solar arrays, realistic discrete modes of gridded-ion propulsion system and trajectory.

4. A hybrid strategy is devised that enables trade studies when only a subset of all the available operating modes are considered. The maximum number of operating modes in this subset is a user-defined input.

5. A novel covariance controller is designed that can follow the prescribed time varying covariance profile for non-linear systems in the presence of model uncertainty.

2. **Orbit Transfers** [1]

Largely for orbit transfer optimizations, preliminary mission design and analysis is conducted assuming two body dynamics model. Fortunately, with this assumption, the natural evolution of the states undergo continuous and well-behaved changes (i.e., the orbits are quasi-elliptical) when weak perturbing force (i.e. low engine thrust) is applied. Over many decades, many propulsion systems have been developed and are still being enhanced that extend our reachability to outer space beyond our mother planet and ultimately, beyond the solar system. In fact, some conceptual engines like Variable I_{sp}, variable thrust (VIVT) engines are invented and researched to aid mainly the mission analysis process. VIVT engines are considered capable of providing infinite combinations of thrust and I_{sp} values within specific bounds such that they lead to insights and a good trade-off between both time and fuel optimal solutions.

The current era of un-manned space travel is dominated by electric propulsion systems; more specifically solar electric propulsion (SEP). Even with this paradigm shift in propulsion technology from chemical engines to SEP, other propulsion systems are still relevant and are used for certain segments of the mission like the use of impulsive maneuver during launch, re-entry or for station keeping. For long duration maneuvers like in case of interplanetary missions to the outer planets and deep space missions, gravity-assist maneuvers using electric propulsion systems have proven to be quite advantageous. The proclivity of low thrust propulsion over chemical propulsion has its reasons rooted into its high specific impulse and improved payload to spacecraft mass ratio. However, the resulting low thrust trajectories exhibit a sequence of intermittent long coasts and continuous thrust profiles with throttling in place of instantaneous impulses that increases the engine operation time, making the optimal control problem (OCP) quite more challenging. Efficient coordinate selection, regularization, use of smoothing techniques, numerical continuation and supplying analytical sensitivities are a key to solving such complex optimization problems.

[1] Reprinted with permission from "Costate mapping for indirect trajectory optimization" by Taheri, Ehsan and Arya, Vishala and Junkins, John, 2021. Astrodynamics, Volume 5(4), 359–371, Copyright 2021 by Springer

2.1 Preliminaries

2.1.1 Dynamics

The dynamics considered in this thesis is corresponding to weakly perturbed Keplerian motion with the assumption of two body dynamics where the central body is considered as a point mass and is taken to be the major source of gravitational perturbation. It is the modelling of the forcing function (the thruster) which varies extensively in different sections like the use of chemical engines, nuclear electric propulsion (NEP), solar electric propulsion (SEP), gridded-ion engines, Hall thrusters etc. A summary plot for some of the propulsion systems are provided in Figure 2.1 to give an I_{sp} vs thrust level overview of their capacity and draw some theoretical comparisons. A wide range of these propulsion systems are used in different space missions depending on the scope, objectives and budget allotted. The deep space exploration missions and a large class of other unmanned missions use the high I_{sp} technologies near the top of the Figure 2.1. As would be shown later, some of the simplified/specialized actuator models are useful for preliminary studies and mission analysis like in conducting back-of the envelope calculations and determining reachability envelopes. Even though most nominal trajectories in this dissertation are evaluated assuming the two body dynamics, the results are still applicable and extendable to high fidelity force models. The generalized control acceleration vector can be parametrized as:

$$\boldsymbol{u} = \frac{T\delta}{mc}\hat{\boldsymbol{\alpha}}, \tag{2.1}$$

where $\hat{\boldsymbol{\alpha}}$ denotes the thrust steering unit vector, δ denotes the throttle input that determines if the thruster is "on" or "off", T stands for the thrust value, m is the mass of the spacecraft and c denotes the exhaust velocity ($c = I_{\text{sp}} g_0$). Depending on the propulsion system, the values of T and I_{sp} can be constants or function of state or tabulated values. The general form of the mass flow rate differential equation can be written as:

$$\dot{m} = -\frac{T\delta}{c} \tag{2.2}$$

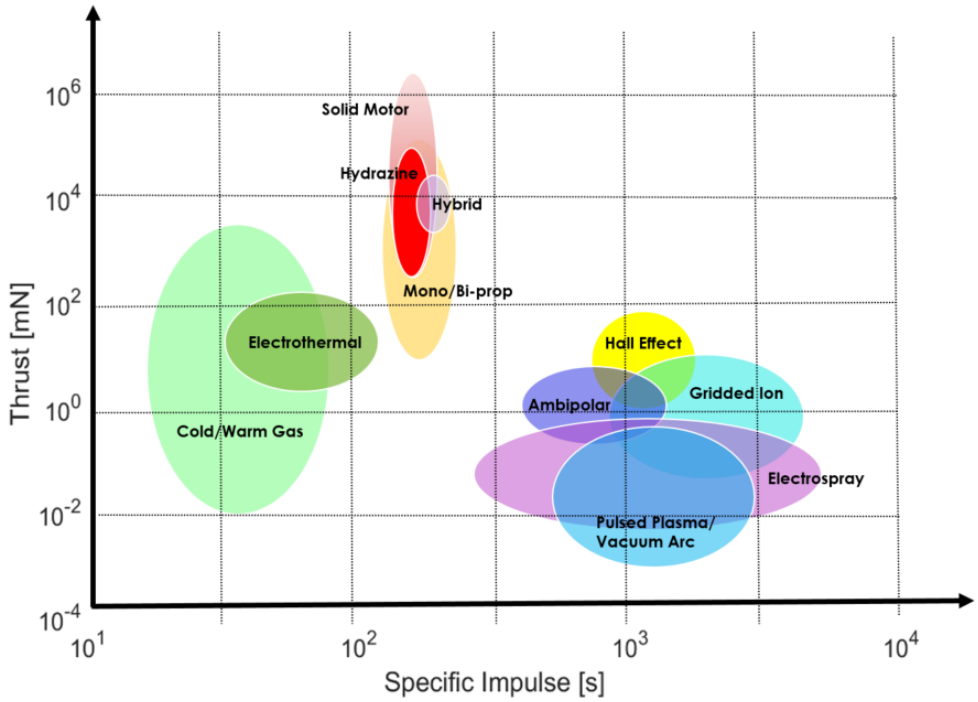

Figure 2.1: Propulsion Systems

2.1.2 Coordinate System

The selection of coordinates to describe system dynamics is integral to efficiently solving any optimization, control or estimation problem not only in the domain of celestial mechanics but every known application. In case of celestial mechanics, the classic choices for conducting state propagation with or without perturbations, have been either a set of orbital elements, Cartesian coordinates or spherical coordinates. Over time, significant effort was poured into developing various transformations and harnessing the ability to find constants of motion, where possible. The classical coordinates often encounter singularities and the "degree of non-linearity" depends on coordinate choices [71]. By exploiting the fact that the translational motion of a spacecraft can be described via a rotating osculating frame embedded in the rigid body, multiple hybrid sets have been researched in literature by use of regularized rotational kinematics in the form of different osculating triads [72]. These different choices aid in eliminating various singularities associated with near zero inclinations and eccentricities.

Moreover, when formulating an indirect optimal control (IOCP) problem which we do in this dissertation, the accuracy of integration is not the sole criteria for selecting a particular set of coordinates. Especially, IOCP problems lead to an augmented state vector by including the co-states associated with each state which are essentially iterated upon to solve a two point boundary value problem (TPBVP). The convergence rate of the gradient based solver used to solve these TPBVPs is affected by the coordinate choice. There is also utility in developing methods for a simple transformation of the converged co-states of the IOCP problem seamlessly from one choice of coordinates to other as detailed in [73]. This straightforward transformation exploits the fact that in the same frame of reference, the Hamiltonian on the optimal solution remains invariant to the coordinate set leading to:

$$\boldsymbol{\lambda}_{\boldsymbol{x}}(t)^{\top}\left[\frac{\partial \boldsymbol{\varrho}}{\partial \boldsymbol{y}}\right]\Bigg|_{t} = \boldsymbol{\lambda}_{\boldsymbol{y}}(t)^{\top}. \tag{2.3}$$

where $\boldsymbol{\varrho}$ represents a non-linear one-to-one continuous and invertible mapping between two different coordinate sets (state variables), say set $\boldsymbol{y}(t)$ and set $\boldsymbol{x}(t)$ written as $\boldsymbol{x}(t) = \boldsymbol{\varrho}(\boldsymbol{y}(t))$. Here $\boldsymbol{\lambda}_{\boldsymbol{x}}$ and $\boldsymbol{\lambda}_{\boldsymbol{y}}$ are the co-states associated with the states in the $\boldsymbol{x}$ and $\boldsymbol{y}$ sets respectively.

The following coordinate choices have particularly been used to define the state variables throughout the dissertation.

2.1.2.1 Cartesian

Let $\boldsymbol{x} = [x, y, z, \dot{x}, \dot{y}, \dot{z}]^{\top}$ and $\boldsymbol{u}_{\text{cart}} = [u_x, u_y, u_z]^{\top}$ denote the state and control vectors, respectively, associated with the set of Cartesian coordinates. The equations of motion can be written as

$$\dot{\boldsymbol{x}} = \mathbf{A}_{\text{cart}} + \mathbb{B}_{\text{cart}}\mathbf{u}, \tag{2.4}$$

where $\mathbf{A}_{\text{cart}}$ and $\mathbb{B}_{\text{cart}}$ matrices are defined as

$$\mathbf{A}_{\text{cart}} = \begin{bmatrix} \boldsymbol{v} \\ -\mu \boldsymbol{r}/r^3 \end{bmatrix}, \mathbb{B}_{\text{cart}} = \begin{bmatrix} \mathbf{0}_{3\times 3} \\ I \end{bmatrix}, \tag{2.5}$$

where $\boldsymbol{r} = [x, y, z]^\top$ and $\boldsymbol{v} = [\dot{x}, \dot{y}, \dot{z}]^\top$. Here, I denotes a 3 by 3 identity matrix and $r = ||\boldsymbol{r}||$. Though the dynamics written in Cartesian coordinates delivers simple expressions, it suffers from leading to poor and unreliable convergence due to (i) all state variables being fast variables, (ii) the inability to enforce number of revolutions around the Sun. The second reason especially can lead to jump in solutions even during the numerical continuation process when the co-states on the boundary are iterated upon.

2.1.2.2 Modified Equinoctial Elements (MEEs)

The main reason for selecting the set of MEEs is that they are known to be superior to other sets of elements and coordinates for solving multi-revolution low-thrust trajectories [74, 72]. On the other hand, a notable difficulty in using the set of MEEs is that the resulting algebraic expressions for the dynamics of costates become lengthier compared to when the set of Cartesian coordinates is used. In addition, the disturbances (e.g., solar radiation pressure or third-body perturbations) have to be expressed in the Local-Vertical Local-Horizontal (LVLH) frame moving with the spacecraft. Despite these considerations, it is still computationally attractive to formulate trajectory optimization problems using the set of MEEs. Application of symbolic toolboxes has facilitated and automated the derivation of the required algebraic expressions[75, 76].

Let $\boldsymbol{x}_{\text{MEE}} = [p, f, g, h, k, l]^\top$ denote the vector of MEEs and let $\boldsymbol{u} = [u_r, u_t, u_n]^\top$ denote the unit direction vector of the thrust force with its components expressed in the local-vertical/local-horizontal (LVLH) frame. The MEE set has five slow variables and one (very regular) fast variable. The slow variables are indeed constants of the motion during any coast phase with $\boldsymbol{u} = 0$. The dynamics for MEEs can be written as

$$\dot{\boldsymbol{x}} = \boldsymbol{A}_{\text{MEE}}(\boldsymbol{x}, t) + \mathbb{B}_{\text{MEE}}(\boldsymbol{x}, t)\boldsymbol{u}, \tag{2.6a}$$

$$\dot{m} = -\frac{T}{c}\delta, \tag{2.6b}$$

where $\mathbf{A}_{\text{MEE}} = [0, 0, 0, 0, 0, \sqrt{\mu p}(\frac{\xi}{p})^2]^\top$ and $\mathbb{B}_{\text{MEE}}$ is defined below as

$$\mathbb{B}_{\text{MEE}} = \begin{bmatrix} 0 & \frac{2p}{\xi}\sqrt{\frac{p}{\mu}} & 0 \\ \sqrt{\frac{p}{\mu}}\sin(l) & \sqrt{\frac{p}{\mu}}\frac{1}{\xi}[(\xi+1)\cos(l)+f] & -\sqrt{\frac{p}{\mu}}\frac{g}{\xi}[h\sin(l)-k\cos(l)] \\ -\sqrt{\frac{p}{\mu}}\cos(l) & \sqrt{\frac{p}{\mu}}\frac{1}{\xi}[(\xi+1)\sin(l)+g] & \sqrt{\frac{p}{\mu}}\frac{f}{\xi}[h\sin(l)-k\cos(l)] \\ 0 & 0 & \sqrt{\frac{p}{\mu}}\frac{s^2\cos(l)}{2\xi} \\ 0 & 0 & \sqrt{\frac{p}{\mu}}\frac{s^2\sin(l)}{2\xi} \\ 0 & 0 & \sqrt{\frac{p}{\mu}}\frac{1}{\xi}[h\sin(l)-k\cos(l)] \end{bmatrix}. \tag{2.7}$$

In these equations, two intermediate variables that frequently appear are $\xi = 1 + f\cos(l) + g\sin(l)$, $s^2 = 1 + h^2 + k^2$, and μ is the gravitational parameter of the central body [77].

2.1.3 Optimal Control Problem

The resulting OCPs are solved by two major approaches: direct methods or indirect methods. Direct methods gained popularity with the advent of modern computing capabilities. They have better robustness with respect to the initial guess; although the parameterization often results in a greater number of variables [1]. They also frequently lead to poor approximation of the extremal, especially when the thrust has to be operated over long periods which is the case for low thrust trajectories [5]. Indirect optimization methods [78], on the other hand, do not require an ad hoc parametrization of state or control variables but rather are based on an analytical derivation beginning with variational calculus concepts, which results in boundary-value problems (BVPs). The formulation involves enforcement of constraints by means of Lagrange multipliers (costates) and in the case of state-dependent inequality constraints, the solution becomes especially challenging. The two-point-boundary-value problem (TPBVP) involves missing boundary conditions on the co-state variables, which are not trivial to compute, thus making the solution process iterative. All infinity of extremal trajectories that reach an infinity of terminal states correspond to an infinite number of initial co-states; One must find the particular initial (or, in some cases final) co-states that generate the desired optimal solution satisfying the necessary conditions. Finding the required

initial/final costates is the most challenging issue with the indirect formulation. Hybrid methods which employ the combination of direct and indirect optimization methods utilize Lagrange co-state equations but convert the OCP into a parameter optimization problem solved using non-linear programming (NLP) [79]. In this dissertation, though both direct and hybrid techniques have been leveraged, the primary focus has been on formulating a general version of indirect based optimization formulation and developing homotopy algorithms based on invariant embedding to enhance convergence in the presence of discontinuous controls and constraints.

2.1.3.1 Indirect Optimization

Let $\boldsymbol{x} \in \mathscr{R}^n$ and $\boldsymbol{u} \in \mathscr{R}^m$ denote the set of state and control vectors, respectively, of a dynamical system. The general form of a cost functional in optimal control is expressed as a Bolza problem

$$\underset{\boldsymbol{x}\in\boldsymbol{X},\ \boldsymbol{u}\in\boldsymbol{U}}{\text{minimize}} \quad J = \phi(\boldsymbol{x}(t_0), t_0, \boldsymbol{x}(t_f), t_f) + \int_{t_0}^{t_f} L(\boldsymbol{x}(t), \boldsymbol{u}(t), t)dt,$$

where $\boldsymbol{X}$ and $\boldsymbol{U}$ denote the set of admissible states and controls, respectively, and t_0 and t_f denote the initial and final times, respectively. The state dynamics constitute differential-form type of constraints, which are written collectively as $\dot{\boldsymbol{x}} = \boldsymbol{f}(\boldsymbol{x}(t), \boldsymbol{u}(t), t)$. There are additional path and control constraints as well as endpoint constraints such as:

$$\mathbf{g}_L \leq \mathbf{g}[\boldsymbol{x}(t), \boldsymbol{u}(t)] \leq \mathbf{g}_U \tag{2.8}$$

$$\chi_L \leq \chi[\boldsymbol{x}(t_0), \boldsymbol{u}(t_0), \boldsymbol{x}(t_f), \boldsymbol{u}_(t_f), t_0, t_f] \leq \chi_U \tag{2.9}$$

Denoting $\boldsymbol{\lambda}_{\boldsymbol{x}}$ as the costate vector associated with the state vector, $\boldsymbol{x}$, the optimal control Hamiltonian can be defined:

$$H = L(\boldsymbol{x}(t), \boldsymbol{u}(t), t) + \boldsymbol{\lambda}_{\boldsymbol{x}}^{\top} \boldsymbol{f}(\boldsymbol{x}(t), \boldsymbol{u}(t), t). \tag{2.10}$$

Let $\Phi = \phi + \boldsymbol{\nu}^{\top}\boldsymbol{\psi}$, where $\boldsymbol{\nu}$ are the set of Lagrange multipliers introduced to augment a set of non-linear equality constraints at the initial and final time instants, $\boldsymbol{\psi}(\boldsymbol{x}(t_0), \boldsymbol{x}(t_f), t_0, t_f) = \mathbf{0}$.

Calculus of variation dictates that the total variation (including the variations in the initial and final time) of the augmented cost functional should be zero on an extremal solution, which can be written as

$$\begin{aligned}\delta J_a = &\left[\frac{\partial \Phi}{\partial \boldsymbol{x}(t_0)} + \boldsymbol{\lambda}(t_0)^T\right]\delta \boldsymbol{x}_0 + \left[\frac{\partial \Phi}{\partial t_0} - H(t_0)\right]\delta t_0 \\ &+ \left[\frac{\partial \Phi}{\partial \boldsymbol{x}(t_f)} - \boldsymbol{\lambda}(t_f)^T\right]\delta \boldsymbol{x}_f + \left[\frac{\partial \Phi}{\partial t_f} + H(t_f)\right]\delta t_f \\ &+ \int_{t_0}^{t_f}\left[\left(\frac{\partial H}{\partial \boldsymbol{x}(t)} + \dot{\boldsymbol{\lambda}}^T\right)\delta \boldsymbol{x}(t) + \left(\frac{\partial H}{\partial \boldsymbol{u}(t)}\right)\delta \boldsymbol{u}(t) + \left(\frac{\partial H}{\partial \boldsymbol{\lambda}(t)} - \dot{\boldsymbol{x}}^T\right)\delta \boldsymbol{\lambda}(t)\right] dt + \boldsymbol{\psi}\delta \boldsymbol{\nu}^T.\end{aligned} \tag{2.11}$$

where J_a denotes the augmented cost functional. Note that the variation is derived for a case in which t_0, t_f, $\boldsymbol{x}_0$ and $\boldsymbol{x}_f$ are all fixed. Thus, the entire variation occurs along the trajectory and appears in the integrand and the Euler-Lagrange equations are always satisfied along extremal trajectories. On equating Eq. (2.11) to zero as necessary conditions leads to the following co-state differential equations:

$$\dot{\boldsymbol{\lambda}} = -\left[\frac{\partial H}{\partial \boldsymbol{x}(t)}\right]^T, \quad \frac{\partial H}{\partial \boldsymbol{u}(t)} = 0 \tag{2.12}$$

and additional transversality conditions at initial or final time from the terms outside the integrand in Eq. (2.11) arise, wherever applicable. It is not always possible to evaluate the optimal control history using Eq. (2.12) if the control variable is discrete in nature, affine in the Hamiltonian, singular for some part of the trajectory or is constrained. The weak form of Pontryagin's Minimum Principle (PMP) is then popularly used necessary condition to determine optimal values of the control variables in its admissible set ($u \in \Omega$) such that:

$$u^* = \arg\min_{u \in \Omega} H(\boldsymbol{x}^*(t), \delta(t), \boldsymbol{\lambda}^*(t)). \tag{2.13}$$

In case of space trajectories, the capability to throttle ($\delta \in 0, 1$) leads to a discrete control variable ($u = \delta(t) u_{\max}$) that can be evaluated using PMP. To determine the optimal throttle (δ), split the Hamiltonian into terms that do not depend on δ denoted by H_0 and the terms containing δ linearly are grouped in H_δ as shown in Eq. (2.14). Here, H_δ act as the *switching function* (SF), the sign of

which determines if δ takes the value of zero or one.

$$H = H_0 - H_\delta \delta, \tag{2.14}$$

$$H_0 = \boldsymbol{\lambda}^\top \boldsymbol{A}_{\text{MEE}}(\boldsymbol{x}, t), \tag{2.15}$$

$$H_\delta = \frac{T}{c}\left[\lambda_m - \frac{c}{m}\mathbb{B}_{\text{MEE}}^\top \boldsymbol{\lambda}_{\boldsymbol{x}} \hat{\boldsymbol{\alpha}} - 1\right] \tag{2.16}$$

Traditionally, in case of inequality constraints on state and control or both, more rigorous techniques involving Kuhn Tucker conditions and other methods are used. These techniques are limited in the most general necessary conditions applications [78]. The case of singular arcs are not treated in this work since they rarely occur in space flight.

2.1.3.2 Numerical Continuation

The importance of numerical continuation methods for solving trajectory optimization problems using indirect based methods cannot be overemphasized. There are two kinds of continuation procedures that are followed in this dissertation: (i) Intrinsic/Indirect continuation (ICO) (ii) Extrinsic/Direct continuation (DCO). Direct continuation deals with continuation directly imposed on the absolute value of the quantity (state or control) while indirect continuation involves continuation of a quantity (state or control) with respect to a functional change tuned by a separate parameter (typically called the continuation or embedding parameter). A few examples of a DCO is finding a family of solutions by sweeping launch time or number of revolutions or thrust value. Therefore, DCO continuation is done as part of the outer wrapper and does not participate in solving the TPBVP while for ICO, the parameter is embedded in the dynamics and hence influences the shooting method (used to solve the posed TPBVP) directly. For time-optimal orbit transfers, it is known that the thruster remains "on" during the entire time of flight while switching is observed in fuel-optimal trajectories and such a control is called bang-bang or bang-off-bang control due to its discontinuous binary on and off characteristics. The discrete discontinuous switched nature of control δ (bang-bang structure) makes the solution of the TPBVP challenging [6] mainly due to

the necessity of precisely solving for each of many zeros of the switch function. The concept of smoothing methods in solving the IOCPs for space maneuvers was introduced by Bertnand et al [6] consisting of quadratic, logarithmic and extended logarithmic techniques specifically to smooth the bang-off-bang control profiles allowing propagation using standard integrators. These techniques utilize a continuation parameter which is typically embedded into the cost functional affecting the necessary conditions of optimality.

In this work, however, we use hyperbolic tangent smoothing (HTS) introduced by Taheri and Junkins [51]. The HTS method is particularly advantageous since (i) the derivation of the first-order necessary conditions remains intact, (ii) unlike traditional indirect approaches, it circumvents time-consuming switch detections, and (iii) control input (i.e., engine throttling input) is approximated by a continuously differentiable function with its immediate implications. The last item is particularly helpful in that: (i) it is possible to use adaptive step-size integration schemes to speed-up numerical simulations, and (ii) analytic sensitivity calculations become significantly easier. Moreover, due to control smoothing, it is significantly easier to enhance convergence performance of solvers that rely on Newton and/or Quasi-Newton update iterative schemes by high-accuracy sensitivity information such as those obtained through the State Transition Matrix (STM) method [76]. In this setting, implementation of the STM method is facilitated since the entire trajectory is smooth, and the control is infinitely differentiable. Thus, there is no need to construct an additional transition matrix to patch the discontinuities in the standard implementation of the STM method when solving non-smooth trajectories with analytical sensitivities [7]. Ultimately, the smooth control input can be brought arbitrarily close to the well-known "optimal" bang-off-bang profiles through a homotopic sweep over a rigorously continuous family of neighbouring solutions.

$$\delta^* \approx \delta(S,\rho) = 0.5\left[1+\tanh\left(\frac{S}{\rho}\right)\right]. \tag{2.17}$$

For example, the control input, δ is constructed through a simple algebraic operation on the switching function that defines a one-parameter family of controls which approaches the bang-bang switch structure as the smoothing parameter approaches zero. Under HTS, optimal value of

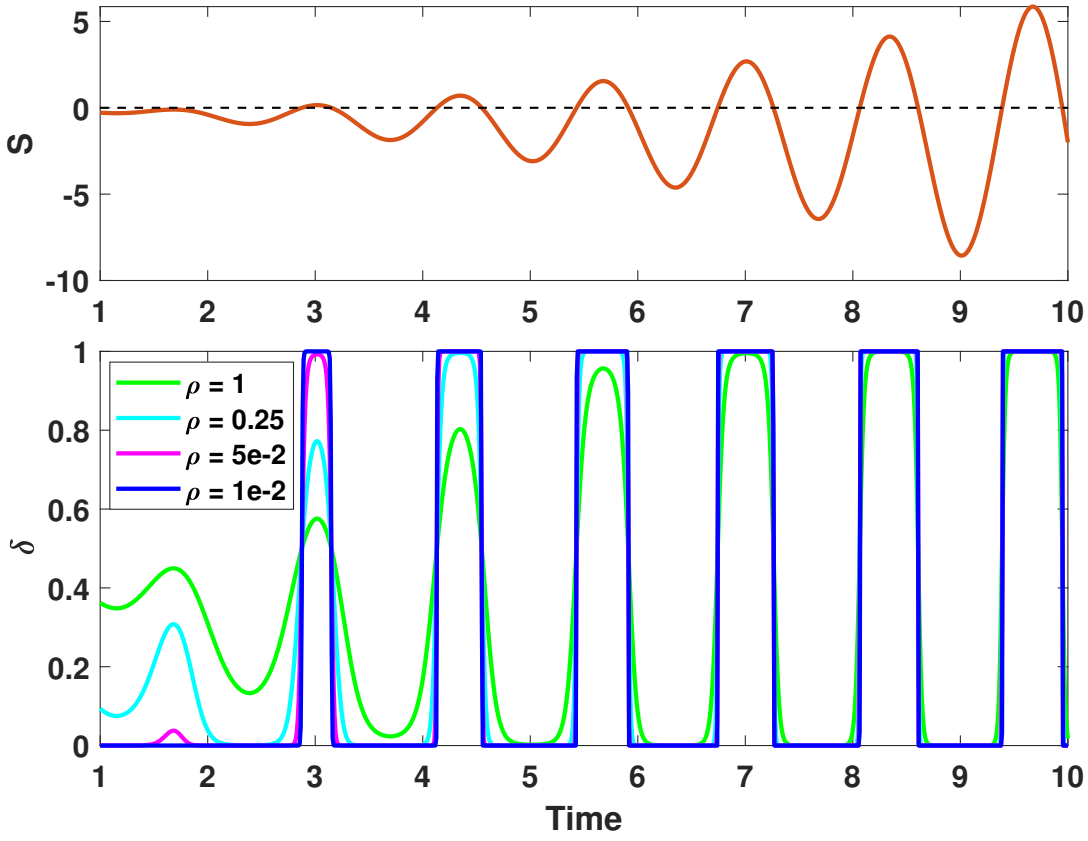

Figure 2.2: Demonstration of the HTS method for approximating a sign function for different value of ρ

throttling, δ^* is coupled with the value of the switching function through a smoothing parameter ρ per Eq. (3.31). In order to approach the actual bang-bang control, ρ should be made suitable small such that $\frac{S}{\rho}) \rightarrow \tanh 10 = 0.999999996 \approx 1$,. This equivalence is shown in Figure 2.2 for the value of δ obtained for a particular S function and a set of ρ values.

An extension of HTS, is introduced by Taheri et al, especially for handling the min-max structure that involves amalgamation of constraint conditions. When writing programs, a standard practice is to distinguish between different mode-switching conditions by using "if-then" commands. However, the presence of many "if-then" conditional statements leads to non-smoothness and complications in constructing algorithms that must precisely locate many unknown acceleration jump switch times. This leads to both algorithm complexity and unreliable convergence of boundary-value problems. The CSC framework [30] presents an alternative approach wherein a set of distinct conditions that govern the value of a particular control are systematically combined with the help of homotopy parameters. Remarkably, the resulting differential equations do not have any mathematical acceleration discontinuities (even though the underlying optimal control and mode switch discontinuities are homotopically approached, the accelerations do have relatively sharp control and mode transitions). The governing differential equations are solved with an algorithm implementation that does not involve any "if-then" conditions through the notion of "distance measures" to the local zeros of the constraint functions that will be used as the argument of the $tanh$ function.

Thus, a family of $tanh$ functions act as activation for the constraint and switch functions. The multiplicative incorporation of (many) activation functions allows smooth transitions between overlapping constraints, rendering dominance of one control variable over others; a summation over all possible conditions results in a complete recipe for converting any instantaneous switches over competing controls and control mode switches into a continuous composite structure. While the multiplication of activation functions seems highly non-linear, in practice, it turns out for well-isolated switching all of these activation functions, except one associated with a particular local control switch or mode switch, are typically very nearly zero. Of course, as the equations are prop-

agated, the values of the activation functions change accordingly and "pop-up" to smoothly switch with controllable sharpness, as the corresponding constraint ($g = 0$) conditions are approached. This dissertation extends the above smoothing methods to include more rigorous optimization using discrete control variables and describes mathematical and numerical constructs to accommodate a set of inequality constraints which are not only function of instantaneous states and costates but also are an explicit function of time.

For numerical continuation, the standard procedure is to begin the numerical procedure with a relatively large value of the continuation parameter, say, $\rho = 1$ or $\rho = 0.5$, and to reduce the value of ρ in a sequential manner, solving an optimal trajectory for each ρ value and using the converged co-state to initiate the TPBVP iteration for the subsequent smaller ρ value. Especially in case of smoothing multiple switching functions with multiple continuation parameters using the HTS method, the magnitude of the starting value of the continuation parameter is also dependent on the magnitude of the constraint condition ('g' in $\tanh\left(\frac{g}{\rho}\right)$). In order to approximate the actual instantaneous change in control inputs, all ρ_i values should be systematically made as small as possible (a small fraction of the maximum value of g). It is also useful to non-dimensionalize the constraint function by scaling it by its allowable range. The $g_{\max}$ in each of the HTS expression $\tanh\left(\frac{\frac{g}{|g_{\max}|}}{\rho}\right)$ can be revised based on the largest $|g_{\max}|$ encountered for the previous ρ value. This non-dimensionalization of the range of the g function permits a more universal behaviour of the HTS smoothing and facilitates the use of one homotopy parameter for smoothing many different discontinuities. Typically, values in range $1.0\times10^{-1}-1.0\times10^{-2}$ (times the range of $|g|$) have been found to result in solutions that are sufficiently indistinguishable from their discontinuous counterparts to declare "engineering optimality". With $\tanh\left(\frac{1}{0.1}\right) = \tanh 10 = 0.999999996 \approx 1$, the switch function approximations become exact much quicker than the corresponding ρ approaches zero.

2.1.3.3 Analytical Sensitivities

The resulting TPBVP are solved using gradient based solvers which compute the sensitivity of the final boundary conditions with respect to the change in the design variables (here co-states)

by a finite difference method. The analytical expressions for the state transition matrix (STM) (to retrieve sensitivity information) with the HTS method further enlarges the domain of convergence of the shooting method and enhances the solution convergence performance. The derivation of state transition matrices for smooth differential equations are likewise continuous and are more readily numerically integrated than their discontinuous counterparts. This is owing to the reliable step-size adaptation used in most modern numerical differential equation solvers to maintain precision. Assuming $\boldsymbol{\psi}(\boldsymbol{x}(t_f), t_f)$ as boundary conditions and $\boldsymbol{\lambda}(t_0)$ as design variables, the first order sensitivity can be written as:

$$\frac{\partial \boldsymbol{\psi}(\boldsymbol{x}(t_f), t_f)}{\partial \boldsymbol{\lambda}(t_0)}, \tag{2.18}$$

which can be evaluated using chain rule as:

$$\frac{\partial \boldsymbol{\psi}(t_f)}{\partial \boldsymbol{\lambda}(t_0)} = \frac{\partial \boldsymbol{\psi}}{\partial \boldsymbol{z}}\bigg|_{t_f} \frac{\partial \boldsymbol{z}(t_f)}{\partial \boldsymbol{z}(t_0)} \frac{\partial \boldsymbol{z}(t_0)}{\partial \boldsymbol{\lambda}(t_0)}. \tag{2.19}$$

Recognizing that $\boldsymbol{\Phi}(t_f, t_0) = \partial \boldsymbol{z}(t_f)/\partial \boldsymbol{z}(t_0)$, where $\boldsymbol{\Phi}$ is the STM with its dynamics given in Eq. (2.20) and $\boldsymbol{z} = [\boldsymbol{r}^T, \boldsymbol{v}^T, m, \boldsymbol{\lambda}_{\boldsymbol{v}}^T, \boldsymbol{\lambda}_{\boldsymbol{v}}^T, \lambda_m]^T$. The states-co-states vector is augmented by the STM and is evaluated at each time step using the differential equation

$$\dot{\boldsymbol{\Phi}} = \boldsymbol{F}\boldsymbol{\Phi}; \;\; \boldsymbol{\Phi}(t_0, t_0) = I, \tag{2.20}$$

where I denotes a 14 by 14 identity matrix and $\boldsymbol{F}$ (in Eq. (2.20)) is given below

$$\boldsymbol{F} = \frac{\partial \boldsymbol{\Gamma}}{\partial \boldsymbol{z}} = \begin{bmatrix} \mathbf{0}_{3\times3} & \boldsymbol{I}_{3\times3} & \mathbf{0}_{3\times1} & \mathbf{0}_{3\times3} & \mathbf{0}_{3\times3} & \mathbf{0}_{3\times1} \\ \boldsymbol{F}_{21} & \mathbf{0}_{3\times3} & \boldsymbol{F}_{23} & \mathbf{0}_{3\times3} & \boldsymbol{F}_{25} & \boldsymbol{F}_{26} \\ \mathbf{0}_{1\times3} & \mathbf{0}_{1\times3} & F_{33} & \mathbf{0}_{1\times3} & \boldsymbol{F}_{35} & F_{36} \\ \boldsymbol{F}_{41} & \mathbf{0}_{3\times3} & \mathbf{0}_{3\times1} & \mathbf{0}_{3\times3} & \boldsymbol{F}_{45} & \mathbf{0}_{3\times1} \\ \mathbf{0}_{3\times3} & \mathbf{0}_{3\times3} & \mathbf{0}_{3\times1} & -\boldsymbol{I}_{3\times3} & \mathbf{0}_{3\times3} & \mathbf{0}_{3\times1} \\ \mathbf{0}_{1\times3} & \mathbf{0}_{1\times3} & F_{63} & \mathbf{0}_{1\times3} & \boldsymbol{F}_{65} & F_{66} \end{bmatrix}, \tag{2.21}$$

$$\boldsymbol{F}_{21} = -\frac{\mu \boldsymbol{I}}{r^3} + \frac{3\mu \boldsymbol{r}\boldsymbol{r}^T}{r^5},\ \boldsymbol{F}_{23} = -\frac{T_{\max}\boldsymbol{\alpha}}{2m^2}\left[1+\tanh(G)\right] - \frac{\operatorname{sech}^2(G)T_{\max}c||\boldsymbol{\lambda_v}||\boldsymbol{\alpha}}{2m^3\rho},\ F_{33} = \frac{T_{\max}||\boldsymbol{\lambda_v}||\operatorname{sech}^2(G)}{2m^2\rho}$$

$$\boldsymbol{F}_{25} = \frac{T_{\max}\boldsymbol{I}}{2m||\boldsymbol{\lambda_v}||} - \frac{T_{\max}\boldsymbol{\lambda_v}\boldsymbol{\lambda_v}^T}{2m||\boldsymbol{\lambda_v}||^3} + \frac{T_{\max}\operatorname{sech}^2(G)c\boldsymbol{\lambda_v}\boldsymbol{\lambda_v}^T}{2m^2\rho||\boldsymbol{\lambda_v}||^2} - \frac{T_{\max}\tanh(G)\boldsymbol{\lambda_v}\boldsymbol{\lambda_v}^T}{2m||\boldsymbol{\lambda_v}||^3} + \frac{\tanh(G)T_{\max}\boldsymbol{I}}{2m||\boldsymbol{\lambda_v}||},$$

$$\boldsymbol{F}_{26} = \frac{T_{\max}\operatorname{sech}^2(G)\boldsymbol{\alpha}}{2m\rho},\ \boldsymbol{F}_{35} = \frac{-T_{\max}\operatorname{sech}^2(G)\boldsymbol{\lambda_v}^T}{2||\boldsymbol{\lambda_v}||\rho m},\ \boldsymbol{F}_{36} = \frac{-T_{\max}\operatorname{sech}^2(G)}{2c\rho},\ \boldsymbol{F}_{45} = \frac{\boldsymbol{I}}{r^3} - \frac{3\boldsymbol{r}\boldsymbol{r}^T}{r^5},$$

$$F_{63} = \frac{T_{\max}||\boldsymbol{\lambda_v}||}{m^3} + \frac{T_{\max}||\boldsymbol{\lambda_v}||\tanh(G)}{m^3} + \frac{T_{\max}||\boldsymbol{\lambda_v}||^2\operatorname{sech}^2(G)c}{2m^4\rho},\ F_{66} = \frac{-T_{\max}||\boldsymbol{\lambda_v}||\operatorname{sech}^2(G)}{2m^2\rho},$$

$$\boldsymbol{F}_{65} = -\frac{T_{\max}}{2m^2}\left(\frac{\operatorname{sech}^2(G)\boldsymbol{\lambda_v}^T c}{m\rho} + \frac{\tanh(G)\boldsymbol{\lambda_v}^T}{||\boldsymbol{\lambda_v}||} + \frac{\boldsymbol{\lambda_v}^T}{||\boldsymbol{\lambda_v}||}\right),\ \boldsymbol{F}_{41} = -\frac{6(\boldsymbol{\lambda_v}\boldsymbol{r}^T)}{r^5} - \frac{3(\boldsymbol{\lambda_v}.\boldsymbol{r})\boldsymbol{I}}{r^5} + \frac{15(\boldsymbol{\lambda_v}.\boldsymbol{r})\boldsymbol{r}\boldsymbol{r}^T}{r^7}.$$

where $G = SF/\rho$ and $\boldsymbol{I}$ denotes a 3 by 3 identity matrix.

2.2 Fast Impulsive maneuvers [2]

Impulsive maneuvers have been one of the earliest enabler of space travel and though now more restricted in use, are still revered for their priceless insights into preliminary mission design and providing ballpark numbers for the feasibility space for both minimum time and minimum fuel trajectories. For high thrust interplanetary trajectories with a "burn time" short compared to the time of flight, the impulsive approximation is usually adequate to fly the actual mission. For optimizing multiple impulse maneuvers, a search for the optimal number, time instants, magnitude, and direction of the velocity impulses is carried out to accomplish general three-dimensional multiple-revolution orbit transfers while minimizing the total ΔV [80]. Many direct, hybrid and evolutionary algorithms are traditionally used that conduct trade offs between optimality/accuracy and the computational effort by performing multiple iterations. Due to the parallelizability attribute of these iterations in most cases, graphical processing units have also been utilized to solve million instances of the Lambert's problem [81, 82]. Finding optimal N-multi-impulse, minimum-ΔV trajectories, however, becomes quite challenging for large N, for a number of reasons: (1) gradient-based solvers face difficulty in finding an optimal solution unless started with "high-quality" initial guesses. (2) The performance of the evolutionary algorithms degrades as the number of design variables increase. (3) Direct methods struggle to optimize multi-revolution trajectories, where the bulk of the initial transfer orbits occur near the attracting center [83]. (4) Ambiguity in the unknown optimal number of impulses further increases the problem complexity. Additionally, the solution is frequently non-unique if the number of en-route revolutions are also considered as design variables [20].

Historically, indirect methods have also been either too cumbersome to converge leading to challenging optimization problems as the number of impulses grow into double digits or have suffered from multiple closely located or non-unique solutions [15]. The approach proposed in this dissertation draws its motivation from the ones presented in [20], however, a set of advance-

[2] Reprinted with permission from "Acceleration-based Indirect Methods for Impulsive Trajectory Design" by Taheri, Ehsan and Arya, Vishala and Junkins, John L, 2021. 31st AAS/AIAA Space Flight Mechanics Meeting, Virtual, February 1-February 3, 2021

ments are proposed to facilitate and accelerate the numerical solution procedure by adopting a new two-step solution process. We propose two novel methods that are used in succession to obtain near-optimal many-impulse solutions [84]. Perhaps counter-intuitive, it has been shown [**?**] that beginning with a continuous thrust and using indirect optimal control, we can find the optimum impulsive solutions by sweeping maximum thrust towards infinity. Near-impulsive solutions provide "high quality" initial guesses for the position, time, direction and magnitude of impulses, which can be used by a gradient-based solver to recover the precise impulsive solution that obeys Lawden's optimality conditions. The key observation is that impulsive trajectories can be rigorously viewed as the limiting case of high-acceleration, minimum acceleration or minimum fuel trajectories. The standard methods use the acceleration vector to construct a quadratic cost functional. However, it is important to devise a mechanism to not only enforce the so-called "bang-off-bang" profiles on the acceleration arcs, but also to ensure that the thrust acceleration arcs occur over short time intervals. Thus, a solution to the minimum-acceleration problem, where the thrust acceleration arcs are represented as short finite burn sequences, can approximate the optimal impulsive trajectories as the thrust acceleration magnitude approaches infinity.

The proposed two-step solution procedure developed in this dissertation to obtain the N-impulse trajectory is: 1) the original multi-impulse problem is treated as a rendezvous-type, fuel-optimal problem with the exception that a variable-specific impulse, variable-thrust (VIVT) propulsion system is considered. The variability of the specific impulse spreads the thrust profile along the transfer trajectory to an extent that only a few iterations are frequently needed to get a first-cut solution for prescribed boundary conditions and time of flight. 2) a minimum integral of acceleration based formulation that removes the dependency of the problem formulation on mass, specific impulse and thrust value. This is the continuous version of the minimum Δv problem.

The VIVT based $c_{\max}$ method (see Figure 2.3) provides excellent initial convergence but can provide numerical difficulties during the final continuation iterations. To circumvent this convergence issue, $a_{\max}$ method is proposed for the final iterations. If a linear acceleration is considered in the cost functional, solutions lie entirely on a singular arc. To avoid singular arcs and to enforce

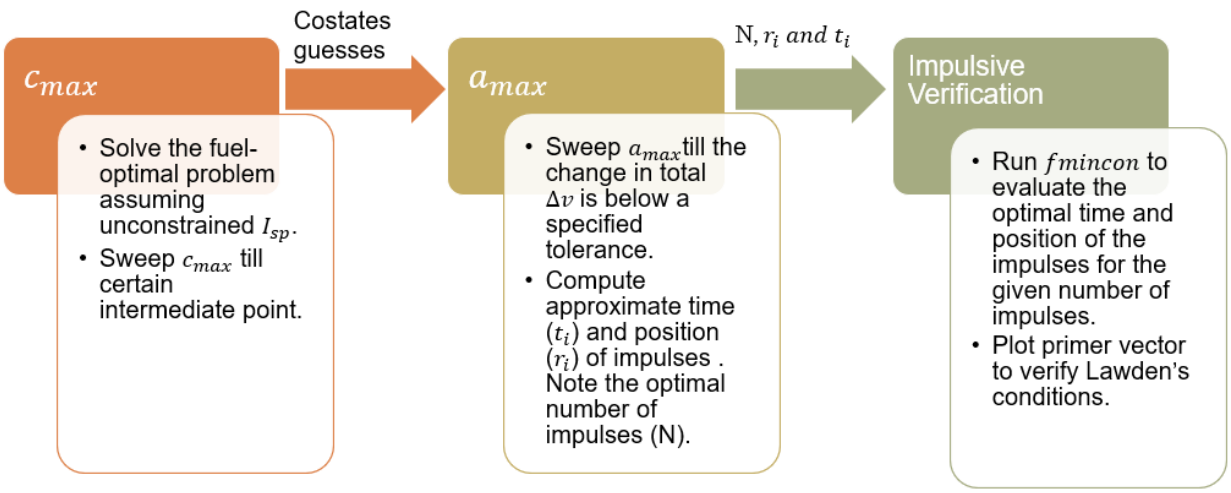

Figure 2.3: Algorithm flow chart.

optimal "bang-off-bang" acceleration profiles, a parameter, $a_{\max}$ is introduced to the problem formulation. This acceleration-based method, as is shown herein, is an elegant formulation to find optimal multi-impulse maneuvers. Furthermore, the continuation performed over the $a_{\max}$ value is observed to be much more well behaved than continuation on the thrust value. More specifically, we find that large steps can be taken in the values of $a_{\max}$ resulting in fewer number of iterations to reach the near-impulsive solution. The solution obtained from the acceleration-based method (that is near-optimal and has a fixed number of impulses) is used as an initial guess for a non-linear programming based method that exploits a Lambert solver and primer vector theory to isolate the final N-impulse solution to a high precision. The proposed two-step algorithm, as is shown herein, builds a viable procedure to find many-impulse spacecraft maneuvers involving $\approx$ 50 orbital revolutions.

The optimal control problem (OCP) is formulated using the set of modified equinoctial elements (MEEs) using the two-body dynamics assumptions to solve for transfer problems as time-fixed, rendezvous-type maneuvers. There are three major steps in the evaluation of the impulsive solutions outlined in Figure 2.3 and explained in three subsections below.

2.2.1 Control Sweep (CS step)

The foremost step in the algorithm is to obtain a near-impulsive solution that is accomplished using two methods in succession; 1) $c_{\max}$ method and 2) $a_{\max}$ method with their details given in the following sections.

2.2.1.1 c_{max} method

This method is based on the operation of VIVT engines that are idealized as being capable of providing a continuous range of values for exhaust velocity and the corresponding thrust. Though heretofore restricted to academic research, the concept of VIVT engines also is a promising preliminary trajectory design tool to obtain various first-cut trajectories with different thrust modulations. The exhaust velocity, $c = I_{\text{sp}} g_0$, is one of the control variables, which can be constrained to lie within the bounds [30] as $\tilde{c} \in [c_{\min}, c_{\max}]$. Here, $c_{\min}$ and $c_{\max}$ denote the minimum and maximum admissible exhaust velocity values, respectively. Therefore, for a VIVT engine, the thrust, T, and time differential equation for mass, $\dot{m}$, can be written as

$$T = \frac{2\eta P}{c}\delta, \qquad\qquad \dot{m} = -\frac{2\eta P}{c^2}\delta. \tag{2.22}$$

In Eq. (2.22), the thruster efficiency, η, is set to 1 (i.e., 100% thruster efficiency) and a constant power, P is assumed to be available for thrusting. Both thrust and mass flow rate depend on 'c' and the throttle input, δ. Therefore, there are three control variables: throttle (δ), direction of the thrust ($\hat{\boldsymbol{\alpha}}$), and the exhaust velocity (c).

With the state dynamics and control variables defined, the cost functional for minimizing fuel

consumption is written as

$$\begin{aligned} &\text{Minimize } \; J = \int_{t_0}^{t_f} \frac{2\eta P}{c^2}\delta \; dt, \\ &\text{subject to :} \\ &\qquad \text{Eqs. (2.6) \& (2.22), } \; \boldsymbol{x}(t_f) - \tilde{\boldsymbol{x}}_d = \mathbf{0}, \; P = P_{\text{use}}, \\ &\qquad \boldsymbol{x}(t_0) = \boldsymbol{x}_0, \;\; m(t_0) = m_0, \; \eta = 1, \end{aligned} \tag{2.23}$$

where t_0 is the initial time, $\boldsymbol{x_0}$ and m_0 are the MEEs and mass of the spacecraft at the initial time, respectively, t_f is the final time, $\Delta t = t_f - t_0$ is the time of flight, P_{use} is the power available for thrusting set by the user and $\tilde{\boldsymbol{x}}_d$ is the desired MEEs at the final time. The (optimal control) Hamiltonian associated with the defined cost functional and state dynamics is

$$H = \frac{2\eta P}{c^2}\delta + \boldsymbol{\lambda}^\top \left(\boldsymbol{A}(\boldsymbol{x}, t) + \frac{T}{m}\mathbb{B}(\boldsymbol{x}, t)\delta\hat{\boldsymbol{\alpha}} \right) - \lambda_m \frac{2\eta P}{c^2}\delta, \tag{2.24}$$

where $\boldsymbol{\lambda} = [\lambda_p, \lambda_f, \lambda_g, \lambda_h, \lambda_k, \lambda_l]^\top$ is the costate vector associated with the MEEs and λ_m is the costate associated with mass. Due to the bi-linear appearance of $\hat{\boldsymbol{\alpha}}$ and ($\delta \geq 0$) in the Hamiltonian, Pontryagin's minimum principle (PMP) is used to find the optimal control direction, which is aligned along the Lawden's primer vector, $\boldsymbol{p} = -\mathbb{B}^\top \boldsymbol{\lambda}$ defined as

$$\hat{\boldsymbol{\alpha}}^* = \frac{\boldsymbol{p}}{||\boldsymbol{p}||} = -\frac{\mathbb{B}^\top \boldsymbol{\lambda}}{||\mathbb{B}^\top \boldsymbol{\lambda}||}. \tag{2.25}$$

According to the PMP, the throttle input, δ, has to be selected such the Hamiltonian is minimized along an extremal solution

$$\delta^* = \arg\min_{\delta \in [0,1]} H(\boldsymbol{x}^*(t), m^*(t), \delta(t), \boldsymbol{\lambda}^*(t), \lambda_m^*(t)), \tag{2.26}$$

and the non-negative thrust switching function that governs the optimal throttle (δ) 'on' or 'off'

modes can be defined as

$$\delta^* = \begin{cases} 1; & \text{for } SF > 0, \forall\, c \in [c_{\min}, c_{\max}], \\ 0; & \text{for } SF \leq 0, \forall\, c \in [c_{\min}, c_{\max}], \end{cases} \tag{2.27}$$

$$SF = \frac{c||\mathbb{B}^\top \boldsymbol{\lambda}||}{m} + \lambda_m - 1. \tag{2.28}$$

The discontinuous structure of the theoretically extremal control, δ^* given in Eq. (2.27), which is in general a sequence of on/off pulses, is made smooth, yet approximated to a high precision, using hyperbolic tangent smoothing (HTS) method [51] as

$$\delta^* \approx \delta(SF, \rho_b) = 0.5 \left[1 + \tanh\left(\frac{SF}{\rho_b}\right)\right], \tag{2.29}$$

where ρ_b is a smoothing parameter that controls the sharpness of the switches of the optimal "bang-off-bang" throttle input. The time rate of change of costates are governed by differential equations obtained from the Euler-Lagrange equations as

$$\dot{\boldsymbol{\lambda}} = -\left[\frac{\partial H}{\partial \boldsymbol{x}}\right]^\top, \qquad\qquad \dot{\lambda}_m = -\frac{\partial H}{\partial m}. \tag{2.30}$$

Optimal values of specific impulse can be characterized using the strong form of optimality, $\partial H/\partial c = 0$, giving an expression for c_{opt} [**?**] as

$$c_{\text{opt}} = \frac{2(1-\lambda_m)m}{||\mathbb{B}^\top \boldsymbol{\lambda}||}. \tag{2.31}$$

Using Eq. (2.31) along with the admissible bounding constraint that $c_{\text{opt}} \leq c_{\max}$, the effective optimal exhaust velocity, ($\tilde{c}$), becomes

$$\tilde{c} = \begin{cases} c_{\max}, & \text{if } c_{\text{opt}} \geq c_{\max}, \\ c_{\text{opt}}, & \text{if } \ c_{\text{opt}} \leq c_{\max}. \end{cases} \tag{2.32}$$

In order to accommodate the above inequality condition imposed on the selection of $\chi_{c_{\max}}$, smooth structure of $\tilde{c}$ is obtained by the use of an activation function such as

$$\tilde{c} = \chi_{c_{\max}} c_{\max} + (1 - \chi_{c_{\max}}) c_{\text{opt}} \tag{2.33}$$

where the activation function is constructed with the help of the HTS method as

$$\chi_{c_{\max}} = 0.5 \left[1 - \tanh \left(\frac{c_{\max} - c_{\text{opt}}}{\rho_c} \right) \right],$$

As per PMP, Hamiltonian should be minimized over all the set of admissible controls. Therefore, $c_{\max}$ is used to evaluate the SF in Eq. (3.16) to allow the VIVT engine to be ON, if at least one admissible value of c exists that makes the power switching function, SF, positive. In case of the unconstrained formulation, the inequality given in Eq. (2.32) does not get used since $c_{\max}$ is set to a high enough value such that $\tilde{c} = c_{\text{opt}}$ is always followed. This also removes the presence of any throttle discontinuity as PMP dictates the thruster to be always 'on' in this case.

Additionally, we have the mass costates terminal boundary condition $\lambda_m(t_f) = 0$ since final spacecraft mass, $m(t_f)$, is free. Thus, the set of final boundary conditions can be defined as

$$\mathbf{\Gamma} = \left[(\boldsymbol{x}(t_f) - \tilde{\boldsymbol{x}}_d)^\top, \lambda_m(t_f) \right]^\top = \mathbf{0}. \tag{2.35}$$

The optimal control expressions along with the state and costate and boundary conditions form a two-point boundary-value problem (TPBVP). More specifically, state dynamics, Eqs. (2.6) and (2.22), costate dynamics, Eq. (2.30), extremal control expressions, Eq. (2.25), Eq. (2.29), and Eq. (2.33) along with the set of final constraints, Eq. (2.35), define the TPBVP associated with the $c_{\max}$ method. In fact, the TPBVP is a root-finding problem that can be written as

$$\mathbf{\Gamma}(\boldsymbol{\eta}(t_0); \mathbf{\Theta}) = \left[(\boldsymbol{x}(t_f) - \tilde{\boldsymbol{x}}_d)^\top, \lambda_m(t_f) \right]^\top = \mathbf{0}, \tag{2.36}$$

where $\boldsymbol{\eta}(t_0) = [\boldsymbol{\lambda}(t_0)^\top, \lambda_m(t_0)]^\top$ denotes the unknown costates at the initial time and $\boldsymbol{\Theta} = [\rho_b, \rho_c, c_{\max}]$ denotes the three continuation parameters of the resulting TPBVP. Note that for solving each TPBVP, $\boldsymbol{\Theta}$ is fixed, but the continuation parameters will be modified to guide the solution to the desired one. For the unconstrained case in which the constraint (given in Eq. (2.32)) is removed from the problem formulation, $\boldsymbol{\Theta} = c_{\max}$. Upon obtaining an optimal solution for the unconstrained version, a continuation procedure is initiated (with $\boldsymbol{\Theta} = [\rho_b, \rho_c, c_{\max}]$) in which the value of $c_{\max}$ can be swept from a high value (ideal engine) to a low value (chemical engine) following a DCO method regime to ultimately obtain near-impulsive solutions.

Typically, the introduction of the constraint ($c_{\min} \leq c \leq c_{\max}$) in the exhaust velocity is considered to represent the performance constraints of a realistic engine. But even with a propulsion model featuring unconstrained and unrealistically high-I_{sp} engine, the VIVT propulsion modelling has been found to yield excellent first-cut optimized trajectories with relatively arbitrary boundary conditions. There are two major advantages of using the unconstrained VIVT solution to kick-start the optimization: 1) the fuel-optimal solution of the unconstrained version of the VIVT modelling uses the optimal I_{sp} at all times (see Eq. (3.26)) resulting in a continuous thrust trajectory ($\delta = 1$) with no control discontinuities. Hence, this inherently smooth control facilitates numerical convergence, and 2) the only control variable affecting the thrust and mass flow rate (Eq. (2.22)) is c_{opt}, which is a function of the instantaneous mass (see Eq. (2.31)). This allows flexibility in choosing near arbitrary initial mass and time of flight. The exhaust velocity values using arbitrary mass and power values despite being unrealistic, aid in better selection of these parameters in consecutive steps of the solution procedure (see Figure 2.3). Referring to Figure 2.3, the above ''minimum continuous Δv" formulation actually has a simpler to look at mathematical structure than the $c$max or $a_{\max}$ optimal control approaches. However, moving left to right in Figure 2.3 is recommended in solving the two-point boundary value problem implicit in Eqs (2.36) because this is a high confidence route to establish the starting co-states.

In summary, the original difficult-to-solve optimal control problem is embedded in a three-parameter (i.e., ρ_b, ρ_c and $c_{\max}$) family of neighboring OCPs (see Eq. (2.36)). $c_{\max}$ is usually swept

first, then ρ_b and ρ_c are simultaneously swept. A standard numerical continuation is used to solve the problem in which the converged costates of the previous iteration are used as an initial guess to bolster convergence of the subsequent iterations. An adaptive sweep of the homotopy parameter means we can virtually guarantee we are initiating each iteration sufficiently close to ensure rapid quadratic convergence. In practice, large steps (only 3-4 iterations) in $c_{\max}$ can be taken to obtain a near-impulsive solution for simple maneuvers. One primary difficulty encountered in the $c_{\max}$ method is the occasional occurrence of encountering near zero mass values for a randomly selected initial guess for costates especially when a low $c_{\max}$ value is set (typically during the last iterations). Note that lower $c_{\max}$ values are ideal to approximate impulsive thrust arcs (i.e., high thrust in Eq. (2.22)). Therefore, instead of going to a minimum fuel approach, a second method is proposed to circumvent this occasional problem.

2.2.1.2 a_{max} method

Impulsive solutions contain only velocity-level information. A pure integral of acceleration formulation is proposed that removes the dependency of the problem formulation to mass, specific impulse and thrust value. The removal of these parameters makes the problem substantially easier given that the mass state and its associated costate (i.e., ($\dot{m}$ & $\dot{\lambda}_m$)) are removed from the formulation of the OCP. A fixed-time, rendezvous-type, minimum-Δv trajectory optimization problem is considered with a cost functional defined in Lagrange form as

$$\underset{\boldsymbol{a}\in\boldsymbol{\Omega}}{\text{minimize}} \quad J = \int_{t_0}^{t_f} ||\boldsymbol{a}|| \, dt, \tag{2.37}$$

where t_0 and t_f are the initial and final times, respectively, and $\boldsymbol{\Omega}$ denotes the set of admissible acceleration vectors. Obviously the integral of acceleration is a velocity change and as acceleration impulses approach large $a_{\max}$ values and short time intervals, Eq. (2.37) is the continuous equivalent of maximizing total Δv. The extremal solution that minimizes this cost functional lies entirely on a singular arc since the control is unbounded and it also appears linearly in the optimal control Hamiltonian.

To avoid singular arcs and to enforce optimal "bang-off-bang" acceleration profiles, a bound on maximum acceleration, $a_{\max}$, is introduced to the problem formulation. In this modification of the formulation, the thruster induced acceleration is rewritten as, $\boldsymbol{a} = a_{\max}\hat{\boldsymbol{\alpha}}\delta$, where $a_{\max}$ is used to embed the original OCP into a family of neighboring OCPs and as before, the throttle function is $\delta(t) \in 0 \leq \delta(t) \leq 1$. Therefore, the modified cost functional for minimizing Δv as the integral of acceleration can be stated as

$$\begin{aligned} &\text{Minimize } \; J = \int_{t_0}^{t_f} \delta a_{\max} \; dt, \\ &\text{subject to :} \\ &\qquad \text{Eq (2.6)}, \; \boldsymbol{x}(t_f) - \tilde{\boldsymbol{x}}_d = \boldsymbol{0}, \; \boldsymbol{x}(t_0) = \boldsymbol{x}_0, \; a_{\max} : \text{ user defined.} \end{aligned} \tag{2.38}$$

Upon writing the Hamiltonian as

$$H = \delta a_{\max} + \boldsymbol{\lambda}^\top \left[\boldsymbol{A}(\boldsymbol{x}, t) + a_{\max}\mathbb{B}(\boldsymbol{x}, t)\delta\hat{\boldsymbol{\alpha}}\right], \tag{2.39}$$

the optimal thrust direction is still governed by $\hat{\boldsymbol{\alpha}}^*$ (see Eq. (2.25)). The costate dynamics are derived using Euler-Lagrange equation as

$$\dot{\boldsymbol{\lambda}} = -\left[\frac{\partial H}{\partial \boldsymbol{x}}\right]^T. \tag{2.40}$$

Employing the PMP to determine δ, the smooth throttle input can be written as

$$\delta^* \approx \delta(SF, \rho_b) = 0.5\left[1 + \tanh\left(\frac{SF}{\rho_b}\right)\right], \tag{2.41}$$

where $SF = ||\mathbb{B}^\top\boldsymbol{\lambda}|| - 1$. The TPBVP associated with the cost functional, Eq. (2.38), the state dynamics, Eq. (2.6), the costates given in Eq. (2.40), the control inputs given in Eqs. (2.25) and (2.41), can be written as a non-linear root-finding problem given in Eq. (2.42)

$$\boldsymbol{\Gamma}(\boldsymbol{\eta}(t_0); \boldsymbol{\Theta}) = \boldsymbol{x}_{\text{MEE}}(t_f) - \tilde{\boldsymbol{x}}_d = \boldsymbol{0}, \tag{2.42}$$

where $\boldsymbol{\Theta} = [\rho_b, a_{\max}]$ denotes the continuation parameters of the resulting TPBVPs. Thus, a two-parameter family of neighboring OCPs is formed, with a reduced number of equations, simpler form of the switching function, no dependence on engine parameters, less number of constraints and only two continuation parameters. In Eq. (2.42), there is a total of six scalar final constraints.

There are notable advantages of the $a_{\max}$ method: 1) The number of differential equations is reduced to 12 with mass removed, 2) The selection of exhaust velocity as a control variable is not required, and 3) We have found that this optimization process is very well-behaved and large steps in $a_{\max}$ can be taken without getting trapped in intermediate valleys, which could otherwise make convergence difficult [20]. Following the DCO methods, the value of $a_{\max}$ is swept from a relatively low to a high value until the thrust acceleration arcs become narrow enough and the change in Δv with change in $a_{\max}$ becomes very tiny. The numerical continuation procedure for solving the resulting TPBVPs is identical to the $c_{\max}$ method. However, the set of continuation parameters consists of only two parameters, i.e., ρ_b and $a_{\max}$. The former is used to enforce bang-off-bang acceleration profile, whereas the latter is used to approach, with high accuracy, the minimum-Δv maneuvers. We would like to emphasize that both $c_{\max}$ and $a_{\max}$ methods usually lead to near-optimal (minimum Δv) solutions for "simple" problems (e.g., the first two problems that we considered in this work). It is only for "difficult to converge" problems that a two-step procedure is recommended per Figure 2.3, to initiate the $a_{\max}$ algorithm. It is important to note, sweeping $a_{\max}$ over a feasible range generates an extremal field map of optimal solutions for various maximum acceleration levels. This map may be useful in sizing of engines for the non-impulsive low thrust case, not merely a tool to find the impulsive high thrust limit case.

2.2.2 Primer Vector Theory (PVT) step

In this sub-section, a straightforward procedure of extracting the results from the CS step is described, which supplies a very good initial guess to obtain the exact impulsive solution that satisfies Lawden's necessary conditions.

2.2.2.1 *Extraction of Impulses*

Each narrow thrust arc obtained from the previous step is treated as an individual impulse. The midpoint of each individual short finite burn arc is taken as the point of impulse and the time and position vector stamp for each of these midpoints is noted. The direction of the primer vector at this mid-point is also collected to approximate the direction of the impulse and the integral of acceleration over the short burn arcs approximates the velocity impulse magnitude.

The quality of this starting estimate is important, especially to determine the number of impulses, which is not required to be introduced as a design variable. The only design variables that are required to be iterated upon are the positions and time of the interior as well as departure and arrival impulses (if the problem happens to have impulses at the boundaries). The starting values from the $a_{\max}$ solution are typically excellent, so efficient convergence to the final solutions can be expected. This approximate optimal impulsive solution can feature both *late departure* or *early arrival* but does not allow an increase in the time of flight.

2.2.3 Impulsive verification

The time of flight (and the trajectory as a consequence) is divided into time segments featuring an impulse at each end. On each intervening coast arc, two-body dynamics is assumed (in the current implementation) and the transfer arc is computed using a Lambert solver. Utilizing excellent estimates of the times, directions, and magnitudes of the velocity impulses from the previous step, a Nonlinear Programming (NLP) solver, MATLAB's *fmincon* is used to minimize the cost defined as [20]

$$\text{Minimize } J = \sum_{k=1}^{N} \Delta v_k, \tag{2.43}$$

where, Δv_k is the magnitude of the k-th impulse. The starting velocities ($\Delta v(t_k)$) obtained by integrating the converged $a_{\max}$ acceleration impulses centered on t_k. The starting positions, $\boldsymbol{r}(t_k)$, are just corresponding positions from the converged $a_{\max}$ solution. The design variables for *fmincon* are the time of flight of each segment (Δt_k) and the position of impulses ($\boldsymbol{r}_k$) with appropriate bounds set on each. Upon convergence of *fmincon*, the primer vector, $\boldsymbol{p}$, is plotted using the

procedure outlined in [85] and [86]. The resulting primer vector of the optimized solution is verified against Lawden's necessary conditions. Violation of these necessary conditions has been used to determine sub-optimality of impulsive solutions [80, 87] and hence is used as a prerequisite validation check for an extremal impulsive solution.

Upon convergence of *fmincon*, the primer vector, $\boldsymbol{p}$, is computed by propagating the equations [85]

$$\boldsymbol{p}(t) = \boldsymbol{\phi}_{11}\, \boldsymbol{p}(\tau) + \boldsymbol{\phi}_{12}\, \dot{\boldsymbol{p}}(\tau), \tag{2.44a}$$

$$\dot{\boldsymbol{p}}(t) = \boldsymbol{\phi}_{21}\, \boldsymbol{p}(\tau) + \ \boldsymbol{\phi}_{22}\, \dot{\boldsymbol{p}}(\tau), \tag{2.44b}$$

$$\boldsymbol{\Phi}(t,\tau) = \begin{bmatrix} \boldsymbol{\phi}_{11} & \boldsymbol{\phi}_{12} \\ \boldsymbol{\phi}_{21} & \boldsymbol{\phi}_{22} \end{bmatrix}. \tag{2.44c}$$

Here, $\boldsymbol{\Phi}$ is the relevant subset of the state transition matrix (STM) of a dynamical system mapped from any time τ to time 't' such that $\tau,\ t \in [t_0, t_f]$ and follows the differential equation defined as [88]

$$\dot{\boldsymbol{\Phi}} = \boldsymbol{F}\boldsymbol{\Phi};\ \ \boldsymbol{\Phi}(t_0, t_0) = I, \tag{2.45}$$

where I denotes a n by n identity matrix with n denoting the number of differential equations and $\boldsymbol{F}$ denoting the Jacobian matrix evaluated for the equations of motion given in Eq. (2.5). The initial and final value of the primer vector ($\boldsymbol{p}$) are:

$$\boldsymbol{p}(t_0) = \frac{\boldsymbol{\Delta v}(t_k)}{\Delta v(t_k)},\ \ \boldsymbol{p}(t_f) = \frac{\boldsymbol{\Delta v}(t_{k+1})}{\Delta v(t_{k+1})}. \tag{2.46}$$

where t_0 and t_f are the times of first and last impulse.

The most significant difficulty encountered in this work is the sensitivity of the resulting TP-BVPs with respect to initial costates in the case of many revolution trajectories. To circumvent this problem, a two-step process is defined, where the c_{max} method is quick to converge for the initial iterations but can be tedious in the later iterations when the c_{max} value is set quite low to

recover near-impulsive solutions. Therefore, for an intermediate value of $c_{\max}$ depending on the convergence hiccups, the costates and the associated acceleration value from the solution are used to feed the $a_{\max}$ method to get the final near-optimal, near-impulsive solution. Additionally, analytical sensitivities via solutions of the state/co-state state transition matrix differential equation [76] are computed at each time to feed to the solver without which convergence becomes difficult as the dimensionality becomes large. The details are given in [75, 76].

2.2.4 Numerical Example

Three examples are presented: The heliocentric phase of two interplanetary maneuvers from 1) Earth to Mars (E2M), 2) Earth to Dionysus (E2D) and 3) A Geocentric maneuver from a GTO to a circular orbit with a radius equal to the distance from the Earth to the L1 point of the Earth-Moon system (GTO2L1).

2.2.4.1 Earth to Mars (E2M)

In order to demonstrate the utility of the $c_{\max}$ method, a simple (classical) rendezvous example from Earth to Mars is solved with the following MEE boundary conditions: $p(t_0) = 1.0005515$ (AU), $f(t_0) = -0.0029454$, $g(t_0) = 0.0162404$, $h(t_0) = 1.0847571 \times 10^{-5}$, $k(t_0) = 8.446336 \times 10^{-7}$ and $L(t_0) = 7.4484263$. For the target state, $p_d = 1.5103483$ (AU), $f_d = 0.0854214$, $g_d = -0.0378510$, $h_d = 0.0104734$, $k_d = 0.01228042$ and $L_d = 17.4484552$.

As explained before, first a solution with unconstrained VIVT formulation is obtained, which exhibits a continuous thrust profile as shown in Figure 2.4. Here, the increase in the values of I_{sp} causing sudden drop in the thrust value compensates for the areas where the optimality would have warranted a coast arc. As lowering of $c_{\max}$ parameter by use of constrained VIVT formulation is conducted, coast arcs start to appear. Two of these iterations are shown in Figure 2.5 and Figure 2.6 which are plotted for $\rho_b = \rho_c = 1 \times 10^{-5}$.

Unlike the $I_{\text{sp,max}} = 1500$s case (see Figure 2.5), where c_{opt} is still smaller than the set value for $c_{\max}$ at some time instances, the exhaust velocity is completely saturated at $c_{\max}$ when $I_{\text{sp,max}} = 800$ s as shown in Figure 2.6. Any lowering in $c_{\max}$ from this point is equivalent to a thrust continuation

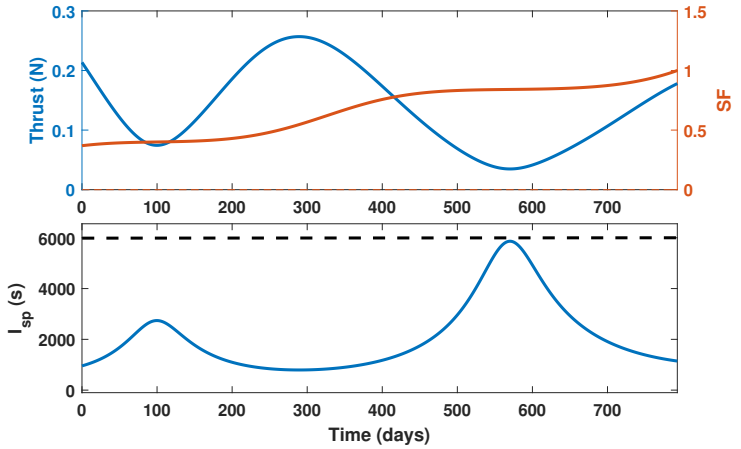

Figure 2.4: Thrust profile and I_{sp} vs. time for the E2M problem (unconstrained VIVT formulation).

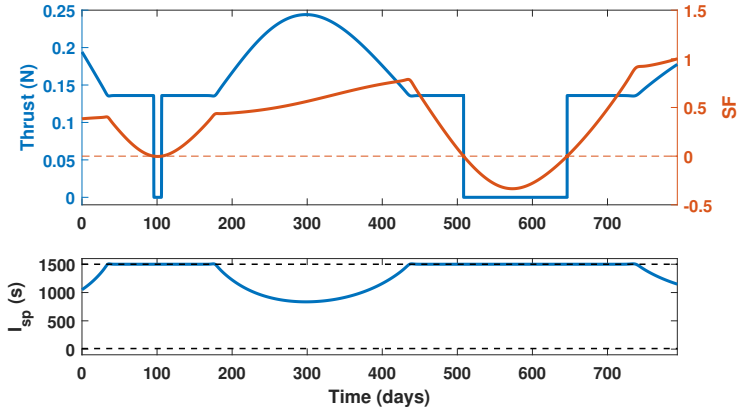

Figure 2.5: Thrust profile and I_{sp} for the E2M problem with $I_{\text{sp,max}} = 1500s$.

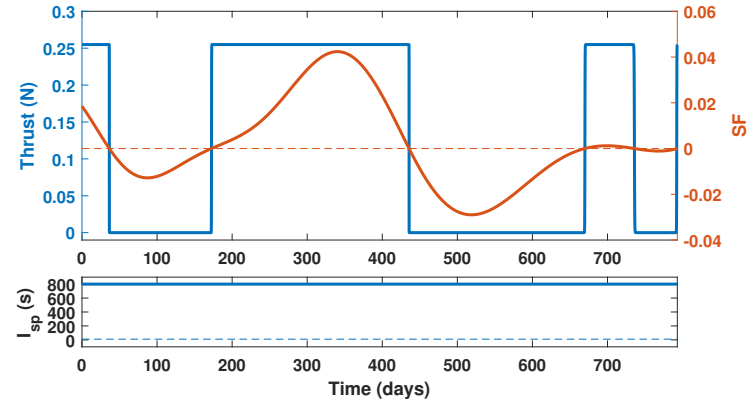

Figure 2.6: Thrust profile and I_{sp} for the E2M problem with $I_{\text{sp,max}} = 800s$.

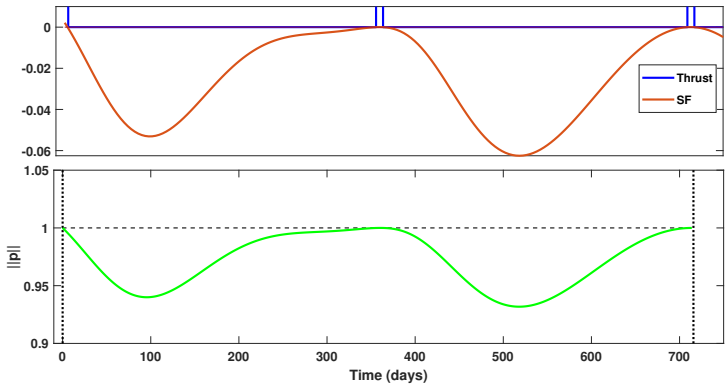

Figure 2.7: Thrust and switching function of approximate low-thrust impulsive trajectory (top) and norm of the primer vector associated with the optimal impulsive trajectory (bottom) for the E2M problem.

process. The final near impulsive, three impulses solution depicted in Figure 2.7 corresponds to a $\Delta v_{\text{total}} = 5.62$ km/s. The details on the time and magnitude of impulses for this near-optimal near-impulsive solution are given in Table 2.1. As is evident, the magnitude of the Δv impulses differ from the starting estimate in the 3^{rd} significant digit and are graphically identical on the solar scale.

Table 2.1: Comparison of the E2M Impulsive solutions.

c_{max} solution	
Δv_{total} (km/s)	5.62
Time of impulses(days)	[1.9922, 360.6356, 715.29368]
Magnitude of impulses (km/s)	[1.425, 1.928, 2.268]
PVT solution	
Δv_{total} (km/s)	5.6109
Time of impulses (days)	[0.0198817, 360.6553, 713.7880
Magnitude of impulses (km/s)	[1.439 , 1.891, 2.281]

The solution obtained from the above procedure in terms of number of impulses, position and time of impulses is fed into the non-linear solver (PVT step described in Section 3.3.1) as an initial

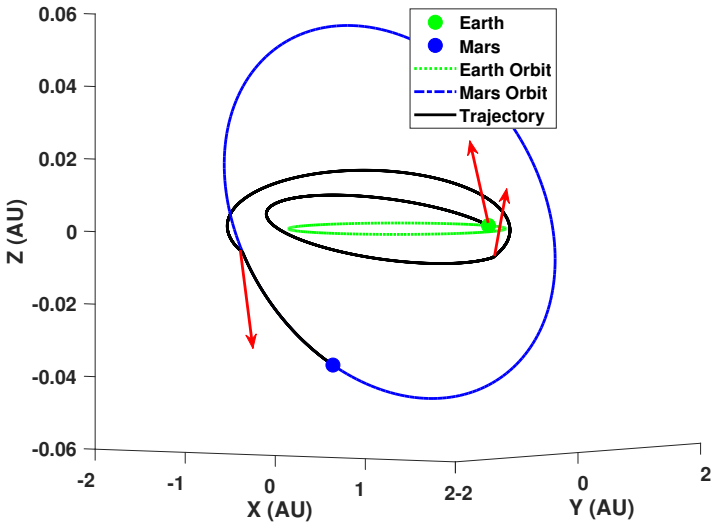

Figure 2.8: Minimum-ΔV, three-impulse trajectory for the E2M problem with red arrows indicating impulses.

guess to converge to the exact impulsive maneuver. The optimal primer vector obtained from the converged solution of *fmincon* (see Figure 2.7), satisfies Lawden's conditions. Notice that the obtained primer vector profile matches the switching function obtained from the CS step. The total ΔV (Δv_{total}) from this PVT step is 5.6109 km/s with some small variation in the departure time from the CS step solution. The complete comparison of the optimal impulsive solution obtained from CS and PVT is given in Table 2.1. The optimal impulsive trajectory obtained from PVT is given in Fig. 2.8.

2.2.4.2 Earth to Dionysus (E2D)

A difficult rendezvous problem with multiple orbital revolutions around the Sun is solved in this section using the $a_{\max}$ method. Though the E2D problem can be solved using both $c_{\max}$ and $a_{\max}$ methods, the latter is chosen to provide the reader clarity over both the methods. The E2D problem has recently emerged as another standard problem in its own right having been studied in great detail in [20] with different ΔV solutions and time of flight associated with different number of revolutions. The impulsive solution associated with 5 orbital revolutions,

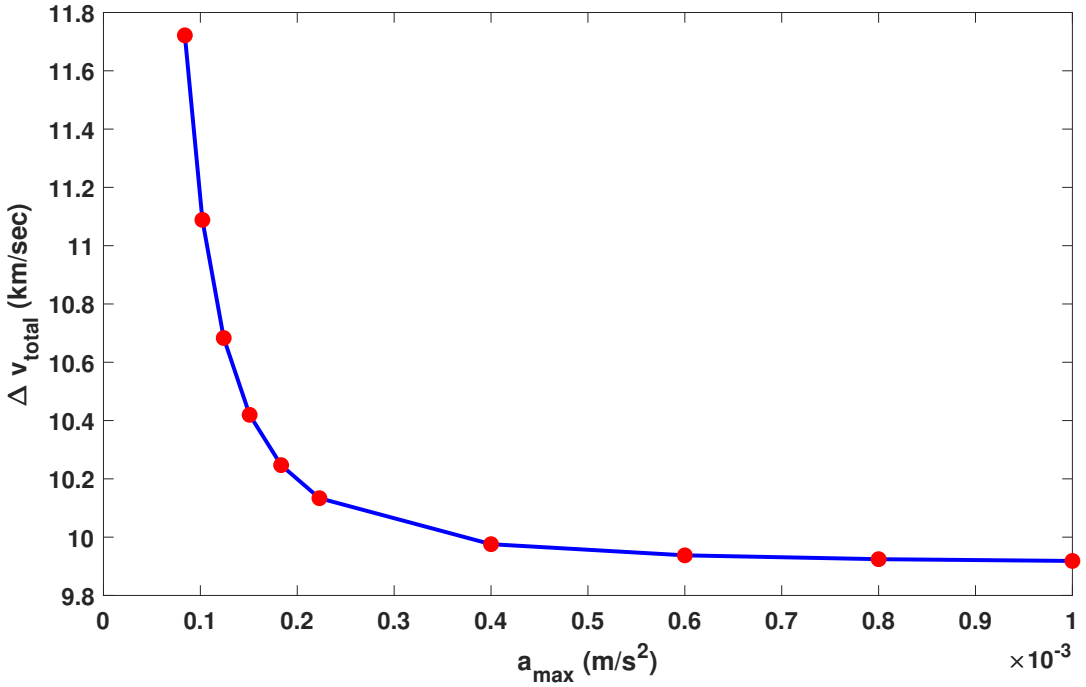

Figure 2.9: Continuation trend for Δv_{total} vs $a_{\max}$ for the E2D problem.

($N_{\text{rev}} = 5$), is solved in this work with a fixed time of flight of 3534 days and boundary conditions (in MEEs) defined as: $p(t_0) = 0.9996943$ (AU), $f(t_0) = -0.00376679$, $g(t_0) = 0.01628689$, $h(t_0) = -7.7020614 \times 10^{-6}$, $k(t_0) = 6.1881685 \times 10^{-7}$ and $L(t_0) = 14.1618925$. For the final target state, $p_d = 1.5536970$ (AU), $f_d = -0.5199481$, $g_d = 0.0161831$, $h_d = 0.0104734$, $k_d = 0.1181395$ and $L_d = 46.3302403$.

Starting from a relatively low value of $a_{\max}$, a continuation procedure of increasing $a_{\max}$ is conducted until the change in Δv_{total} is below a prescribed threshold (e.g., 1% relative to its previous value) as shown in Figure 2.9. For each value of $a_{\max}$ in the continuation step, the continuation parameter ρ_b (defined in Eq. (2.41)) is decreased till 1.0×10^{-3} to capture thrust acceleration arcs with an acceptable accuracy for the next $a_{\max}$ iteration. Notice the large $a_{\max}$ continuation steps. For $\rho_b = 1.0 \times 10^{-3}$, all the thrust arcs might not be sufficiently sharp but to save computational effort, the continuation in ρ_b could be stopped as we already have enough information to reliably initiate the next iteration. The final result corresponding to $a_{\max} = 1.0 \times 10^{-3}$ m/s^2 is shown in

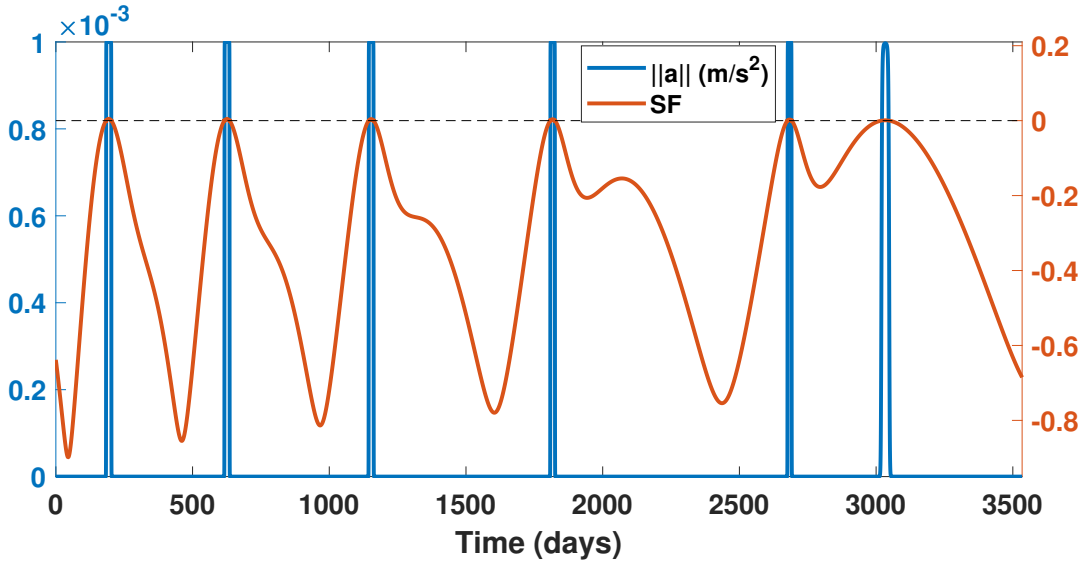

Figure 2.10: Thrust profile with the switching function for the E2D problem with $a_{\max} = 1.0 \times 10^{-3}$ m/s^2.

Figure 2.10.

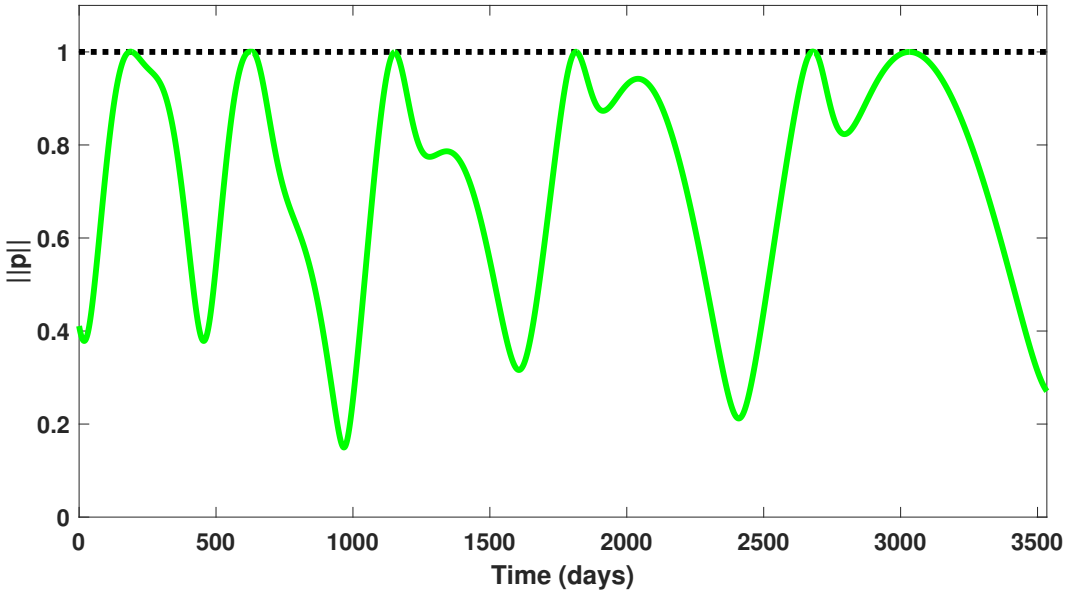

Figure 2.11: Primer vector magnitude vs. time for the E2D problem with $N_{\text{rev}} = 5$.

Figure 2.11 shows the time history of the primer vector magnitude associated with the impulsive solution that displays excellent satisfaction of Lawden's necessary conditions. Since all impulses are intermediate impulses, the primer vector derivative is zero at the time of impulses and $||\boldsymbol{p}|| = 1$ where $\|\boldsymbol{p}(t)\|$ is a local maxima [86]. Figure 2.12 shows the impulsive trajectory, where the first five impulses are applied at the perihelion passages of the intermediate elliptical orbits and the last impulse is applied at the intersection of the last elliptical orbit with the orbit of the asteroid Dionysus. This last impulse changes the inclination and the other parameters of the orbit of the spacecraft.

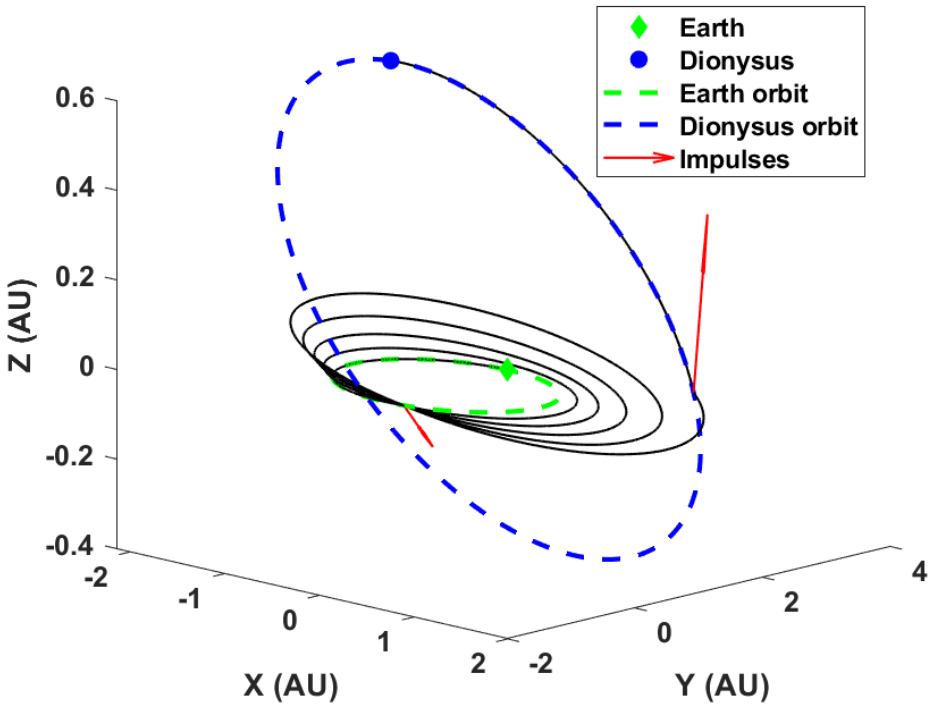

Figure 2.12: Minimum-ΔV, six-impulse trajectory for the E2D problem.

An early-arrival has happened where the last impulse establishes a rendezvous with asteroid Dionysus. For the remainder of the time of flight, both the spacecraft and the asteroid trajectories are the same until the marked location of Dionysus on its orbit. The importance of impulsive

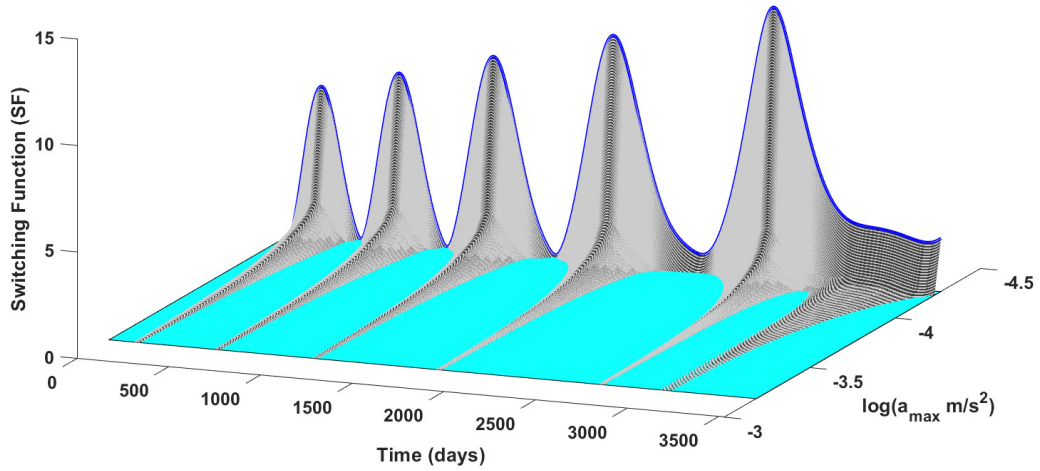

Figure 2.13: Maximum acceleration sweep switch surface for Earth to Dionysus maneuver.

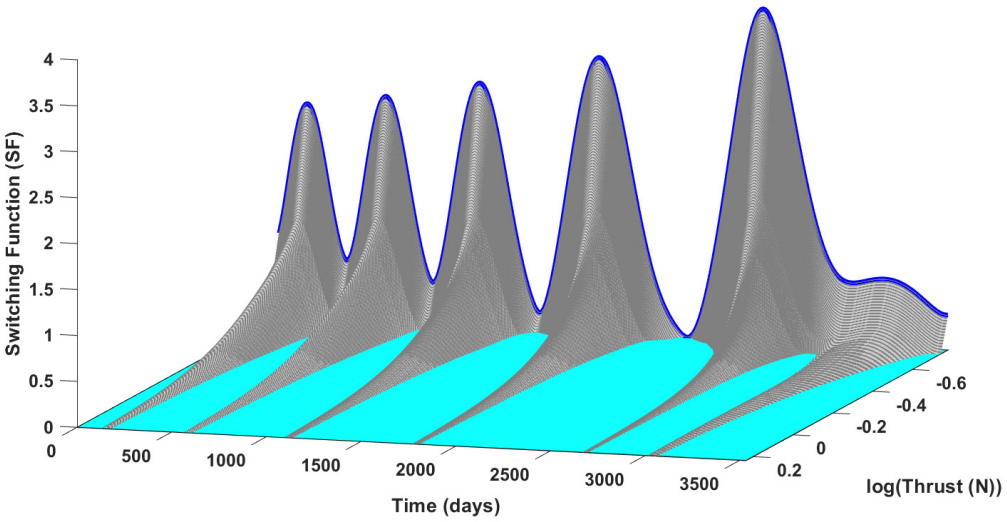

Figure 2.14: Maximum thrust sweep switch surface for Earth to Dionysus maneuver.

maneuvers for reachability analysis can be observed in the significant reduction in the time of flight with ideal impulsive solutions even when the original continuous thrust acceleration was applied along the trajectory.

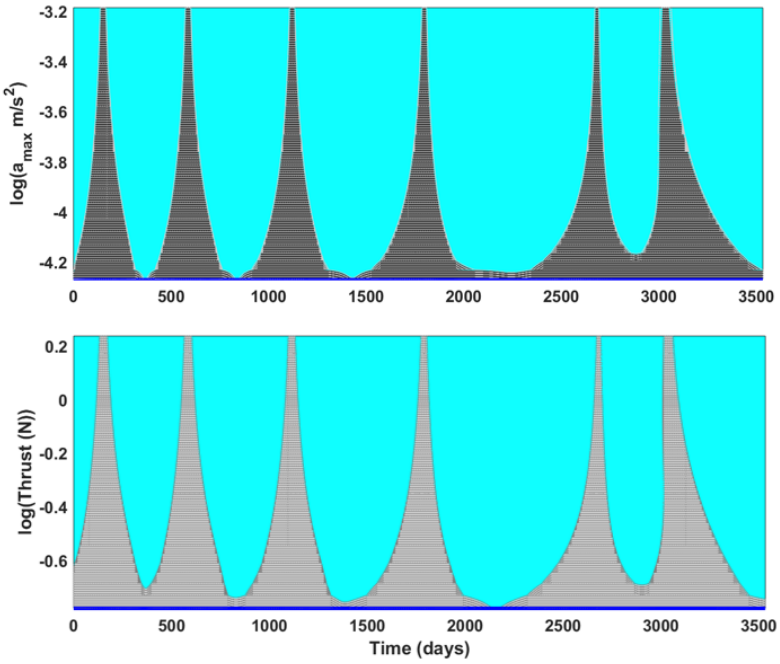

Figure 2.15: 2D slice of acceleration (top) an thrust (bottom) switch surfaces (S=0 contours).

In fact, the effective time of flight can be considered to be from the first impulse till the last impulse and the early and late coast arcs are redundant. The shift in the time of flight can be observed very clearly if $a_{\max}$ (opposed to thrust sweeps in [**?**]) is swept to generate a surface. This switching function for minimum surface shown in Figure 2.13) is quite similar to the thrust surface corresponding switching function surface (for minimum fuel with T swept) as shown in Figure 2.14. Notice, there are some different times for the zero crossing of the switching function near the peaks of the Himalayas when the control variable ($a_{\max}$ or T) is relatively small. The two surfaces are almost identical for the impulsive limits (see Figure 2.15) corroborating to the fact that both approaches approach the impulsive maneuver and the impulsive maneuver is independent of the

thrust performance and mass of the engine. This thruster independence is harnessed especially in the acceleration switch surfaces which provides different manifolds of trajectories possible for the fixed boundary conditions and a upper limit set on the time of flight and accleration values ($a_{\max}$). In fact, the optimization process underlying Figure 2.13 is simply the finite acceleration, finite pulse duration generalization of the impulsive minimum Δv optimization. This also provides an improved reachability analysis where the minimum acceleration value pertaining to the continuous control solution for a particular $a_{\max}$ value aids in engine selection.

Table 2.2: Comparison of the approximate and optimal minimum-ΔV solutions for the E2D problem.

$a_{\max}$ solution		PVT solution	
Δv_{total} = 9.9183 km/s		Δv_{total} = 9.90742 km/s	
Time (days)	ΔV (km/s)	Time (days)	ΔV (km/s)
193.377	1.6488	193.246	1.722
626.049	1.6097	629.608	1.4666
1153.166	1.5501	1152.099	1.6231
1816.915	1.4525	1816.969	1.44027
2683.504	1.2759	2683.731	1.2689
3033.693	2.3811	3032.192	2.3858

Notice the approximate six impulse times and the impulse magnitude again agree with the PVT optimal values to differences in the 3^{rd} or 4^{th} digit.

2.2.4.3 GTO to L1 (GTO2L1)

A challenging rendezvous problem of GTO2L1 involving 50 revolutions is solved. The MEE boundary conditions for this maneuver are:

$$\boldsymbol{x}_0 = [0.2765649\ (\text{DU}), 0.725, 0, 0.06116262, 0, 0]^\top,$$

$$\tilde{\boldsymbol{x}}_d = [7.74\ (\text{DU}), 0, 0, 0, 0, 317.3009]^\top.$$

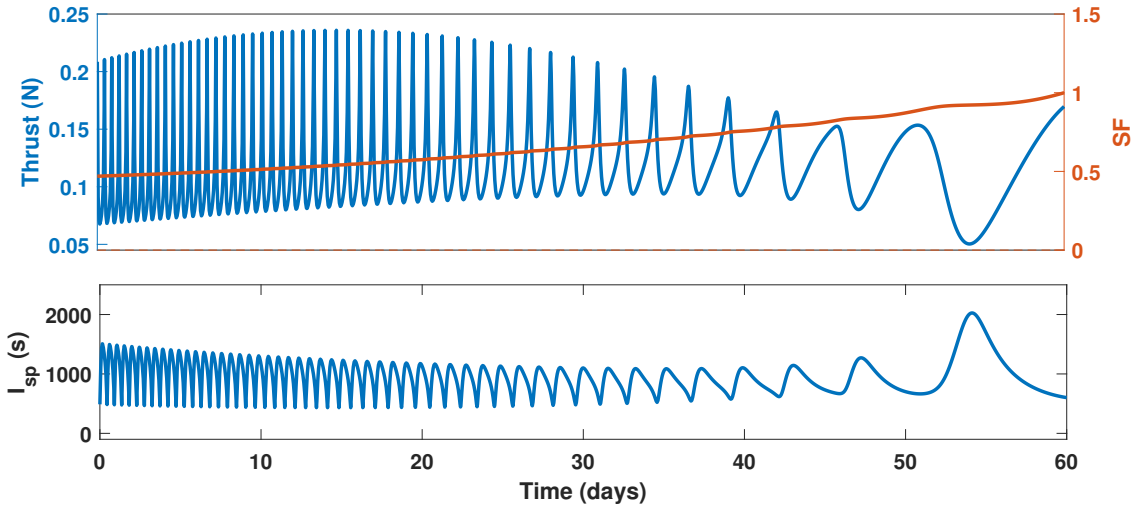

Figure 2.16: Optimal thrust and switching function profiles for the GTO2L1 problem using unconstrained I_{sp} in c_{max} method.

The other parameters are $P_{\text{use}} = 1000$ watts, and $m_0 = 250$ kg, $\Delta t = 60$ days and number of revolutions is equal to 50. The solution to the unconstrained c_{max} method displays a continuous thrust profile as depicted in Fig. 2.16 with a $\Delta v_{\text{total}} = 2.99$ km/s and the largest value of I_{sp} recorded as 2024.42 seconds. The specific impulse is reduced to an $I_{\text{sp}_{\text{max}}} = 1000$ seconds before handing

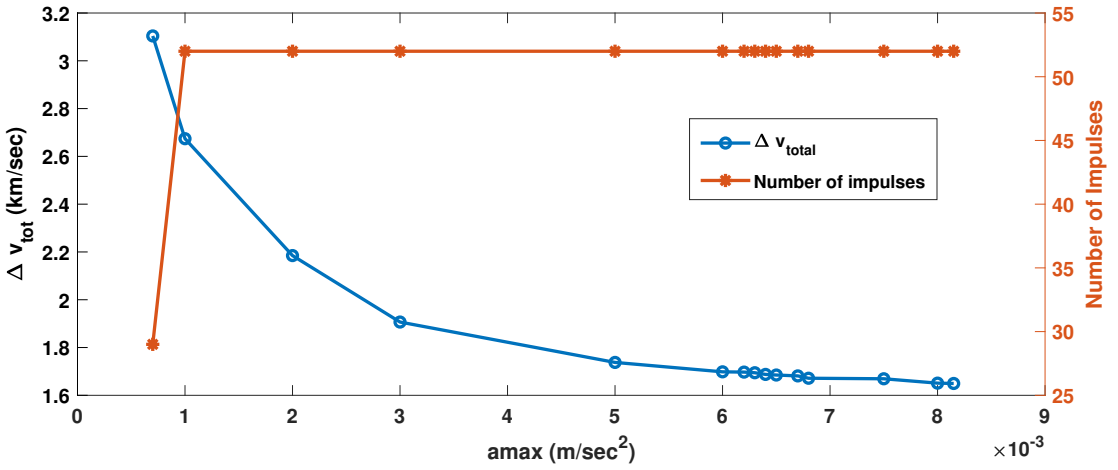

Figure 2.17: ΔV, departure time and number of impulses are plotted against the sweeping parameter a_{max} for the optimal approximate impulsive trajectory for the GTO2L1 problem.

over the converged costates and $a_{\max}$ value of 7×10^{-4} m/s^2 to the $a_{\max}$ method. The value of $a_{\max}$ is then swept from 7×10^{-4} to 8×10^{-3} m/s^2 beyond which ΔV does not change significantly (see Fig. 2.17). The final optimal approximate impulsive solution obtained for $a_{\max} = 7.5 \times 10^{-3}$ m/s^2 consists of neither a late departure nor an early arrival with a $\Delta v_{\text{total}} = 1.66.08$ km/s attributed to 52 impulses.

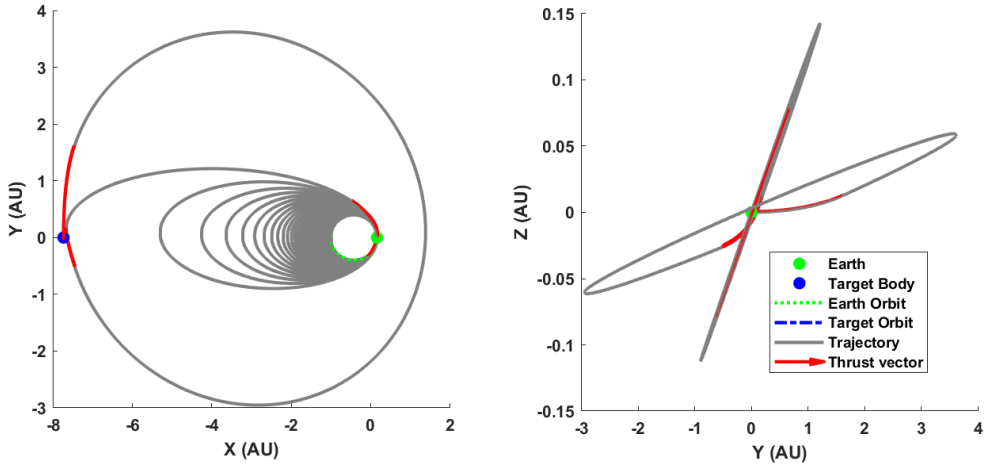

Figure 2.18: Optimal approximate impulsive trajectory for the GTO2L1 problem.

Every orbital revolution consists of a finite burn close to the perigee to raise the semi-major axis. Majority of the expensive inclination change is achieved in the last few orbits when the spacecraft is far from the Earth, which results in large magnitude impulses as shown in Fig. 2.20. The last (non-linear programming) verification step is not obtained for this maneuver as the convergence of NLP solver deteriorates drastically when a large number of design variables (208 in this case) are involved. This example shows the power of viewing the impulsive case as a limiting case of an indirect function space trajectory optimization approximations. We can solve higher dimensionality minimum impulse problems via the $a_{\max}$ function space algorithm than via discrete non-linear programming.

Therefore, the results indicate that both methods ($a_{\max}$ & $c_{\max}$) are capable of obtaining near-

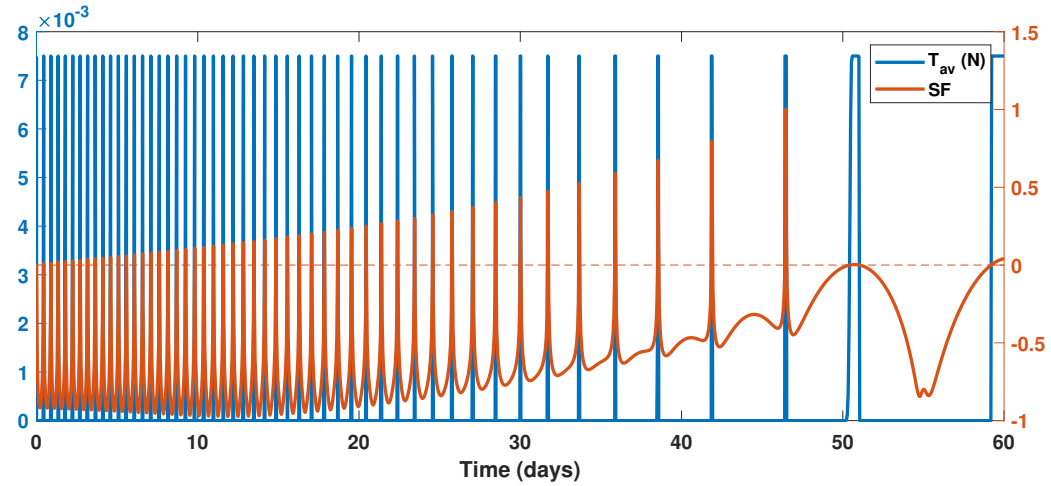

Figure 2.19: Acceleration and switching function profile for the GTO2L1 problem for $a_{\max} = 7.5e^{-3}m/s^2$

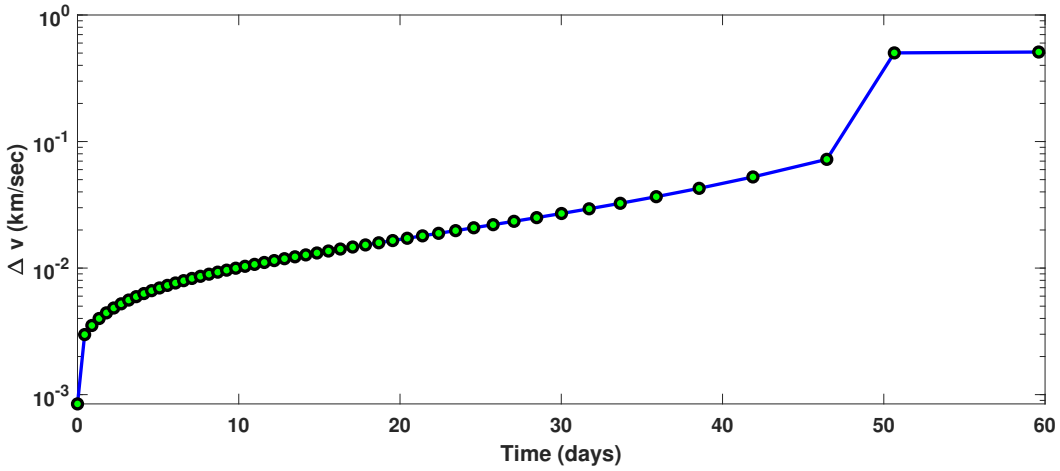

Figure 2.20: Δv distribution for the optimal approximate impulsive trajectory for the GTO2L1 problem plotted on a log scale against time of impulses.

optimal impulsive trajectories for maneuvers with medium levels of complexity. It is for more complex problems like GTO to L1 solved in this work that a two-step process is invoked. Optimal N-impulse orbit transfer maneuvers (with $N > 10$) are rare in the literature due to the absence of an approach to reliably find good starting estimates consistent with optimality principles. Thus, this dissertation and our recent papers address a significant gap. Also, the unconstrained I_{sp} version of solving the TPBVP is observed to be more efficient in terms of convergence than the acceleration squared method traditionally used. This could be due to the direct impact of the high sensitivity with respect to the unknown initial co-states guess vector (that is iterated upon in the procedure) on the acceleration magnitude that makes the problem unstable and infeasible for some set of guesses and therefore numerically challenging. The presented two-step process helps in mitigating the individual shortcomings of both the methods to provide a powerful tool that can especially generate complex impulsive maneuvers. In particular, a near-optimal multi-impulse ($N = 52$ impulses), multi-revolution (50 revolutions) maneuver is generated using the proposed method. While in a practical mission it is difficult to design a trajectory with large number of closely occurring impulses, it is informative to obtain theoretically optimal trajectories. In practice, pruning of the smallest impulses will likely be required or desired.

2.3 Low Thrust Transfer with Inequality Constraints [3]

Indirect optimization methods exploit smoothing based methods and numerical continuation to solve many difficult problems; some of which are practically unsolvable without these tactics. Though, related smoothing methods have also proven to be capable of handling inequality constraints and discontinuous conditions as a function of states and co-states, time explicit constraints especially when time triggers are not configured apriori are not explored heretofore. These temporal "no-go regions" commonly arise in solar electric propulsion (SEP) systems where the operational limits of the engine and solar arrays are riddled with eclipses and thermal tolerance limits, especially for planet-centric or sun proximity missions [89].

In the past few decades, solar energy has emerged as the most prominent power source for employing low-thrust propulsion on a space mission. SEP systems are subjected to occasional power cut-off during eclipses, so battery power sufficient to operate critical sub-systems during eclipses are required. The charge capacity of most small spacecraft is not sufficient to power the SEP system during eclipses. These eclipses occur whenever a body occults the incident Sun rays on the solar arrays. Assuming that the planetary bodies are spherical, two geometrical regions of partial blackout (penumbra) and complete blackout (umbra) are formed. Most frequently, during trajectory optimization the presence of the spacecraft in either of these regions necessitate a coast arc corresponding to the event of resulting solar power cut off. Therefore, SEP propelled missions generally require optimization over both continuous and discrete variables to satisfy different optimization objectives as well as operational constraints. Direct methods have assumed dominance for handling such constraints in trajectory optimization since the dawn of space age, because indirect methods were not sufficiently general and/or numerically implemented in a fashion to reliably handle the diversity of path and control constraints. Recently, many advancements in the field of indirect optimization of low thrust missions have been achieved, culminating in this dissertation that make the preliminary mission design more realistic [90]. The methods enhance multiple trade

[3] Reprinted with permission from "Indirect Based Shadow Modelling with Warm-Up Time" by Arya, Vishala and Woollands, Robyn and Junkins, John, 2022. AAS Guidance, Navigation and Control Conference, Breckenridge, Colorado

studies at the initial stage to make better, more optimal decisions from the onset of the mission design process [91]. Indirect optimization methods guarantee local optimality of the resulting solutions, and however challenging, we now have a reliable approach to accommodate inequality constraints and path constraints in the indirect formulation. As will be evident later in the dissertation, we now have indirect methods that allow exploration of a key issue: no optimality versus simplicity of the control structure.

Planet-centric low thrust maneuvers, especially, involve many orbital revolutions making the task of designing the trajectory itself even without the eclipse consideration, quite challenging. The eclipse duration is mainly the function of altitude, size of the planet and the Sun angle on the spacecraft. Kechichian [92] formulated analytical expressions for capturing the variation in classical elements due to continuous tangential thrusting with coasting enforced during eclipses. A multi-phase formulation was used by Betts [93] to solve for eclipse conscious multi-revolution geocentric trajectories by dividing the pre-eclipse, in-eclipse and post-eclipse into different phases. The orbit error was minimized in the manner similar to using a receding horizon algorithm. A simpler shadow model has been adopted in some works by considering a cylindrical projection of the Earth for the umbral region [94]. Ferrier and Epenoy modelled two concentric cylinders such that the power available within the shell is smoothed from 0% to 100 % by a degree 3 polynomial. However, this modelling does not resolve the discontinuities encountered at the time of the switch. Those switch discontinuities with the cylindrical model assumption are smoothed using HTS by Woollands [95] in which higher order of gravity perturbations are also included by use of the Picard Chebyshev numerical integrator. This cylindrical assumption can become significantly inaccurate in case of high altitude and highly elliptical orbits. Smoothing of these switches is primarily useful to improve numerical accuracy and to embed these constraints smoothly into indirect optimal control approaches.

A conical model is used for a more accurate modelling where the thruster is generally kept off even in the penumbral area where theoretically partial solar energy is still available. This conservative approach can be relaxed of course based on decisions by the analyst, considering bat-

tery capacity etc. Using the conical model, many works have adopted a trajectory optimization approach based on evaluation of the shadow entry and exit times [96, 97, 98] using direct optimization methods. Graham and Rao [99] were the first to use a collocation method to optimize a minimum time transfer such that the minimum time nominal trajectory was used to determine the approximate eclipses entry time. Once, eclipse entry time was evaluated, a forced coast arc and a two body assumption allowed propagation via Keplerian dynamics to evaluate the shadow exit time. The ambiguity in the number of revolutions when a minimum time solution is used for the eclipsed trajectory is another challenge that exists. Aziz et al [41] employed hybrid dynamic differential programming with the dynamics regularized by Sundman transformation to solve the same problem. A combination of smooth functions for conical shadow model were also introduced such that a 450 revolutions low Earth orbit (LEO) to Geo-equatorial orbit (GEO) maneuver is rendered solvable with suitable eclipse considerations. Taheri [100] achieved the same solution but using a simpler smoothing construct using HTS and complex derivatives along with a model that included a higher-fidelity gravity spherical harmonics (of desired order and degree) into the indirect formulation optimization problem. Taheri used a single shooting method for which the Sundman transformation leads to enhancement in numerical convergence for trajectories involving hundreds of revolutions.

For the duration of the eclipse, energy stored in batteries is used to power the payload and essential spacecraft systems. Also, when the spacecraft is in shadow, the temperature of the propulsion system drops significantly. The time needed to revive the solar power processing electronics and the engine post eclipse, such that it is capable to provide maximum thrust, can be referred to as warm up time (Δt_w). This warm up time is dependent on the time duration spent in the shadow, and is also typically dependent on the charge depletion and charge recovery rate of the batteries. The type of constraint that we now consider in solving the above problem can be classified more broadly as a state-triggered, time-dependent inequality constraint on the admissible control. In fact, such inequality control constraints that explicitly depend on both state and time are solved for the first time for trajectory optimization using indirect based methods [**?**]. The problem of eclipse

is chosen in this work for easy demonstration and proof of the invariant embedding concept. The presented smooth algorithm will find utility in many practical scenarios where any operational time limit on the thrusters imposed either due to science acquisition requirements, communication constraints with ground station or thermal tolerances can be accommodated.

In this work, a custom-made invariant embedding algorithm is devised to model eclipse constraints with warm up time with the help of comprehensive smoothing. The algorithm not only embeds parametric continuation in the form of functional smoothing for every 'if-then' condition but also lays the foundation for smoothly evaluating cumulative time to impose temporal constraints. The HTS smoothed switch functions approximate with near-arbitrary precision all of the corresponding discontinuous switches, as a limiting case, when the embedding homotopy parameter is swept towards zero. The main example of the operational inequality state and time dependent constraint that is solved here is the inclusion of warm-up time in the indirect optimization which is a typical requirement associated with every engine to regain its full thrusting potential. The warm up time is evaluated as a user-defined fraction of the time spent in the shadow for every eclipse occurrence during the maneuver.

2.3.1 Rendezvous Problem Formulation

The optimal control problem (OCP) is formulated using the set of modified equinoctial elements (MEEs) with equations of motions given in Section 2. Since the problems solved in this paper involves planet-centric manuevers to invoke eclipse conditions, the power generated by the solar array does not vary significantly as the heliocentric distance hardly varies through several revolutions. Therefore, a simplified thrust power model is considered where a constant power leads to a constant thrusting capability. Hence, the engine modelling for this problem mimics the nuclear electric propulsion model. Therefore, without loss of generality we have considered $P_{\text{av}} = P_0$ and have parametrized the control acceleration vector as

$$\boldsymbol{a} = \frac{2\eta P_0}{mc}\delta\hat{\boldsymbol{\alpha}}, \tag{2.47}$$

Here, $\delta \in [0, 1]$ will be realized as a multiplicative smoothed representation of all switches in the thrust profile triggered by fuel-optimality, eclipses or forced coasts due to warm up time. The construction of δ for this specific problem is of the form:

$$\delta = \delta_b \delta_s \delta_w \tag{2.48}$$

The mathematical expression to evaluate all three $\delta' s$ individually at each time step throughout the maneuver will be derived shortly. Even when we have included δ_s into the throttle function δ, δ_s essentially aids in calibrating the fraction of sunlight that is accessible to the spacecraft (incident on the solar arrays) to generate power. In our case, since total power loss is assumed in the penumbral region for simplicity, δ_s takes the value of either 1 or 0 as the case may be. In order to obtain a time-optimal solution, for example, optimal control problem can be stated as

$$\begin{aligned} &\text{Minimize } \; J = \int_{t_0}^{t_f} 1 \; dt \\ &\text{subject to :} \\ &\qquad \text{Equation (2.6)}, \\ &\qquad \boldsymbol{x}(t_f) - \tilde{\boldsymbol{x}}_d = \mathbf{0}, \\ &\qquad \boldsymbol{x}(t_0) = \boldsymbol{x}_0, m(t_0) = m_0, \end{aligned} \tag{2.49}$$

where t_0 is the initial time, $\boldsymbol{x_0}$ and m_0 are the MEEs and mass of the spacecraft at the initial time, t_f is the final time which is also a design variable, $\Delta t = t_f - t_0$ is the time of flight, and $\tilde{\boldsymbol{x}}_d$ is the desired MEEs at the final time. The Hamiltonian associated with the defined OCP can be written as:

$$H = 1 + \boldsymbol{\lambda}^\top \left(\boldsymbol{A}(\boldsymbol{x}, t) + \frac{2\eta P_0 \delta}{mc} \mathbb{B}(\boldsymbol{x}, t) \hat{\boldsymbol{\alpha}} \right) - \lambda_m \frac{2\eta P_0}{c^2} \delta, \tag{2.50}$$

where $\boldsymbol{\lambda} = [\lambda_p, \lambda_f, \lambda_g, \lambda_h, \lambda_k, \lambda_l]^\top$ and λ_m is the costate associated with mass. The control direction, $\hat{\boldsymbol{\alpha}}$ is along Lawden's primer vector $\mathbf{P} = \mathbb{B}^\top \boldsymbol{\lambda}$) as per PMP.

$$\hat{\boldsymbol{\alpha}}^* = -\frac{\mathbf{P}}{||\mathbf{P}||}, \tag{2.51}$$

and the other control variable, the throttle δ which is written as a product of three smoothed δ functions namely, $\delta_b, \delta_s, \delta_w$ enforce coasts arcs due to fuel-optimality, shadow occurrences and warm up time respectively. Out of the three δ variables, δ_b for a minimum time solution comes out to be identically 1 throughout the maneuver to enforce continuous thrusting for an optimal maneuver time (in the absence of eclipses).

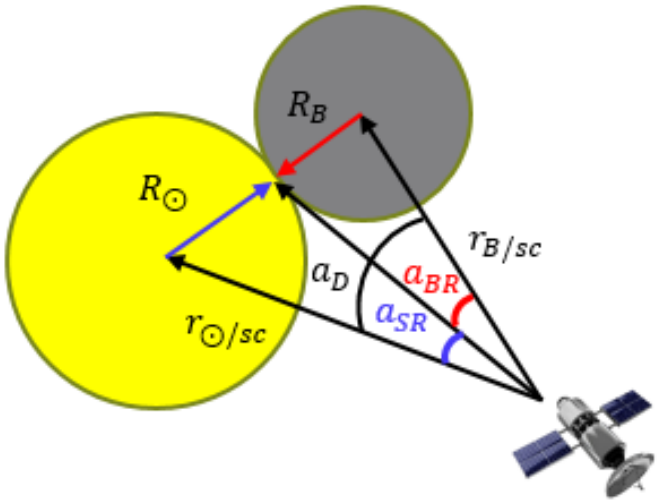

Figure 2.21: Schematic for a time explicit control operational constraint.

2.3.2 Eclipse Modelling

The eclipse constraints are modeled using general approximations and a body of assumptions like spherical planetary bodies. Due to the large astronomical distance between the Earth and the

Sun, the apparent diameter of the Sun becomes relatively small. On ignoring Earth's oblateness and surrounding atmosphere, overlapping circular disks as is shown in Figure 2.21 can be used as a preliminary approach for modelling the eclipses [41]. In Figure 1, R_Θ and R_B denote the mean radius of the Sun and occulting body, respectively, r_Θ/sc denotes the position of the Sun with respect to the spacecraft, and R_B/sc denotes the position of the occulting body relative to the spacecraft. The apparent angles (a_{BR} and a_{SR}) and the apparent distance (a_D) can be derived as [41]

$$a_{SR} = \arcsin\left(\frac{R_\Theta}{r_{\Theta/sc}}\right), \tag{2.52}$$

$$a_{BR} = \arcsin\left(\frac{R_B}{r_{B/sc}}\right), \tag{2.53}$$

$$a_D = \arccos\left(\frac{\boldsymbol{r}_{\Theta/sc}^\top \boldsymbol{r}_{B/sc}}{||\boldsymbol{r}_{\Theta/sc}||.||\boldsymbol{r}_{B/sc}||}\right), \tag{2.54}$$

where, $\boldsymbol{r}_{\Theta/sc} = \boldsymbol{r}_\Theta - \boldsymbol{r}_{sc}$ and $\boldsymbol{r}_{B/sc} = \boldsymbol{r}_B - \boldsymbol{r}_{sc}$. Using these angles ($a_{SR}, a_{BR}$ & a_D), umbral, penumbral and no eclipse conditions can be modeled using multiple inequality conditions. Each of these inequality conditions require additional smoothing to transition smoothly from the eclipse to the no eclipse region. In this work, penumbral region is not identified separately therefore just one smooth condition suffices to model the eclipse occurrence:

$$\delta_s = \frac{1}{2}\left[1 - \tanh\left(\frac{g_s}{\rho_s}\right)\right] \tag{2.55}$$

where $g_s = a_{SR} + a_{BR} - a_D$.

2.3.3 Warm-up Time Model

The algorithm that we present in this section holds the key to including a class of time explicit temporal constraints for incorporating a more realistic thrusting capability into trajectory optimization. For example, there can be two kinds of operational constraints; (i) where additional thrust arcs are enforced to adhere to a minimum operational time constraint or (ii) alternatively, additional coast arcs are enforced to accommodate power constraints. Before detailing the algo-

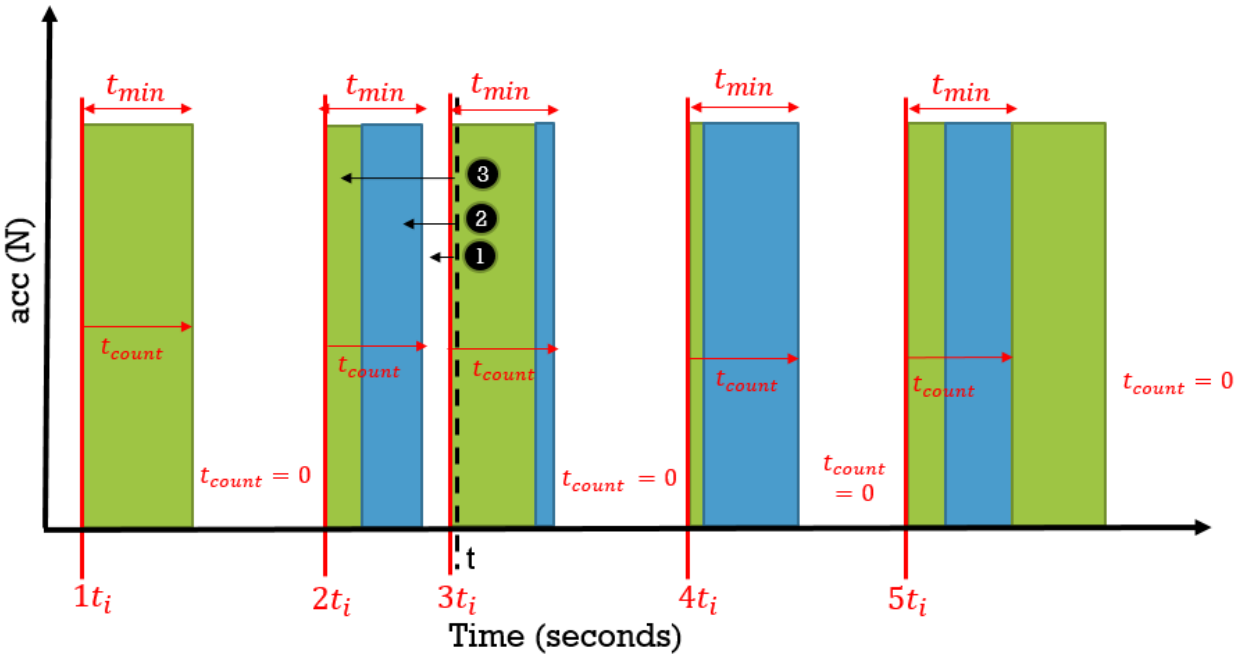

Figure 2.22: Schematic for a time explicit control operational constraint of first kind.

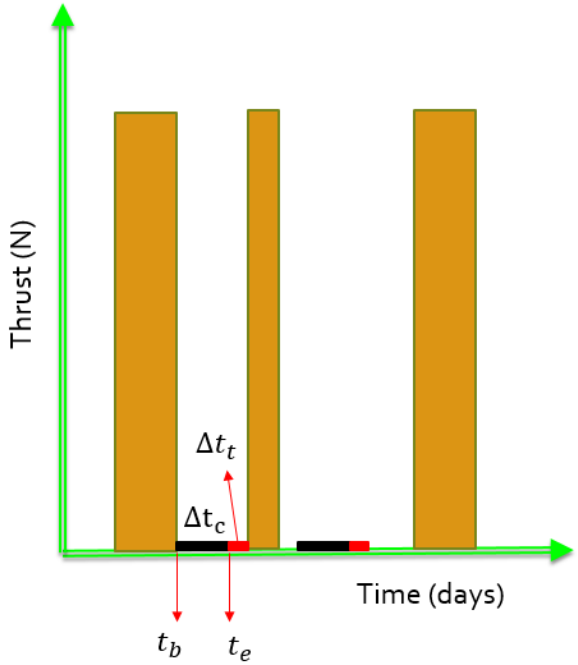

Figure 2.23: Schematic for a time explicit control operational constraint.

rithm, it is important to understand the challenges associated with incorporating this variety of constraints especially with a variable step size integrator. Figure 2.22 shows a general schematic for the operational constraint of first kind where t_{min} denotes the user set minimum time for which the thruster should be 'on'. Five different scenarios in terms of five different composite thrust arcs (each beginning with a it_i such that i=1,2,3,4,5) are shown where the green thrust arc represents the optimal thrust while the blue one represents the forced thrust to satisfy the t_{min} operational limit. The variable t_{count} keeps account of the total time optimal thrust is continuously 'on' starting from the time point it_i and t_{count} is reset to zero when $t_{\text{count}} \geq t_{\text{min}}$. A fair idea of the complexity of a time explicit constraint is provided by three cases marked by black circles in the third scenario (associated with $3t_i$) with the black arrow (starting from time 't') showing three different representative locations (say, marked by t_r) the correction step in an integrator like *ode45* might back trace to. In the first case, t_r goes to the point before $3t_i$ where $t_{\text{count}} = 0$. Since, $t_{\text{count}} = 0$, it is simpler to forward propagate from this point where one can simply coast till a thrust arc is encountered. For the second case, the back tracked t_r goes to the region of forced thrust arc of the second scenario (associated with $2t_i$). At this point $t_{\text{count}} \neq 0$, therefore, t_{count} will have to evaluated as per $2t_i$ and not $3t_i$ to evaluate the remaining time for which the thrust arc has to enforced. In the third case, t_r reaches the region of the optimal thrust arc for scenario 2; therefore, using $2t_i$ time stamp, new t_{count} is evaluated and compared with t_{min}. Clearly all of these " must hit " state dependent times, make numerical integration logic painful. The smoothing technique we introduce makes all of this testing unnecessary and implicitly relies upon an adaptive integrator's standard step size control logic to sense the smoothly embedded δ functions time varying curvature.

In this work, the algorithm to enforce the operational constraints of second kind is described, for which we require to build some time pointers as shown in Figure 2.23. Here, the time pointers like t_b, t_e mark the time stamp for beginning of the activation of a constraint and time stamp for the end of constraint activation respectively. The actual algorithm is presented in terms of a pseudo algorithm. The algorithm kicks off with some initialization of some secondary parameters ($\varrho, \varsigma, \kappa$), certain time pointers and some conditions (g_s for state associated conditions and g_t for

Algorithm: Event Smoothing algorithm for state and temporal constraints

Result: $T_{\text{ap}} = T\delta_s\delta_t$
initialize $t = 0, t_b = 0, t_e = 0, \Delta t = 0, \varsigma = 1, \varrho = 1$;
while $t \leq t_f$ **do**
  $\delta_s = 0.5\left[1 - \tanh\left(\frac{g_s}{\rho_s}\right)\right]$
  Update $t_b = t(1-\delta_s)\varsigma + t_b[1-(1-\delta_s)\varsigma]$
  Update $\varsigma = \varsigma - \varsigma^2(1-\delta_s)$
  $\kappa = \delta_s(1-\varsigma)(1-\varrho)$
  Update $t_e = \kappa t_e + (1-\kappa)t_e$
  $\Delta t_c = \kappa|t_e - t_b| + (1-\kappa)\Delta t_c$
  $\Delta t_t = \beta\Delta t_c$
  $g_t = t - (\Delta t_t + t_e)$
  $\delta t_c = 0.5\left[1 + \tanh\left(\frac{g_t}{\rho_t}\right)\right]$
  $\varrho = \kappa + \varrho(1-\kappa)$
end

time associated conditions). The final output of the algorithm is the applied thrust (T_{ap}) which is a product of constant engine thrust value (T), state constraint throttle function (δ_s) and cumulative time constrained throttle function (δ_t). In the context of the problem solved in this work, state constraint (g_s) represents the event of eclipses and the warm up time condition (g_t) is attributed as the time dependent operational constraint. Even when only one combination of g_s and g_t functions are considered in the sample pseudocode, the algorithm is easily expandable to include more constraint functions by using a combination of products or summation of individual constraints as the case may be. The variable Δt_c provides the cumulative dwell time for a condition/state/operation say the amount of time spent in radiation, or the time recording the temperature build up in case of constant rate of heat absorption by solar arrays etc.. In this particular case, it is used to evaluate the time spent in eclipse. The accurate evaluation of Δt_c is not trivial as it not only depends on the satisfaction of a certain inequality constraint but also on the step size of the integrator. This is one crucial step and also act as a bottleneck in accommodating time explicit constraints with no apriori set time bounds.

The calculation of Δt_c involves multiple situations conditioned at tracing the switch times

of g_s at both the: (i) activation time and, (ii) the deactivation time of the condition g_s. These conditions are generally realized by multiple if-then conditions causing discontinuities whereas here, we have smoothed it using a single continuation parameter, ρ_s. Additionally, in order to capture various equivalent scenarios analogous to the kinds described in Figure 2.22, additional variables and checks are introduced such that not only Δt_c is evaluated correctly but the end time of g_s activation (i.e. t_e) is recorded accurately even when variable step size integrator that goes back and forth on time is perused. If this is not done carefully, the integrator will take thousands of steps to converge making the integration not only extremely slow but unreliable in some cases.

As part of logic leading to evaluation of Δt_c, the intermediate *event trigger logic* variables ϱ, ς & κ are introduced. Specifically, ς=1 indicates that a lookout for a new eclipse encounter is on, while $\varsigma = 0$ indicates continued tracking of the existing eclipse condition. Similarly, $\varrho = 1$ indicated continued tracking of the existing warm up time while $\varrho = 0$ indicates the end of warm up time period and gets updated to the value of 1 only when new warm up time constraint is triggered. These onset and end conditions along with the eclipse activation constraint should be true simultaneously for the warm up time constraint to activate. Therefore, this type of composite trigger conditions is captured as a product of these three individual conditions in κ. These three supporting variables are interdependent and self-updating subjected to the activation and deactivation of one single condition given by the function g_s and their respective current values. Due to the underlying inter-dependencies, the sequence of the steps to update every variable should be strictly followed as given in the event smoothing pseudo-algorithm.

For the specific case of warm up time, the time duration for which a coast is enforced owing to engine wait time is set as β times the time spent in shadow Δt_s. Here, β is specified by the designer depending on the capacity of the battery and the spacecraft size etc. The condition that determines if the coast arc due to warm up time is imposed or not is given by condition g_t which is expressed smoothly by δt_c and the continuation parameter ρ_t. In order to enable the use of variable step size integrator, the condition g_t is evaluated by means of a time stamp t_e so that a time stamp for the end of warm-up time can be obtained to compare the time slot in which the current time 't'

Table 2.3: Coefficients for polynomial interpolation of Sun's position.

	$(.)^4$	$(.)^3$	$(.)^2$	$(.)^1$	$(.)^0$
$x_{\text{sun}}(\hat{t})$	8.2049E4	1.1444E6	-7.4788E6	-4.4379E7	9.7613E7
$y_{\text{sun}}(\hat{t})$	1.1618E5	-9.2258E5	-8.8375E6	3.8624E7	1.1528E8
$z_{\text{sun}}(\hat{t})$	156.8767	29.8668	93.8179	-1.7644E3	-6.4347E3

falls in. This evaluation of t_e requires frequent resets on the intermediate variables so that when the eclipse conditions occurs again, the same algorithm can be re-iterated without errors. Therefore, ϱ, which is really the variable responsible to reset the warm up time evaluation, is updated right at the end subjected to the value of κ.

2.3.4 Numerical Simulation

The duration of the eclipse is evaluated by generating the ephemeris of the Sun with respect to the central body (the Earth in this case) using JPL DE405 data. If for fast computation, the files are mexed (see [75]), the position of the Sun (other planets if needed) are fitted using polynomials of order 4 for the duration of the maneuver. The coefficients of the polynomial for the x,y,z component of Sun's position are given separately in Table 2.3. In order to avoid extreme values for the coefficients caused due to the discrepancy in the scale of time and distance units, the data is normalized before curve fitting using a mean ($\mu_c = 7.370352691858428 \times 10^8$) and standard deviation value ($\sigma_c = 1.9953599425778 \times 10^6$). evaluated on the 'x' data (here, time). Using these values, t is centred at zero and scaled to have unit standard deviation by using:

$$\hat{t} = \frac{t - \mu_c}{\sigma_c} \tag{2.56}$$

Additionally, in order to enhance the convergence of the two point boundary value problem solver, the state variables are normalized. For an Earth centric trajectory optimization problems, canonical units are adopted such that one distance unit (DU) is equal to the mean equatorial radius of the Earth ($R_e = 6378.137$ km), and the gravitational parameter of the Earth is $398,600.4 km^3/s^2$. Scaling of the state variables and time gives rise to corresponding scaling of the co-state variables.

First, an initial guess for the unknown costate vector $\boldsymbol{\lambda}(t_0)$ is generated randomly. Then *fsolve* is invoked to solve the TPBVP with initial values for different continuation parameters (ρ). There are multiple strategies to reduce the value of continuation parameter especially when multiple continuation parameters are used. In this study, there are three continuation parameters that are used, of which ρ_s & ρ_w are used for enforcing the constraint of eclipses and warm up time directly while ρ_p is used to evaluate the cumulative operation time Δt_c. The smallest value for these ρ's is problem dependent and is typically determined by plotting the variation of the cost functional versus the continuation parameter. Since, there are some constraints in this problem which are explicit functions of time, the continuation parameters are lowered to a value consistent with the minimum step size of the variable time step integrator ($\mathcal{O}^{-10}$). The costate vector of the converged solution is used as the initial guess for the next sub-problem. As a numerical example, there are 3 "stepping stones" problems that are solved:

1. Minimum time solution
2. Minimum time solution with eclipse constraint
3. Minimum time solution with eclipse and warm-up time constraint

The solution for the first problem feeds into determining a good starting guess (especially the time of flight) for solving the TPBVP associated with the next problem.

2.3.5 Results

The specific case of warm up time (which is defined as the time duration post an eclipse such that the engine has to wait before it is allowed to thrust) is used as an example here. This operational limit is an ideal case to show the efficacy of the algorithm because the warm up time is set as a user defined fraction of the time spent in shadow. Also, eclipses are observed in planet-centric maneuvers which generally involve a larger number of revolutions, making the problem challenging. Such problems are known to benefit greatly from analytical sensitivities for which smoothness of the differential equations is important. Therefore, the proposed algorithm is tested

	a(km)	ecc	inc (deg.)	Ω (deg.)	ω (deg.)	ν (deg.)
$\boldsymbol{X}_0$	24505	0.725	7	0	0	0
$\boldsymbol{X}_f$	42165	0.001	$1e^{-4}$	0	0	pi

Table 2.4: GTO-GEO maneuver boundary conditions

on a maneuver from a GTO to GEO with the Keplerian elements given in Table 2.4 where 'a' is the semi major axis, 'ecc' is eccentricity, 'inc' is inclination, 'Ω' is the right ascension of the ascending node (RAAN), 'ω' is the argument of perigee and 'ν' being the true anomaly. Here, the true anomaly (ν) for GEO indicates the osculating angular position ($\leq 2\pi$) of the spacecraft at the final time on the final revolution and does not indicate the number of en-route revolutions around the Sun (Nrevs) that are required to reach the target final state.

T (N)	0.187
I_{sp} (s)	3100
m_0 (kg)	400
β	0.4

Table 2.5: Spacecraft Parameters

In fact, the problem of finding a global optimal minimum time solution with respect to Nrevs is a tough problem in itself, which is not considered here, but is studied in [101]. In order to obtain a feasible solution, minimum time solution was first evaluated with free final longitude (i.e free Nrevs). The number of revolution observed from this converged solution was rounded off to get the nearest integer number to solve the minimum time rendezvous problem again pertaining to a fixed number of revolutions this time. The same number of Nrevs is considered when incorporating both eclipse and warm up time constraints for drawing logical comparisons among the three cases. It is recognized, that in some circumstances, incorporating eclipse constraints (with the implicit loss of thrust during eclipses) may render the target orbit elements being not reachable with the Nrevs corresponding to the case where eclipses are ignored. This situation was not encountered in

the case discussed in this dissertation, but the remedy is clear: reduce Nrevs by one until a feasible solution satisfying the necessary conditions (for a local extremal) is achieved. The spacecraft parameters are given in the Table 2.5. These parameters are based on a Hall thruster used on a medium sized spacecraft of 400kg. Using the Hall thruster, a minimum time solution associated with 90 Nrevs was solved for all three cases. The trajectory for the minimum time solution is not shown as it is graphically not very different from when eclipse encounters are factored into the optimization.

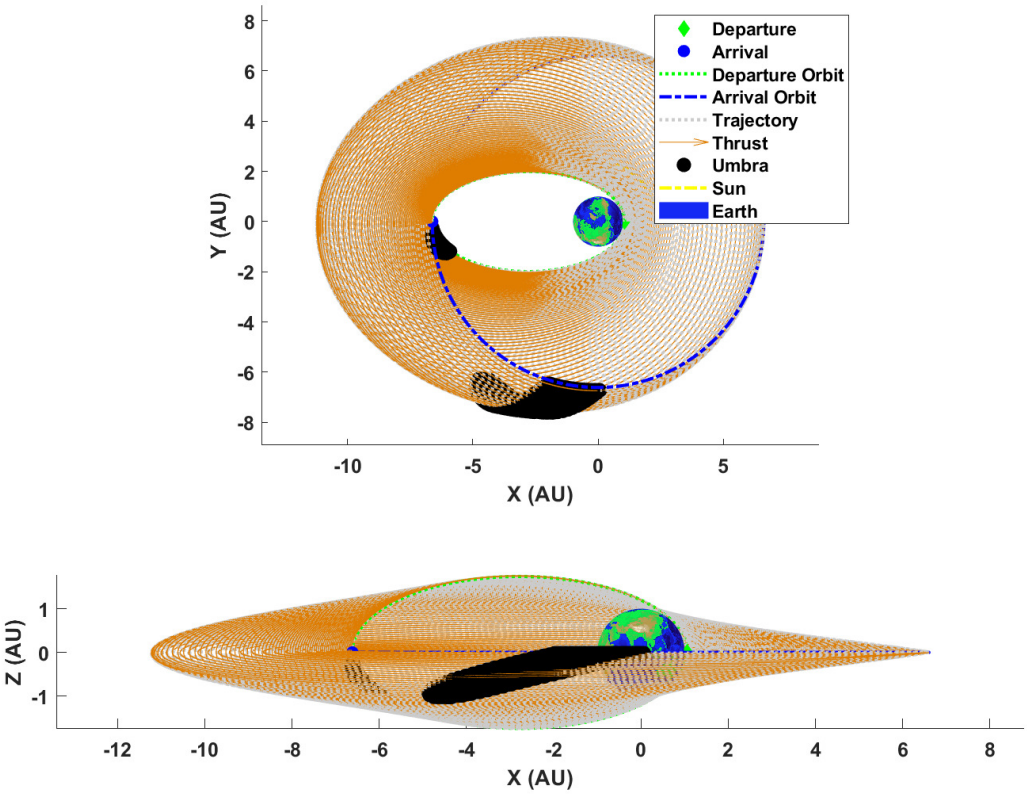

Figure 2.24: Minimum time trajectory for the GTO to GEO maneuver with thrust history reflecting eclipse constraints.

Figure 2.24 shows the time-optimal trajectory when eclipse conditions are considered. A gradual and steady change in inclination is brought about by a low thrust engine such that the semi-

major axis of the weakly perturbed intermediate orbits go farther out than GTO. With the launch date as April 1, 2021, the eclipses seem to occur in two batches; one very close to the launch time and the other very close to arrival as shown in Figure 2.25. A separate study can be done in relation to the launch time which influences the total time spent in eclipse. Another study can be done with respect to the selection of initial or final RAAN. If an alternate non-zero Ω value is chosen for GTO or GEO, it is clear that the duration of shadow has the potential of significantly reducing. The time penalty of 3 days is observed due to the occurrence of eclipses as compared to the non-eclipsed minimum time solution of 71.1 days as given in Table 2.6. The coast arcs due to the eclipse are all close to the osculating apoapsis causing less fuel loss as compared to the periapsis coasts.

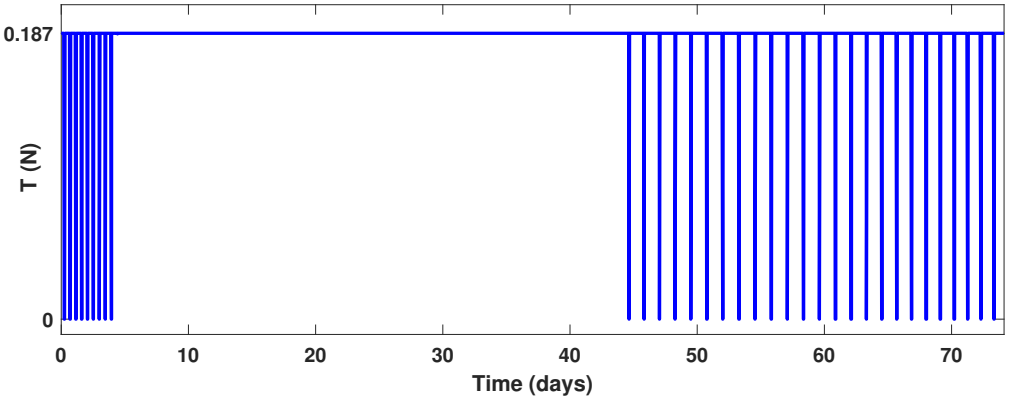

Figure 2.25: Thrust profile for the GTO to GEO maneuver with coast arcs owing to eclipse and warm up constraints.

The numerical challenge of accommodating such short coast or thrust arcs using any smoothing method is not trivial. The tolerances of the integrator also needs to be lowered to influence the step size to be small enough such that very short control arcs are captured. When the constraint of warm up time is included into the optimization problem, the time of flight increases by half a day as compared to the eclipsed solution. The optimized trajectory for this case is shown in Figure 2.26 where the red shaded area immediately following the black region of eclipse shows the spatial

placement of the forced coast arc. The coast arcs due to eclipses alone move around a bit when coasts arcs due to warm up time are introduced but no substantial shift is observed on this scale. The coast arcs associated with warm up time are only 40% the duration of eclipse coasts; making the adaptive step size control of the numerical integration even more important. For capturing such small thrust arcs, it is generally observed that the time associated continuation parameters have to be lowered to very small values ($\mathcal{O}^{-8}$) to capture these short, near bang-off- bang thrust profiles.

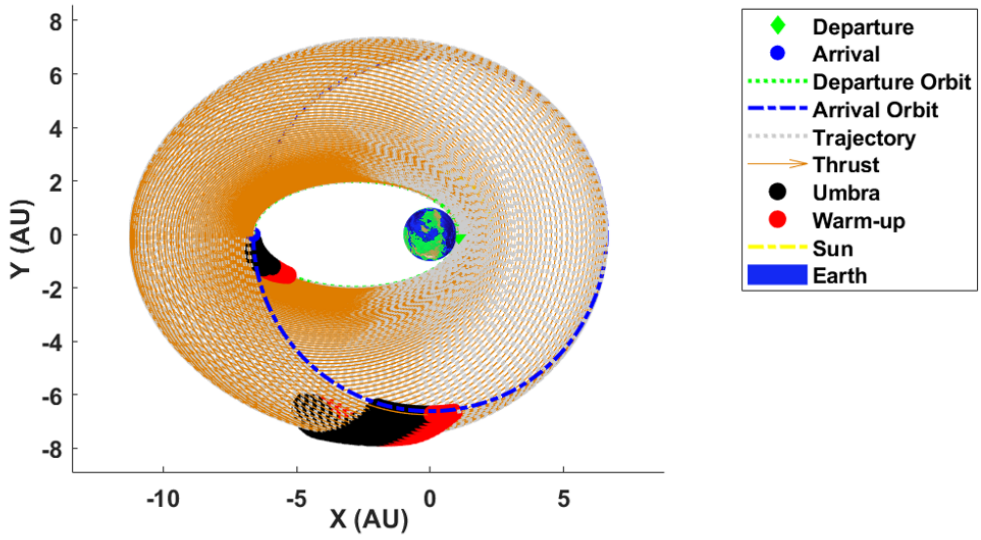

Figure 2.26: Trajectory for the GTO to GEO maneuver with thrust history, eclipse and warm up times indicated (XY view).

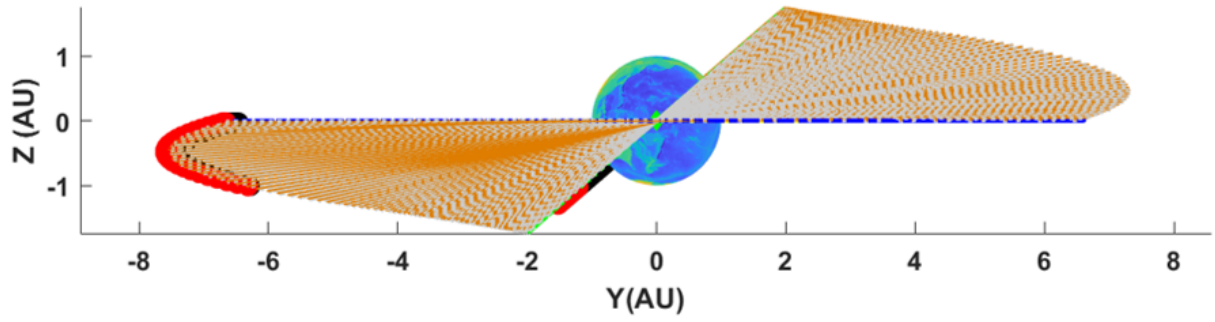

Figure 2.27: Trajectory for the GTO to GEO maneuver with thrust history, eclipse and warm up times indicated (YZ view).

	t_f	m_f
Minimum Time	71.098	362.21
Eclipsed	74.126	361.41
Eclipse+Warm up	75	361.11

Table 2.6: Summary of results

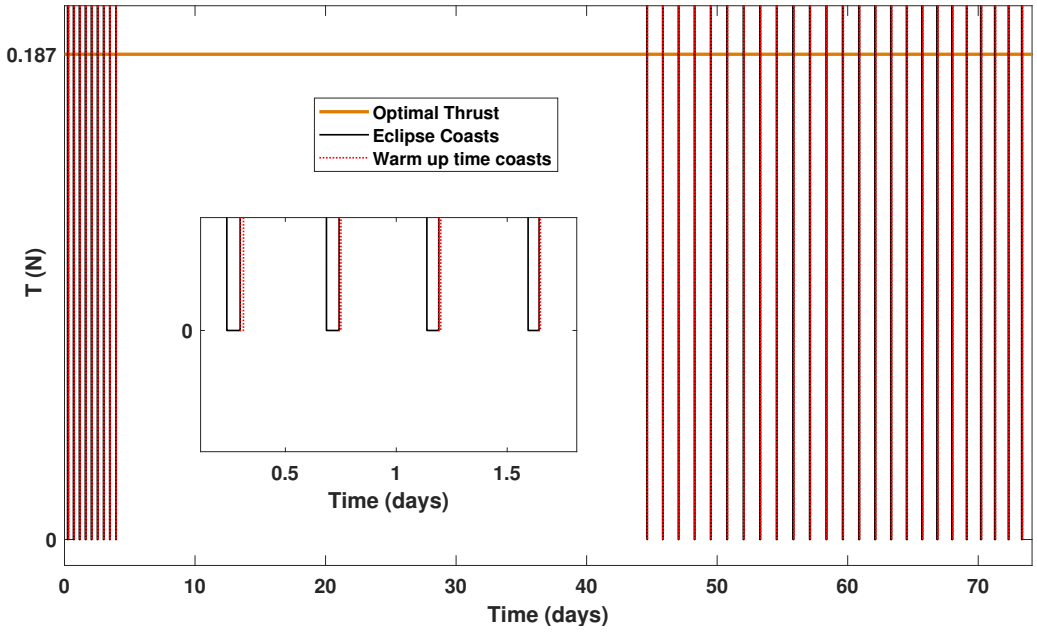

Figure 2.28: Thrust profile for the GTO to GEO maneuver with coast arcs owing to eclipse and warm up constraints.

This approach lays the foundation for including time explicit inequality constraints that are triggered by state dependent inequality constraints associated with the operational limitations of, say, solar electric thrusters. Even though this work specifically solves the problem associated with warm up time in the event of an eclipse, the smoothing logic proposed herein is by no means restricted to this specific application or to the assumed physical model. In fact, the evaluation of warm up time can be improved by including a battery system model to make a more rigorous decision regarding the power cut off based on the state of charge of the battery. In that case, it may turn out that sufficiently short eclipses may not require coasts. This can also be used to

frame a co-optimization problem where battery sizing can be considered, simultaneously with trajectory design. Furthermore, higher-fidelity gravity spherical harmonics can be included to make the trajectory optimization more realistic and useful.

2.4 Gravity Assist Maneuvers [4]

In orbital mechanics and aerospace engineering, a gravitational slingshot, gravity assist maneuver, or swing-by is the use of the relative movement (e.g. orbit around the Sun) and gravity of a planet or other astronomical object to alter the path and speed of a spacecraft, typically in order to save propellant, time, and expense. The swing-by manuever was first studied by R.H. Battin [102] during the 1960s and quickly emerged as a key enabler for solar missions. Trajectory optimization utilizing gravity assist maneuvers generally lead to solving a multi-point boundary value problem (MPBVP) with many discrete variables like choosing the sequence for flybys of the gravity assist planets, launch time, time of gravity assist, altitude of the flyby assists etc. In the current state-of-the-art-practice, gravity-assist maneuvers are continuous events that are modelled and optimized by high-fidelity tools like Mystic [103] and Copernicus [104]. These tools however required a skilled user and insight to generate an approximate starting trajectory. For preliminary studies, simplified patched-conic gravity-assist models are frequently adopted to generate an approximate trajectory, where the position vector of the spacecraft matches the flyby body, but its velocity undergoes an instantaneous change. Direct methods are most commonly applied in the trajectory optimization iterations. This work focuses more on the indirect formulation for fuel-optimal trajectories, but to deal with the inequalities and the presence of multiple solutions associated with gravity-assist maneuvers, a hybrid strategy is implemented using a two-level hybrid optimization scheme [105]. The presented algorithm uses a constrained search space particle swarm optimization (PSO) as the outer optimizer, and an indirect low-thrust optimization technique as the inner optimizer. PSO here performs a global search over an admissible region for some of the design variables (including departure time, inter-planetary travel times and gravity-assist parameters). These design variables, in turn, fix some of the boundary conditions for the inner optimizer, which seeks to find a fuel-optimal trajectory between the fixed boundary conditions (and with a given fixed time of flight). The indirect method makes use of continuation and HTS to reduce the sharpness of control switches in

[4] Reprinted with permission from "Gravity-Assist Fuel-Optimal Low-Thrust Trajectory Design Using Hybrid Optimization Techniques" by Arya, Vishala and Taheri, Ehsan and Woollands, Robyn and Junkins, John, 2019. 70th International Astronautical Congress (IAC), Washington D.C., United States

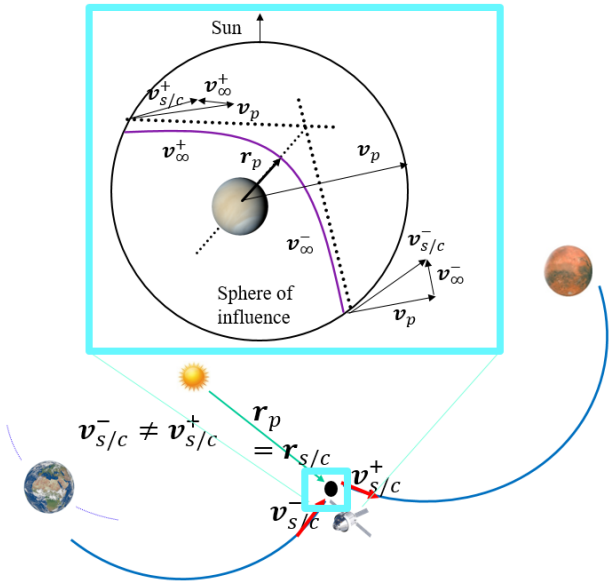

Figure 2.29: Schematics for a patched-conic fly-by maneuver.

early iterations and thereby greatly enhance numerical convergence.

2.4.1 Gravity Assist Formulation

Figure 2.29 depicts the schematics of an un-powered gravity-assist maneuver, which is adopted in this study. In this model, the position vector of the spacecraft, $\mathbf{r}_{s/c}$, is equal to the position vector of the gravity assist planet, $\mathbf{r}_p$ at the time of the gravity assist denoted by t_{ga}.

$$t_{ga}^{-} = t_{ga}^{+} = t_{ga}, \tag{2.57}$$

$$\boldsymbol{r}_{sc}t_{ga}^{-} = \boldsymbol{r}_{sc}t_{ga}^{+} = \boldsymbol{r}_p \tag{2.58}$$

where the superscripts '-' and '+' correspond to the time instants immediately before and after the gravity assist, respectively. For many preliminary calculations, the time to traverse the planet's sphere of influence (on an approximate hyperbolic transfer orbit relative to the planet) is neglected, i.e. the Δv due to encountering the planet is assumed to be instantaneous and at a point on the solar scale. Of course, these approximation can be relaxed in the second phase of the preliminary trajectory design. The incoming and outgoing hyperbolic excess velocity vectors ($\mathbf{v}_{\infty}^{-}$ and $\mathbf{v}_{\infty}^{+}$)

are aligned with the asymptotes of the transfer hyperbola as shown in Figure 2.29. The velocity vectors of the spacecraft (relative to the Sun) before and after the gravity-assist maneuver can be written as:

$$\mathbf{v}_{s/c}^{-} = \mathbf{v}_p + \mathbf{v}_{\infty}^{-}, \;\; \mathbf{v}_{s/c}^{+} = \mathbf{v}_p + v_{\infty}^{+}, \tag{2.59}$$

$$v_{\infty} = \left|\left|\mathbf{v}_{\infty}^{-}\right|\right| = \left|\left|\mathbf{v}_{\infty}^{+}\right|\right|. \tag{2.60}$$

The magnitude of the hyperbolic excess velocity vector remains constant during the gravity assist while the gain in velocity is attributed solely to the rotation of the velocity vector by angle . This rotation angle depends on the closest distance, $r_p = \; ||\mathbf{r}_p||$, relative to the planet as given by

$$\delta = 2\sin^{-1}\left[\frac{\mu_p}{r_p v_{\infty}^2 + \mu_p}\right] \tag{2.61}$$

where μ_p is the gravitational parameter of the flyby planet. The minimum allowable value for r_p is constrained due to planet's atmosphere or radiation conditions (or other operational constraints). This constraint is defined by mission designers as it restricts the maximum gain in velocity obtained due to gravity assist manifesting itself as an upper bound on the value of the rotation angle, δ. There are infinite possibilities of flyby hyperbolas that can characterize the flyby trajectory. In this work, a spherical formulation of $\mathbf{v}_{\infty}^{-}$ using two angles, α, β and magnitude of the excess velocity, v_{∞} is adopted. This formulation allows us to prescribe appropriate bounds on the angles in order to generate constructive gravity-assist maneuvers (i.e., those that lead to a gain in velocity). Figure 2.30 illustrates the intermediate frames and the rotations required to transform $\mathbf{v}_{\infty}^{+}$ from trajectory frame to ecliptic (inertial) frame using angles $\alpha, \; \beta$ and δ and Eqs. (2.62a,b,c) translates the description into the mathematical relations used for the frame change.

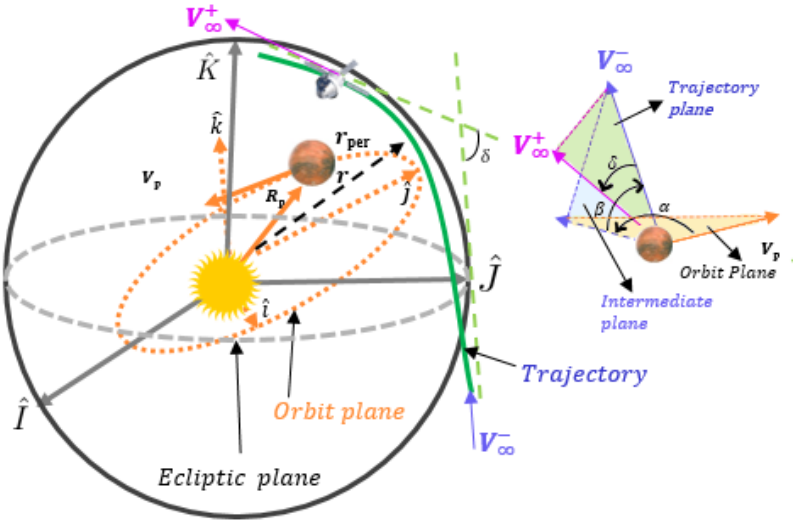

Figure 2.30: Spherical formulation of $\boldsymbol{v}_\infty^-$.

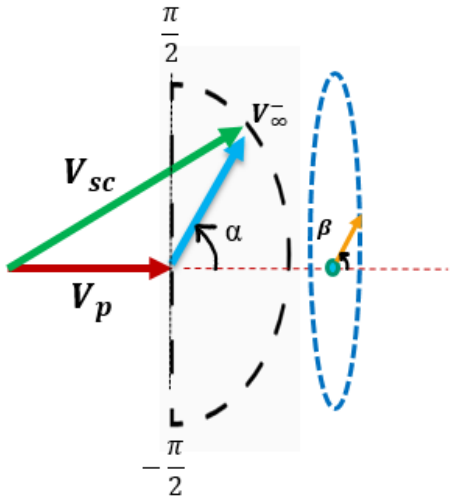

Figure 2.31: Spherical angles used to orient $\mathbf{v}_\infty^-$.

$$\mathbf{v}_\infty^-\big|_q = v_\infty \begin{bmatrix} -sin\ \alpha\ cos\ \beta \\ cos\ \alpha\ cos\ \beta \\ sin\ \beta \end{bmatrix} \tag{2.62a}$$

$$\mathbf{v}_\infty^-|_i = [D_1]\mathbf{v}_\infty^-|_q, \tag{2.62b}$$

$$D_1 = \left[\frac{(\mathbf{v}_p \times n_p)^\top}{||\mathbf{v}_p \times n_p||}, \frac{\mathbf{v}_p^\top}{||\mathbf{v}_p||}, \mathbf{n}_p^\top \right] \tag{2.62c}$$

where, $\mathbf{v}_p$ is the velocity of the gravity-assist planet and $\mathbf{n}_p$ is the unit vector normal to the gravity-assist planet. Subscripts 'i' and 'q' denote the frame in which the vectors are expressed in, namely, 'i' for inertial and 'q' for the frame attached to the gravity-assist planet. As shown in Figures 2.30 and 2.31, α represents the azimuth angle and β the elevation angle, both of which are used to define a 3-1 rotation of the velocity vector of the planet to give $\mathbf{v}_\infty^-$, which undergoes additional rotation in the trajectory plane to get $\mathbf{v}_\infty^+$. With $\mathbf{v}_\infty^-$ defined, another additional coordinate is needed to fully characterize the hyperbola, an angle θ, also known as B-Plane angle, that is modelled using an intermediate frame defined by three orthogonal unit vectors as follows:

$$\hat{\boldsymbol{S}} = \frac{\boldsymbol{v}_\infty^-}{||\mathbf{v}_\infty^-||}, \hat{\boldsymbol{T}} = \frac{\hat{\boldsymbol{S}} \times \hat{\boldsymbol{N}}}{||\hat{\boldsymbol{S}} \times \hat{\boldsymbol{N}}||}, \hat{\boldsymbol{R}} = \hat{\boldsymbol{S}} \times \hat{\boldsymbol{T}}. \tag{2.63}$$

Here, $\hat{\boldsymbol{S}}$ is a unit vector in the direction of the incoming excess hyperbolic velocity vector $(\mathbf{v}_\infty^-)$ and $\hat{\boldsymbol{N}}$ is a unit vector in the direction of the velocity of the gravity-assist planet. Since the maneuver occurs in the heliocentric frame, the following direction cosine matrices can be used to

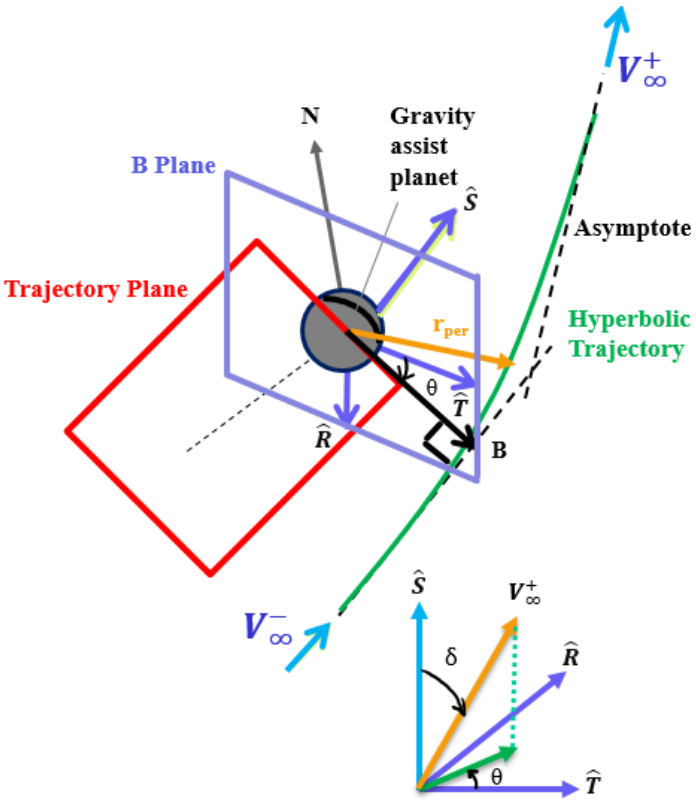

Figure 2.32: Definition of B Plane for gravity-assist.

obtain $\mathbf{v}_\infty^-$ and $\mathbf{v}_\infty^+$ in a Sun-centered inertial frame:

$$\mathbf{v}_\infty^+\big|_i = [\mathbf{D_2}]\ \mathbf{v}_\infty^-\big|_b \tag{2.64}$$

$$D_2 = v_\infty[\hat{\boldsymbol{S}}, \hat{\boldsymbol{T}}, \hat{\boldsymbol{R}}] \begin{bmatrix} \cos\delta \\ \sin\delta\cos\theta \\ \sin\delta\sin\theta \end{bmatrix} \tag{2.65}$$

where, subscript 'b' is used for an intermediate frame defined by its unit vectors as $\left[\hat{\boldsymbol{S}},\ \hat{\boldsymbol{T}}, \hat{\boldsymbol{R}}\right]$. Unit vectors $\hat{\boldsymbol{T}}$and $\hat{\boldsymbol{R}}$ define a plane known as B Plane, which is perpendicular to $\mathbf{v}_\infty^-$ as is shown in Figure 2.32. Therefore, five design variables, $\alpha, \beta, \theta, v_\infty$, and r_p fully characterize a gravity-assist maneuver. Since we are interested only in maneuvers that lead to velocity gain, the following ranges are considered: $\alpha \in \left[-\frac{\pi}{2}, \frac{\pi}{2}\right], \beta \in [-\pi,\ \pi], \theta \in [-\pi,\ \pi]$ as shown in Figure 2.31. The

bounds on the other design variables (which will be introduced later: $t_0, \Delta t_i, v_\infty$ and r_p) depend on the mission scenario and are set accordingly by the designer.

2.4.2 Inner Solver

Taheri et al [72] have shown for zero-revolution enroute orbit transfers that Cartesian coordinates perform better than the set of modified equinoctial elements. In our model, only heliocentric phases of trajectories are considered, where the spacecraft is predominantly under the gravitational acceleration of the Sun. All other disturbing accelerations (e.g., solar radiation pressure and third-body perturbations) are ignored. The dynamics is described using Cartesian coordinates with $\mathbf{x} = [\mathbf{r}, \mathbf{v}, m]^T$ as the state vector and the control input, $\mathbf{u} = \delta T_0 \boldsymbol{\alpha}$, is parametrized through engine throttling (ON/OFF) setting ($\delta \in [0, 1]$), the thrust direction unit vector, $\boldsymbol{\alpha}$, and the maximum thrust, T_0. The standard state dynamics for Cartesian coordinates described in Section 1 is used. The inner solver essentially solves a standard TPBVP assuming NEP propulsion system and evaluates the fuel-optimal solution for every segment given the boundary conditions populated by the outer solver.

2.4.3 Hybrid Optimization Formulation

The problem is formulated in two tiers with the upper tier used for setting the boundary conditions and gravity assist parameters, and the lower tier for computing the fuel-optimal trajectory for that specific set of boundary conditions. Impulsive maneuvers are oftentimes used for these formulations to obtain a well-phased starting solution that can be used to kick-off the low thrust solution. In these cases, we use a Lambert solver in the inner loop, to generate good initial guesses, which is later replaced by a low-thrust solver. For low-thrust trajectories with gravity-assist opportunities, the complexity grows dramatically with the increase in number of gravity-assists, which is preceded by use of an evolutionary algorithm (PSO) to find attractive starting regions and increase the probability of finding the global optimal solution for a given launch window. PSO can be driven by several decisions involving the swarm size, inter-weighting of the personal and global best velocities, and their acceleration terms [106]. Gravity-assist trajectory optimization problems are known

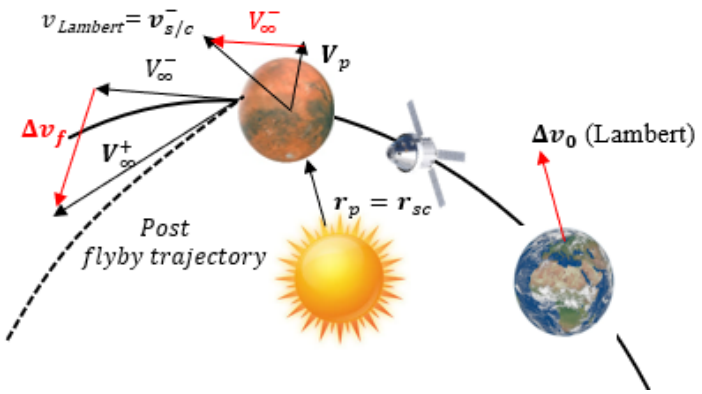

Figure 2.33: Impulsive gravity-assist transfer schematic.

to have several basins of attractions requiring several heuristic iterations to do global then local explorations using PSO, to ensure a high likelihood of global optimality. The design variables for the PSO algorithm involve the launch time (t_0), time of flight for i-th legs (Δt_i), and the gravity-assist parameters (five parameters per gravity assist, as described in previous sub-section), where i varies from 1 to $n_p + 1$ and n_p is the number of planetary flybys during the mission. The entire optimization is conducted in a sequential manner with judicious selection of initial guesses depending on the mission requirements. There are three main phases of the formulation: 1) Impulsive starting estimate generator, 2) Low-thrust optimization, and 3) Thrust continuation. It is difficult to know a priori, the judicious bounds for the launch time and time of flight for each leg since multiple planets with different orbit periods are to be visited sequentially. Therefore, first each leg of the problem is approximately solved using a two-impulse maneuver using a Lambert solver, with PSO used in the outer loop with an objective to minimize the total Δv. Not only does this approach leverage the fast solving attribute of a Lambert solver but the design space is also reduced as the approaching hyperbolic excess velocity vector can be approximately evaluated as a difference of the velocity of the spacecraft on the Lambert arc, and the velocity of the flyby planet at time t_{ga} as shown in the Figure 2.33.

$$\mathbf{v}_{s/c}\left(t_{ga}^{-}\right) = \mathbf{v}_{flb_i} - \mathbf{v}_p, \tag{2.66}$$

$$\mathbf{v}_{s/c}t_{ga}^{+} = \mathbf{v}_{0lb_{i+1}} - \mathbf{v}_p, \tag{2.67}$$

where i denotes the i_{th} leg and $\mathbf{v}_{0lb_i}$ and $\mathbf{v}_{flb_i}$ are the initial and final velocities of the spacecraft on the Lambert arc associated with the i_{th} leg. The design variables for the optimal impulsive maneuver are $t_0, \Delta t_i, \theta$ and r_p ratio (define as the ratio of radius of periapse to planet's radius). Typically, the bounds for t_0 and Δt_i are kept wide enough around the desired launch window to accommodate various solutions. Post optimization in the PSO-Lambert framework, the converged set of design variables are used to produce an initial guess for the low-thrust solver as the Lambert solver is replaced by a gradient based two-point boundary value solver in the second step of the algorithm. For a given type of propulsion, nuclear electric engine in this case with a fixed thrust, T_0 and throttling capability, the fuel-optimal trajectory is computed for a certain T_0 and I_{sp}.

Design Variables	Impulsive [LB,UB]	Low-Thrust [LB,UB]
Launch time (MJD)	[56797, 57892]	[57062, 57162]
E-V TOF (days)	[100,500]	[150, 250]
V-M TOF (days)	[100, 500]	[200, 350]
v_∞ (km/sec)	-	[1, 12]
α (radians)	-	$\left[-\frac{\pi}{2}, \frac{\pi}{2}\right]$
β (radians)	-	$[-\pi, \pi]$
r_p ratio	[1.05, 10]	[1.05, 10]
θ (radians)	$[-\pi, \pi]$	$[-\pi, \pi]$

Table 2.7: Optimal Design Variables

Low-thrust engines operate for a longer period than their impulsive counterparts. Thus, the optimized time of flight obtained for each leg from the PSO-Lambert combination cannot be directly applied. To accommodate the expected increase in time of operation, the bounds for the respective

time of flights are modified likewise. Moreover, to make the impulsive solution realizable for a low-thrust maneuver, a constraint involving a cut-off-ratio is imposed on the impulsive solution as given below:

$$\Delta v_{LT} \geq \varsigma \, \Delta v_{total} \tag{2.68}$$

$$\Delta v_{LT} = \frac{T_0 \Delta t_i}{m_i} \tag{2.69}$$

where ς is the cut-off ratio set as 0.4 in this case, m_i is the mass at the beginning of the i_{th} leg, Δv_{total} is the total Δv incurred for an impulsive transfer, and Δv_{LT} is the approximate Δv available for an equivalent low thrust transfer for a particular T_0. This preliminary process is important to avoid redundant infeasible runs when obtaining fuel-optimal solutions using an indirect approach, which is expensive owing to the iterative guessing of the costates. The MPBVP is broken down into several TPBVPs for the inner indirect solver, which evaluates the fuel-optimal trajectory, leg-wise using the MATLAB solver, fsolve, while feeding the required analytical sensitivities.

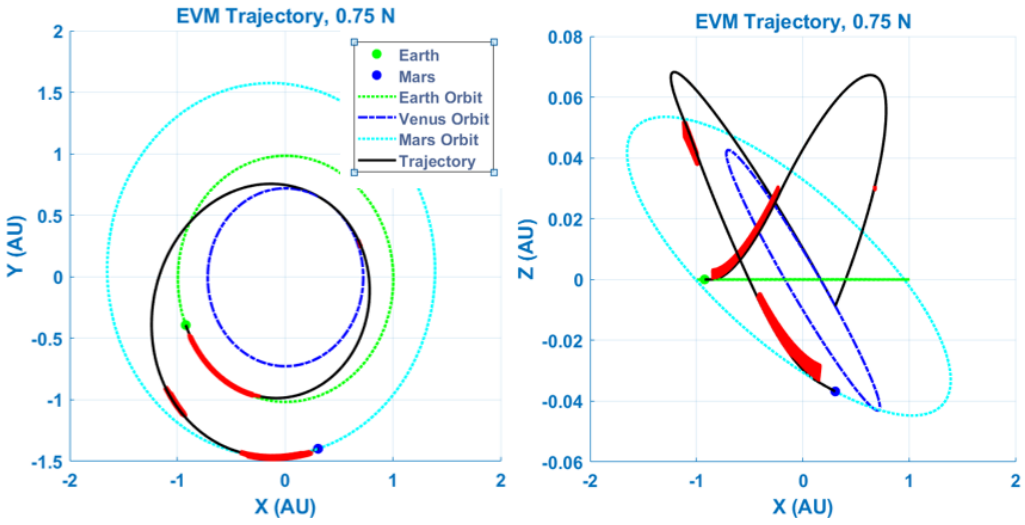

Figure 2.34: Optimal trajectory for the EVM problem with the direction of thrust indicated by red arrows.

Parameter	Value
T_0	0.75 N
I_{sp}	2000 s
m_0	1000 kg

Table 2.8: Engine Specifications

Optimal Design Variables	
t_0 Launch time (MJD)	April 13, 2015
E-V TOF (days)	188.58
V-M TOF (days)	289.59
v_∞ (km/sec)	5.653
α (radians)	0.028
β (radians)	0.23
r_p ratio	1.47
θ (radians)	1.23

Table 2.9: EVM optimal result for the low-thrust transfer with $\rho = 1.0 \times 10^{-6}$.

The EVM problem was formulated using both Cartesian coordinates and MEEs, but Cartesian proved to provide better computation speed for fraction of a revolution trajectories. Though, most of the gravity assist formulations involve a hyperbolic excess velocity at launch, we have assumed that the spacecraft leaves the Earth sphere of influence with zero excess velocity i.e. $\mathbf{v}_\infty = 0$, which corresponds to maximum payload delivery to escape velocity of launch vehicles. The ephemerides of the planets are obtained using the Jet Propulsion Laboratory's (JPL) *SPICE* package in the J2000 inertial frame, while the spacecraft dynamics are propagated using Keplerian approximation. For each leg, an initial guess for the unknown co-state vector $\lambda(t_0)$ is generated randomly and the TPBVP is solved for a certain ρ value. While we generate random $\lambda(t_0)$, we know with virtual certainty that the initial thrust vector (primer vector) will have an acute angle with respect to the Earth's heliocentric velocity vector for transfers to all outer planets, and an obtuse angle for transfers to Venus or Mercury. This truth can be used to constrain or pre-filter PSO iterations on $\lambda(t_0)$. One should be cautious while selecting the minimum value of the continuation parameter, ρ for

which the first cut optimal solution via PSO iterations is evaluated. It is known that the computation time might increase due to either increased number of iterations or increased homotopy steps required to achieve the near bang-bang control profile; however, it has been observed that a higher value of continuation parameter might lead to an erroneous optimal result. For example, for the EVM problem, $\rho = 0.7$ was selected to find an equivalent energy optimal solution. Once, a candidate global optimal solution is obtained, for a relatively large ρ value, the problem is solved using continuation reducing ρ to bring it to 10^{-6} to obtain a corresponding near bang-off-bang optimal solution.

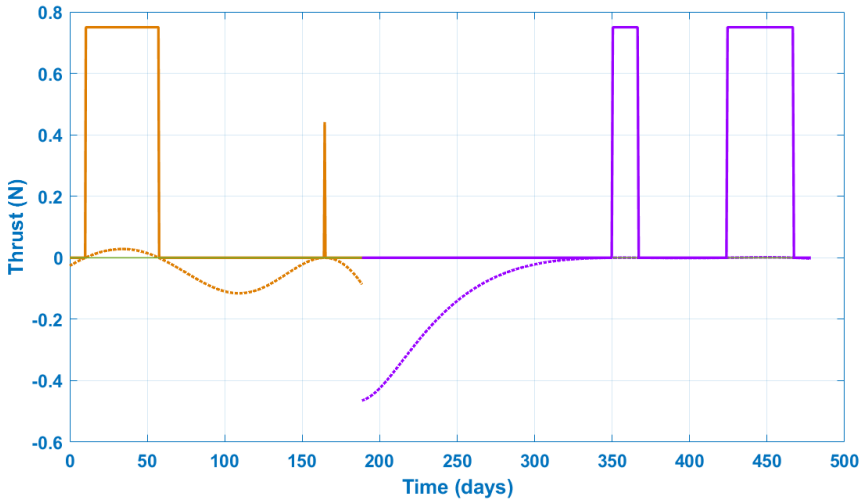

Figure 2.35: Optimal thrust history and switching profile for the EVM problem for $\rho = 10^{-6}$.

2.4.4 Numerical Example

The Earth-Venus-Mars (EVM) problem, which involves only a single gravity assist is solved for a range of thrust values (0.2 N-0.75 N). Our goal is to validate the proposed algorithm and to gain insights associated with thrust continuation in gravity assist problems that have not been highlighted before. The first subsection provides details about the test case in terms of propulsion, bounds and boundary conditions and when a particular maximum fixed thrust value is con-

sidered. The subsequent section compares the final optimized solution corresponding to thrust $T_0 = 0.75N$ obtained using 4 different algorithms and provides the extremal map of PSO runs for both impulsive and low-thrust maneuvers. The last sub-section discusses the thrust continuation and interpretation of the results.

2.4.4.1 Earth-Venus-Mars (EVM) Problem

For the impulsive solution, there are only 5 design variables for PSO as listed in Table 2.7 with the presented bounds. The bounds for the time-of-flight are selected according to the relative time period of the involved planets for a particular leg. The lower bound for r_p ratio is kept as 1.05 (the minimum distance (r_p) being 1.05 times the radius of Venus), which is the most commonly used lower bound for inner planets [107]. Traditionally, no upper bound is assumed for v_∞ , but as the escape velocity for Venus is 10.36 km/sec, so a safe selection of 12 km/sec is made for this example to avoid construction of possible redundant impractical design cases by PSO. For the propulsion system, a nuclear-powered electric engine is selected with throttling "on" and "off" settings, with details given in Table 2.8.

The objective function is the total Δv, i.e minimize the sum of the initial and final Δv's of all involved legs (no deep-space maneuvers are considered). For each leg, the transfer arc is less than one en-route revolution around the Sun. The optimized solution is used as an initial guess for the low-thrust solver, with modified bounds as given in Table 2.7. The design variables such as v_∞, r_p ratio, and the angles α, β, and θ are kept the same but the launch time and time of flight are built around the optimal solution obtained from the impulsive iterations. The optimal solution obtained after 10 complete runs of PSO (with 50 iterations each) is shown in Figure 2.36, and the optimal design variable vector is given in Table 2.9.

There are 4 thrust arcs in total with a very short thrust arc appearing just before the flyby. Figure 2.43 shows a discontinuity in the switching profile, which is expected due to the instantaneous change in the velocity at the time of the gravity assist. There is a drastic change in inclination post gravity assist, which is gradually brought to match the inclination of Mars in the second leg, as shown in Figure 2.34. The Δv gain due to gravity assist is 6.025 km/sec, with the flyby altitude of

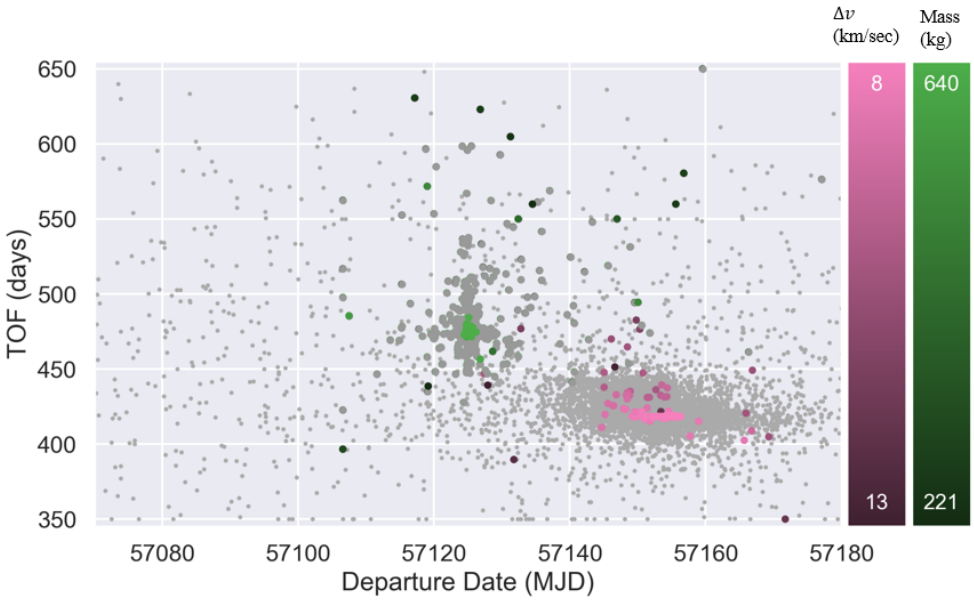

Figure 2.36: Extremal map for EVM impulsive and low-thrust solutions; $T_0 = 0.75N$ via a single PSO run with $\rho = 0.7$.

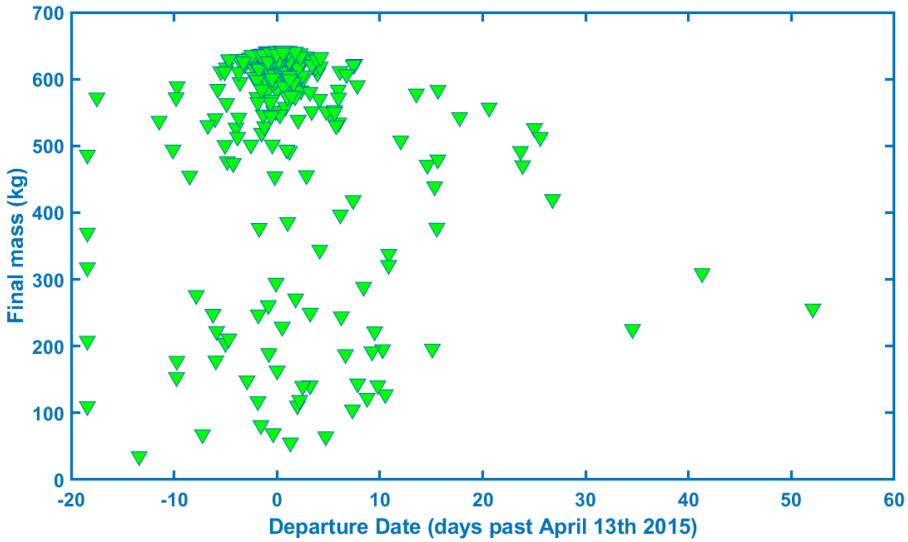

Figure 2.37: Cluster of the converged solutions vs. departure date corresponding to the best PSO initiated iterations of the hybrid solver for EVM, $T_0 = 0.75N$.

2,844 km, a total time of flight of 478.17 days, and a final mass equal to 649.2 kg.

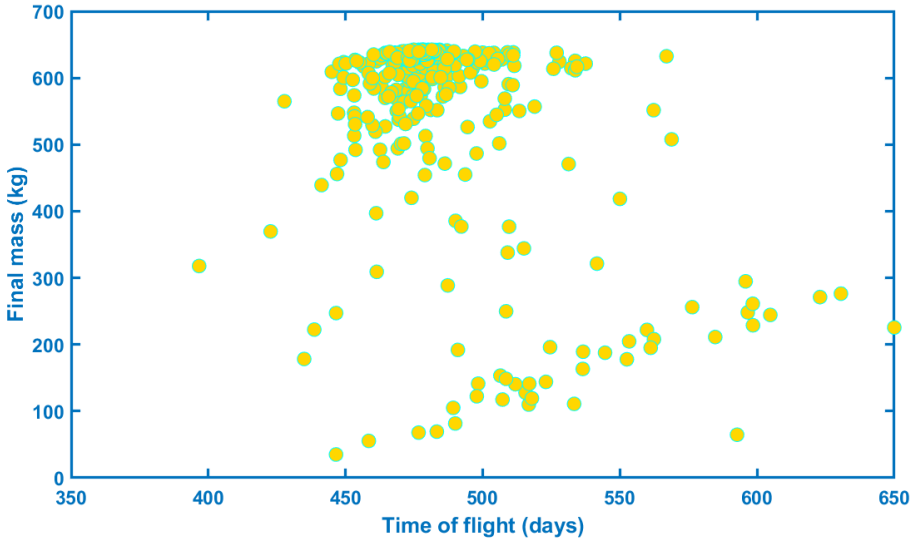

Figure 2.38: Cluster of the solutions vs time of flight corresponding to the best iterations of the hybrid solver for EVM, $T_0 = 0.75N$.

2.4.4.2 Post-analysis of EVM test case

It is always difficult to guarantee convergence to a globally optimal solution. In fact, due to high number of design variables which are non-unique, it is possible to obtain similar values with multiple local combinations of design variables for the objective function. Therefore, it is wise to consider not only the most optimal solution but also the neighbouring solutions. As is clear from the extremal map provided in Figure 2.37 and Figure 2.38, one can deduce that a wide flexibility in terms of launch date and time of flight is available for this problem (150 days in a 500-day mission), with less than 2% increase in fuel consumption. This is a desirable feature of low-thrust trajectories, which can be exploited for mission design to adhere to additional constraints and alternative "measures of goodness" that may not be mathematically expressed formally in the problem. Therefore, these extremal maps provide a better visualization of the objective surface that can aid mission designers. The clustering of points near the optimal solution is observed in

the extremal map due to the large, relatively flat basin of attraction and the convergent nature of the PSO algorithm. The optimized solution for the EVM problem is obtained post several PSO

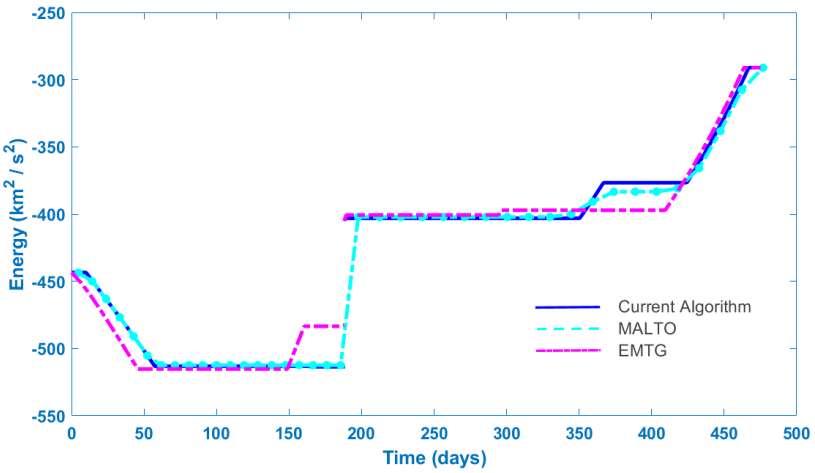

Figure 2.39: Comparison of transfer energy history obtained for the optimal solution from our tool, MALTO, EMTG.

runs and iterations. In order to validate the results obtained by our tool, the same problem is solved using three powerful trajectory optimization tools, namely, MALTO, EMTG and ZOSO. MALTO is a tool developed and used at JPL to obtain optimal solutions for preliminary mission design. MALTO uses a local optimizer which makes use of Sims-Flanagan approach [108] to approximate continuous thrust profiles. Similarly, EMTG is an optimization tool used at NASA Goddard Space Flight Center for computation of optimal trajectories involving gravity-assists, using patched conics approximation (recent version of the EMTG can incorporate continuous flyby maneuvers). EMTG uses Sim-Flanagan approach along with the multiple basin hopping technique to enhance the local nature of the optimizer in an attempt to globally optimal solutions. ZOSO, is another collocation-based tool used at JPL for computation of low-thrust trajectories, and provides a locally optimal solution. The EVM problem was solved using all three solvers with the initial guess generated by the present algorithm, developed in this paper, to obtain the optimal trajectories as summarised in Figure 2.44. The final mass is found to be highest for ZOSO, but the solutions

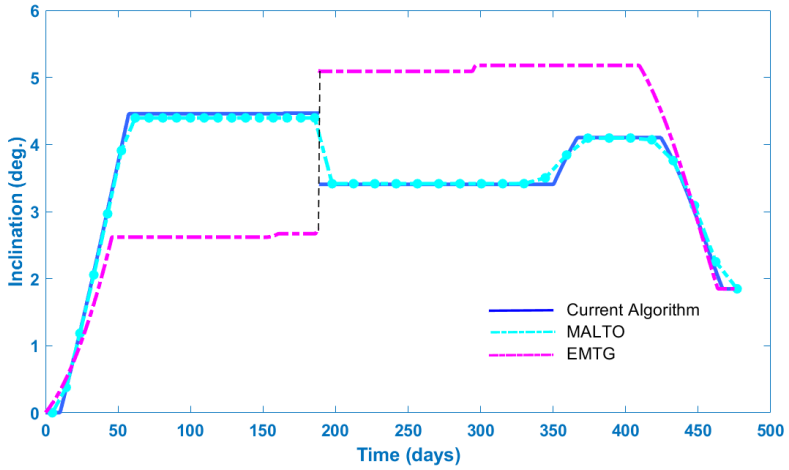

Figure 2.40: Comparison of orbit transfer osculating inclination history for the optimal solution from this work, MALTO, EMTG and ZOSO with the same initial guess.

of all algorithms are within acceptable range with minute differences (less than 1% of the initial mass), which is negligible for preliminary mission design purpose. The changes in energy and inclination due to the gravity-assist maneuver, as well as the operation of thruster are shown in Figures 2.39 and 2.40 respectively. The results from the developed tool and MALTO match well while the EMTG solution differs a little with less boost in energy and more boost in inclination gained due to gravity assist. However, the time of flight for the presented method is over six days shorter than the MALTO solution even though the final mass differs by less than 0.3kg.

2.4.4.3 Thrust Continuation

The results in the preceding sub-sections correspond to a fixed maximum thrust value of $T_0 = 0.75N$. In this section, our goal is to provide insights into the variations that occur in optimal solutions as the thrust value is changed. In particular, for thrust values ranging from 0.2 N to 0.75 N (with the step size of 0.05 N), two methods are used to obtain optimal solutions: Method 1 involves re-solving the OCP for each thrust value using the hybrid algorithm in the same way as the solution for $T_0 = 0.75N$. Method 2 performs a thrust continuation from 0.75 N down to 0.2 N while keeping the same design vector (boundary conditions), and gravity assist parameters obtained from the optimized solution for the 0.75 N thrust level. In Figure 2.42, the red curve

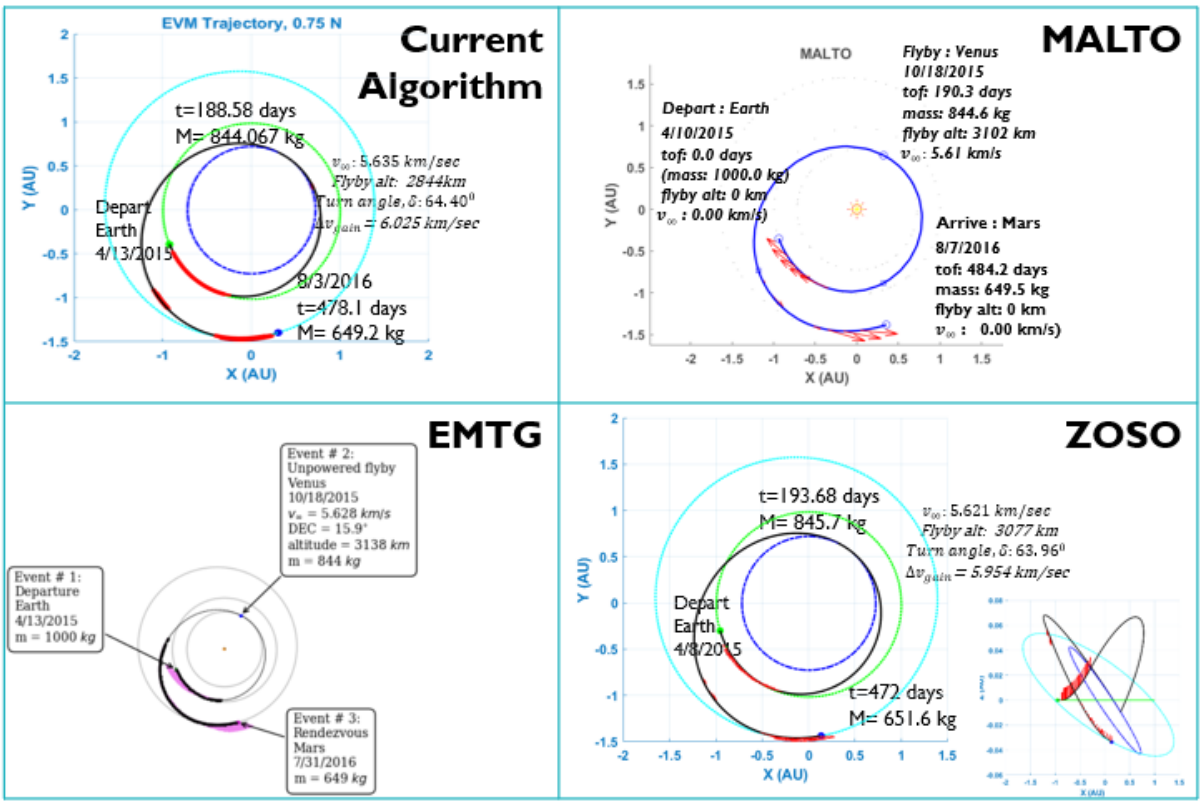

Figure 2.41: Comparison of optimal result obtained using MALTO, EMTG and ZOSO using the same initial guess.

marks the solution from Method 1, while the blue curve is obtained by using Method 2.

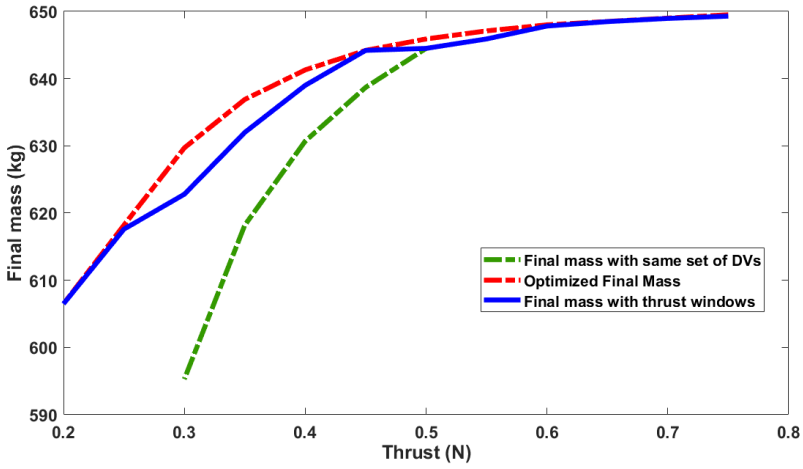

Figure 2.42: Comparison of final mass obtained against varying nominal thrust using three different strategies.

No converged solution could be found for thrust values below 0.2 N, as thrust becomes saturated for this time-of-flight, for the E-V leg, as shown in Figure 2.43. This indicates the 0.2N is approximately the minimum thrust satisfying the constraints, i.e. the reachability boundary. The placement of these two curves (red and blue) can be used effectively through what we call as a thrust envelope. Each thrust envelope merely represents a thrust range that share common boundary conditions and gravity assist parameters of the OCP. The extremals of the thrust range are determined by the condition that the drop in final mass, pertaining to consecutive thrust values, is not higher than a prescribed threshold value (1% final mass).

There are three thrust envelopes used to obtain the orange curve in Figure 2.42, these are [0.45-0.75], [0.35-0.45] and [0.2-0.35]. The difference in the final mass, marked by the red and orange curves, is not greater than 1% of the initial mass. Utilization of the concept of admissible thrust envelopes eliminates the requirement for conducting computationally demanding simulations for these intermediate thrust values, while providing near-fuel-optimal solutions. Moreover, the costates of the converged solution from any of the thrust values within a thrust envelope can

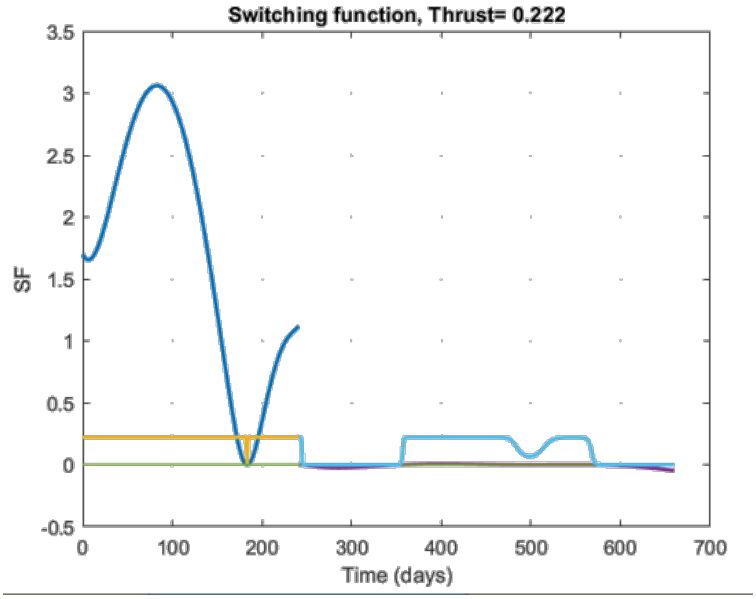

Figure 2.43: Near-Optimal thrust profile for EVM for $T_0 = 0.222N$.

be used as a good initial guess, with high confidence of efficient convergence, for all other thrust values in that envelope.

Using the concept of the thrust envelope, one can easily obtain the switch function equal to zero contour plot by stacking the switching profiles, corresponding to different thrust values, to obtain a continuous thrust profile map (namely, the optimal switching surfaces analogous to those introduced by Taheri and Junkins [**?**]). Figure 2.44 depicts the contour associated with the EVM problem for all infinity of optimal trajectories with an admissible/feasible thrust level. Dark blue regions denote the thrust arcs, whereas the grey regions denote the coast arcs. Note that this contour plot depicts the variation of thrust and coast arcs for different values of thrust. In Ref [**?**], the contour plots were generated for fixed-time, rendezvous-type low-thrust trajectories (with no gravity-assist), whereas, Figure 16 provides an extension by incorporating varying boundary conditions (departure time and time of flight) and a discontinuity in the switching profile at the time of gravity assist. It is observed that the departure time shifts backwards as the nominal thrust is lowered, with an expected increase in time of flight. Thus the idealized case with no gravity assist introduced in [**?**] now gives rise to a much more versatile generalization. Also, interestingly,

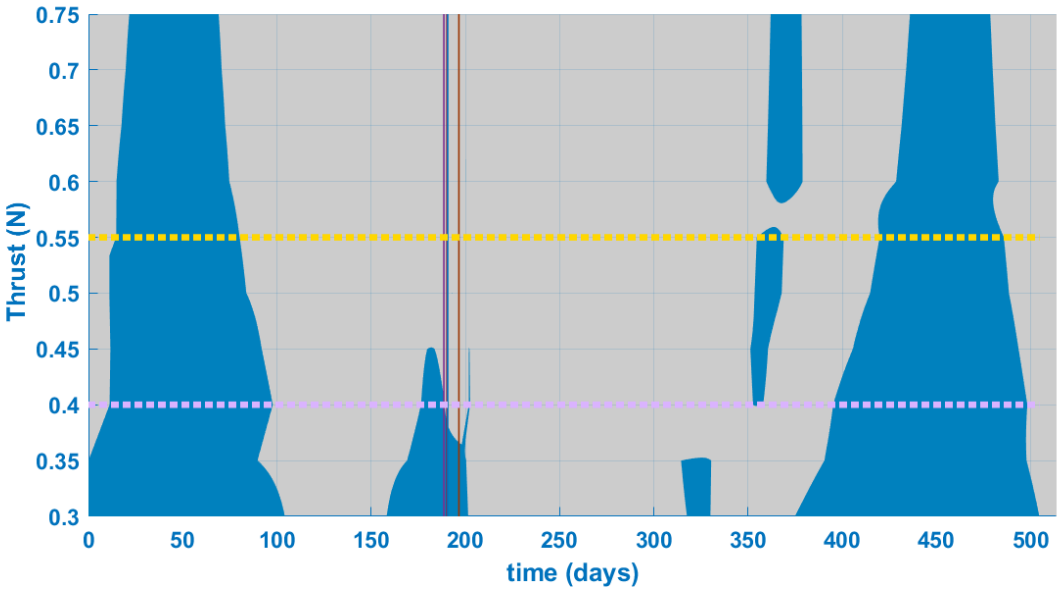

Figure 2.44: Contour plot of optimal switching surface.

one observes how at the time of the gravity assist, the thrust arc duration gets larger for lower values of thrust. A step size of 0.05 N was used to obtain this contour plot.

The main feature of the presented algorithm is the ability to explore the objective surface to provide a global optimal solution. The notion of "thrust envelopes" is introduced, that helps in reducing the expensive computations when generating an extremal field map for various thrust values. Also, this algorithm exploits the inherently parallelizable capability of PSO to provide a major speed up in computation, as well as build confidence that all feasible basins of attraction have been found to initiate final design iterations.

3. Optimization of Propulsion System and other Spacecraft Sub-systems Selections in Interplanetary Mission Design

Ideally, spacecraft should be designed for maximum "efficiency" and payload deliverance, but in practice, a number of factors (e.g., the complexity of available technology and operational constraints) impact the optimization process. Technology-dependent design parameters include the specific mass of the solar arrays, tank mass ratio and the thruster efficiency. Other design parameters that can be optimized (over their admissible set) are the electric power of the solar arrays, minimum electric processing system (EPS) power consumption and the specific impulse of the thruster. In many instances, there is set of discrete design choices, based on available technologies for sub-systems. Motivated by the complexity of the multiplicity of design issues, we introduce a co-optimization framework that optimizes the trajectory and obtains the optimal values of these spacecraft's parameters and design space with the objective of maximizing the net payload delivered. This generalized optimization approach enables mission designers to ascertain suitability metrics for different thrusters and solar array sizing as a stepping stone to achieve a higher level systems approach for mission design optimization. The methods introduced in this chapter permit an effective way to accommodate the level of complexity that arises in simultaneous indirect optimal design of the SEP system and the mission trajectory.

3.1 Payload Optimization [1]

For optimization at the systems level, it is of practical interest to optimize the trajectory jointly with the spacecraft parameters to maximize the useful payload mass. The useful payload mass generally comprises of the primary payload and other spacecraft sub-systems like a part of the power supply system (PSS), which is necessary for the payload operations. Adopting the spacecraft mass breakdown presented by Petukhov [1], it is assumed that the mass of the spacecraft can be

[1] Reprinted with permission from "A composite framework for co-optimization of spacecraft trajectory and propulsion system" by Arya, Vishala and Taheri, Ehsan and Junkins, John L, 2020. Acta Astronautica, Volume 178, 773–782, Copyright 2021 by Elsevier

expressed in terms of the payload mass, power supply propulsion unit (PSPU) mass and propellant storage and fuel feeding system (PSFS) mass as shown in Figure 3.1. The initial mass of the

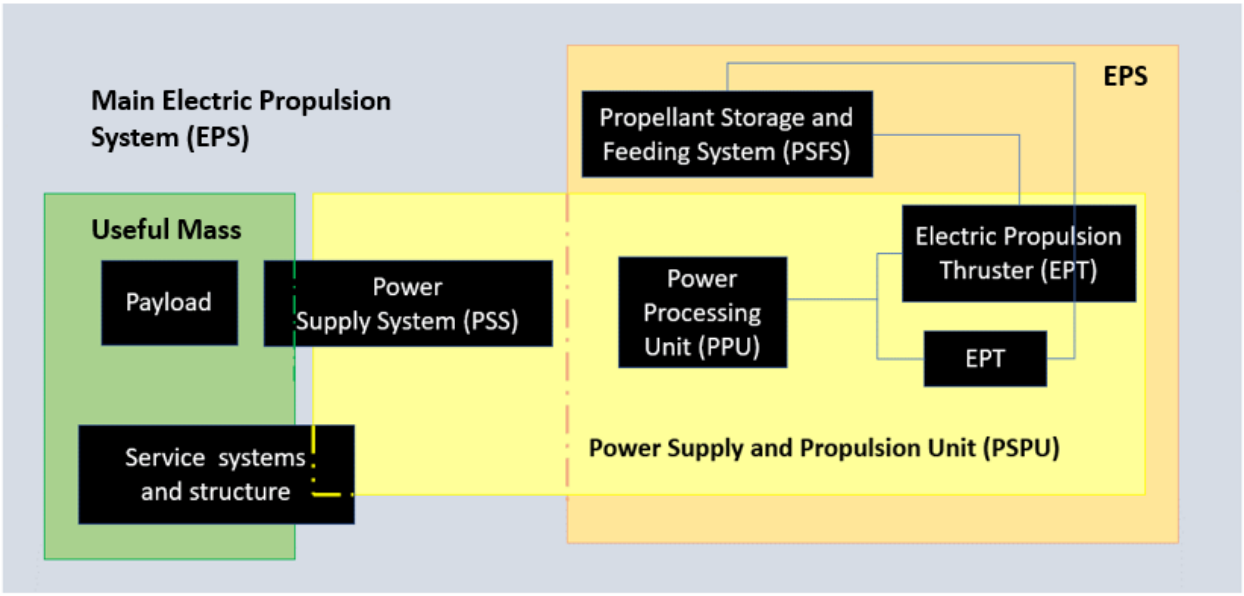

Figure 3.1: Spacecraft payload and electric propulsion sub-system mass breakdown.

spacecraft, m_0, can also be derived as a function of the launch velocity to optimize the parameters of launch vehicle in a co-optimization scheme. However, we do not include m_0 as an optimization choice in the present study. The initial mass will be treated as a constraint. Obviously, in principle, m_0 could be swept to generate a family of designs. The initial mass can be written as a sum of sub-system masses as:

$$m_0 = m_u + m_{\text{PSPU}} + m_{\text{PSFS}}, \tag{3.1a}$$

$$m_u = m_0 - \gamma_1 P_{\text{BL}} - \gamma_2 P_{\text{av}} - (1 + a_{\text{tk}}) m_p, \tag{3.1b}$$

where m_u is the useful mass, m_{PSPU} is the mass of the PSPU, m_{PSFS} is the mass of the PSFS, γ_1 is the specific mass of solar arrays in (kg/kW), γ_2 is the specific mass of the power regulator unit and solar array drives of the PSS for the EPS power supply and the EPS itself (kg/kW), a_{tk} is

the tank mass ratio coefficient, which is equal to the ratio of dry mass of PSFS and unconsumed remnants of propellant at the end of the flight to the mass of utilized propellant, and m_p is the mass of EPS' propellant consumed at the end of a transfer. Mass of the solar arrays is parametrized and approximated as linearly proportional to the nominal power generated (P_{BL}) i.e. $m_{\text{SA}} = \gamma_1 P_{\text{BL}}$.

The most constraining criteria for the nominal power generated (P_{BL}) is the size of the solar arrays, which can be a technology-driven constraint. Also, bulkier solar arrays might redundantly increase the mass of the spacecraft in addition to the issues associated with the flexible structure of solar arrays. The considered model judiciously captures the mass penalty incurred due to the size of solar arrays equivalent to the magnitude of P_{BL} thus allowing for the necessary trade-off decisions to be included in mission optimization. It encapsulates the major disposable mass sources in a spacecraft whose consumption can be duly optimized. This concurrent optimization empowers the designers to more formally and rigorously justify the main characteristics of a spacecraft for a certain mission as well as maximize overall efficiency in terms of the net delivered payload. If variable-I_{sp} engine is considered, the payload optimization problem becomes so much more challenging to solve as compared to fuel optimization due to: 1) the fact that the available power is constrained by the size of the solar arrays and is coupled with the design of trajectory itself, 2) the frequently non-smooth changes in the feasible input power that is bounded between a maximum and a minimum value, and 3) that the numerical sensitivity owing to the highly non-linear relationship of the specific impulse is intensified along with the implicit requirement to precisely locate the apriori unknown mode switch times.

The trajectory state dynamics is represented using MEEs from Eq: 2.6 where the acceleration vector is:

$$\boldsymbol{a} = \frac{2\eta P_{\text{av}}}{mc}\delta\hat{\boldsymbol{\alpha}}, \tag{3.2}$$

Here, P_{av} is the power available for thrusting, η is thruster efficiency. Due to the bang-off-bang structure the anticipated optimal thrust history (and similarly the bang-off-bang structure of P_{av})

observed in fuel-optimal trajectories, we have used the throttle $\delta \in [0, 1]$. Note that the original control input is the available power, P_{av}, that will be sent to an engine. However, instead of defining the power as the control input, we have considered a multiplicative factor, δ, as the control input. The optimal structure of the multiplicative factor, δ^*, exhibits multiple switches in the example which is solved here. In the sub-section 3.1.1, we use the HTS method to smooth this non-smooth control input. In a more general setting, the thruster efficiency, η, can be a function of exhaust velocity, EPS power consumption and the configuration in case of multiple engines. In one of the numerical cases (EDP4) given in the present study, linear or quadratic variation of η are considered separately to provide a comparison as per the two recent linear and quadratic models in the literature [29] given below:

$$\eta_l = \beta_{l0} + \beta_{l1} I_{\text{sp}}, \tag{3.3}$$

$$\eta_q = \beta_{q0} + \beta_{q1} I_{\text{sp}} + \beta_{q2} I_{\text{sp}}^2, \tag{3.4}$$

where, $\beta_{l0} = 0.2916$, $\beta_{l1} = 0.9624 \times 10^{-4} s^{-1}$, $\beta_{q0} = 0.1424$, $\beta_{q1} = 1.9231 \times 10^{-4} s^{-1}$ and $\beta_{q2} = -0.1499 \times 10^{-7} s^{-2}$.

3.1.1 Power Modelling of Variable-I_{sp} SEP Engines

Depending on solar array size and the technology used, solar arrays are designed to produce a nominal power value at the heliocentric distance of 1 AU, typically defined at the time of launch as P_{BL}. The simplest and dominant degradation of power available from a given solar array is proportional to the $1/r^2$ reduction in the solar energy flux, where r denotes the distance from the Sun to the spacecraft. Another factor to consider in variation of nominal power over time is the degradation usually observed in the efficiency of solar arrays, especially for multi-year missions. Time degradation is not considered in this section.

The available power to the Electric Processing System (EPS) is typically not only a function of P_{BL}, but it also changes as the heliocentric distance of the spacecraft varies. Nonetheless, this power can be considered as constant for some optimization procedures, in which case, one has to

ensure the sufficiency of the nominal power to operate the thruster at the maximum heliocentric distance occurring during the maneuver. The power generated by solar arrays can be approximated empirically as

$$P_{\text{SA}} = \frac{P_{\text{BL}}}{r^2}\left[\frac{d_1 + d_2 r^{-1} + d_3 r^{-2}}{1 + d_4 r + d_5 r^2}\right], \tag{3.5}$$

where $[d_1, d_2, d_3, d_4, d_5]$ have the (for example) empirical values [1.1063, 0.1495, -0.299, -0.0432, 0] to model the radial dependence of performance variation for a particular solar array design [109]. Here, the solar array power consists of two multiplicative terms: 1) a dominant governing term that is inversely proportional to the square of the distance from the Sun, and 2) a multiplying distance-dependent factor (in bracket) that is a function of a particular design. If a discrete family of decisions are considered, of course, the d_i coefficients in Eq. (3.5) would require experimental or theoretical study for each design.

The power generated by the solar arrays, P_{SA}, can only partially be utilized for the operation of the thrusters. The power available for thrusting is limited by a maximum power available, P_{max}, to the Power Processing Unit (PPU) required for voltage regulation and the duty cycle (incorporated as η_d in the formulation) of the PPU. Virtually, all solar-powered propulsion systems incorporate a duty cycle to give a convenient "knob" for both mission designers and flight control engineers to throttle down from P_{max}, if desired or required, for a variety of reasons. Power can also be delimited by rotating the normal to the working plane of solar arrays to maintain necessary thermal profile of the solar arrays as the spacecraft approaches the Sun. The power available to the PPU is equal to P_{SA} less the power load allocated to operate the spacecraft systems, PL, which is assumed to be a constant. Therefore, the power available for operation of thrusters, P_{av} can be written as [29]:

$$P_{\text{av}} = \begin{cases} \eta_d P_{\text{max}}; & \text{for } P_{\text{SA}} \geq PL + P_{\text{max}}, \\ \eta_d (P_{\text{SA}} - PL); & \text{for } P_{\text{SA}} < PL + P_{\text{max}}. \end{cases} \tag{3.6}$$

Note that P_{max} is the maximum power that can be handled by the PPU design, which is a constant that is set according to the mission and the engine selection. Most thrusters feature a

minimum power as well as a maximum power bound. Below the specified minimum power, P_{min}, the thrusters cannot be turned on.

Equation (3.6) indicates that the available power may switch instantaneously between two different values depending on the value of power. Such abrupt changes can have adverse numerical consequences when we are solving OCPs. Specifically, each of the unknown switch times must be isolated at high precision and be adopted as end points of integration steps. Any errors in isolating these switch times accumulate and can lead to inefficient, inaccurate and unreliable convergence of optimal control algorithms. Thus, the many-switch non-smooth control structure (in power) demonstrated in Eq. (3.6) is handled using the HTS method by use of an embedding process with a smoothing parameter, ρ_p. The degree of smoothing in HTS could be tuned to isolate the switch times to essentially machine precision, or can simply be constantly tuned to a "sufficiently sharp" degree that makes a negligible departure from optimality. The details are given in sub-section 3.1.2.

Variable-Impulse Variable-Thrust (VIVT) engines have the ability to modify their specific impulse value through which it is possible to modulate the thrust value. Such a flexibility is shown to constructively affect optimized trajectories both in terms of time and fuel consumption. In formulation of the OCPs, the exhaust velocity, $c = I_{\text{sp}} g_0$, is adopted as a control input within some prescribed bounds as per the engine selection and the desired mission:

$$c^* = \begin{cases} c_{\text{max}}; & \text{for } c_{\text{opt}} \geq c_{\text{max}}, \\ c_{\text{opt}}; & \text{for } c_{\text{opt}} \in [c_{\text{min}}, c_{\text{max}}], \\ c_{\text{min}}; & \text{for } c_{\text{opt}} \leq c_{\text{min}}, \end{cases} \tag{3.7}$$

where c_{min} and c_{max} are the minimum and maximum admissible exhaust velocity and c_{opt} is the optimal exhaust velocity value. Applying optimal control principles allows us to derive an explicit algebraic expression for c_{opt} in terms of the instantaneous value of states and costates. The algebraic expression will change for different formulations as is summarized in Eq. (3.17). c_{opt} may be non-

smooth due to the constraint $c_{\text{min}} \leq c_{\text{opt}} \leq c_{\text{max}}$, but then non-smooth discontinuities near c_{min}, c_{max} can be eliminated using invariant embedding, as discussed below.

3.1.2 Invariant Embedding

Any non-smoothness in the control inputs hinders convergence mainly due to the arduousness of precisely locating the zeroes of their respective constraint equations [6], which we denote by g_C, g_P and g_B for exhaust velocity, power and throttle control inputs, respectively. The bang-bang structure of the control inputs is smoothed by the HTS method on the basis of the sign of the so-called switching function (SF) (see Eq. (3.16)) as

$$\delta^* \approx \delta(SF, \rho) = 0.5 \left[1 + \tanh\left(\frac{SF}{\rho}\right)\right]. \tag{3.8}$$

In order to apply the CSC construct to the exhaust velocity, 3 activation functions are required (corresponding to 3 "if-then" conditions), $\chi_{c_{\text{min}}}$, $\chi_{c_{\text{max}}}$ and $\chi_{c_{\text{opt}}}$; to provide a composite smooth structure of c^* as

$$c^* = \chi_{c_{\text{min}}} c_{\text{min}} + \chi_{c_{\text{opt}}} c_{\text{opt}} + \chi_{c_{\text{max}}} c_{\text{max}}, \tag{3.9}$$

where each of the three activation functions (χ) is constructed with the help of the HTS method to replace the "if-then" conditions by three "controllably sharp" smooth functions:

$$\begin{aligned}
\chi_{c_{\text{min}}} &= 0.5 \left[1 - \tanh\left(\frac{g_{c_{\text{min}}}}{\rho_c}\right)\right], \\
\chi_{c_{\text{opt}}} &= 0.5 \left[1 - \tanh\left(\frac{g_{c_{\text{opt,1}}}}{\rho_c}\right)\right] \times 0.5 \left[1 - \tanh\left(\frac{g_{c_{\text{opt,2}}}}{\rho_c}\right)\right], \\
\chi_{c_{\text{max}}} &= 0.5 \left[1 - \tanh\left(\frac{g_{c_{\text{max}}}}{\rho_c}\right)\right].
\end{aligned}$$

The switching conditions (constraints) corresponding to exhaust velocity that are used in the

three activation functions are defined as zeroes of the following four functions

$$g_{c_{\text{min}}} = c_{\text{opt}} - c_{\text{min}}, \qquad g_{c_{\text{opt},1}} = c_{\text{min}} - c_{\text{opt}},$$

$$g_{c_{\text{max}}} = c_{\text{max}} - c_{\text{opt}}, \qquad g_{c_{\text{opt},2}} = c_{\text{opt}} - c_{\text{max}}.$$

Similarly, the discontinuous structure of available power can be smoothed by the CSC construct to give smooth composite homotopic power function embedded with the continuation parameter, ρ_p, as:

$$P_{\text{av}} = \eta_d \left[\chi_p P_{\text{max}} + (1 - \chi_p)(P_{\text{SA}} - PL)\right] \chi_{\text{pm}}, \tag{3.11}$$

$$\chi_p = 0.5 \left[1 + \tanh\left(\frac{g_p}{\rho_p}\right)\right], \tag{3.12}$$

where $g_p = P_{\text{SA}} - (P_{\text{max}} + PL)$ as per the condition described in Eq. (3.6). In order to ensure that the thruster is "on" only when the P_{av} is higher than P_{min}, P_{av} obtained through Eq. (3.12) is multiplied with χ_{pm} where $\chi_{\text{pm}} = 0.5 \left[1 + \tanh\left(\frac{g_{\text{pm}}}{\rho_p}\right)\right]$ and $g_{\text{pm}} = P_{\text{av}} - P_{\text{min}}$. Each of the smoothing parameters (i.e., ρ_i ($i \in \{p, c, b\}$) corresponds to a sub-problem (each sub-problem corresponds to solving a TPBVP) that is arbitrarily near a neighbouring converged solution.

3.1.3 Indirect OCP

While indirect optimal control is rarely attempted on a hybrid problem of this complexity, we show a systematic approach is indeed computationally feasible. First, a detailed review of all the building blocks used to construct the OCP cost functional is presented. The objective is to maximize the useful mass (i.e., the payload plus necessary subsystems to support the payload). This section establishes the OCP posed as a TPBVP with optimality conditions.

In order to model the cost functional of the OCP in Lagrangian form, we have expressed the useful mass (see Eq. (3.1b)) in terms of two main terms, m_{PSPU} and m_{PSFS}. The term m_{PSPU} consists of a constant term (mass of the solar arrays $= \gamma_1 P_{\text{BL}}$) and a position varying term, $\gamma_2 P_{\text{av}}$. When we insert it inside the integrand, m_{PSPU} is divided by ($\Delta t = t_f - t_0$) for the purpose of scaling as

shown in Eq. (3.35).

The advantage of including the m_{PSPU} inside the integral is to factor the influence of change in position (heliocentric distance) on the cost function. The second term consists of m_{PSFS}, which involves the mass of the consumed propellant and is denoted as m_p in Eq. (3.1b). The value of m_p can simply be evaluated as the integral of differential equation of mass given in Eq. (2.6) over the total time of flight.

Therefore, the final OCP can be stated as

$$\text{Minimize } J = \int_{t_0}^{t_f} \left[\frac{\gamma_1 P_{\text{BL}} + \gamma_2 P_{\text{av}}}{\Delta t} + \frac{(1 + a_{\text{tk}}) 2\eta P_{\text{av}} \delta}{c^2} \right] dt,$$

$$\begin{aligned} &\text{subject to :} \\ &\qquad \text{Equation (2.6)}, \\ &\qquad \boldsymbol{x}(t_f) - \tilde{\boldsymbol{x}}_d = \mathbf{0}, \\ &\qquad \boldsymbol{x}(t_0) = \boldsymbol{x}_0, m(t_0) = m_0, \\ &\qquad c \in [c_{\text{min}}, c_{\text{max}}], \end{aligned} \tag{3.13}$$

where t_0 is the initial time, $\boldsymbol{x_0}$ and m_0 are the MEEs and mass of the spacecraft at the initial time, t_f is the final time, $\Delta t = t_f - t_0$ is the time of flight, and $\tilde{\boldsymbol{x}}_d$ is the desired MEEs at the final time.

If our goal is not to optimize P_{BL}, it is possible to remove it from integrand, which means that we can simply remove the term $\gamma_1 P_{\text{BL}}/\Delta t$. However, the reason that we keep this term in the integrand is that in EDP3, EDP4 and EDP5, we will optimize the initial value of the P_{BL}. Therefore, in order to get the correct costate dynamics for P_{BL}, we need to retain it in the Lagrangian so that when we use the Euler-Lagrange equation (namely, $d\lambda_{P_{\text{BL}}}/dt = -[\partial H/\partial P_{\text{BL}}]$), correct expressions

are obtained. The Hamiltonian associated with the defined OCP can be written as:

$$H = \frac{\gamma_1 P_{\text{BL}} + \gamma_2 P_{\text{av}}}{\Delta t} + \frac{2(1+a_{\text{tk}})\eta P_{\text{av}}}{c^2}\delta + \boldsymbol{\lambda}^\top \left(\boldsymbol{A}(\boldsymbol{x},t) + \frac{2\eta P_{\text{av}}\delta}{mc}\mathbb{B}(\boldsymbol{x},t)\hat{\boldsymbol{\alpha}} \right) - \lambda_m \frac{2\eta P_{\text{av}}}{c^2}\delta, \tag{3.14}$$

where $\boldsymbol{\lambda} = [\lambda_p, \lambda_f, \lambda_g, \lambda_h, \lambda_k, \lambda_l]^\top$ and λ_m is the costate associated with mass. Considering the control inputs ($\hat{\boldsymbol{\alpha}}$, c and δ), since $\hat{\boldsymbol{\alpha}}$ and δ appear bi-linearly in the Hamiltonian, Pontryagin's Minimum Principle (PMP) has to be used. This further leads to the formation of the power switching function, SF, which governs the throttle 'on' or 'off' condition subjected to a constraint of exhaust velocity as

$$\delta^* = \begin{cases} 1; & \text{for } SF > 0, \forall\, c \in [c_{\text{min}}, c_{\text{max}}], \\ 0; & \text{for } SF \leq 0, \forall\, c \in [c_{\text{min}}, c_{\text{max}}], \end{cases} \tag{3.15}$$

$$SF = \frac{c||\mathbf{P}||}{m} + \lambda_m - 1. \tag{3.16}$$

Singular controls, which occur if the switching function remains zero over a finite time interval, are not treated in this work. On looking for regions where switching functions did not have a simple isolated zeros, we did not find any in our numerical solutions. Costates dynamics can be evaluated by Euler-Lagrange equation, $\dot{\boldsymbol{\lambda}} = -\left[\frac{\partial H}{\partial \boldsymbol{x}}\right]^\top$.

On the other hand, c is contained non-linearly and may have an interior optimal c_{opt} satisfying $c_{\text{min}} \leq c_{\text{opt}} \leq c_{\text{max}}$ and $\frac{\partial H}{\partial c} = 0$. Therefore, for characterizing the optimal values of specific impulse, strong form of optimality is used, $\frac{\partial H}{\partial c} = 0$. Different expressions for the optimal exhaust velocity are determined as per the dependence of the thruster efficiency on I_{sp}, as is given in Eq. (3.17a) in case of constant efficiency, Eq. (3.17b) for linear dependence and Eq. (3.17c) for

quadratic dependence on I_{sp}:

$$\text{constant} : c_{\text{opt}} = \frac{2m(1-\lambda_m)}{||\mathbf{P}||}, \quad \text{if } c_{\min} \leq c_{\text{opt}} \leq c_{\max}, \tag{3.17a}$$

$$\text{linear} : c_{\text{opt}} = \frac{2\beta_{l0}(1-\lambda_m)m}{\beta_{l1}m(\lambda_m-1)+\beta_{l0}||\mathbf{P}||)}, \quad \text{if } c_{\min} \leq c_{\text{opt}} \leq c_{\max}, \tag{3.17b}$$

$$\text{quadratic} : c_{\text{opt}} = -\frac{\beta_{q2}||\mathbf{P}||(\sqrt{Q1}-Q2)^{\frac{1}{3}}}{3\times 2^{\frac{1}{3}}} - \frac{2^{\frac{1}{3}}(-\beta_{q0}||\mathbf{P}||+\beta_{q1}m(1-\lambda_m)}{(\sqrt{Q1}-Q2)^{\frac{1}{3}}},$$

$$\text{if } c_{\min} \leq c_{\text{opt}} \leq c_{\max}, \tag{3.17c}$$

$$Q1 = 108\beta_{q2}^3||\mathbf{P}||^3(-\beta_{q0}||\mathbf{P}||+\beta_{q1}m(1-\lambda_m))^3$$

$$+ (54\beta_{q0}\beta_{q2}^2||\mathbf{P}||^2m(\lambda_m-1))^2,$$

$$Q2 = 54\beta_{q0}\beta_{q2}^2||\mathbf{P}||^2m(\lambda_m-1),$$

Similarly, the relations given in Eq. (3.7) hold and the CSC method is used to make a composite control similar to the one presented in Eq. (3.9) for each one of the cases given above.

In case of a VIVT engine, PMP dictates that the Hamiltonian should be minimized over the set of admissible controls. Therefore, the thruster should be ON, if at least one admissible value of c exists that makes the power switching function (SF) positive. Therefore, the power switching function in Eq. (3.16) features $c_{\max}$ in place of c. One additional boundary condition arises due to transversality condition $\lambda_m(t_f) = 0$ as the mass of the spacecraft at final time, $m(t_f)$, is free.

In this work, for payload optimization, P_{BL} is considered a design variable. Therefore, the state vector $[\boldsymbol{x}, m]^\top$ is augmented by P_{BL} and is written as $\boldsymbol{z}^\top = [\boldsymbol{x}^\top, m, P_{\text{BL}}]$. The set of state dynamics is augmented with one additional differential (trivial) equation ($dP_{\text{BL}}/dt = 0$). As a consequence of augmentation of the state dynamics, the set of state-costate dynamics consists of 16 differential equations. Since the value for the additional design variable, P_{BL}, is fixed at all times, ($\dot{P}_{\text{BL}} = 0$) and P_{BL} is free at both initial and final times, additional boundary conditions which is setting the corresponding terminal costates to zero as:

$$\lambda_{P_{\text{BL}}}(t_0) = 0, \qquad \lambda_{P_{\text{BL}}}(t_f) = 0.$$

Similarly, if c_{min} and c_{max} are also introduced as design variables, the state vector can be augmented by two more terms with their corresponding differential equations being $dc_{\text{min}}/dt = 0$ and $dc_{\text{max}}/dt = 0$. Four additional boundary conditions ($\lambda_{c_{\text{min}}}(t_0) = \lambda_{c_{\text{min}}}(t_f) = 0$ and $\lambda_{c_{\text{max}}}(t_0) = \lambda_{c_{\text{max}}}(t_f) = 0$), have to be introduced.

Therefore, this joint optimization defined by augmented state dynamics Eq. (2.6) (augmented by $\dot{P}_{\text{BL}} = 0$, $\dot{c}_{\text{min}} = 0$, $\dot{c}_{\text{max}} = 0$ as per the case) and costate dynamics ($\dot{\boldsymbol{\lambda}} = -\left[\frac{\partial H}{\partial \boldsymbol{x}}\right]^{\top}$) over smooth and regularized controls/variables established in Eqs. (3.31), (3.9), (3.12) and thrust direction (Eq. (4.35)) to minimize the cost function Eq. (3.35) is converted into a two-point boundary-value problem subject to the boundary conditions given in Eq. (3.37):

$$\boldsymbol{\psi} = \left[\left[\boldsymbol{x}(t_f) - \tilde{\boldsymbol{x}}\right]^{\top}, \lambda_m(t_f), \lambda_{P_{\text{BL}}}(t_f), \lambda_{c_{\text{min}}}(t_f), \lambda_{c_{\text{max}}}(t_f)\right]^{\top} = \mathbf{0}. \tag{3.18}$$

To facilitate reader's understanding of the components of the TPBVP used in each of the different cases discussed in the results section, a summary is provided in Table 3.1.

3.1.4 Numerical Example Cases

In order to draw insights from comparisons on the improvement of the final mass when the optimization problem is augmented with additional flexibility, five formulations for the Earth to Dionysus rendezvous problem are considered (EDP1-5):

- EDP1: Maximize final mass with a fixed-I_{sp} engine (this is the traditional approach for preliminary mission design).
- EDP2: Maximize final mass with a variable-I_{sp} engine and with fixed values for P_{BL}, $I_{\text{sp,min}}$, and $I_{\text{sp,max}}$.
- EDP3: Maximize the *useful mass* delivered with a variable-I_{sp} engine; P_{BL} as a design variable and with fixed values for $I_{\text{sp,min}}$ and $I_{\text{sp,max}}$.
- EDP4: Maximize the useful mass delivered with a variable I_{sp}-engine with variable thruster efficiency (as a function of I_{sp}); P_{BL} as a design variable and fixed values for $I_{\text{sp,min}}$ and

Table 3.1: Summary of different cases for the TPBVP

Minimize fuel (EDP1 & 2): $J = \int_{t_0}^{t_f} \frac{2\eta P_{\text{av}}\delta}{c^2}$ dt Maximize Payload: $J = \int_{t_0}^{t_f} \left[\frac{\gamma_1 P_{\text{BL}}+\gamma_2 P_{\text{av}}}{\Delta t} + \frac{(1+a_{\text{tk}})2\eta P_{\text{av}}\delta}{c^2}\right] dt$		
Case & Optimization Variables	Optimality Conditions	Boundary Conditions
EDP1: $\hat{\alpha}$, δ	Eq. (4.35) Eq. (3.24)	$\boldsymbol{x}(t_f) - \tilde{\boldsymbol{x}}_d = \mathbf{0}$ $\lambda_m(t_f) = 0$
EDP2: $\hat{\alpha}$, δ, c	Eq. (4.35), Eq. (3.24) Eq. (3.17)a	$\boldsymbol{x}(t_f) - \tilde{\boldsymbol{x}}_d = \mathbf{0}$ $\lambda_m(t_f) = 0$
EDP3: $\hat{\alpha}$, δ, P_{BL}, c	Eq. (4.35) Eq. (3.24) Eq. (3.17)a	$\boldsymbol{x}(t_f) - \tilde{\boldsymbol{x}}_d = \mathbf{0}$ $\lambda_m(t_f) = 0$ $\lambda_{P_{\text{BL}}}(t_0) = 0$ $\lambda_{P_{\text{BL}}}(t_f) = 0$
EDP4: $\hat{\alpha}$, δ, P_{BL}, $\eta(I_{\text{sp}})$, c	Eq. (4.35), Eq. (3.24) Eq. (3.17)b (Linear η) Eq. (3.17)c (Quadratic η)	$\boldsymbol{x}(t_f) - \tilde{\boldsymbol{x}}_d = \mathbf{0}$ $\lambda_m(t_f) = 0$ $\lambda_{P_{\text{BL}}}(t_0) = 0$ $\lambda_{P_{\text{BL}}}(t_f) = 0$
EDP5: $\hat{\alpha}$, δ, P_{BL}, c c_{min}, c_{max}	Eq. (4.35) Eq. (3.24) Eq. (3.17)a	$\boldsymbol{x}(t_f) - \tilde{\boldsymbol{x}}_d = \mathbf{0}$ $\lambda_m(t_f) = 0$ $\lambda_{P_{\text{BL}}}(t_0) = 0$ $\lambda_{P_{\text{BL}}}(t_f) = 0$ $\lambda_{c_{\text{min/max}}}(t_0) = 0$ $\lambda_{c_{\text{min/max}}}(t_f) = 0$

$I_{\text{sp,max}}$.

- EDP5: Maximize the useful mass delivered with a variable-I_{sp} engine; P_{BL}, $I_{\text{sp,min}}$, and $I_{\text{sp,max}}$ as design variables.

Observe that for cases EDP2-EDP5, I_{sp} is not explicitly optimized, however it is implicitly optimized when c is an optimization variable.

Table 3.2: Spacecraft parameters; γ_1, γ_2 and a_{tk} are taken from [1] and P_{BL}, P_{max} and PL are adopted from [2].

	EDP1/2	EDP3	EDP4	EDP5
P_{BL} (kW)	11	[10,25]	[10,25]	[10,25]
P_{max} (kW)	6.5	6.5	6.5	6.5
P_{min} (kW)	0.6	0.6	0.6	0.6
PL (kW)	0.8	0.8	0.8	0.8
$I_{\text{sp,min}}$ (s)	2200	2200	2200	[1500,6750]
$I_{\text{sp,max}}$ (s)	3400	3400	3400	[6760,12000]
η	0.68	0.68	Eqs. (3.3) & (3.4)	0.68
η_d	0.94	0.94	0.94	0.94
γ_1 (kg/kW)	10	10	10	10
γ_2 (kg/kW)	15	15	15	15
a_{tk}	0.1	0.1	0.1	0.1

While the bounds on the exhaust velocity (or I_{sp}) are implemented implicitly using CSC, the bounds on P_{BL} and $c_{\text{min/max}}$ are implemented using a different approach in the EDP3, EDP4 and EDP5 cases. Note that MATLAB's *fsolve* does not impose bounds on the design variables. Therefore, in order to ensure that the values generated by *fsolve* always remain within the prescribed range, we have used the following mapping (for example, shown for just P_{BL}),

$$P_{\text{BL}} = 0.5\left[(P_{\text{BL,lb}} + P_{\text{BL,ub}}) + (P_{\text{BL,ub}} - P_{\text{BL,lb}})\sin(x)\right], \tag{3.19}$$

where x is the new design variable (which is an angle) and $P_{\text{BL,lb}} = 10$ kW and $P_{\text{BL,ub}} = 25$ kW per Table. 3.8. Observe that Eq. (3.19) is a form of continuous invariant embedding that

implicitly imposes $P_{\text{BL,lb}} \leq P_{\text{BL}} \leq P_{\text{BL,ub}}$. This numerical artifice allows us to treat bounded design variables without imposing a constraint on the variable. In addition, the new design variable x can take any value. The same continuous embedding is used for $I_{\text{sp,min}} \in [1500, 6750]$ s and $I_{\text{sp,max}} \in [6760, 12000]$ s in EDP5.

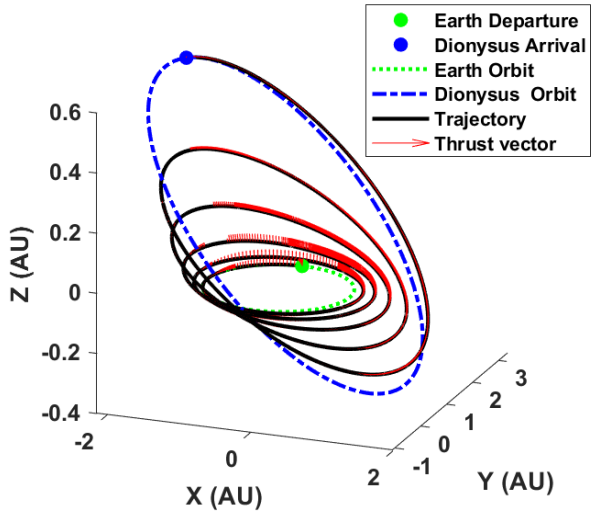

Figure 3.2: EDP1: Optimal trajectory with the direction of thrust indicated by red arrows for $\rho_b = \rho_p = 1.0 \times 10^{-4}$ and $\rho_c = 1.0 \times 10^{-5}$.

The spacecraft is assumed to leave the Earth with zero hyperbolic excess velocity, i.e., $\|\boldsymbol{v}_\infty\| = 0$. The multiple-revolution, multi-year nature of the optimal trajectory has made it an excellent benchmark in a number of recent works [75, 51]. The current example is inspired by [75], where Nuclear Electric Propulsion (NEP) constant specific impulse engine with nominal thrust as 0.32 N and $I_{\text{sp}} = 3000$ s was used. Departing on December 23, 2012 from Earth, the spacecraft took 3534 days to rendezvous with Dionysus. The position and velocity vectors of the Earth at the departure

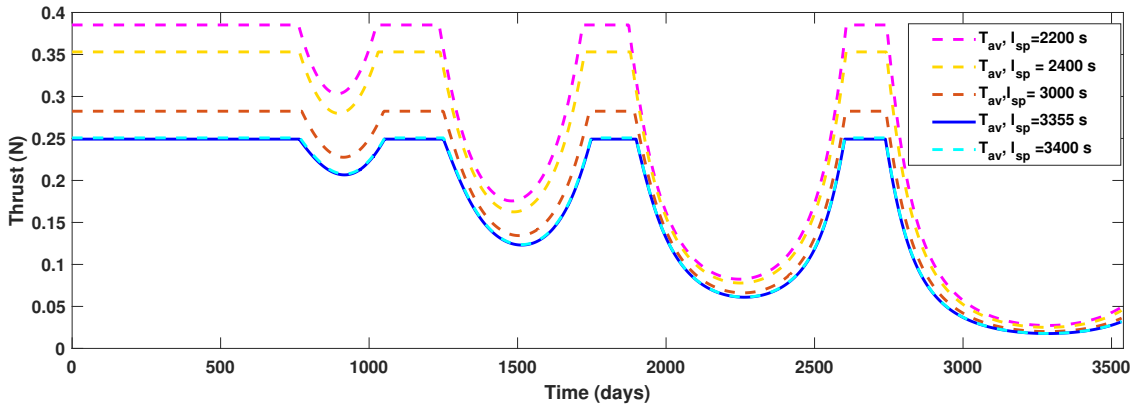

Figure 3.3: EDP1: Comparison of thrust profile for different test runs to determine the most fuel-optimal solution with fixed I_{sp} values.

date and the final position and velocity for Dionysus are [75]:

$$\boldsymbol{r}_E = [-4561588.65006029, 147076954.664376, -2259.9459243617]^\top \text{km},$$

$$\boldsymbol{v}_E = [-30.265097, -0.8486854, 0.0000505]^\top \text{km/s},$$

$$\tilde{\boldsymbol{r}} = [-305026788.667814, 307051467.941918, 82899899.5682193]^\top \text{km},$$

$$\tilde{\boldsymbol{v}} = [-4.23872656978066, -13.436307899221, 0.56536256928611]^\top \text{km/s}.$$

In Ref. [76], the number ($N_{\text{rev}} = 5$) of revolutions around the Sun was identified to result in the most fuel-optimal trajectory when the spacecraft is equipped with one NEP engine. To incorporate N_{rev} into the formulation, final true longitude is set as $l_f = l_f + 2\pi N_{\text{rev}}$. Care must be taken to make l_f (i.e., the true longitude of the target point) greater than l_0 (i.e., the true longitude of the initial point) by addition of appropriate multiples of 2π before N_{rev} are factored in.

The presence of local extremals and the triple homotopy structure make the solution procedure challenging. Though, HTS and CSC convert the problem from an MPBVP to a TPBVP and significantly enlarges the domain of convergence, numerical difficulties can arise. Numerical sensitivity

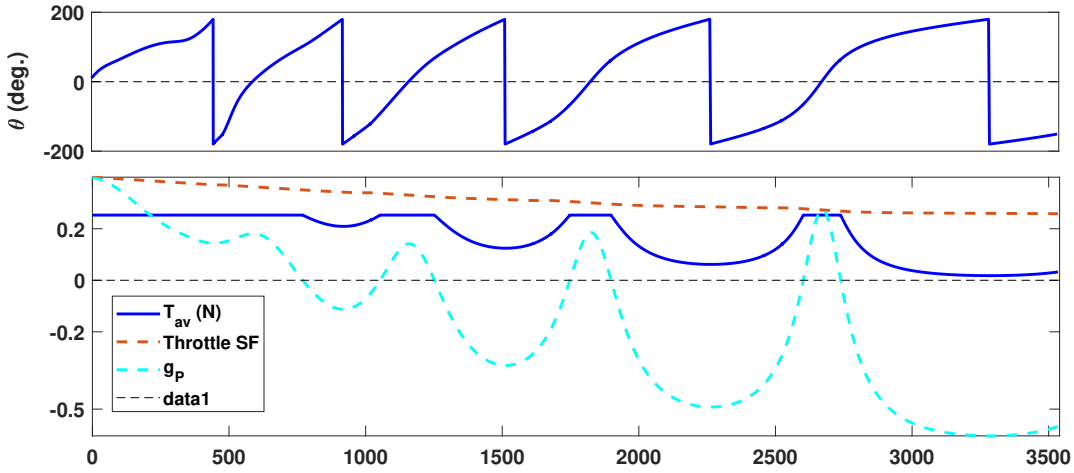

Figure 3.4: EDP1: Variation in osculating true anomaly, thrust profile and acceleration (log scale) vs. time; $\rho_b = 1 \times 10^{-4}$, $\rho_p = 1 \times 10^{-4}$.

of a triple homotopy problem is two folds: 1) There can be turning points in the homotopic hypersurface (depicting the root solving function) in the parameter space leading to singular Jacobian, and 2) The relative values of the three continuation parameters can lead to an ill-conditioned problem at some intermediate step. Note also that the existence of a continuous homotopy path and the existence of a root are generally not guaranteed. Nevertheless, homotopy/continuation methods are extremely important tools that vastly enhance convergence. Turning points were not encountered in the numerical results of this dissertation.

As mentioned, five cases (EDP-1 through 5), are considered involving different levels of design fidelity and therefore, extent of simultaneous spacecraft and trajectory design optimization. As expected, improved results are observed when the additional spacecraft design flexibility is incorporated into the optimization problem. All cases except for EDP4 assume constant thruster efficiency. This assumption is dealt with in EDP4 where two models of varying degree of fidelity for thruster efficiency values are implemented to capture the impact on the results.

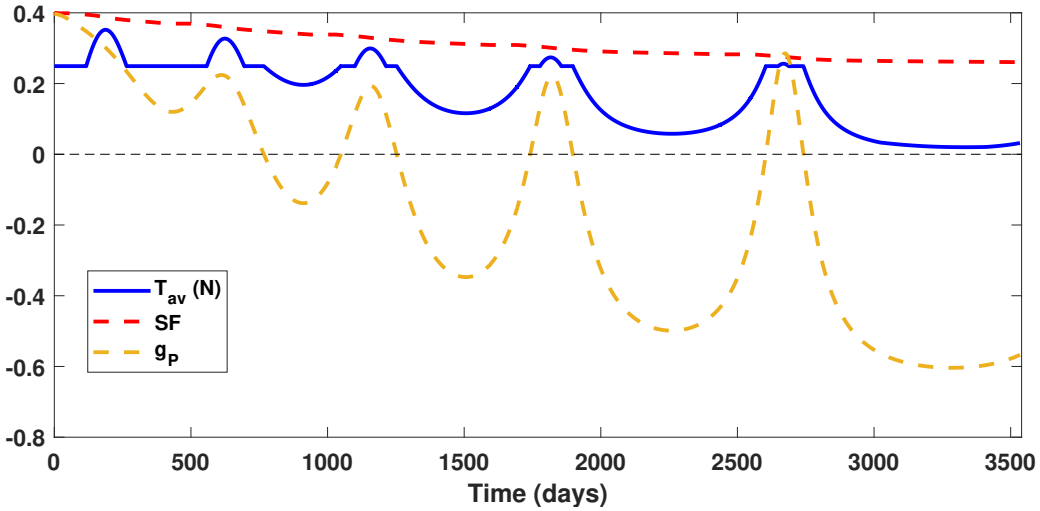

Figure 3.5: EDP2: Thrust profile, power activation constraint and switching function vs. time; SF and g_P are both normalized by 10000 for better visibility of thrust profile.

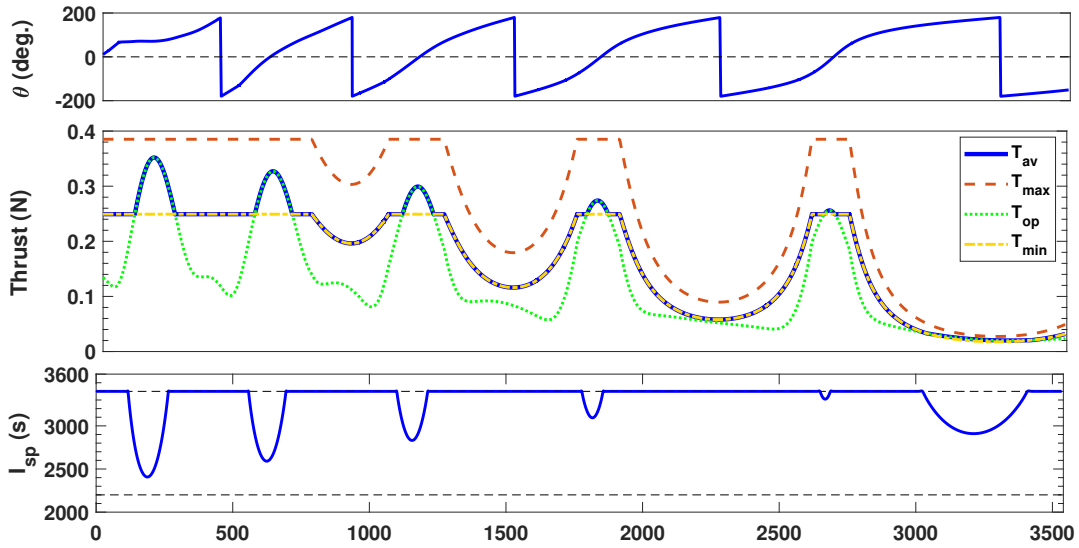

Figure 3.6: EDP2: osculating true anomaly, thrust profile and I_{sp} vs. time; $\rho_b = \rho_p = 1 \times 10^{-4}$ and $\rho_c = 1 \times 10^{-5}$.

3.1.4.1 Earth to Dionysus Problem 1-3 (EDP1-EDP3)

In the case of EDP1, the value for the fixed I_{sp} is determined on the basis of a study summarized in Table 3.3. Several I_{sp} cases in the range [2000, 3450] seconds were run of which a few are reported here with the final mass and peak thrust (T_{peak})in the thrust profile (see figure 3.3) registered during the maneuver. It can be observed that maximum final mass is obtained corresponding to $I_{\text{sp}} = 3355$ s, which is also close to the average I_{sp} ($I_{\text{sp}_{\text{avg}}} = \frac{\sum_{t=0}^{t_f} I_{\text{sp}}(t)}{t_f}$) evaluated for the optimized variable-I_{sp} (Case EDP2) profile (See Table 3.12). Our approach specifies N_{rev} and looks for the local extremal for each feasible N_{rev}, although there is no formal proof of this empirical truth. Numerical studies indicates as for the related results of reference [20] that there was only one local extremal for each feasible N_{rev}. Note that the results correspond to fixed-time, fuel-optimal, rendezvous-type maneuvers. The minimum of all local minimals found was adopted as the believed-to-be global extremal.

Table 3.3: EPD1: Final mass for a range of I_{sp} values for a fixed-I_{sp} thruster.

I_{sp} (s)	2200	2400	3000	3350	3355	3360	3400
T_{peak} (N)	0.3852	0.3531	0.2824	0.2529	0.2525	0.2522	0.2492
m_f (kg)	2343.3	2411.8	2543.8	2580.67	2580.7	2580.5	2574.1

Since there is negligible graphical difference among the trajectories on a solar scale except for the thrust profile, for all five cases, the trajectory shown in Figure 3.2 can be considered as a qualitative depiction of the trajectory for all five problems (EDP1 to EDP5). The differences in the profile of thrust, and I_{sp} are detailed for each case in Figures 3.4, 3.6, 3.8, 3.11, 3.12 and 3.13. Five of these figures consist of three subplots containing the osculating true anomaly (θ), thrust profile, I_{sp} profile stacked below one another. T_{av} denotes the thrust that is computed using the available power, P_{av} as

$$T_{\text{av}} = \frac{2\eta P_{\text{av}}}{c^*}.$$

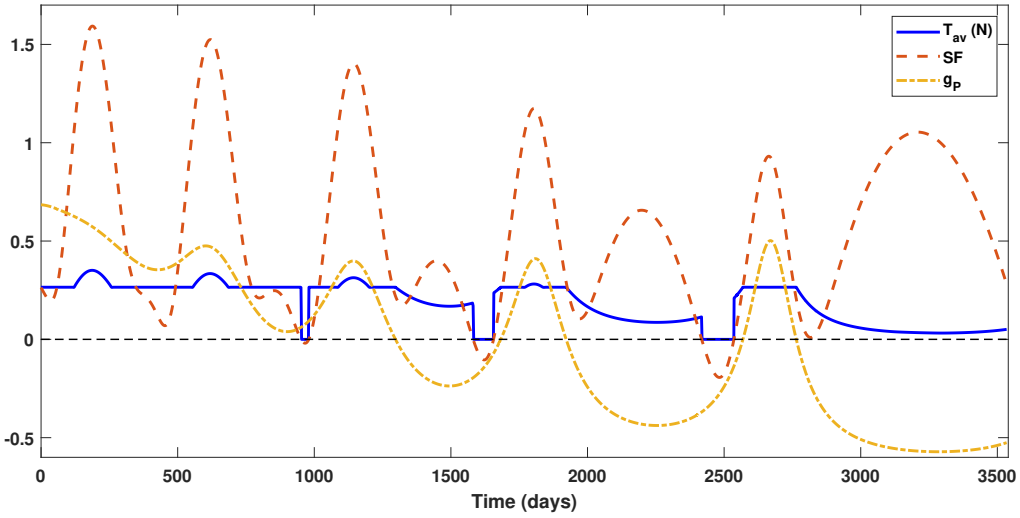

Figure 3.7: EDP3: thrust profile, power activation constraint and power switching function vs. time; g_P is normalized by 10000 for better visibility of thrust profile.

The thrust profile subplots in Figures 3.6, 3.8, 3.11, 3.12 and 3.13 feature the final thrust profile (T_{av}) along with three dashed lines that correspond to $T_{\text{min}} = \frac{2\eta P_{\text{av}}}{c_{\text{max}}}$, $T_{\text{op}} = \frac{2\eta P_{\text{av}}}{c_{\text{opt}}}$ and $T_{\text{max}} = \frac{2\eta P_{\text{av}}}{c_{\text{min}}}$, where c_{opt} is defined in Eq. (3.17). As expected, the applied thrust magnitude (T_{av}) always remains within the defined bounds of T_{min} and T_{max} while jumping to T_{op} during the perihelion of the quasi-elliptic trajectories as shown in all the cases. Since in the case of Fixed-I_{sp} thruster (EDP1), $c_{\text{min}} = c_{\text{opt}} = c_{\text{max}}$, the boundaries of T_{min} and T_{max} formed in the other four cases simply coincide for this one. The dashed lines shown in the thrust subplot of Figure 3.4 refer to the switching function (see Eq. 3.16) and the power activation constraint, g_P (see Eq. 3.12). Similarly, Figures 3.5 and 3.7 map the effect of switching and power activation functions on the thrust profile displaying how the thrust drops (refer Eq. (3.6)) when g_p becomes negative for EDP2 and EDP3, respectively.

For both cases, Figures 3.6 and 3.8 show that the thruster switches to a high thrust at the quasi-perihelion ($\theta \approx 0^\circ$) passages, which can be seen as little bumps in the thrust profile. Concurrently, a dip is observed in the I_{sp} values during the maximum thrust arcs. In fact, it can be observed that the thrust profile attains T_{op} value about the perihelion for both EDP2 and EDP3.

Furthermore, EDP3 consists of three coast arcs while there are none observed in EDP1 and

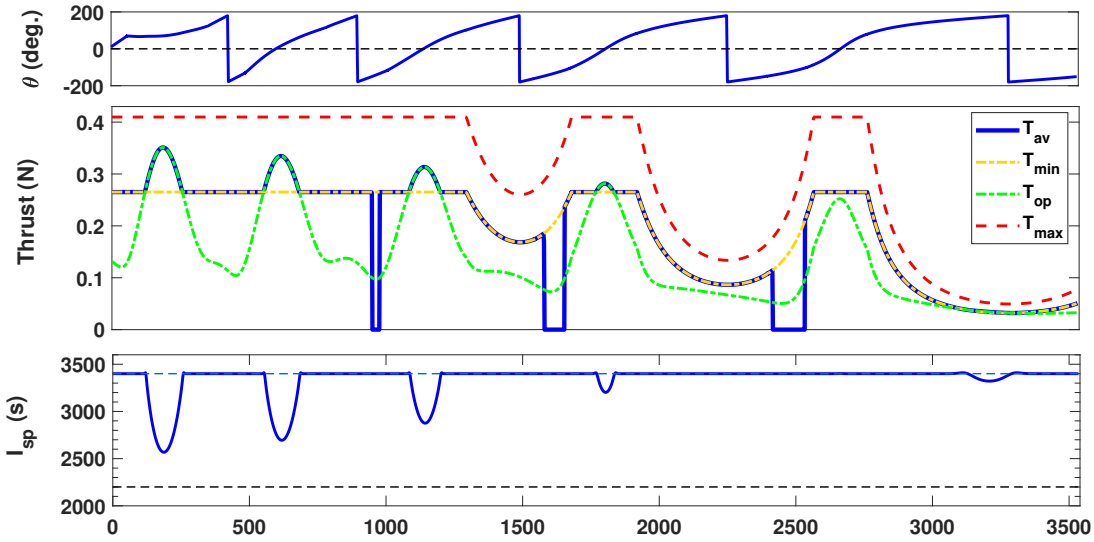

Figure 3.8: EDP3: The osculating true anomaly, thrust profile, and I_{sp} vs. time; $\rho_b = \rho_p = 1.0 \times 10^{-4}$ and $\rho_c = 1.0 \times 10^{-5}$.

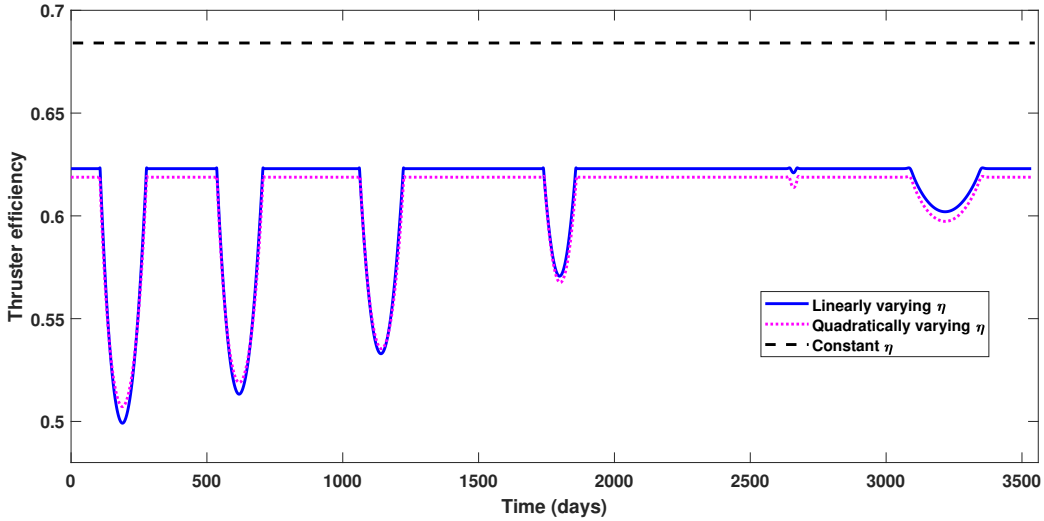

Figure 3.9: EDP4: Comparison of evolution of thruster efficiency for linear and quadratic modelling.

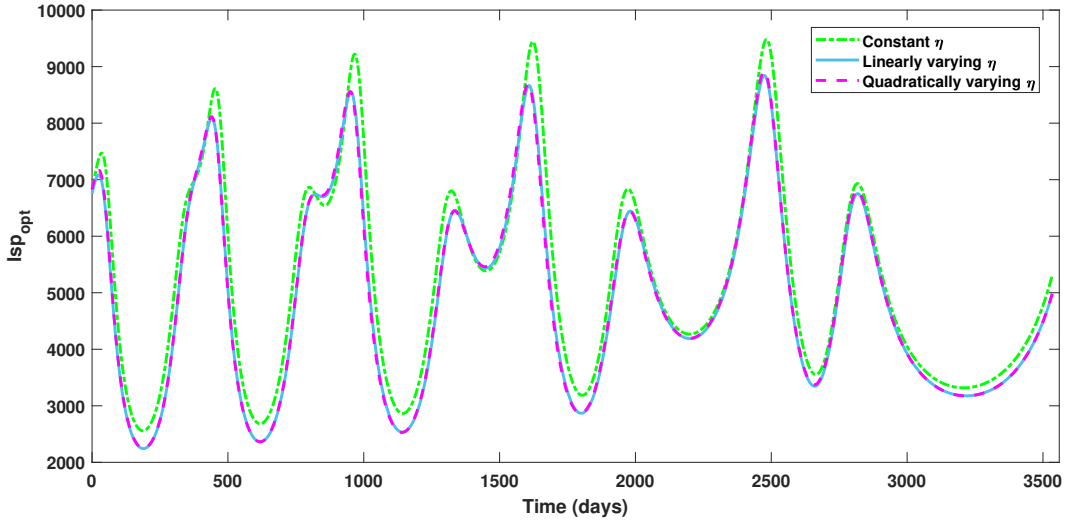

Figure 3.10: EDP4: Comparison of time history of optimal I_{sp} for constant, linear and quadratic modelling of thruster efficiency.

EDP2 as the switching function never gets negative for these two problems (see Figures 3.4 and 3.5). This behavior can be attributed to more power available (optimal P_{BL}= 13.8 kW) in case of EPD3 as compared to EPD1 and EPD2 (P_{BL}= 11 kW), allowing for some coast arcs. In case of EDP2, the thruster is always "on" and T_{av} follows the T_{min} profile except during the perihelion passages where it follows T_{op}.

3.1.4.2 Earth to Dionysus Problem 4 (EDP4)

EDP4 accommodates the variation of thruster efficiency with I_{sp} modeled either linearly or quadratically dependent on I_{sp}, which alters the inverse relation between available thrust and exhaust velocity existing earlier in the case of constant efficiency. The thrust available is lower than observed in the case of constant efficiency depending on the efficiency variation as shown in the Figure 3.9. For a comparison, the resulting optimal exhaust velocity owing to the varied (linearly or quadratically) thruster efficiency model, the $I_{sp,opt}$ values for all three models are plotted in Figure 3.10. Thrust profiles for both the linear and quadratic variation display similar trends of thrusting (T_{op} at the time of pseudo-periapsis) as in the cases EDP1-3. Both (linear and quadratic) cases feature two coast arcs and similar thrust and I_{sp} profiles as shown in Figures 3.11 and 3.12. Due

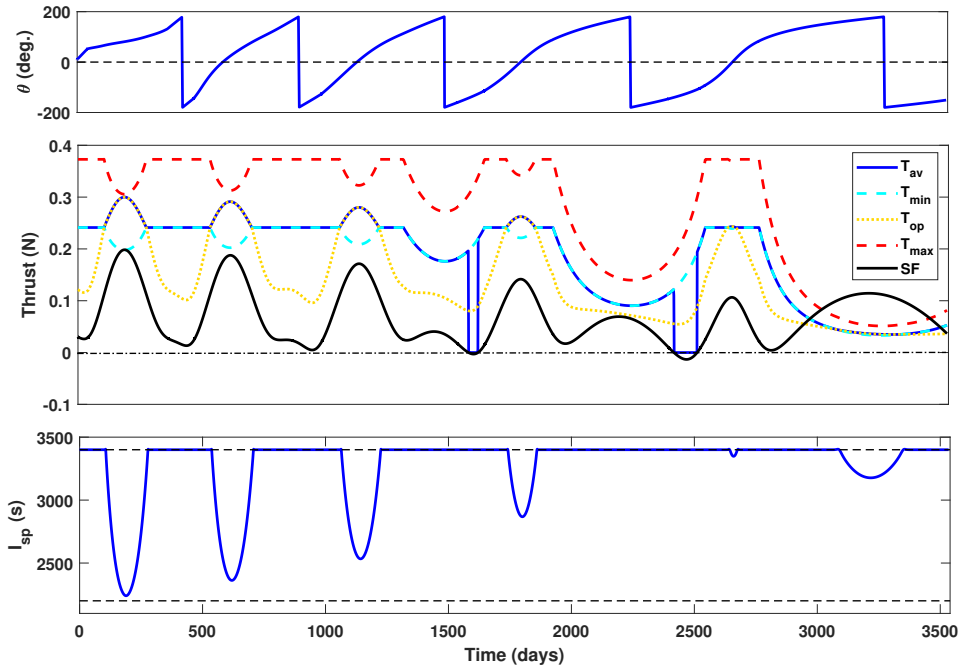

Figure 3.11: EDP4: The osculating true anomaly, thrust profile, and I_{sp} vs. time for linearly varying efficiency,η_l; $\rho_b = \rho_p = 1.0 \times 10^{-4}$ and $\rho_c = 1.0 \times 10^{-5}$.

to lower thruster efficiencies than in EDP3 case, EDP4 features one less coast arc than in EDP3, despite requiring higher power than EDP3.

Post solving EDP1 through EDP4, an opportunity to optimize the lower and upper bounds of the exhaust velocity is noticed, to gather insights on how much increasing the maximum exhaust velocity can lead to maximization of delivered payload. Therefore, EDP5 is formulated where c_{min} and c_{max} are inducted as additional design variables. The optimal maximum I_{sp} (11,246 sec) for this maneuver is very high, and at present not achievable by any known engine. As is frequently the case allowing optimization of physical variables may lead to insights, but in this case, we see that I_{sp} (or c) should have imposed a physically realizable upper bound. It is important to note that including higher fidelity modeling does not always result in higher predicted performance. Adding more design flexibility must go hand in hand with imposing physical bounds on all design freedoms, otherwise you may get an insanely high "optimal" say, I_{sp} like in the case of EDP5. One can observe in Fig 3.13 that T_{av} approximately follows the curve T_{op} at all times, which is expected

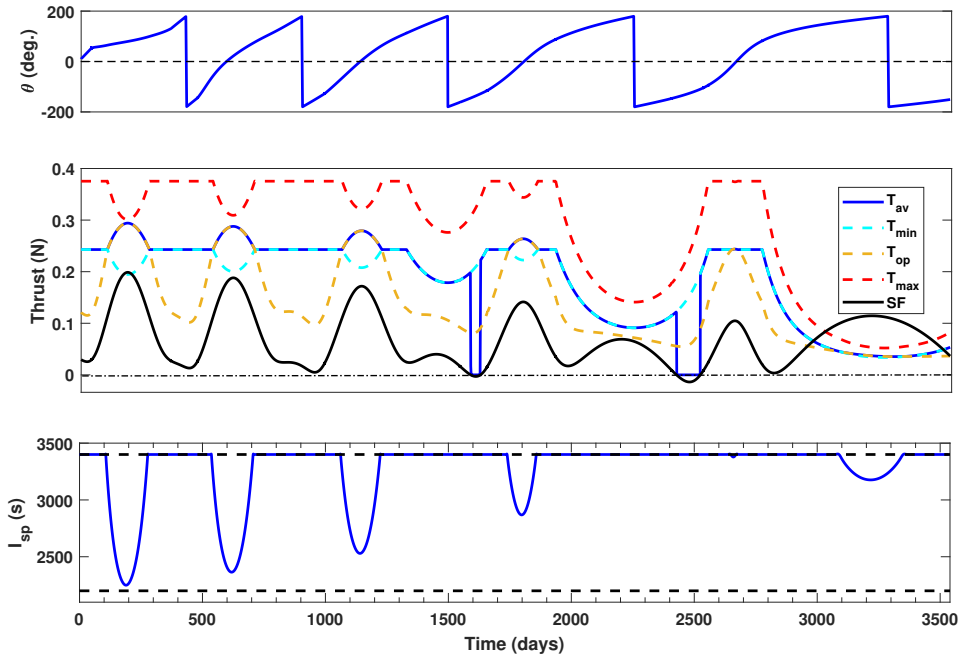

Figure 3.12: EDP4: The osculating true anomaly, thrust profile, and I_{sp} vs. time for quadratically varying η_q; $\rho_b = \rho_p = 1.0 \times 10^{-4}$ and $\rho_c = 1.0 \times 10^{-5}$.

Table 3.4: Comparison of results of five cases (EDP1-5) for Earth-to-Dionysus problem.

	EDP1	EDP2	EDP3	EDP4$^*_a$	EDP4$^*_b$	EDP5
P_{au} (kW)	11	11	13.8	14.98	15.053	19.61
T_{peak} (N)	0.2525	0.3519	0.3508	0.30	0.2941	0.376
$I_{\text{sp}_{\text{avg}}}(s)$	3355	3355.93	3371.54	3291.85	3347.76	5468.76
m_f (kg)	2580.7	2603.8	2643.77	2566.87	2569.25	2842.06
m_u (kg)	2237.2	2261.95	2272.85	2176.85	2178.18	2432.65
m_{SA}(kg)	110	110	138.06	149.8	150.5	196.1
m_{PSPU} (kg)	201.65	201.65	235.56	247.31	247.94	293.61
m_{PSFS}(kg)	1561.25	1536.39	1491.85	1576.48	1573.87	1273.73

*EDP4$_a$ and EDP4$_b$ refer to the linear and quadratic efficiency respectively.

when c_{min} and c_{max} are chosen by the optimization algorithm. Interestingly, the T_{av} also drops from the EDP3 case and there are no coast arcs in contrast to 3 coast arcs observed in EDP3. As can be observed in Fig 3.13, c_{opt} always remain within the bounds of c_{min} and c_{max}. The resulting curve for the exhaust velocity is smooth for small values of smoothing parameters, but the process still requires CSC for the interim values. The results of this case are verified with the outcome of optimizing payload with unconstrained variable I_{sp} as both cases should lead to identical results.

Table 3.12 compares EDP1-5 on the basis of power generated at 1 AU (P_{au}, maximum thrust, average I_{sp}, final mass, useful mass delivered with mass of the power systems, masses of power subsystems and the mass of the solar panels. A breakdown of the initial mass for each of the cases is presented as per Eq. (3.1a), where m_{PSPU} and m_{PSFS} are added to m_u to provide the initial mass. Mass of the solar arrays (included in m_{PSPU}) is only dependent on P_{BL} and is mentioned to give the reader an idea about the size of arrays involved for each of the cases.

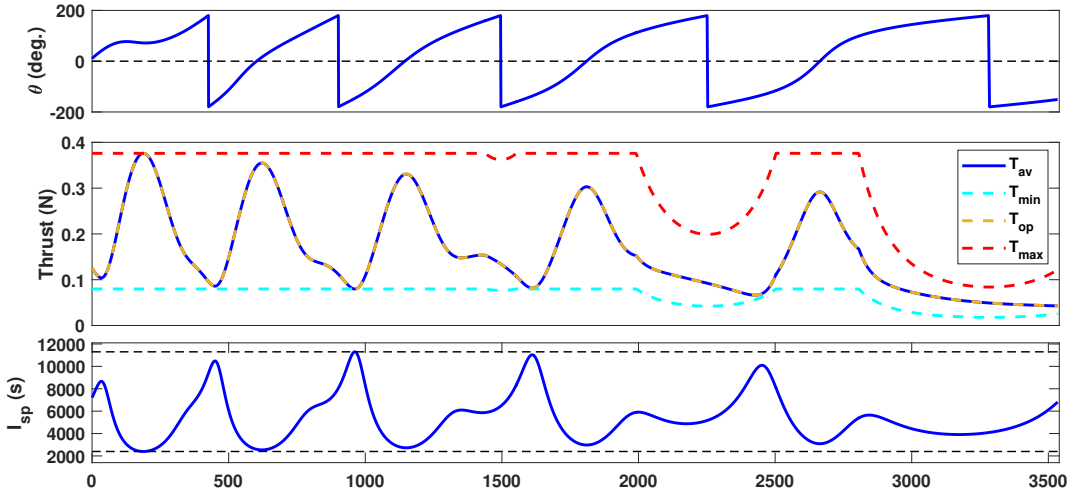

Figure 3.13: EDP5: The osculating true anomaly, thrust profile, and I_{sp} vs. time; $\rho_b = \rho_p = 1.0 \times 10^{-4}$ and $\rho_c = 1.0 \times 10^{-3}$.

The power model parameters of EDP1 are kept the same as EDP2 for all the evaluations reported in Table 3.12. EDP1 leads to less final mass and less useful mass delivered than both EDP2

and EDP3. Though the mass of the solar panels is higher (by approximately 28 kg) in case of EDP3 due to higher value of P_{BL}, an increment of 40 kg in final mass and approximately 11 kg in delivered payload mass is observed when co-optimization is conducted in EDP3 over the EDP2 solution. Though EDP1 and EDP2 did not aim at maximization of useful mass delivered, the payload and the solar array mass reported in Table 3.12 are evaluated for comparison using the same parameters (i.e., $\gamma_1, \gamma_2, a_{tk}$) used in EDP2, mentioned in Table 3.8. In case of EDP4, the final payload delivered does not change by much ($\sim$2 kg) in between the two cases with varying efficiencies but drops significantly ($\sim$96 kg) from that of EDP3 case with a constant efficiency. This suggests that while thruster efficiency is important, a simple linear model is adequate to represent thruster efficiency variations. As for EDP5, the resulting optimal solution is significantly improved in terms of payload by $\sim$159 kg with higher power requirement (by 5.6 kW) with respect to EDP3. However, the absence of a constraint on $I_{\text{sp}_{\text{max}}}$ means this case needs further study. It is expected that the relative advantage to EDP4 would be significantly less.

3.2 Fuel-Optimization with Ion-Gridded Engines [2]

Application of idealized constant-specific-impulse, constant-thrust electric thruster performance models like shown in the previous sections is quite common for spacecraft trajectory design. However, incorporation of realistic performance models of multi-mode electric thrusters leads to notable challenges, and at the same time, offers unprecedented system-level optimization opportunities. These discrete gridded-ion electrical thrusters, in principle, are capable of providing a few thousand operation modes realized by the fine resolution of the current and voltage beams. Only a handful of these modes, however, are considered for a particular mission owing to the implicit necessity of laboratory calibration of each mode and also the increased hardware requirements for operating each mode. Each mode requires apriori experimental characterization. A method that is used to deal approximately with the discontinuity in modes is to use polynomial approximations [36, 22]. These polynomial approximations are constructed to encapsulate the collective contribution of the different modes [110]. The weights in these polynomial approximations are set proportional to how frequently certain modes are used [36]. These approximations offer smoothness that enhances the numerical convergence of the gradient-based solvers, but result in an inaccurate application- specific representation of the net thruster performance. These discrete modes' variables are most generally not a monotonic function of each other or the vehicle state variables, therefore interpolation frequently encounters difficulties.

This section introduces a novel method that is capable of considering all feasible engine modes and then selects the mode that minimizes the Hamiltonian using Pontryagin's minimum principle (PMP). The approach leads to many switches between operating modes and frequently leads to convergence difficulties, which can be eliminated by smooth embedding that approaches each sharp switch in a homotopic fashion. The proposed construct is also structured to reveal which subset of all the available engine modes that should be included with an associated known sacrifice in optimality. A critical subset of modes can be identified as 'integral' modes which define the

[2] Reprinted with permission from "Low-thrust gravity-assist trajectory design using optimal multimode propulsion models" by Arya, Vishala and Taheri, Ehsan and Junkins, John L, 2020. Journal of Guidance, Control, and Dynamics, Volume 44(7), 1280–1294, Copyright 2021 by American Institute of Aeronautics and Astronautics

minimum number of modes that should be considered to achieve an essentially "optimal" performance (with respect to the prescribed performance index). Finding these 'integral' modes serves dual purposes: 1) It accounts for a close-to-accurate thrusting capability available with an engine to provide improved prefatory estimates of the preliminary mission-critical parameters. 2) Out of the thousands of operation modes that an engine maybe capable of, a fraction of these are ideally established pre-flight [36] to help reduce complexity associated with building power processing unis (PPUs) and other support systems. Some extra modes can be further added to the 'integral' set of modes in order to fortify robustness of the mission to conceivable mode failures.

3.2.1 Power Modelling

The efficiency of solar arrays degrades over time due to radiation and aging. This degradation can have a significant detrimental effect on power generation in multi-year interplanetary missions. Variation in power due to the change in the heliocentric distance and the timely degradation can be written as [22]

$$P_{\text{SA}} = \frac{P_{\text{BL}}}{r^2}\left[\frac{d_1 + d_2 r^{-1} + d_3 r^{-2}}{1 + d_4 r + d_5 r^2}\right](1-\sigma)^t, \tag{3.20}$$

where $[d_1, d_2, d_3, d_4, d_5]$ have the example empirical values [1.1063, 0.1495, -0.299, -0.0432, 0] to model a particular solar array design performance variation with radial distance, 'r' measured in AU [109]. The degradation factor is denoted by σ (typically a best-estimated degradation of 2 to 4 %/year) and t is used for the time elapsed since launch in years. Please note that the example coefficient values correspond to a particular solar array and power management system on a particular spacecraft. Also, if the coefficients [1, 0, 0, 0, 0] are selected, Eq. (3.20) collapses to the simplest $1/r^2$ power model. The size of solar arrays can be set roughly by heuristic experience and depending on the minimum and maximum heliocentric distance expected during the maneuver. Therefore, the power available for thrusting is evaluated as per the same smooth inequality conditions (Eq. (3.12)) in Section 3.1.

3.2.2 Optimal Control Problem Formulation

The objective is to minimize propellant consumption, which for a fixed initial dry mass of the spacecraft corresponds to maximizing the final mass. To present a general formulation of the problem, we have defined the cost functional as an integral of mass flow rate, $\dot{m}$ (which is assumed to be negative) as

$$\begin{aligned} &\underset{T,\dot{m},\hat{\alpha}}{\text{Minimize}} \;\; J = \int_{t_0}^{t_f} -\dot{m} \;\; dt, \\ &\text{subject to :} \\ &\qquad \text{Equation (2.6)} \\ &\qquad \boldsymbol{x}(t_f) - \tilde{\boldsymbol{x}}_d = \mathbf{0}, \\ &\qquad \boldsymbol{x}(t_0) = \boldsymbol{x}_0, m(t_0) = m_0, \end{aligned} \tag{3.21}$$

where t_0 is the initial time, $\boldsymbol{x_0}$ and m_0 are the MEEs and mass of the spacecraft at the initial time, t_f is the final time and $\tilde{\boldsymbol{x}}_d$ is the desired MEEs at the final time. This general formulation of cost functional is chosen since we are planning to formulate different propulsion systems and $(T, \dot{m})$ is governed differently for each modelling.

The Hamiltonian associated with the defined OCP can be written as

$$H = -\dot{m}(\delta) + \boldsymbol{\lambda}^\top \left(\boldsymbol{A}(\boldsymbol{x}, t) + \frac{T(\delta)}{m} \mathbb{B}(\boldsymbol{x}, t) \hat{\boldsymbol{\alpha}} \right) + \lambda_m \dot{m}(\delta), \tag{3.22}$$

where $\boldsymbol{\lambda} = [\lambda_p, \lambda_f, \lambda_g, \lambda_h, \lambda_k, \lambda_l]^\top$ is the costate vector associated with the MEEs and λ_m is the costate associated with mass. $\delta \in [0, 1]$ is used to denote engine throttling input which is absorbed in the T and $\dot{m}$ expressions. Irrespective of the thruster modelling, δ appears linearly in the expressions of T and $\dot{m}$ as it will be shown later for each case. Upon substitution of T and $\dot{m}$ in Eq. (3.22), the Hamiltonian is an affine function of δ. Since both $\hat{\boldsymbol{\alpha}}$ and δ appear bi-linearly in the Hamiltonian, Pontryagin's minimum principle (PMP) is used. The optimal control direction is

aligned along the Lawden's primer vector, $-\mathbb{B}^\top\boldsymbol{\lambda}$, and optimal throttle is determined as

$$\hat{\boldsymbol{\alpha}}^* = -\frac{\mathbb{B}^\top\boldsymbol{\lambda}}{||\mathbb{B}^\top\boldsymbol{\lambda}||}, \qquad \delta^* = \arg\min_{\delta\in[0,1]} H(\boldsymbol{x}^*(t), \delta(t), \boldsymbol{\lambda}^*(t)). \tag{3.23}$$

A power switching function (SF) governs the optimal throttle 'on' or 'off' times such that

$$\delta^* = \begin{cases} 1; & \text{for } SF > 0, \forall\ c \in [c_{\text{min}}, c_{\text{max}}], \\ 0; & \text{for } SF \leq 0, \forall\ c \in [c_{\text{min}}, c_{\text{max}}], \end{cases} \tag{3.24}$$

The expression for the SF is evaluated for each propulsion model as per the expression of T and $\dot{m}$. Costate dynamics can be evaluated by Euler-Lagrange equation, $\dot{\boldsymbol{\lambda}} = -[\partial H/\partial \boldsymbol{x}]^\top$ and $\dot{\lambda}_m = -\partial H/\partial m$. Additionally, $\lambda_m(t_f) = 0$ since final mass, $m(t_f)$, is not specified.

3.2.2.1 Modelling of VIVT Engines

VIVT engines modulate the thrust value to constructively affect optimized trajectories both in terms of time and fuel consumption such that:

$$T = \frac{2\eta(c)P_{\text{av}}}{c}\delta, \qquad \dot{m} = -\frac{2\eta(c)P_{\text{av}}}{c^2}\delta. \tag{3.25}$$

In this work, linearly varying η as a function of I_{sp} is assumed per the relation given in Table 3.5. Our studies indicate that a linear approximate is accurate enough for preliminary studies [43]. Note T and $\dot{m}$ are a bilinear function of P_{av} and δ, but is a non-linear function of c. A linear approximation leads to the expression for the optimal exhaust velocity, c_{opt} [90] given as

$$c_{\text{opt}} = \frac{2(1-\lambda_m)m}{\left(\frac{\eta_{l1}}{\eta_{l0}}\right) m(\lambda_m - 1) + ||\mathbb{B}^\top\boldsymbol{\lambda}||)}, \ \ c_{\text{min}} \leq c_{\text{opt}} \leq c_{\text{max}}, \tag{3.26}$$

where, η_{l0} and η_{l1} are obtained when η is fitted using a linear function in I_{sp} and their values are given in Table 3.5. Note that only the ratio of the η's in Eq. (3.26) affects c_{opt}. Since VIVT modelling imposes bounds on the minimum and maximum exhaust velocity permissible as per

Table 3.5: Coefficients for polynomial interpolation of control variables for SPT-140.

	$(.)^5$	$(.)^4$	$(.)^3$	$(.)^2$	$(.)^1$	$(.)^0$
T($P_{\text{av}}, \delta = 1$)	0	-3.174	-9.759	1.785	63.94	215.7
$\dot{m}(P_{\text{av}}, \delta = 1)$	-0.09917	-0.07603	0.3288	-1.39	1.214	16.25
$\eta(I_{\text{sp}})$	0	0	0	0	0.07551	0.06316

the engine selection, the effective optimal exhaust velocity (c^*) is bounded by those limits. The capability to change specific impulse as a continuous function makes the VIVT modelling the most flexible and efficient propulsion modelling. Even when the propulsion model is not physically realistic for a known engine, the VIVT modeling acts as a computational model candidate for a first layer optimization due to its capability in providing insights into the most optimal result to maximize final mass when the control variables are ultimately bounded as per the engine selection.

3.2.2.2 Polynomial-Based Modelling of Thruster's Performance

In order to enhance convergence, modelling of thrusters' performance is frequently achieved using polynomial approximations. For instance, operation modes of the Hall-effect SPT-140 thruster are summarized in Table 3.6. The data in Table 3.6 represent a 2D grid of the thrust, T, specific impulse, I_{sp}, mass flow rate, $\dot{m}$, and thruster efficiency, η, as a function of power input to the thruster.

It is a challenge to obtain numerical convergence for both direct and indirect based methods if discrete setting of the engine propulsion model is considered. To circumvent the issue of numerical sensitivities or lack of uniqueness that can cause convergence 'chatter' or challenge robustness due to a lack of resolution in the quasi-Newton step, polynomial interpolations are frequently preferred by the designers for preliminary studies. Therefore, T and $\dot{m}$ are approximated as a function of power using a polynomial fit on a selected subset of operation points as

$$\dot{m} = -\sum_{i=0}^{n_m} c_{m_i} P^i \delta, \qquad T = \sum_{i=0}^{n_T} c_{T_i} P^i \delta, \tag{3.27}$$

where n_m and n_T represent the degree of polynomial used for $\dot{m}$ and T, respectively. Here, c_{m_i}

Table 3.6: Operation modes of the Hall-effect SPT-140 thruster [3].

Mode #	Power (W)	Thrust (mN)	$\dot{m}$ (mg/s)	I_{sp} (sec)	η
1	4989	263	13.9	1929	0.5
2	4620	270	16.5	1670	0.48
3	4589	287	17.8	1647	0.5
4	4561	264	16.4	1645	0.47
5	4502	260	16.2	1641	0.46
6	4375	246	14	1790	0.49
7	3937	251	17.5	1461	0.46
8	3894	251	17.5	1464	0.46
9	3850	251	17.5	1464	0.47
10	3758	217	13.9	1597	0.45
11	3752	221	13.9	1617	0.47
12	3750	215	13.6	1614	0.45
13	3460	184	17.1	1099	0.29
14	3446	185	20.4	925	0.24
15	3402	189	16.3	1181	0.32
16	3377	201	15.8	1302	0.38
17	3376	175	18.2	979	0.25
18	3360	198	14.7	1371	0.4
19	3142	191	13.8	1409	0.42
20	3008	177	11.4	1579	0.46
21	1514	87	6.1	1449	0.41

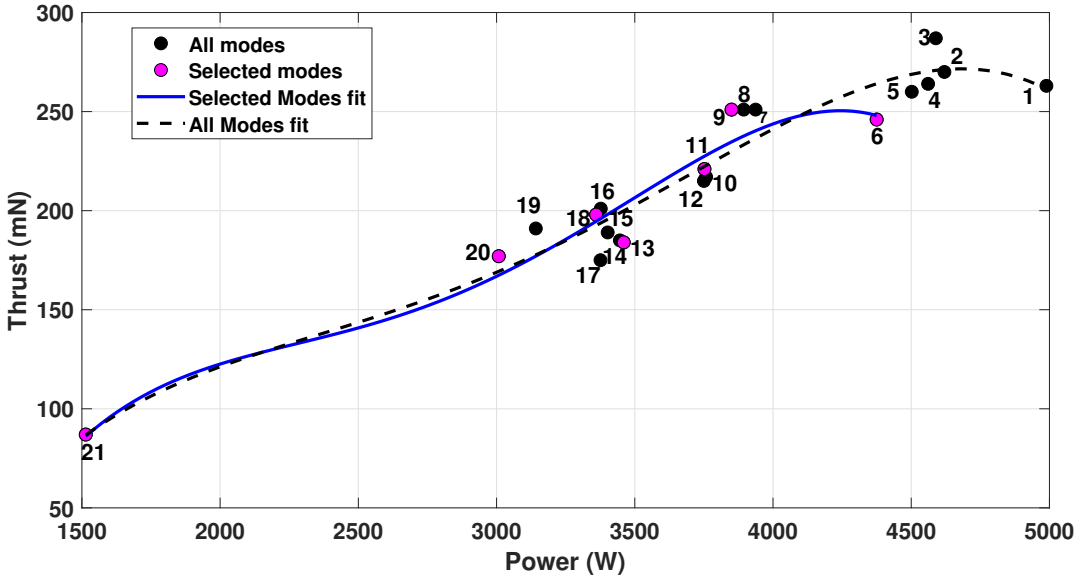

Figure 3.14: The best fit curve for thrust vs. power taking into account both all modes and selected modes. Out of the 21 operation modes of SPT-140, 7 modes (pink circles) are selected.

and c_{T_i} denote coefficients used to approximate $\dot{m}$ and T, respectively. Depending on the thruster model and the operating conditions, the degree of the polynomial and coefficients are altered on the data weighted to obtain a "best" fit to approximate the aggregate affect of relevant discrete operation modes. The degree of these polynomial fits is typically less than 7. In this work, one SPT-140 thruster is used and polynomial approximations similar to the process shown in Eq. (3.27) are formulated to obtain the best curve fits as shown in Figures 3.14, 3.15 and 3.16 for thrust, specific impulse, and efficiency, respectively. As is evident in Figure 3.15, the 21 discrete modes for the SPT-140 engine pose a curve fit challenge.

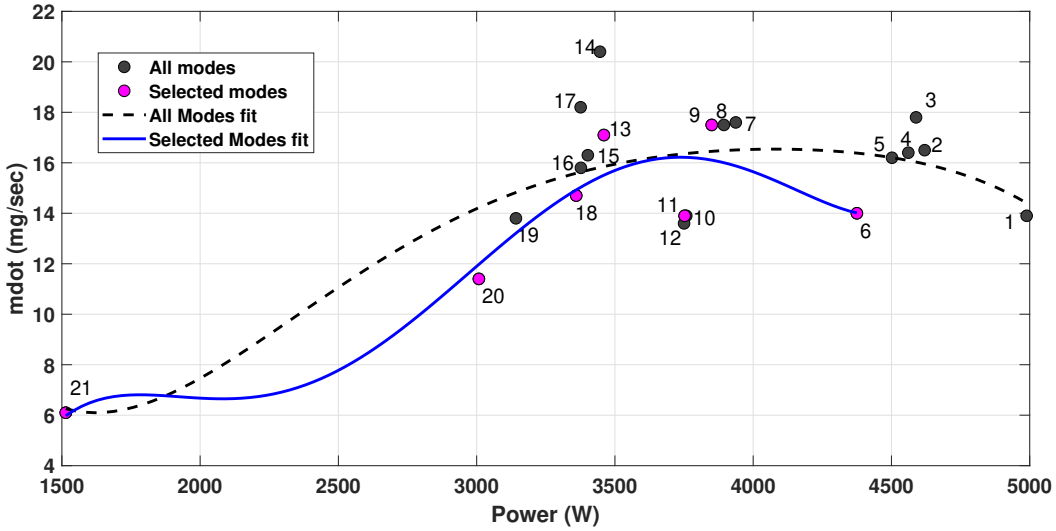

Figure 3.15: The best-fit curve for mass flow rate vs. power taking for all and a few selected modes. Out of the 21 operation modes of SPT-140, 7 modes (pink circles) are selected.

There are two fitting curves (blue and black) provided in Figures 3.14 and 3.15 corresponding to the best fit obtained when all modes are considered or when only a few selected (7 in number) modes are used for the curve-fitting process, respectively. The selection of these 7 modes is done after roughly grouping close operating modes and selecting a single representative mode from each group for the fitting purpose. It can be observed that the fitting curve does not largely improve (apart from being a lower-degree polynomial) when fewer (selected) modes are considered (refer

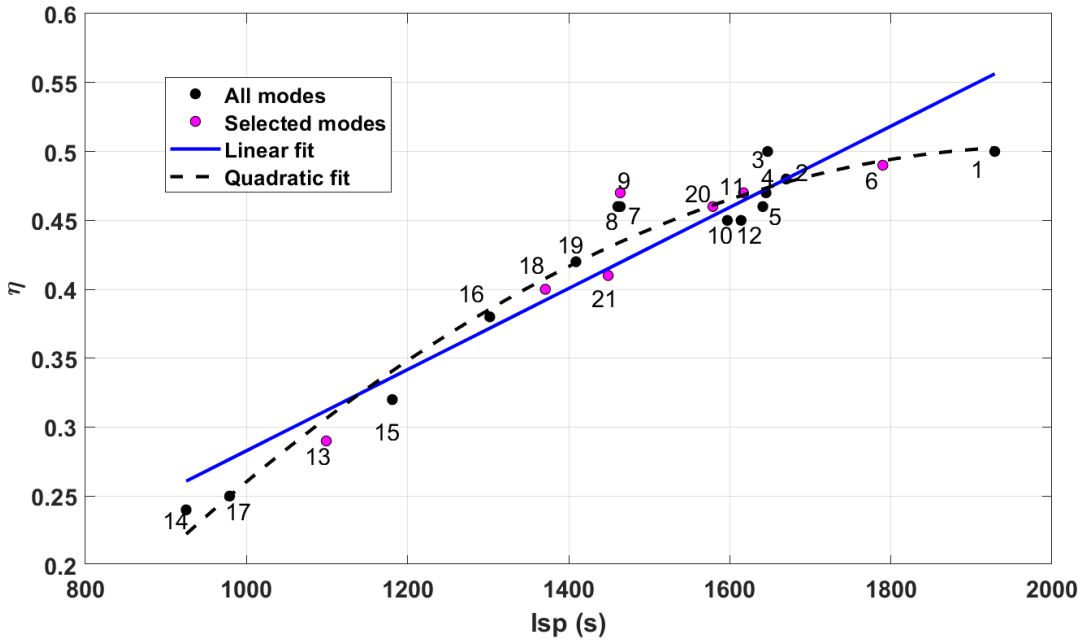

Figure 3.16: The best fit curve (linear and quadratic) for thruster efficiency (η) vs. I_{sp} for all modes. Out of the 21 operation modes of SPT-140, 7 modes (pink circles) are some selected modes.

to the blue curve in Figures 3.14, 3.15 and 3.16). Though a lower-degree polynomial can be obtained for the selected modes, the sensitivity of such curve fits, when parameters go beyond the valid domain during the continuation process, is considerable. Therefore, the best curve fit corresponding to all the modes (black curve) is used in the evaluation to help widen the domain of convergence.

Table 3.5 summarizes the coefficients for a fifth-degree polynomial fitted to all operation modes. Since, as per Figure 3.16, the quadratic curve provides a marginally better fit than the linear case (also shown in Ref. [43]), linear dependency of η on I_{sp} is assumed with its coefficients reported in Table 3.5. The optimal throttle δ^* (refer Eq. (3.27)) in this case is determined using the switching function SF defined as

$$SF = \frac{||\mathbb{B}^\top \boldsymbol{\lambda}||c}{m} + \lambda_m - 1. \tag{3.28}$$

3.2.2.3 Multi-Mode Performance Modeling

The polynomial fits introduced earlier encapsulate the compound performance of the engine over the defined subset of operation modes over the admissible power range of the thruster. Therefore, the performance derived from these models (however good the curve fitting is) still results in erroneous and sub-optimal results compared to when the actual discrete modes are employed as is discussed in [39]. This work, therefore, defines the optimal approach for the implementation of the smooth approximate version of discrete modes propulsion modelling. Alternatively, we consider dispensing with the curve fit altogether and ask if we can use PMP to locally select the optimal mode. WE find that invariant embedding with HTS is an attractive way to directly select the optimal mode. An algorithm for selecting optimal discrete modes via invariant embedding is given as a pseudo code below:

Algorithm: Selection of Optimal Discrete Modes

Result: $T = 2\boldsymbol{\eta_m}^\top \boldsymbol{T}_{\text{sel}}$, $\dot{m} = -2\boldsymbol{\eta_m}^\top \dot{\boldsymbol{m}}_{\text{sel}}$
initialize $i = 1$;
while $i \leq N_m$ **do**
  $\boldsymbol{P_w}(i) = 0.5\left[1 + \tanh\left(\frac{P_{\text{av}} - \boldsymbol{P}_{\text{sel}}(i)}{\rho_c}\right)\right]$
  $\boldsymbol{SF}(i) = \frac{\boldsymbol{c}_{\text{sel}}(i)||\mathbb{B}^\top \boldsymbol{\lambda}||}{m} + \lambda_m - 1$
  $\boldsymbol{S_\delta}(i) = 0.5\left[1 + \tanh\left(\frac{\boldsymbol{SF}(i)}{\rho_b}\right)\right]$
  $i = i + 1$
end
$\boldsymbol{S_L} = \boldsymbol{S_\delta} \circ \boldsymbol{P_w}$
$\boldsymbol{S_H} = \dot{\boldsymbol{m}}_{\text{sel}} + \frac{\boldsymbol{T}_{\text{sel}}}{m}||\mathbb{B}^\top \boldsymbol{\lambda}|| - \lambda_m \dot{\boldsymbol{m}}_{\text{sel}}$
$\boldsymbol{S_m} = \boldsymbol{S_H} \circ \boldsymbol{S_L}$
initialize $i = 1$;
while $i \leq N_m$ **do**
  $\boldsymbol{\eta_m}(i) = 0.5\left[1 - \tanh\left(\frac{-1 + \boldsymbol{S_m}(i)}{\rho_m}\right)\right] \prod_{j=1}^{N_m}\left(0.5\left[1 + \tanh\left(\frac{\boldsymbol{S_m}(i) - \boldsymbol{S_m}(j)}{\rho_m}\right)\right]\right)$
  $i = i + 1$
end

In the proposed algorithm, N_m is the number of modes selected out of the 21 modes available

for the SPT-140 thruster, and $\boldsymbol{P}_{\text{sel}}$, $\boldsymbol{c}_{\text{sel}} = \boldsymbol{I}_{\text{sp}_{\text{sel}}} g_0$, $\dot{\boldsymbol{m}}_{\text{sel}}$ and $\boldsymbol{T}_{\text{sel}}$ define the corresponding N_m selected operation modes (expressed as column-wise vectors) for power, I_{sp}, mass flow rate, $\dot{m}$, and thrust taken from Table 3.6. The value of N_m can include all operation modes (21 in this case) or it could represent a fraction of the original set. Selection of operation modes is mission specific, but can be based on 1) power generation capacity due to the solar arrays and power capacity of PPU (P_{max}), and 2) the estimated maximum heliocentric distance encountered during the maneuver. Some lower power (thrust) modes can also be added especially to cater to unforeseen events encountered during the actual mission. In the event that there are several modes that are close to each other, one mode can be selected to reduce chatter in control variables and avoid possible rapid switches between modes. Moreover, from an operational standpoint, having a fewer number of operation modes with negligible performance loss reduces complexity and improves the reliability of the propulsion system. The pseudocode provides a general algorithm for ascertaining the optimal selection of modes (according to PMP) out of N_m modes at each time instant irrespective of the engine used.

Firstly, out of the selected modes, a set of admissible modes are obtained that correspond to lesser power requirement than P_{av}. In other words, at each instant of time during the propagation of the differential equations, only a few (or as a limiting case of all) N_m modes can be activated from a power-availability point of view. But, such a selection (filtering or pruning) has to be achieved in a smooth manner, which is achieved by defining a "distance measure" in the form of power difference (i.e., $P_{\text{av}} - \boldsymbol{P}_{\text{sel}}$). This distance measure is passed as the input argument of the hyperbolic tangent function and the results are stored in the elements of $\boldsymbol{P}_{\boldsymbol{w}}$. The elements of this vector will be either 0 or 1 depending on the power admissibility of the respective mode. In order to have control over the smoothing, a continuation parameter, ρ_c, is introduced for power-driven constraints. We emphasize that the elements of the $\boldsymbol{P}_{\boldsymbol{w}}$ vector belong to the range [0,1] depending on the value of the continuation parameter per definition of the hyperbolic tangent smoothing [51].

A second filtering has to be performed to take into account the standard fuel-optimality criterion. The switching function of each mode is formed and is used as the argument of the hyperbolic

tangent function to obtain the throttling factor for each mode ($\boldsymbol{S_\delta}$). According to how we defined δ, when the switching function is positive, the throttle for that mode is set to 1. However, non-smooth transitions are made smooth by introducing a continuation parameter, ρ_b.

The admissible modes using the above two filtering steps are denoted by $\boldsymbol{S_L}$ vector, which is obtained by using a Hadamard multiplication operator (denoted by $\circ$) on the two vectors, $\boldsymbol{P_w}$ and $\boldsymbol{S_\delta}$. This multiplication step is important step since both factors determine the modes that pass power-admissibility and optimality criteria. According to PMP, if the switching function (SF) is positive, we have to select the mode that results in the least value of the Hamiltonian. The PMP is implemented using the definition of $\boldsymbol{S_H}$ vector. Note that $\dot{m}_{\text{sel}} = T_{\text{sel}}/c_{\text{sel}}$ relation does not necessarily hold as per the data given in Table 3.6. Therefore, it might not be possible to take $\dot{m}_{\text{sel}}$ as a common factor in the expression given in $\boldsymbol{S_H}$. On the other hand, if a common factor can be extracted, $\boldsymbol{S_H}$ will simply become ($\boldsymbol{SF} \circ \dot{\boldsymbol{m}}_{\text{sel}}$).

$\boldsymbol{S_m}$ vector carries mode-wise information of admissibility of a particular mode as well as the contribution of that mode towards the Hamiltonian. As can be seen from the data in Table 3.6, the relation between the power available and the control variables (say, T and $\dot{m}$) is not monotonic. Thus, a sorting scheme is required to isolate the mode that results in the least value of the Hamiltonian. However, the standard sorting and selection strategy is inherently a non-smooth operation. In order to overcome this inherent non-smoothness, a smooth scheme is devised to construct the $\boldsymbol{\eta_m}$ vector. Extraction of the $\dot{m}$ and T is achieved through dot product of $\boldsymbol{\eta_m}$ vector with $\boldsymbol{T}_{sel}$ and $\dot{\boldsymbol{m}}_{sel}$. In order to compensate for the multiplications in the last 'while' loop, a coefficient of 2 is needed. The negative in the mass time rate of change ($\dot{m} = -2\boldsymbol{\eta}_{\boldsymbol{m}}^{\top}\dot{\boldsymbol{m}}_{\text{sel}}$) is needed to make it consistent with the formulation of optimal control problems. In the initial steps of the continuation procedure, and when the continuation parameters are large, all modes may contribute to T and $\dot{m}$. As the value of the smoothing parameters (ρ_c, ρ_b and ρ_m) are reduced, optimal isolated modes emerge autonomously.

A representative example (with four modes) is considered to explain the results after applying the steps outlined above. Four modes are selected from the throttle table, i.e., $N_m = 4$ as

{6,11,13,20}. The following vectors are extracted for the respective modes as

$$\boldsymbol{P}_{\text{sel}} = [4375, 3752, 3460,3008]^\top, \;\; \boldsymbol{c}_{\text{sel}} = [1790, 1617, 1099, 1579]^\top g_0, \;\; \dot{\boldsymbol{m}}_{\text{sel}} = [14, 13.9, 17.1, 11.4]^\top.$$

In order to evaluate the expressions, the following values are considered: $m_0 = 2400$ kg, $\lambda_m = 0.89$, $||\mathbb{B}^\top \boldsymbol{\lambda}|| = 88500$, $P_{\text{av}} = 4$ kW, and $\rho_b = \rho_c = \rho_m = 1.0 \times 10^{-5}$. For these values and upon following the steps outlined above, the algorithm will lead to the following vectors

$$\boldsymbol{P}_w = [0, 1, 1, 1]^\top, \;\; \boldsymbol{SF} = [0.0191, 0.0081, -0.0325, 0.0044]^\top, \;\; \boldsymbol{S_\delta} = [1, 1, 0, 1]^\top,$$
$$\boldsymbol{S_L} = [0, 1, 0, 1]^\top, \;\; \boldsymbol{S_m} = [0, 0.1126, 0, 0.0502]^\top, \;\; \boldsymbol{\eta_m} = [0, 0.5, 0, 0]^\top.$$

Therefore, mode #11 gets selected as per the algorithm for this simple example. $\dot{m}$ and T values of mode #11 will be used until the next switch in the operation mode or shut-down of the thruster occurs due to optimality criterion since all elements of $\boldsymbol{\eta_m}$ will be zero in such situations.

The smooth representations of the discontinuous control variables (δ, c,P_{av}) introduced during the OCP formulation are obtained in this section using the CSC method.

Throttle: Throttling factor, δ, that represents the bang-bang structure of the thruster due to the throttle "on" and "off" conditions, plays the same role in all three propulsion formulations. $\delta(\in [0, 1])$, in this study, is the product of three different δ values. Each one of the throttling factors corresponds to a different discontinuous event as given below

$$\delta = \delta_b \delta_f \delta_k, \tag{3.30}$$

where δ_b ($\in [0, 1]$) is decided as per the optimality criteria of minimizing the Hamiltonian according to PMP. δ_f ($\in [0, 1]$) enforces any desired coast arcs at the points during mission critical events or for orbit determination purposes and are decided apriori. δ_k ensures that the thruster is not operated when P_{av} is less than the rated minimum operational power of the thruster. Each of these

δ coefficients leads to a bang-bang structure, which requires smoothing to obtain:

$$\delta_b^* \approx \delta(SF, \rho) = 0.5 \left[1 + \tanh\left(\frac{SF}{\rho_b}\right)\right], \tag{3.31a}$$

$$\delta_f = 0.25 \left[1 + \tanh\left(\frac{t_{\text{start}} - t}{\rho_f}\right)\right] \left[1 - \tanh\left(\frac{t_{\text{end}} - t}{\rho_f}\right)\right], \tag{3.31b}$$

$$\delta_k = 0.5 \left[1 + \tanh\left(\frac{P_{\text{av}} - P_{\text{min}}}{\rho_k}\right)\right], \tag{3.31c}$$

where t_{start} and t_{end} denote the beginning and end time stamps of the forced coast arcs. Most thrusters also have a minimum operational power requirements below which they cannot operate, which is denoted here as P_{min}. Also, δ_k takes into account the lack of power to switch the thruster On. The smoothing procedures for exhaust velocity and power can be followed from previous section. Each of the smoothing parameters (i.e., ρ_i ($i \in p, c, b, f, k, m$) corresponds to one parameter family of sub-problems (each sub-problem corresponds to solving a TPBVP) that is arbitrarily near a neighbouring converged solution.

A summary of the difference in propulsion modelling (in terms of $\dot{m}$, T and c) in all three cases is provided in Table 3.7. These three control variables are substituted in the Hamiltonian (Eq. (3.36)) to formulate the OCP.

Table 3.7: Summary of the control inputs and the form of SF for the three propulsion modelling approaches.

	VIVT	Polynomial	Multi-Mode
T =	$\frac{2\eta P_{\text{av}}}{c}\delta$ (Eq. (2.22))	$\sum_{i=0}^{n_T} c_{T_i} P_{\text{av}}^i \delta$, (Eq. (3.27))	$2\boldsymbol{\eta}_m^\top \boldsymbol{T}_{\text{sel}}$
$\dot{m}$ =	$-\frac{2\eta P_{\text{av}}}{c^2}\delta$, (Eq. (2.22))	$-\sum_{i=0}^{n_m} c_{m_i} P_{\text{av}}^i \delta$ (Eq. (3.27))	$-2\boldsymbol{\eta}_m^\top \dot{\boldsymbol{m}}_{\text{sel}}$
c =	Eq. (3.9)	$\frac{T}{\dot{m}}$	c $\in$ Selected Modes
SF =	$\frac{\|\|\mathbb{B}^\top \boldsymbol{\lambda}\|\| c_{\text{max}}}{m} + \lambda_m - 1$	$\frac{\|\|\mathbb{B}^\top \boldsymbol{\lambda}\|\| c}{m} + \lambda_m - 1$	$\frac{\|\|\mathbb{B}^\top \boldsymbol{\lambda}\|\| c}{m} + \lambda_m - 1$

3.2.3 Results

The transfer from Earth to asteroid Psyche via Mars gravity assist (E-M-P) is solved using the three considered formulations for propulsion model for the SPT-140 engine. In the VIVT modelling, the power range of the engine is taken into account. The three cases are to maximize the final mass using PF1) a VIVT modelling, PF2) a polynomial-based modelling, and PF3) an exact multi-mode modelling.

Table 3.8: Spacecraft parameters used for the three test cases.

	P_{BL} (kW)	P_{max} (kW)	P_{min} (W)	PL (W)	I_{sp} range (s)	η	η_d	σ
PF1	20	4.65	1.514	780	[925-1800]	0.68	0.95	0.02
PF2	20	4.65	1.514	780	[925-1800]	0.68	0.95	0.02
PF3	20	4.375	1.514	780	[925-1929]*	[0.24,0.49]*	0.95	0.02

*As per Table 3.6.

Canonical units are used for scaling where AU is used for scaling distances, and the Time Units (TU) is equal to $\frac{1}{2\pi}$ year. The ephemerides of the concerned celestial bodies are taken from JPL DE435 and JPL AST343DE430 files. As explained before, the hybrid optimization is solved with the PSO in the outer-solver, while the inner-solver seeks to solve the resulting TPBVP for each of the thruster modelling. A single-shooting scheme is used to solve the resulting TPBVPs using MATLAB's *fsolve*. The initial guesses for the unknown costate vector $\boldsymbol{\lambda}(t_0) = [\lambda_p, \lambda_f, \lambda_g, \lambda_h, \lambda_k, \lambda_l]^\top$ and λ_m are generated randomly and the TPBVP is solved followed by continuation of the five parameters, ρ_b, ρ_p, ρ_c, ρ_m, ρ_f, and ρ_k. The spacecraft parameters used in the considered problems are obtained according to Table 3.6 and the resulting bounds on the parameters of power modelling are summarized case-wise in Table 3.8. According to Table 3.9, coast arcs are enforced at three places: one immediately after launch, one prior to flyby and one immediately after flyby. The bounds on the PSO design variables are defined in Table 3.10. These bounds are selected based on the Psyche mission constraints.

Table 3.9: Design parameters for the E-M-P mission.

Launch window (t_0)	2020-2021
Time of flight (Δt)	3.5 – 5.2 years (Illumination at Psyche dictates arrival time)
Initial mass range (kg)	2600 – 2900
Sequence considered	Earth-Mars-Psyche
Coasts required	$\geq$ 90 days post launch and $\geq$ 60 days pre and >15 days post flyby
Minimum altitude at GA (km)	500
Propellant used (kg)	$<$ 950
Engine	SPT-140 (Hall thruster)
Launch vehicle	Falcon Heavy R
Launch V_∞ (km/sec)	5.37 – 5.49

Psyche is the largest metal asteroid in our solar system and is a target body in a planned future NASA mission. The science objective of the mission is to map the surface of the asteroid for 19 to 20 months conducted in 4 stages of decreasing altitude [33]. The illumination of the surface of the asteroid is one of the important criteria to attain the required science objectives. Figure 6 in Ref. [34] uses a gray-scale map to depict the percentage of the surface of Psyche illuminated during 2021 to 2032 time interval. Arrival at the beginning of the white patches (i.e., illumination $\geq 90\%$) is ideal. The trajectory for the mission is designed by NASA JPL using a high-fidelity tool, MYSTIC. A number of mission boundary conditions and constraints that are used in setting up this example are summarized in Table 3.9.

According to the reported trajectories in Refs. [33] and [34], the initial mass of the spacecraft is kept within the range [2600, 2900] kg with the constraint on the propellant consumption to be less than 950 kg. Depending on the specified range of initial mass desired post launch, a range of v_{∞_L} values is considered (see Table 3.9) as per the performance of the chosen launch vehicle, Falcon Heavy Reusable. In order to approach Psyche close to the optimal lighting conditions (white patches in Figure 6 in Ref. [34]), the bounds on the PSO design variables like launch time and time of flight are determined and reported in Table 3.10.

As expected, the value of the final mass delivered to Psyche is heavily influenced by the rigor

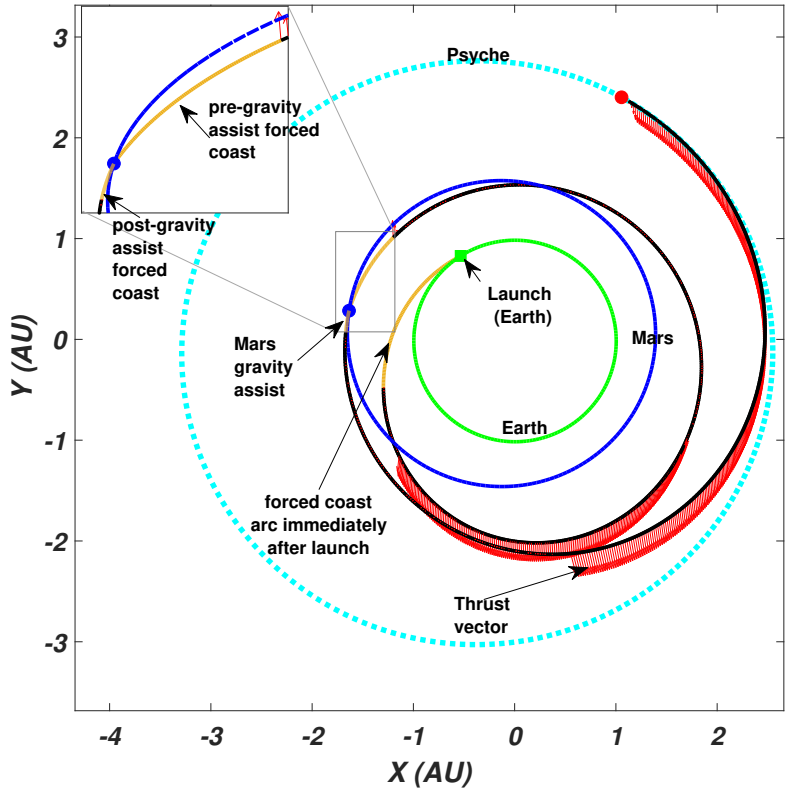

Figure 3.17: The optimal VIVT trajectory. Trajectories obtained using other propulsion modelling are graphically identical.

Table 3.10: Design variables of the PSO with bounds and the final converged solution.

	Bounds	Solution
Launch date	[1.1.2020 - 5.31.2021]	Jan 23rd, 2021
E-M Δt (days)	[500, 850]	800.01
M-P Δt (days)	[500, 900]	850
B-plane piercing γ (rad)	$[-\pi, \pi]$	0.693
r_p ($\times$ Mars radius)	[1.147, 4]	1.147 (altitude 500 km)
α (rad)	$\left[-\frac{\pi}{2}, \frac{\pi}{2}\right]$	-1.115
β (rad)	$[-\pi, \pi]$	0.1244
flyby v_∞ (km/sec)	[1, 10]	4.108
$v_{\infty,L}$(km/sec)	[5.37, 5.49]	5.376
α_L	$[-\pi, \pi]$	-2.499
β_L	$\left[-\frac{\pi}{2}, \frac{\pi}{2}\right]$	-0.08

of the approach taken to model the SPT-140 thruster. However, since on a solar scale, there is not much visible difference among the trajectories except for the thrust profile, the trajectory shown in Figure 3.17 can be considered as a qualitative depiction for all three problems. The time duration of the forced coast arc immediately after launch is set to 90 days. However, the thruster does not operate for an additional 40 days (due to optimality and proper phasing). The time duration of the forced coast arcs before and after the flyby are set to 60 and 15 days, respectively, which is enforced using Eq. (3.31b).

The differences in the profile of thrust and I_{sp} are detailed for each case in the form of three subplots containing the osculating true anomaly (θ), thrust profile, T_{av}, and I_{sp} profile. Here, T_{av} denotes the thrust that is computed using the available power, P_{av}. The thrust profile subplots feature the optimal thrust profile (T_{av}) along with three dashed lines that correspond to T_{min}, T_{max} and T_{op} defined as

$$T_{\text{min}} = \frac{2\eta P_{\text{av}}}{c_{\text{max}}}, \qquad T_{\text{op}} = \frac{2\eta P_{\text{av}}}{c_{\text{opt}}}, \qquad T_{\text{max}} = \frac{2\eta P_{\text{av}}}{c_{\text{min}}},$$

where c_{opt} is defined in Eq. (3.26) for PF1. T_{op} is the same as T_{av} for PF3 and T_{op} is not evaluated for the PF2 case. For PF2 and PF3, T_{min} and T_{max} denote the minimum and maximum thrust entries within the considered modes. The plots do not include the time of coasting post launch but the coast arcs enforced before and after the flyby are evident in Figures 3.18 and 3.19. The thrust histories of the two segments are denoted by solid blue color lines. The typical values for all smoothing parameters used to obtain the final result is less than 1.0×10^{-5}.

3.2.3.1 PF1: VIVT Modelling

After several runs and iterations of the hybrid optimizer with PSO and inner solver with PF1 modelling, the values for the converged solution are reported in Table 3.10. In Figure 3.18, we observe that the applied thrust magnitude (T_{av}) always follows T_{min} since the optimal exhaust velocity required to extremize the Hamiltonian is always greater than c_{max}. This is typically observed when the time of flight is long enough to allow minimum thrusting at all times to rendezvous with

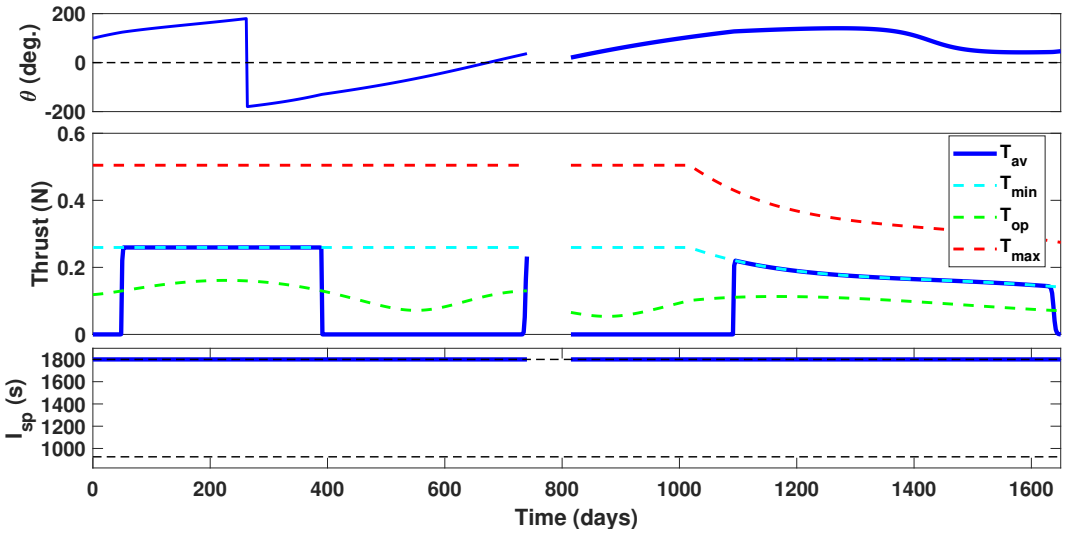

Figure 3.18: PF1: Time histories of the osculating true anomaly, thrust profile and specific impulse.

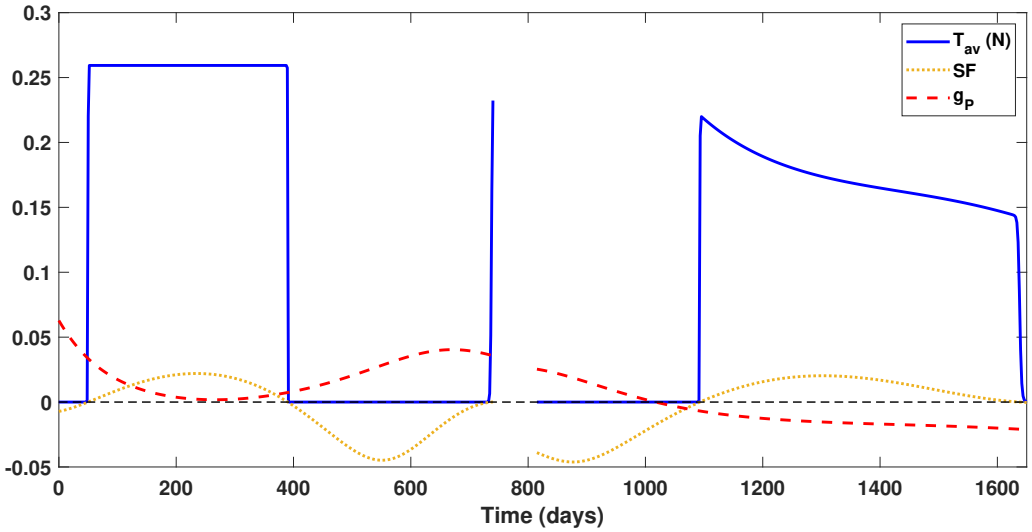

Figure 3.19: PF1: Thrust profile, power activation constraint and switching function vs. time; SF and g_P are both normalized by 10000 for better visibility of thrust profile.

the target asteroid. If one reduces the time of flight of mission (as a constraint), switching in the exhaust velocity profile will appear. The observed discontinuities in the osculating true anomaly and thrust profile are due to gravity assist and the forced coast arcs. The flight time is 4.76 years with final mass delivered, $m_f \sim 1965$ kg and the propellant bill of $\sim$ 890 kg (<950 kg constraint (see Table 3.9)).

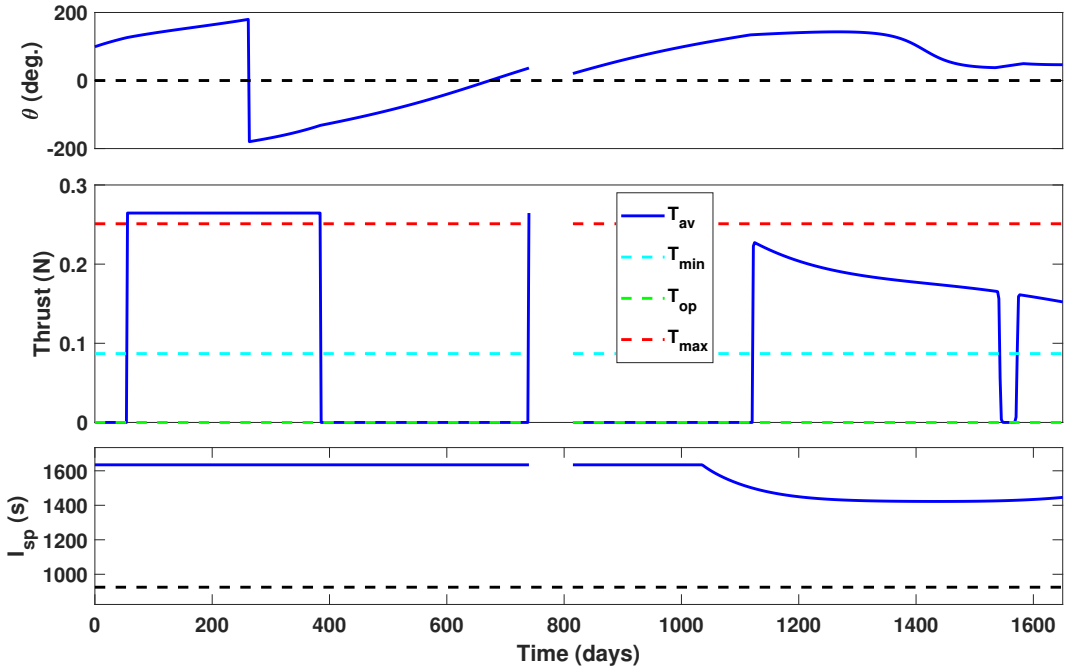

Figure 3.20: PF2: Osculating true anomaly, thrust profile, and specific impulse vs. time.

The g_p plot in Figure 3.19 shows how power generated by the solar arrays (P_{SA}) in the first segment (E-M) is always high enough to allow maximum PPU operating power (P_{max}) be available for thrusting. The converged solution of PF1 in terms of boundary conditions is used for initial iterations for both PF2 and PF3 propulsion models. In other words, for PF2 and PF3, only the inner-level solver of the hybrid optimizer is used to optimize the solutions for different propulsion models and determine fuel-optimal trajectories. This ensures a fair comparison between the three propulsion modeling approaches. VIVT modeling provides greater (than typical low thrust)

amenability towards flexible time of flights to provide optimal solutions and optimal I_{sp} time histories. This is one of the primary reasons for using this modeling to determine the boundary conditions (launch date, time of flight for each segment and other parameters). The coefficients of the polynomials derived to evaluate thrust and $\dot{m}$ as a function of P_{av} are given in Table 3.5.

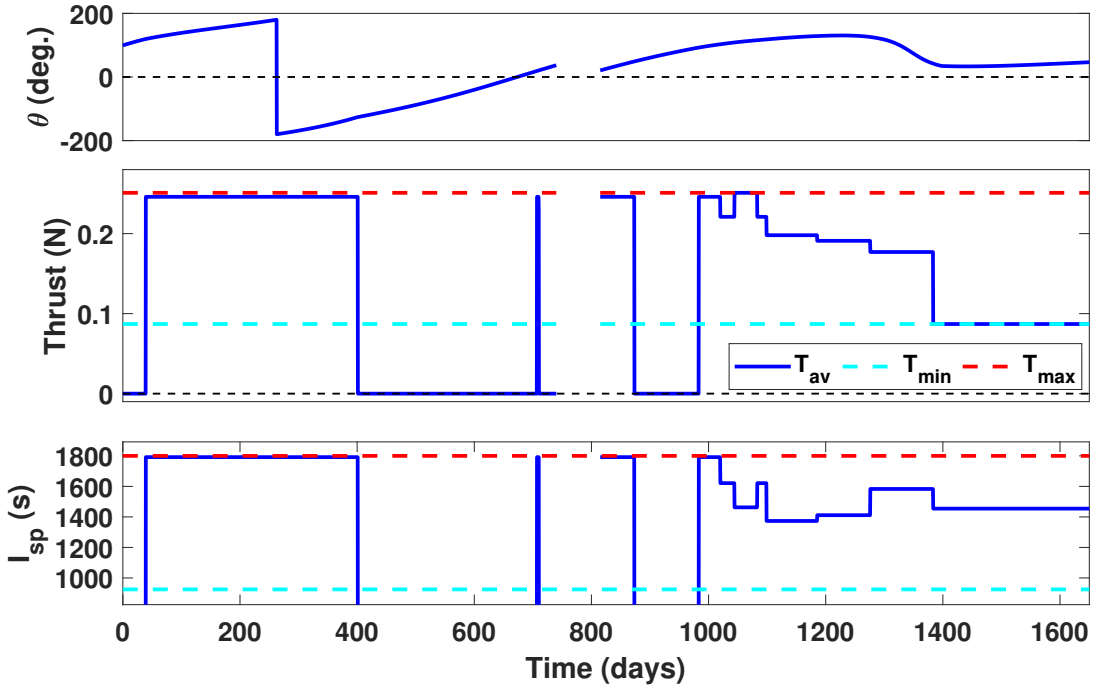

Figure 3.21: PF3: Osculating true anomaly, thrust, and I_{sp} vs. time; the gaps in the I_{sp} profile at the time of coasting denote undefined values.

3.2.3.2 PF2: Polynomial-Based Modelling

In case of PF2, the polynomial approximation gives inferior final mass as compared to PF1, partly due to the specific dependencies (operation modes) of the thrust and mass flow rate on power. Also, due to errors in the polynomial approximation the actual engine behaviour is not as accurately captured compared to PF3. The thrust profiles for PF1 and PF2 look very similar but the thrust magnitude in case of PF2 is higher in the first segment (Earth-to-Mars phase) and lower

in the second segment (Mars-to-Psyche phase) as compared to PF1. In the second segment, when the power generated by solar arrays is especially low at the end of the maneuver, the interpolated approximation of a lower-I_{sp}, high-thrust mode is engaged. In Figure 3.20, the I_{sp} value smoothly declines as the spacecraft rendezvous with Psyche. Since polynomial-based approximations of $\dot{m}$ and T only capture the aggregate behaviour of the individual operation modes and is an approximation of the discrete an disjoint engine modes, slight violation is observed in thrust profile relative to the actual maximum thrust limit, $T_{\text{max}} = 0.251$ N. Recall that these bounds correspond to the actual minimum and maximum thrust limits according to Table 3.6.

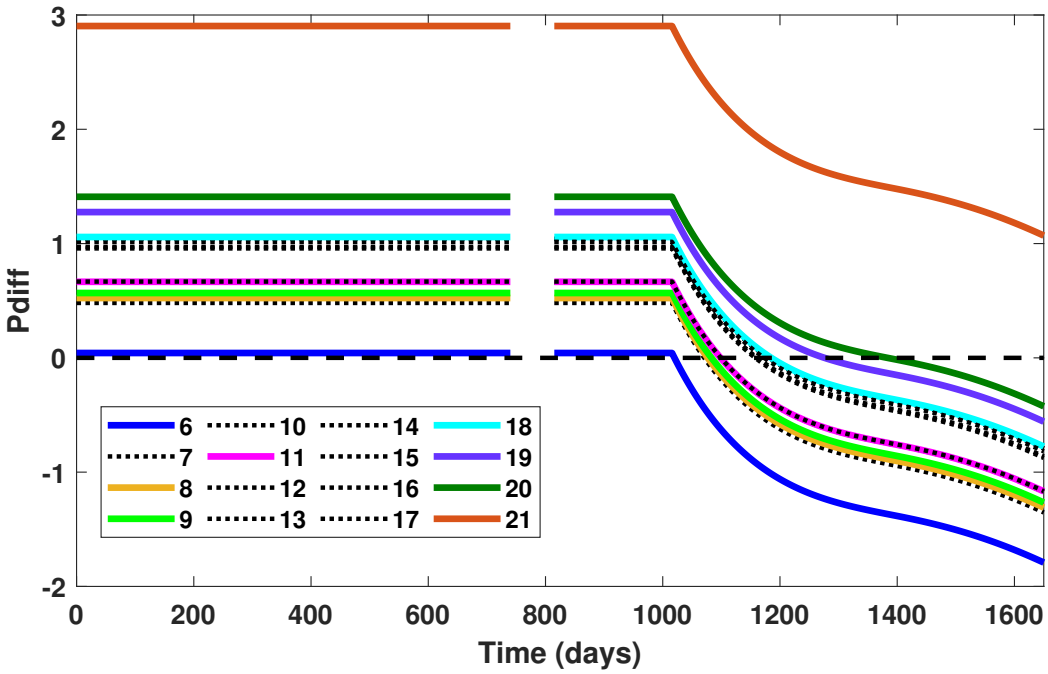

Figure 3.22: PF3: Plot of power differential function ($P_{\text{av}} - P_{\text{sel}}$) in kW corresponding to each mode vs. time.

3.2.3.3 PF3: Multi-Mode Modelling

In case of PF3, Figure 3.21 shows that the thrust profile features several switches since different operation modes are engaged. As the spacecraft steers farther from the Sun, low-power modes are

engaged (cf. Table 3.11 sorted as per power). Since Table 3.6 is arranged in descending order of the operating power, all the modes below a power admissible mode are also power admissible. Specifically, Figure 3.22 shows that during the first 1000 days, all the operation modes except for the first 5 modes are admissible from a power-availability standpoint. The SF associated with each mode governs the engagement of each mode. As seen in Figure 3.23, there are three intervals during which the SF value for all modes is negative. This occurs during the first ~ 40 days at the beginning of the first segment (a late departure), close to the end of the first segment ($\sim$[440-620] days), and near the beginning of the second segment ($\sim$[900-980] days). And these time intervals correspond to the coast arcs appearing in the thrust profile shown in Figure 3.21.

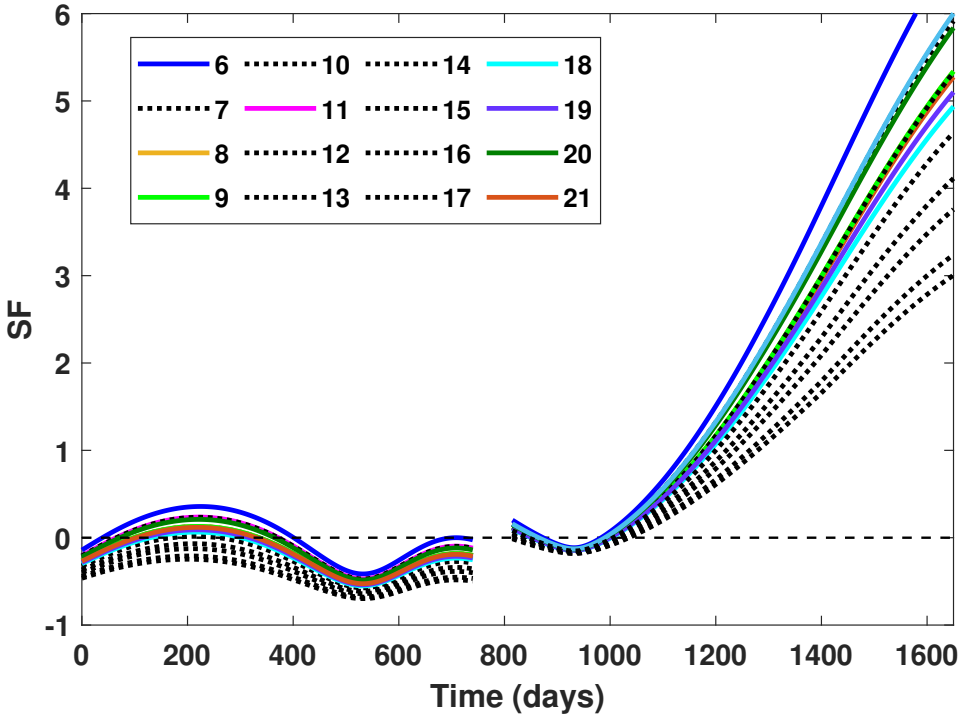

Figure 3.23: PF3: Plot of switching function (SF) corresponding to each mode vs. time.

The power availability and SF decide only the admissibility of a certain mode and do not guarantee optimality. According to PMP, the optimal mode is dictated by the minimization of the

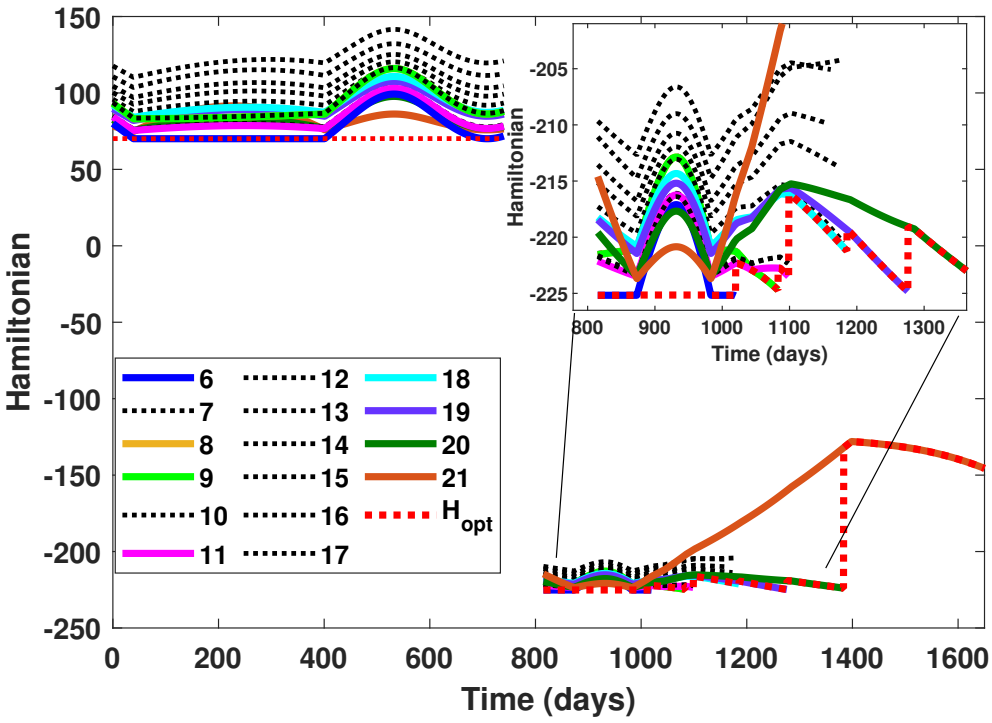

Figure 3.24: PF3: Plot of Hamiltonian corresponding to each mode vs. time.

Hamiltonian function, which is plotted in Figure 3.24 (red dashed line is the optimal Hamiltonian plot). At times even when the 6^{th} mode minimizes the Hamiltonian the most, it is not admissible from the power criteria, leading to engagement of other lower power modes. Therefore, the optimal mode selection is made using the Hamiltonian function in Figure 3.24 *only from the set of the power-admissible operation modes* determined from Figure 3.22.

Therefore, simultaneous study of the data in all three plots; Figures 3.22, 3.23, and 3.24 is required to determine which mode is most optimal to select. For example, in Table 3.6, one can see that the highest mass flow rate and the lowest I_{sp} (leading to $SF < 0$) is associated with the 14^{th} mode, a combination of which results in a higher Hamiltonian value than its neighbouring modes. Therefore, the 14^{th} mode is never engaged. In fact, for most cases the feature of extremely low I_{sp} alone is enough for the non-selection of those modes due to the $SF < 0$ condition. Nevertheless, modes with lower I_{sp} values can still get selected if no better mode is power admissible. Owing to the limited power availability at greater distance from the Sun, i.e., towards the end of the trajectory,

the 20^{th} and 21^{st} modes get engaged. From Table 3.6, notice that the 7^{th}, 8^{th} and 9^{th} modes possess similar operation characteristics (i.e., with respect to thrust, mass flow rate and I_{sp}). Therefore, one can possibly select one mode out of the three with little (to near zero) sacrifice in optimality for all the times when $P_{\text{av}} \geq 3.937$ kW. For further explanation, all the 'integral' modes are listed

Table 3.11: Selected Operation Modes of SPT-140 for E-M-P mission.

#	Group	Power (Watts)	Thrust (mN)	$\dot{m}$ (mg/s)	I_{sp} (sec)	η
6	G2	4375	246	14	1790	0.49
8	G2	3894	251	17.5	1464	0.46
9	G2	3850	251	17.5	1464	0.47
11	G3	3752	221	13.9	1617	0.47
18	G5	3360	198	14.7	1371	0.4
19	G5	3142	191	13.8	1409	0.42
20	G5	3008	177	11.4	1579	0.46
21	G5	1514	87	6.1	1449	0.41

in Table 3.11. The selection of these 8 'integral' modes out of all the modes can be understood by comparing the selected modes with their neighbours in Table 3.6. For better understanding, we have classified all the modes in 5 groups:

1. G1: {#1, #2, #3, #4, #5}

   These modes require the highest power to operate among all the operating modes. Owing to the set value of P_{max} and η_d, these modes are never power admissible and hence are never selected.

2. G2: {#6, #7, #8, #9}

   Among these modes, the 6^{th} mode possesses the highest I_{sp} value, but has a lower $\dot{m}$ value. This combination somehow leads to the selection of 6^{th} mode over modes 8^{th} and 9^{th} whenever all of them are power admissible. In this particular trajectory optimization example, mode 7^{th} is never selected over modes 8^{th} and 9^{th} due to its lower I_{sp} and same value for $\dot{m}$.

3. G3: {#10, #11, #12}

   The modes appearing in this group are associated with very close operating power requirements. The 11^{th} mode is evidently more superior to modes #10 and #12 owing to its higher I_{sp} and $\dot{m}$ values.

4. G4: {#13, #14, #15, #16, #17}

   All modes in this group feature lower I_{sp} values (compared to other groups). Also, the operating power requirement for the modes in this group is close and accounts for a small range of (~ 84 W). Therefore, the selection of these modes seem less likely.

5. G5: {#18, #19, #20, #21}

   This group features moderate I_{sp} values and have the lowest operating power requirement among all the modes. The selection of these modes can be anticipated to be mostly driven by low power availability.

Needless to say, this qualitative analysis was possible only after obtaining an optimal solution and is not generally intuitive enough to provide mode selection with certainty prior to the optimization. The mode selection process is a complicated function of time and the distance from the Sun. As can be seen from Table 3.11, the optimal modes selected belong to Groups 2 and 5 for majority of the time duration.

Table 3.12: Comparison of results of the Earth-Mars-Pysche problem using VIVT, polynomial and optimal discrete modes propulsion models using an SPT-140 thruster.

	VIVT	Polynomial	Discrete Modes
T_{peak} (N)	0.2693	0.258	0.251
$I_{\text{sp}_{\text{avg}}}(s)$	1800	1744	1625.16
m_f (kg)	1964.7	1833.7	1718.9

Although the power available for thrusting in all three cases (PF1, 2, and 3) is almost the same (there are only minor differences in the three trajectories), they result in significant differences

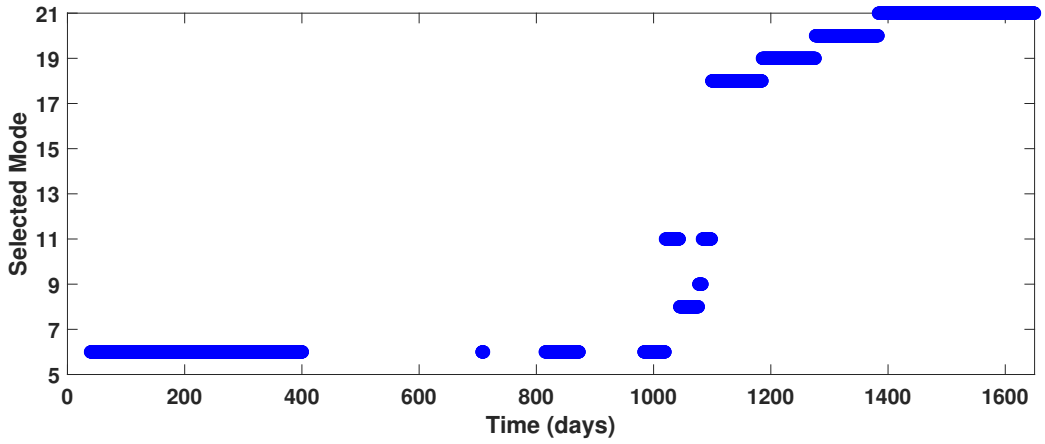

Figure 3.25: PF3: Optimal thrust mode selection vs. time.

in final masses (131 kg less for PF2 and 245.8 kg for PF3 as compared to PF1) owing to their different thrust and mass flow rate adaptations of the same engine. Table 3.12 compares PF-1,2,3 on the basis of maximum thrust (T_{peak}), average I_{sp} ($I_{\text{sp}_{\text{avg}}} = (\Sigma_t I_{\text{sp}}(t))/\Delta t$), and final mass. VIVT modelling features highest values for both $I_{\text{sp}_{\text{avg}}}$ and T_{peak}. In fact, curiously the trend in the $I_{\text{sp}_{\text{avg}}}$ and T_{peak} for the three cases is same as the trend in the final mass achieved. The power model parameters are kept the same for all the evaluations reported in Table 3.12.

It should be clear that the VIVT trajectory design was merely a first step to efficiently establish insights and a ballpark set of initial co-states to initiate the polynomial and discrete mode trajectory designs. Note the VIVT trajectory is not physically realizable. Likewise, the polynomial model of the discrete modes is provided for comparison owing to its frequent use in literature. It is shown to not accurately capture the engine operational modes. However, it provides even better initial costate estimates for the optimal discrete mode trajectory design. Only the optimal discrete mode solution is fully consistent with the SPT-140 thruster nodes. This success in solving such a tremendously challenging problem indicates the improved capability of indirect based methods in handling discrete control variables.

3.3 Discrete Modes Multi-disciplinary Design Optimization [3]

Typical systems engineering processes focus on hierarchical decomposition of design and development tasks. Such approaches offer a very linear structure of simple relationships, but are quickly overwhelmed by system interactions in complex systems. By solving a Multidisciplinary Design Optimization (MDO) problem designers can simultaneously improve the design and reduce the time and cost of the design cycle [111] early in the design process. In space mission design, spacecraft consists of several sub-systems and their performance is typically coupled. For instance, the power sub-system produces power for operation of other sub-systems as well as the power needed to operate the thrusters. In case of Solar Electric Propulsion (SEP), power generated by solar arrays, which is a function of distance of the spacecraft from the Sun, affects the performance of the thruster [112]. The presence of power cross coupling between independent units of the spacecraft system inspires the use of co-optimization techniques and calls for appropriate numerical simplifications to optimize these complex spacecraft sub-systems over both continuous and discrete design variables [113]. As shown in the previous section and Figures 3.21 to 3.25, the frequently disjoint set of experimentally characterized modes in case of gridded-ion engines, especially if there is a large number of modes, defy any heuristic idea of the resulting performance of the engine.

Payload-mass optimization introduces further complexity to the optimization task because the power (which serves as one of the admissibility criteria for the selection of modes) is predominantly affected by the size of the solar arrays and the trajectory of the spacecraft (distance from the Sun vs time). Thus, we are faced with a co-optimization or MDO problem in which the spacecraft design parameters and the trajectory are coupled and in the most rigorous approaches, must be optimized simultaneously. The size (area) of solar arrays is a continuous variable, whereas the operating modes of a particular low-thrust engine are discrete. In addition, the trajectory optimization problem consists of characterizing the optimal direction of the thrust vector, with the

[3] Reprinted with permission from "Electric thruster mode-pruning strategies for trajectory-propulsion co-optimization" by Arya, Vishala and Taheri, Ehsan and Junkins, John L, 2021. Aerospace Science and Technology, Volume 116, 106828, Copyright 2021 by Elsevier

possibility of switching the thruster ON and OFF per optimality criterion. Using indirect methods, the optimal control problem (OCP) becomes a multi-point boundary-value problem, the solution of which characterizes the exact sequence of the optimal thrust modes. Without making any apriori assumptions, the algorithm proposed here reveals the subset of all considered modes essential for optimizing the cost functional (i.e., to maximize the net payload mass). While obtaining the set of optimal operating modes is insightful, one question has to be addressed: Is it possible to prune the set of optimal modes to establish sub-optimal solutions with a modest sacrifice on optimality? A major contribution of this work is to answer the mentioned question by proposing a mode-pruning algorithm that reveals the impact of removing certain modes from the set of *optimal* modes. This mode-pruning algorithm allows sub-optimal modelling of the trajectory-spacecraft system with a controlled loss in optimality and thereby offers the possibility of trading performance versus system complexity.

3.3.1 Problem Formulation

We use a set of modified equinoctial elements (MEEs), $\boldsymbol{x} = [p, f, g, h, k, l]^\top$ and spacecraft mass, m as state variables to formulate the equations of motion as

$$\dot{\boldsymbol{x}}(t) = \boldsymbol{f}(\boldsymbol{x}, \boldsymbol{a}) = \boldsymbol{A}(\boldsymbol{x}, t) + \mathbb{B}(\boldsymbol{x}, t)\boldsymbol{a}, \tag{3.32}$$

where, $\boldsymbol{a} = T\delta\hat{\boldsymbol{\alpha}}/m$ denotes the propulsive acceleration expressed in the Local-Vertical/Local-Horizontal (LVLH) frame of the spacecraft. The value of the thrust at any instant depends on the operating mode chosen thus providing a saw-tooth like acceleration profile. The time rate of change of mass depends on the selected mode as

$$\dot{m} = -\dot{m}(mode), \tag{3.33}$$

Spacecraft system: A simplified breakdown of the spacecraft sub-systems for the purpose of co-optimization is assumed in this work similar to Section 3.1 and is described in Figure 3.26. The

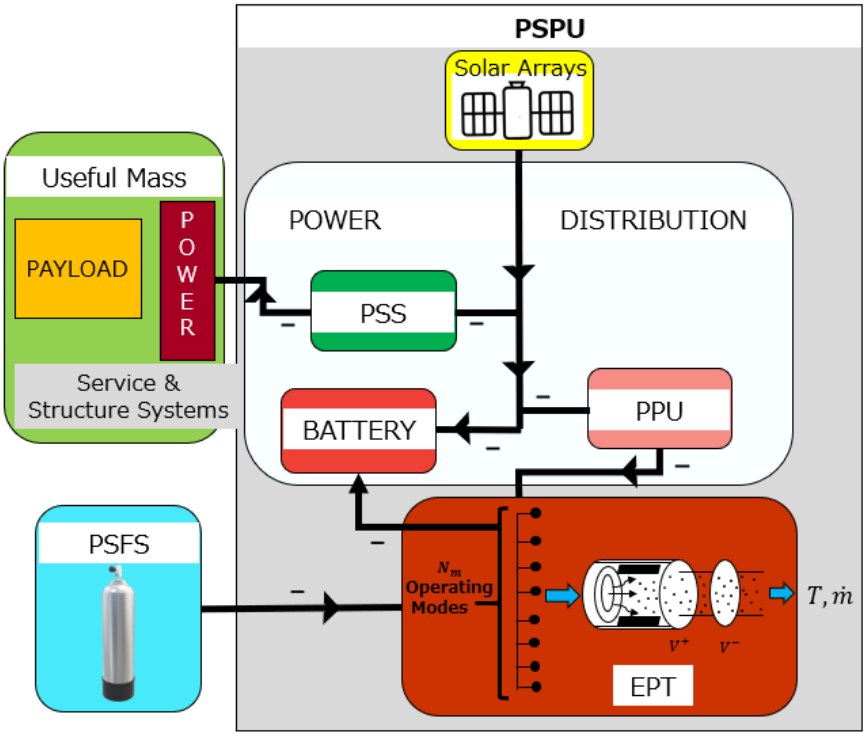

Figure 3.26: Payload and propulsion sub-system mass breakdown.

useful payload mass is generally comprised of a primary payload and a part of the power supply system (PSS), which is essential for payload sustenance and operations [**?**]. Assuming a constant initial mass, m_0 (held fixed in this work, though it can be swept to reveal a family of optimal designs), the mass breakdown can be written as

$$m_0 = m_u + m_{\text{PSPU}} + m_{\text{PSFS}}, \tag{3.34a}$$

$$m_u = m_0 - \gamma_1 P_{\text{BL}} - \gamma_2 P_{\text{max}} - (1 + a_{\text{tk}}) m_p, \tag{3.34b}$$

Notice that when compared to the Eq. (3.1b) in Section 3.1, P_{max} in the place of P_{av} is used in the above equation as the engine modes of an ion-gridded thruster are operable at a specific and the PPU are designed such that the P_{max} value is greater than the maximum power requirement of any available mode. Therefore, it is more reasonable to use P_{max} in the equation as P_{av} could be way larger than P_{max}. As can be observed in Table 3.6 [3], every operating mode is associated with

a corresponding thrust, T, specific impulse, I_{sp}, mass flow rate, $\dot{m}$, and thruster efficiency, η and a specific operating power. Depending on the power requirement of the optimal mode selected at each time instant, there can be some excess power that can be stored in a battery. In practical applications of course, the thruster might not perform exactly as given in the tabulated data presented in Table 3.6 retaining some excess power and propellant mass offers margins to take these uncertainties into account via guidance (see covariance control in Chapter 4). Engine failures, variation in engine performance and missed-thrust events are not considered in this section.

3.3.2 Maximum-Payload-Mass Optimal Control Problem

The objective is to maximize the net delivered payload mass over all admissible operation modes. The problem is stated as a minimization of a Lagrange-form cost functional as

$$\underset{\text{modes, } \hat{\boldsymbol{\alpha}},\delta,\ P_{\text{BL}}}{\text{Minimize}} \quad J = \int_{t_0}^{t_f} \left[\frac{\gamma_1 P_{\text{BL}} + \gamma_2 P_{\text{max}}}{\Delta t} + (1 + a_{\text{tk}})\dot{m} \right] dt,$$

$$\text{subject to :}$$

$$\begin{aligned} &\text{Equations (2.6)\&(3.33)}, \\ &\boldsymbol{x}(t_f) - \tilde{\boldsymbol{x}}_d = \mathbf{0}, \\ &\boldsymbol{x}(t_0) = \boldsymbol{x}_0, m(t_0) = m_0, \\ &P_{\text{max}} = P_{\text{m}}, \end{aligned} \tag{3.35}$$

where t_0 is the initial time, $\boldsymbol{x_0}$ and m_0 are the initial MEEs and mass of the spacecraft at the initial time (t_0), t_f is the final time, $\Delta t = t_f - t_0$ is the time of flight, and $\tilde{\boldsymbol{x}}_d$ is the desired MEEs at the final time. P_m is the mission-defined maximum power capacity of the PPU. Note that the term $\gamma_2 P_{\text{max}}$ in the cost functional is a known constant and can be removed from the Lagrange cost without affecting the optimal solution. T and $\dot{m}$ are evaluated at each time instant such that the Hamiltonian is minimized over the admissible controls and admissible modes (see Eq. (3.36)).

The Hamiltonian associated with the defined OCP can be written as

$$H = \gamma_1 P_{\text{BL}}/\Delta t + (1 + a_{\text{tk}})\dot{m} + \boldsymbol{\lambda}^\top \boldsymbol{f} - \lambda_m \dot{m}, \tag{3.36}$$

where $\boldsymbol{\lambda} = [\lambda_p, \lambda_f, \lambda_g, \lambda_h, \lambda_k, \lambda_l]^\top$ is the costate vector associated with the MEEs and λ_m is the costate associated with mass. The direction of thrust vector, $\hat{\boldsymbol{\alpha}}$ and throttle, δ, has to be determined using PMP. Costates dynamics are derived by the Euler-Lagrange equation, $\dot{\boldsymbol{\lambda}} = -[\partial H/\partial \boldsymbol{x}]^\top$, $\dot{\lambda}_m = -\partial H/\partial m$ $\dot{\lambda}_{P_{\text{BL}}} = -\partial H/\partial P_{\text{BL}}$. Payload-mass optimization inducts an additional design variable, P_{BL}, to size the solar arrays as per the power requirements of the mission. Higher capacity solar arrays (with large P_{BL} values) facilitate the admissibility of the higher power modes but leads to increase in the mass of the solar arrays. Therefore, an optimization can be performed to ultimately lead to maximum payload mass delivery.

In order to incorporate mass of solar arrays into the optimization process, the state vector is augmented by P_{BL} resulting in a modified state vector, $\boldsymbol{z}^\top = [\boldsymbol{x}^\top, m, P_{\text{BL}}]$. Since P_{BL} remains constant throughout the trajectory, the state dynamics is augmented by a trivial additional differential equation ($dP_{\text{BL}}/dt = 0$) and by virtue of P_{BL} being free at both initial and final times, the corresponding transversality conditions $\lambda_{P_{\text{BL}}}(t_0) = \lambda_{P_{\text{BL}}}(t_f) = 0$ are obtained. Additionally, $\lambda_m(t_f) = 0$ since spacecraft mass, $m(t_f)$, is also free at final time. The optimal performance of the engine in terms of T and $\dot{m}$ and the optimal throttle condition (δ) are determined using PMP over the admissible modes and are dealt with in detail in the next section.

3.3.3 Mode Optimization with Discrete Modes

The engine considered in this work is an SPT-140 Hall thruster and it has a total of 21 operating modes (see Table 3.6). The mathematically smooth but ultimately near instantaneous switches that accommodate selection of optimal modes of operation at each time out of these available 21 operating modes is achieved as per the algorithm provided in the Section 3.2. Because sub-optimal pruned solutions are sought, a reduced set of available modes must get tested and selected. This "outer loop" task is achieved through the Discrete Genetic Algorithm (DGA) whose purpose is to

select a fixed set of modes and to determine the best solution. The nomination of the fraction of modes considered for optimization can be mission driven, or constrained by the hardware (PPU) capacity, P_{max}, or can be self-imposed for conducting trade studies. The resulting OCP is subjected to the boundary conditions given in Eq. (3.37) as

$$\boldsymbol{\Gamma}(\boldsymbol{\eta}(t_0);\boldsymbol{\Theta}) = \left[[\boldsymbol{x}(t_f) - \tilde{\boldsymbol{x}}_d]^\top, \lambda_m(t_f), \lambda_{P_{\text{BL}}}(t_f)\right] = \mathbf{0}, \tag{3.37}$$

where $\boldsymbol{\eta}(t_0) = [\boldsymbol{\lambda}(t_0)^\top, \lambda_m(t_0), P_{\text{BL}}]^\top$ denotes the unknown costates at the initial time along with solar array beginning-of-life power at 1 AU and $\boldsymbol{\Theta} = [\rho_b, \rho_p, \rho_c, \rho_m]$ denotes the vector of continuation parameters of the resulting TPBVP. Thus, we have managed to form a four-parameter family of neighboring TPBVPs and the set of continuation parameters are used to obtain the solution to the original difficult-to-solve OCP. The costate associated with P_{BL} at initial time, $\lambda_{P_{\text{BL}}}(t_0)$, is not a design variable since its value is zero due to the transversality condition.

3.3.4 Optimal Mode-Pruning Algorithm

The first step defined in the previous sub-section is necessary as it ultimately provides a small subset of all the available modes that can be treated as the minimum number of operating modes per optimality principle. This provides an upper bound on the maximum number of useful modes and serves as a base case ("the best one can do for the bearable level of complexity") for comparison with the subsequent sub-optimal solutions with pruned modes. This also aids in reducing the dimensionality of the problem and simplifies the solution procedure.

Heuristic pruning index (defined in Eq. (3.38)) can be used to evaluate the contribution of the i^{th} thrust mode towards optimality as

- i) Frequency of use of the i^{th} mode (ω_i),
- ii) Net duration of the use of the i^{th} thrust mode during the entire maneuver (Δt_i), and
- iii) The admissibility of other neighboring modes when a particular mode is selected (n_{ad_i}).

$$\xi_i = \frac{\omega_i \, \Delta t_i}{1 + n_{\text{ad}_i}}. \tag{3.38}$$

The metric defined in Eq. (3.38) may be used to characterize "the more contributing modes." This metric has been found particularly helpful when the modes are pruned under the assumption that power available for thrusting, P_{av}, is not allowed to change. The coupling of power (P_{av}) and admissibility of the modes as well as the jumbled distribution of thrusting (T & $\dot{m}$) capability of the operating modes (as evident in Table 3.6), makes the pruning difficult and non-intuitive. Moreover, owing to low dependence of the total number of modes on the initial costates (design variables of the shooting method) application of pure indirect-based methods becomes difficult.

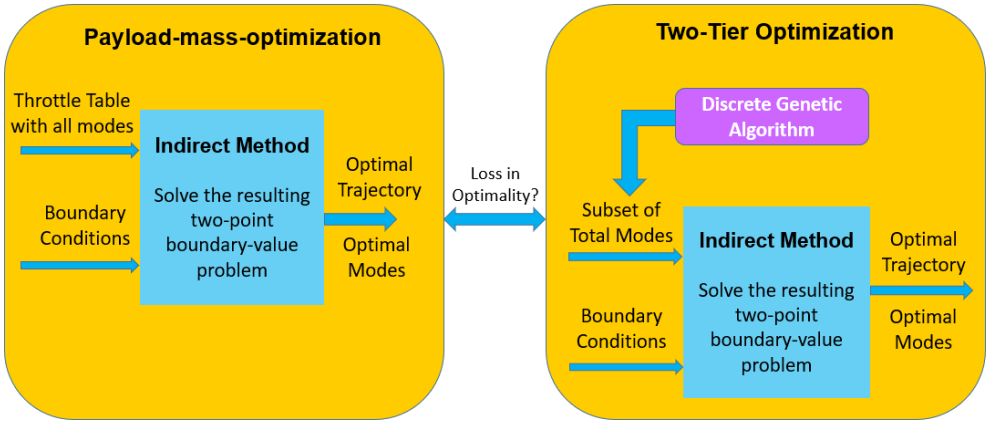

Figure 3.27: Comparison of All-Mode optimization (left block) to two-tier optimization (right block) .

A two-tier hybrid formulation is proposed in this paper for mode pruning with a discrete genetic algorithm (DGA) used in the outer tier (see Figure 3.27). The left block summarizes the solution methodology when all modes are considered (i.e., All-Mode optimization). The right block summarizes the two-tier hybrid formulation. In addition, it is possible to quantify the loss in optimality since the theoretically "best" solution is available for comparison as the outcome of the left block . In the two-tier optimization, the number of design variables of the outer tier is equal to the number of modes considered for the optimization, N_{sel}. The lower and upper bounds of each design variable are identical and ranges from $[1, N_{\text{tot}}]$ where N_{tot} is the number of all the modes available (21 in this case). Considering all existing modes as candidates for the pruned solution is important

since it can occasionally happen that a mode once rejected at one level of pruning becomes optimal for subsequent pruned solutions. Therefore, the outer tier provides candidate configurations of N_{sel} operating modes that are used by the inner-tier solver. If repetition in the modes is encountered in the N_{sel} modes selected by DGA, a high penalty value is returned without executing the inner-tier solver.

The inner-tier solver is comprised of an invariantly embedded indirect-based, low-thrust solver, which can be visualized as a neighboring family of OCPs. Each OCP in this family corresponds to a solved TPBVP associated with a particular value of the smoothing parameters, i.e., ρ_i ($i \in \{p, b, c, m\}$). Thus, the inner-tier solver is identical to the All-Mode optimization with the exception that the number of modes is smaller (ultimately reduced to a minimal subset of modes that ensure optimality to within some tolerance of performance degradation). It was observed that the costates from the fuel optimal solution serves as a good starting guess for the multi-mode solutions (no convergence failures have occurred for the largest ρ_i trajectories). The computational burden is not only proportional to the number of considered operating modes, but also how close the admissible operating modes are to each other. For instance, in case of close operating points, the sorting algorithm for the selection of most optimal mode at each time requires a smaller final value of the continuation parameter (ρ_m) which adds to the computational burden.

3.3.5 Results

A rendezvous maneuver from Earth to comet 67P/ Churyumov–Gerasimenko is solved with a fixed time of flight of 1776 days and the initial mass of the spacecraft as $m_0 = 3000$ kg. The departure ($\boldsymbol{r_E}, \boldsymbol{v_E}$) and arrival ($\boldsymbol{r_G}, \boldsymbol{v_G}$) states are given as

$$\boldsymbol{r_E} = [-1671985.956644, -151914424.309981, 1699.375105]^\top \text{ km},$$
$$\boldsymbol{v_E} = [29.307044, -0.596900, -0.000411]^\top \text{ km/sec},$$
$$\boldsymbol{r_G} = [-465627493.144610, -50530561.307303, 40190127.950002]^\top \text{ km},$$
$$\boldsymbol{v_G} = [-9.721779, -14.629481, -0.234945]^\top \text{ km/sec}.$$

The formulation leads to a variety of optimal solutions corresponding to the user defined N_{sel} modes where $N_{\text{sel}} \in [1, N_{\text{tot}}]$. We emphasize that P_{BL} is kept as a design variable for every pruned

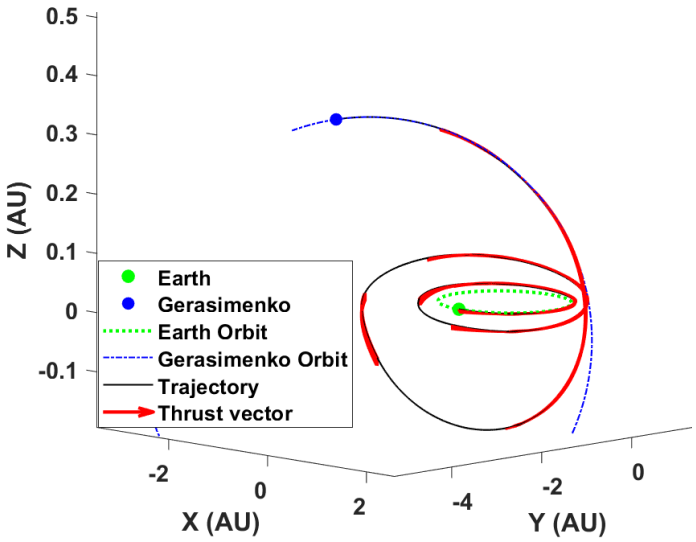

Figure 3.28: Three-dimensional view of the optimal trajectory for the most optimal solution.

case and is kept within the range [10, 30] kW. Other spacecraft parameters are as follows: $\sigma = 0.02$, $P_{\text{max}} = 4.863$ kW, $P_{\text{sys}} = 0.59$ kW, $\eta_d = 0.95$, $\gamma_1 = 10$, $\gamma_2 = 15$ and $a_{\text{tk}} = 0.1$. Due to smoothing, the original multi-point boundary-value problem is converted into a TPBVP and is solved by a single-shooting scheme using MATLAB's *fsolve* solver.

Starting from the theoretically best (all modes) solution, the modes are pruned as per the case-by-case specification set for the total number of modes allowed to operate during the entire maneuver. A single representative trajectory for all these cases is shown in Figure 3.28 since the trajectories for all the cases have minor solar scale graphical differences. However, plots of thrust profiles are presented. Table 3.13 presents a comparison in terms of spacecraft mass breakdown and the details on the optimal modes used throughout the trajectory. The terms P_{BL}, m_u, m_{PSFS}, m_{PSPU} are explained in Eqs. (3.1a) and (3.1b) and $m_f = m_0 - m_p$, where m_p is the mass of the pro-

pellant used. There are five categories of plots included for each pruned case; (i) Corresponding to each considered N_{sel} modes, power availability is evaluated at each time instant, and is denoted by Pdiff = $P_{\text{sel}} - P_{\text{av}}$. Therefore, a positive value of Pdiff indicates that the particular mode is power admissible, (ii) Similarly, SF is evaluated for every mode to check which modes satisfy $SF > 0$ condition to allow the thruster to be 'ON', (iii) the time history of the Hamiltonian corresponding to each mode is plotted to verify that the minimum (optimal) Hamiltonian (H_{opt}) is achieved.

The Hamiltonian is plotted for each operating mode, which is power admissible at a given time and the black dashed lines represent the Hamiltonian associated with the operating modes that do not get selected. (iv) Time histories of the thrust profile T_{av}, switching function SF and g_p (refer to Eq. (3.12)) corresponding to the optimal solution are also provided for each case. (v) A combined plot displaying the history of the operation of different modes for all cases. Of the above category of figures, category (i) and (ii) are listed in Table 3.14 and category (iii) and (iv) are tabulated in Table 3.15. Since, it is observed that the osculating true anomaly does not change significantly for all the pruned solutions, a representative osculating true anomaly plot is used with the thrust plots in Table 3.15 to provide additional insights.

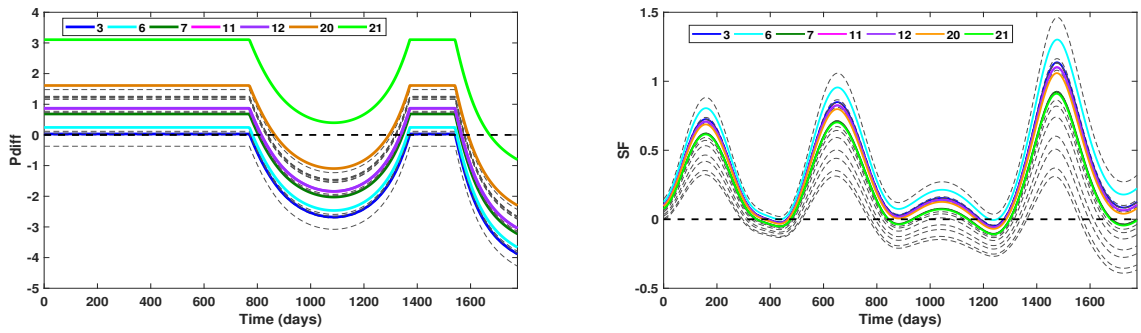

Figure 3.29: Time histories of power differential (Pdiff) and SF for operating and non-operating (black) modes for $N_{\text{sel}} = N_{\text{tot}}$ case.

All-mode solution: The optimum value obtained for P_{BL} is 11.19 kW. The size of the solar arrays is generally kept large enough to allow thrusting at the maximum heliocentric distances, but

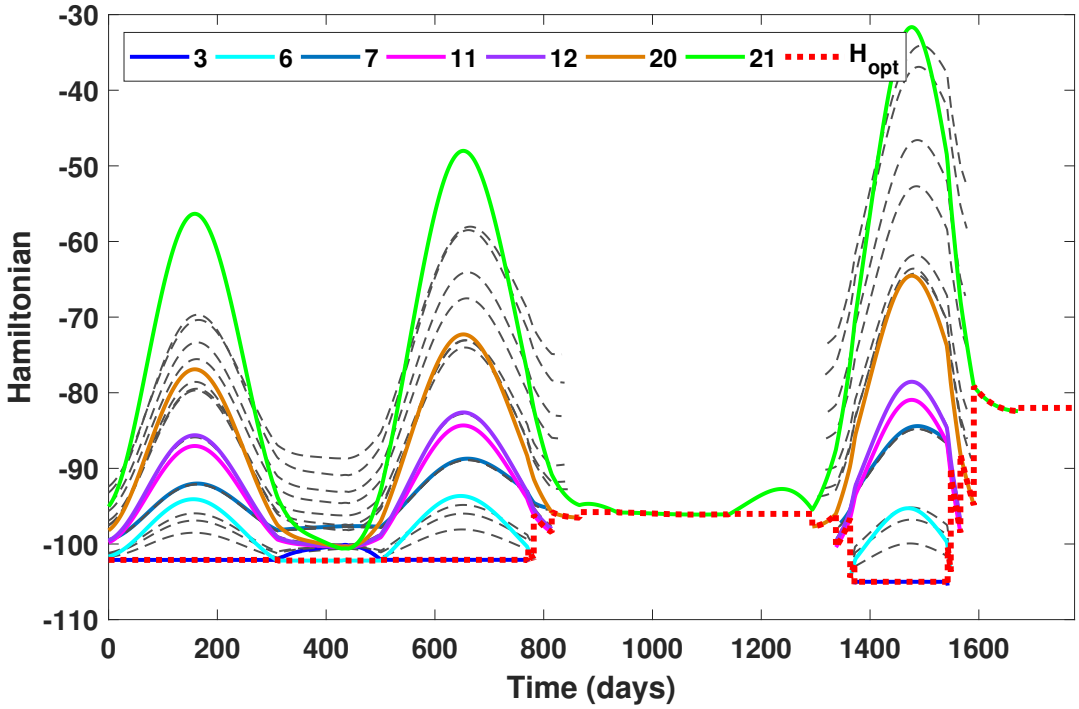

Figure 3.30: Profiles of the Hamiltonian for operating and non-operating (black) modes for $N_{\text{sel}} = N_{\text{tot}}$ case.

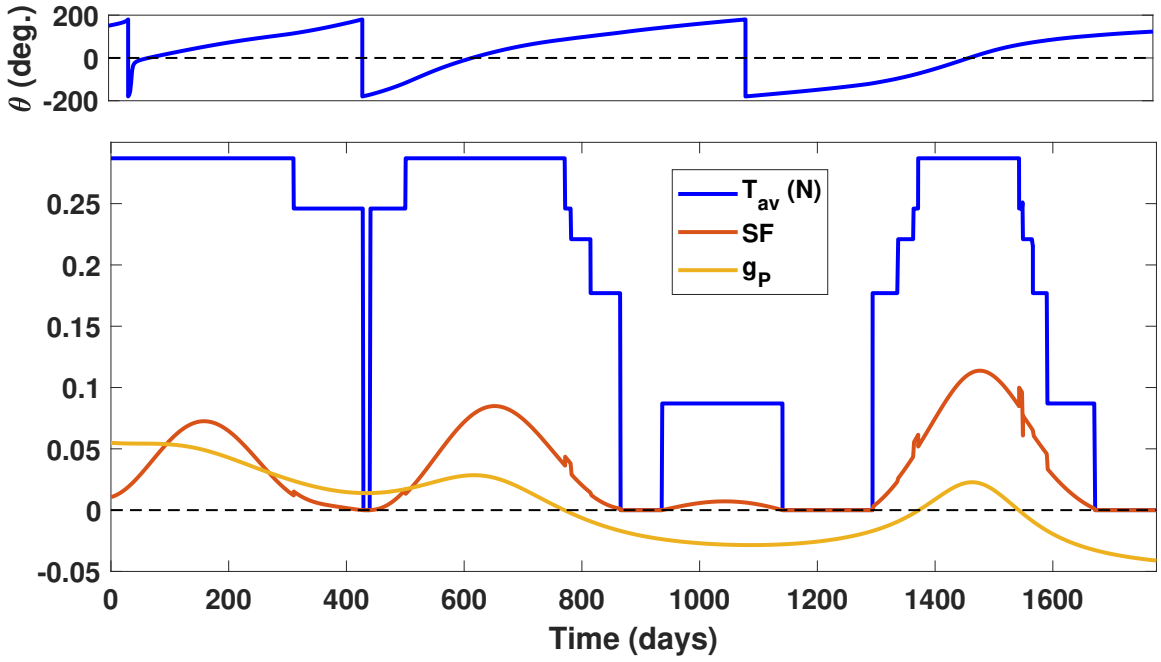

Figure 3.31: Time histories of thrust, SF and g_p for $N_{\text{sel}} = N_{\text{tot}}$ case.

the trajectory-propulsion co-optimization in this case leads to a smaller size solar arrays that do not produce enough power for thrusting at arrival (see Figure 3.29).

In order to interpret the results, the switching function and/or power admissibility plots should not be analyzed independently. The ultimate selection of the mode is achieved through the minimization of the Hamiltonian. Therefore, Figure 3.30 is a more important plot for conclusive remarks. For instance, mode #3 is selected during the first 300 days as it minimizes the Hamiltonian the most. However, for the next 100 days, mode #6 results in a lower value of the Hamiltonian leading to its selection. For the next time period of 15 days, none of the modes are selected and the thruster is OFF since the switching function is negative for all modes (cf. Figure 3.29) for that period. Thus, these plots have to be cross-checked in order to understand the decisions underlying the optimal thrust profile.

The same reasoning has to be followed for the remainder of the trajectory and in the ensuing results. Figure 3.30 displays how the optimal Hamiltonian follows the minimum Hamiltonian (i.e., consistent with PMP) value along the trajectory making various switches among the seven selected optimal modes. There are 21 mode-switches in Figure 3.31 as different thrust values are achieved during the maneuver with some coast arcs. As the spacecraft approaches the aphelion, the least-power mode (#21) is engaged due to lack of availability (due to power) of any other mode for thrusting (see the left plot in Figure 3.29). Figure 3.31 also indicates that only 7 modes out of the 21 are used as per payload optimality. From Table 3.6, it can be observed that modes #7, #8, and #9 possess a higher T and $\dot{m}$ value than their neighbouring modes but are scarcely operated due to their low I_{sp}.

Keeping in mind the optimal solution revealed in all-mode case, subsequent pruning of modes is done to obtain solutions corresponding to consecutively decreasing number of total used modes. Having fewer number of operation modes improves the reliability of the propulsion system from an operational standpoint. Therefore investigating the impact of reduced number of modes seems reasonable and is pursued per two-tier hybrid optimization algorithm. The reader is directed to the plots listed in Tables 3.14 & 3.15 to understand the pruned cases ($N_{\text{sel}} = 1 - 5$).

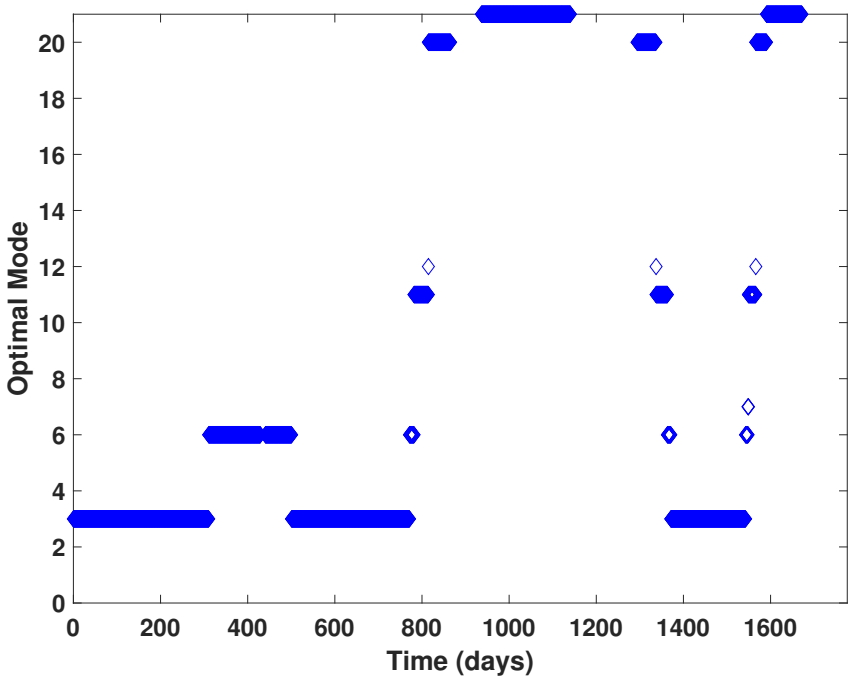

Figure 3.32: Time history of the optimal selected modes for $N_{\text{sel}} = N_{\text{tot}}$ case.

Five-mode solution: By inspecting Figure 3.32, one can observe that modes #7 and #12 are used for a brief time period (corresponding to low values for metric ξ) and therefore, are among the candidate modes for elimination. The removal of these two modes does not have a significant impact on the payload mass as shown in Table 3.13. Note that modes #11 and #12 have similar T, $\dot{m}$ and I_{sp} values (per Table 3.6) with mode #11 being selected over mode #12 due to its better performance. The five-mode solution is in a close neighbourhood of the *optimal* seven-mode solution.

Four-mode solution: The optimal solution led to a final payload mass of ~ 868.56 kg which involved the elimination of mode #6. Since the power requirement of modes #3 and #6 are very close, mode #3 is selected over mode #6 when both are admissible. Also, with the same value of n_{ad} for both modes in the five-mode solution, mode #3 has higher values for both ω and Δt than mode #6 leading to $\xi_3 > \xi_6$ (refer Eq. (3.38)). The same logic cannot be used for the removal of mode #6 in favor of mode #11 as mode #6 is superior in performance when Table 3.6 is consid-

ered. The sub-optimality of mode #11 in comparison to mode #6 is somewhat compensated by the reduction in the mass of the solar arrays required to operate mode #11 resulting in smaller m_{SA} compared to the five-mode solution (refer Table 3.13). The duration of the coast arcs begins to increase (especially the first coast arc) compared to the five-mode solution as the SF corresponding to the selected modes is slightly shifted down in the y-axis.

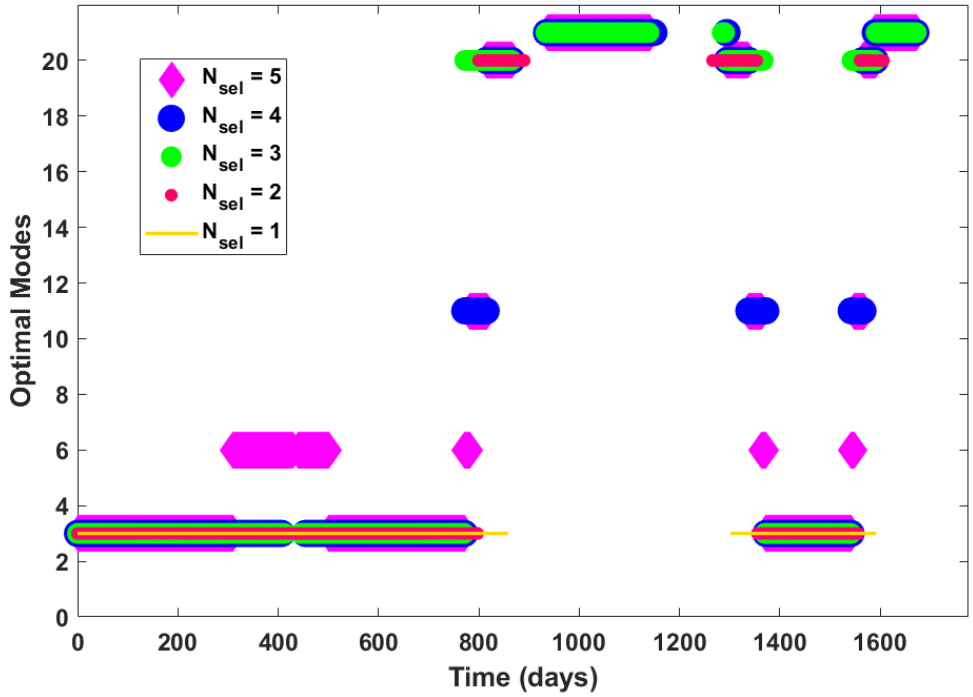

Figure 3.33: Comparison of the time histories of the optimal selected modes for all pruned cases.

Three-mode solution: The three-mode solution suffers a deficit of only ∼11 kg with respect to the four-mode solution. No previously rejected mode appears to be optimal for this case. The three modes selected are modes #3, #20 and #21 of which modes #20 and #21 require the lowest power for operation and offer the lowest thrust but fairly high I_{sp} out of all 21 modes. There is a slight increase (∼0.13 kW) in the value of P_{BL} compared to the four-mode solution to allow longer (as compared to four-mode solution) operation of mode #20 at the aphelion passages (see Figure

Table 3.13: Comparison of masses and P_{BL} for solutions with different number of modes.

N_{sel}	21	5	4	3	2	1
P_{BL} (kW)	11.19	11.2	11.15	11.28	12.65	16.14
m_u (kg)	876.44	876.4	868.56	857.02	846.64	823.54
m_f (kg)	1237.68	1237.65	1230	1220.72	1223.7	1234.47
m_{PSPU} (kg)	(111.9+	(112+	(111.5+	(112.8+	(126.5+	(161.4+
($m_{\text{SA}} + m_{\text{PPU}}$)	72.94)	72.94)	72.94)	72.94)	72.94)	72.94)
m_{PSFS} (kg)	1938.63	1938.64	1946.9	1957.2	1953.9	1942.078
Opt. Modes	[3,6,7,11, 12,20,21]	[3,6,11, 20,21]	[3,11, 20,21]	[3,20,21]	[3,20]	3

3.33).

Two-mode solution: A thruster that is capable of operating at two modes can be desirable for its befitting simplification in capturing the aggregate performance of the engine. The two optimal modes were found to be modes #3 and #20 resulting in a final payload mass of 846.64 kg (see Table 3.13). The solution is shy of the most optimal result by ~ 30 kg and the 3-mode solution by ~ 11 kg. It is generally expected that the two extreme operating modes (the best and the worst in terms of power and thrust) get selected when an optimal two-mode solution is sought. Also, lower power (thrust) modes are typically included to prepare for any unforeseen events (hardware failure, missed thrust) encountered during the actual mission. In this case, when the lowest power mode (#21) is included in place of mode #20, loss of payload mass of 32 kg is observed. Reduced coast arcs (only 2) appear in this solution in comparison to previous pruned solutions (4 coast arcs) due to the significantly reduced thrusting capability of an engine with only two modes.

Single-mode solution: This specific case holds importance in regards to the traditional fuel-optimization carried out in the preliminary stages of trajectory design. This methodology reveals which is the most payload-optimal T_{max} value. Note that since the time of flight and the number of en-route revolutions around the Sun are kept consistent for all the cases, there can be some mode subsets identified, which are deliver insufficient thrust acceleration to complete the maneuver. Our analysis indicates that the minimum thrust required is $T_{\text{max}} \geq 0.24$ N, which reduces the design space for the single-mode problem to modes in the range [1-9]. Unsurprisingly, mode #3 turned out

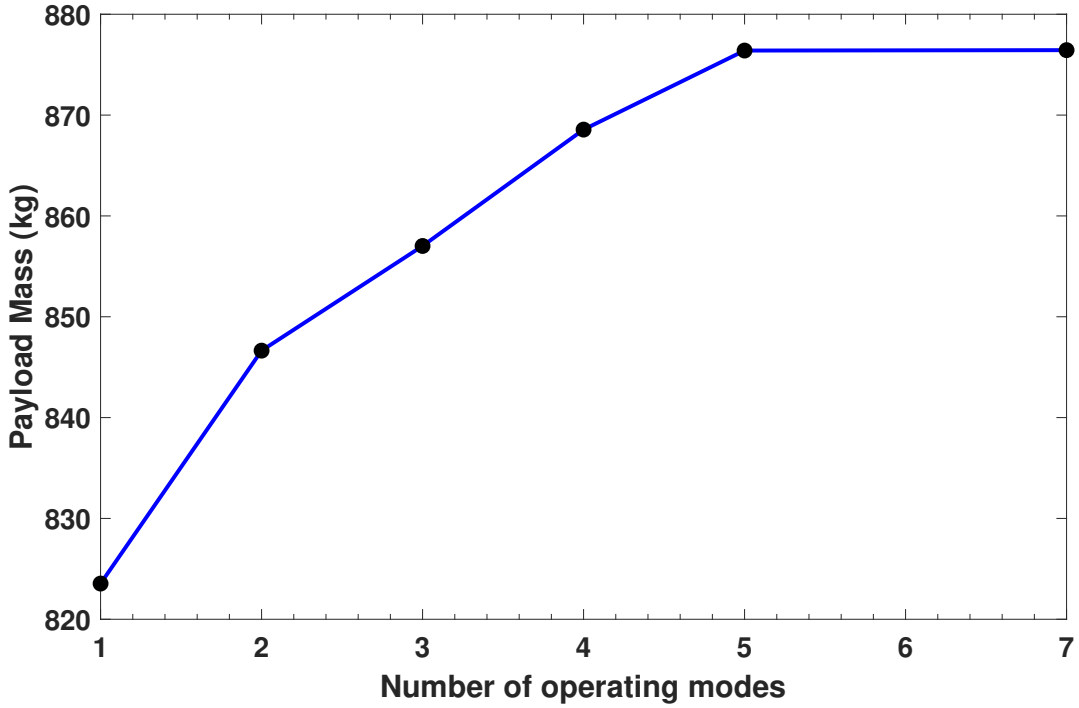

Figure 3.34: Variation of payload mass (m_u) against the number of operating modes.

to be the best among all feasible modes for the selected maneuver. Mode #3 also has the highest value for ξ among all modes in all pruned solutions due to long duration of operation (Δt) and high frequency of use (ω). The mass of the solar arrays required is much higher (by ~ 50 kg) than the most optimal solution (seven-mode solution) and the reduction in the payload delivered is ~ 53 kg. Interestingly, the payload mass delivered is smaller than the two-mode solution, but the final mass is more (fuel-consumption is less). The drop in the payload mass is higher in the transition from a two-mode solution to a single-mode solution than any other consecutive pruned cases as shown in Figure 3.34.

The mode-pruning algorithm leads to reduction in chatter in control variables and helps avoid possible rapid mode switches with a calculated sacrifice on the payload mass (i.e., the optimality criterion). The results indicate that subsequent sub-optimal pruned solutions (with fewer modes) featured optimal modes that are all a subset of the modes selected in the most optimal solution; however, this empirical result, while intuitively reasonable, has not been proven to be universally

the case. We anticipate the methodology underlying these results will find applications in optimal mission design studies where some SEP system variables are subject to optimization, as well as final optimization of trajectories for many low-thrust missions where multiple operating modes must be considered.

Table 3.14: Summary of Pdiff and SF for solutions with different number of modes: $N_{\text{sel}} = \{1, 2, 3, 4, 5\}$

(Pdiff $= P_{\text{av}} - P_{\text{sel}}$)	SF
$N_{\text{sel}} = 5$	
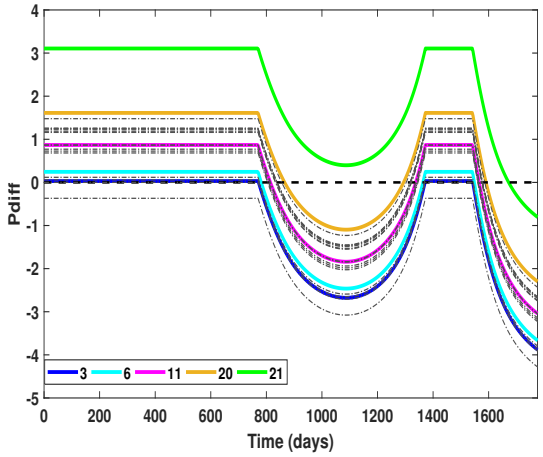	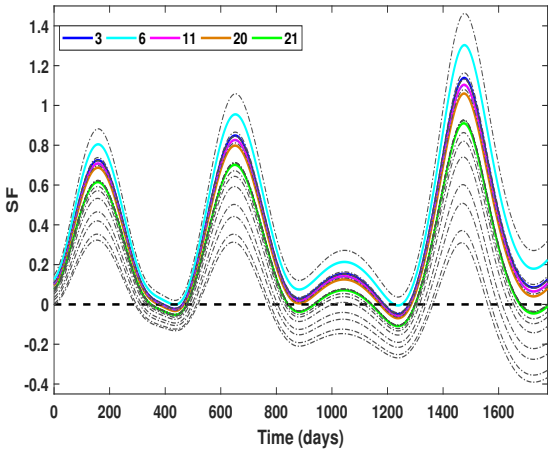
$N_{\text{sel}} = 4$	
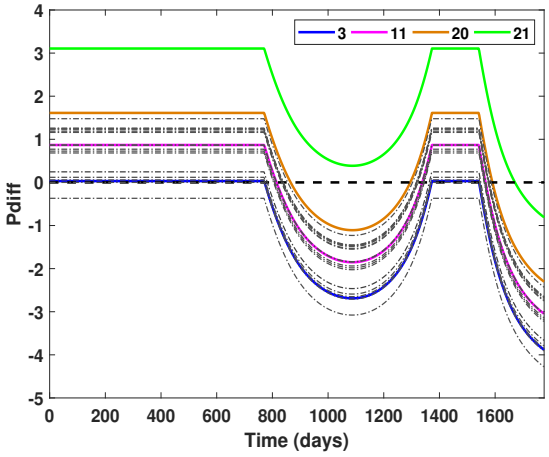	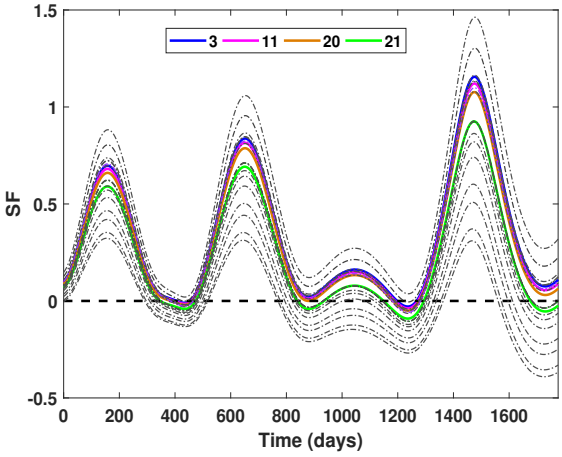
$N_{\text{sel}} = 3$	

Continued on next page

Table 3.14 – continued from previous page

Power differential (Pdiff $= P_{\text{av}} - P_{\text{sel}}$)	SF
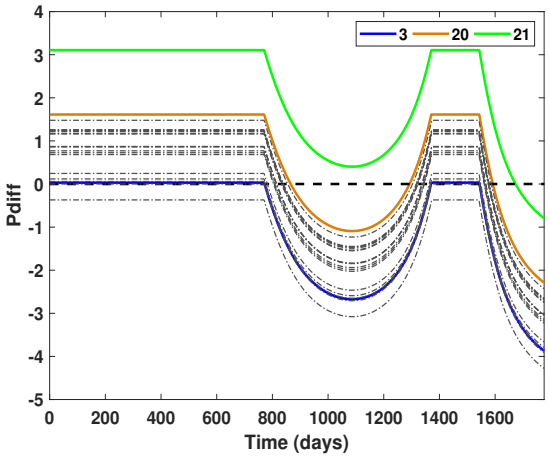	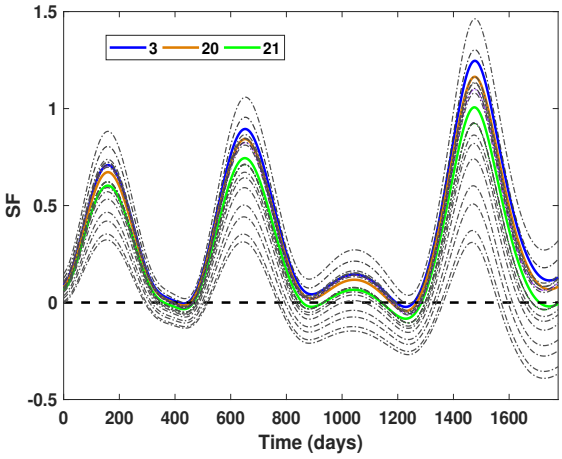
$N_{\text{sel}=2}$	
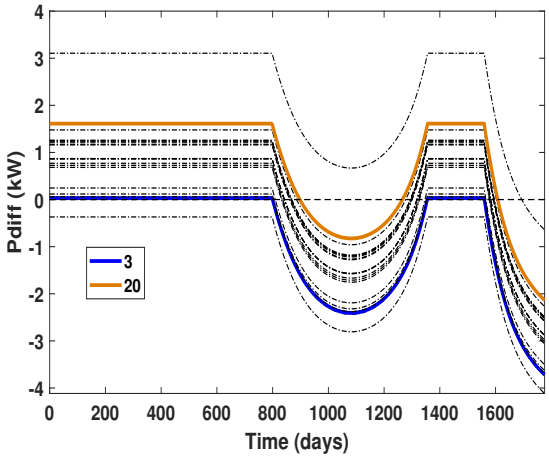	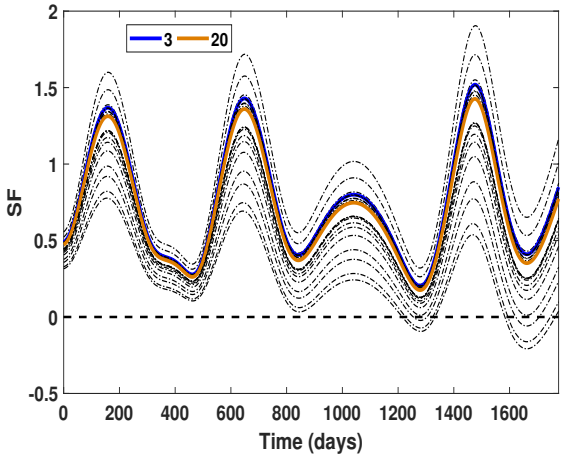
$N_{\text{sel}=1}$	

Continued on next page

Table 3.14 – continued from previous page

Power differential (Pdiff $= P_{\text{av}} - P_{\text{sel}}$)	SF
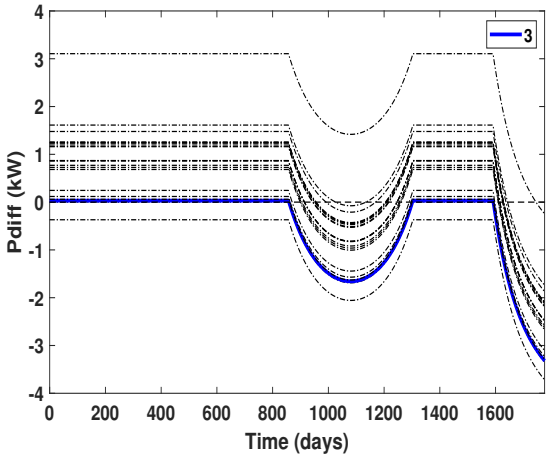	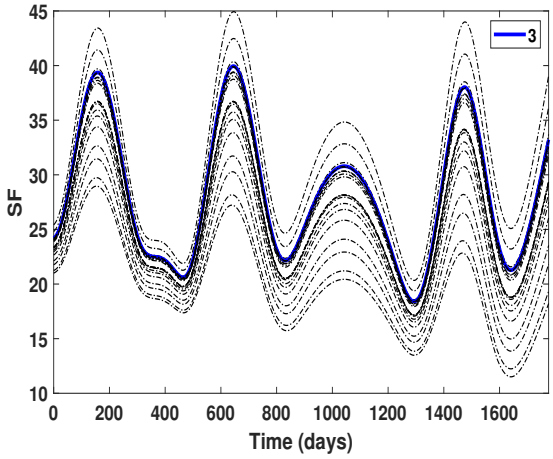

Table 3.15: Thrust, SF, g_p, and Hamiltonian for solutions with different number of modes- $N_{\text{sel}} = \{1, 2, 3, 4, 5\}$

Thrust profile, SF and g_p	Hamiltonian
$N_{\text{sel}} = 5$	
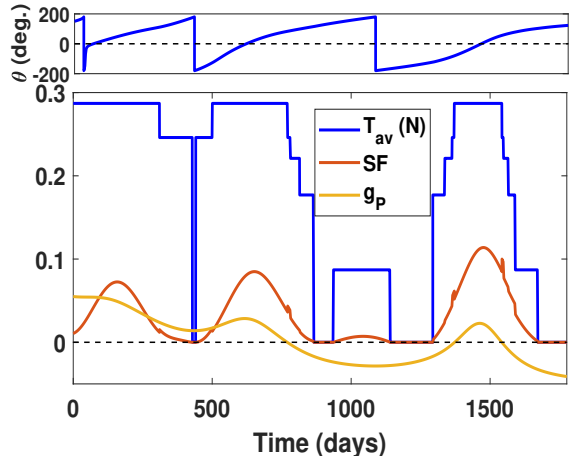	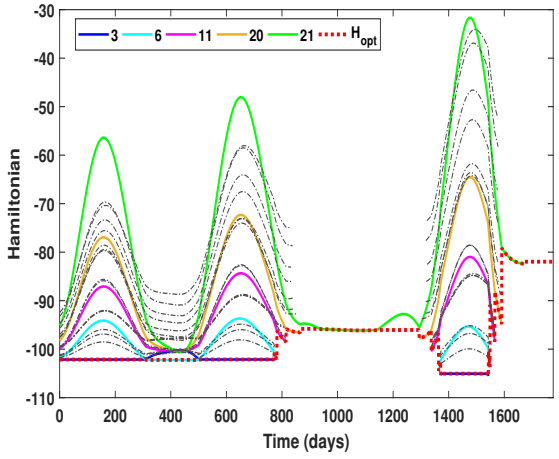
$N_{\text{sel}} = 4$	

Continued on next page

Table 3.15 – continued from previous page

Thrust profile, SF and g_p	Hamiltonian
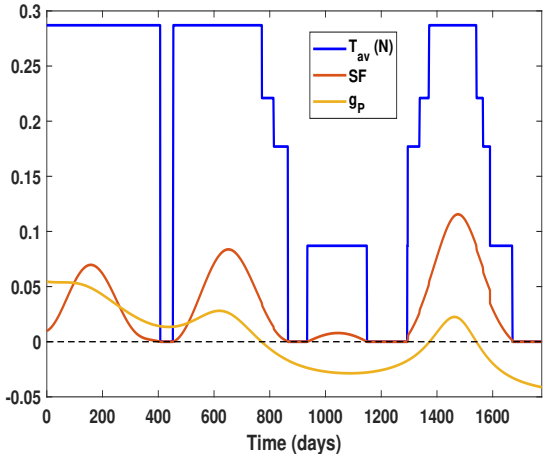	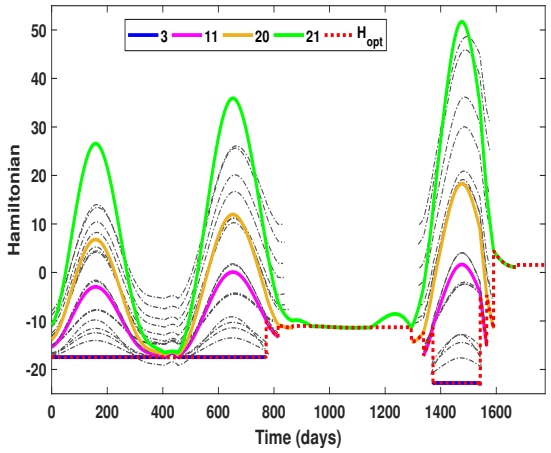
$N_{\text{sel}} = 3$	
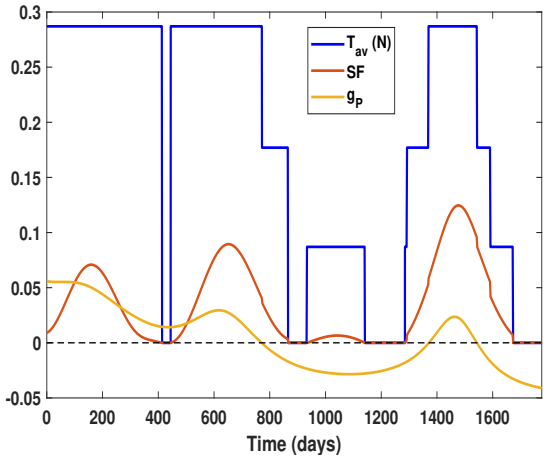	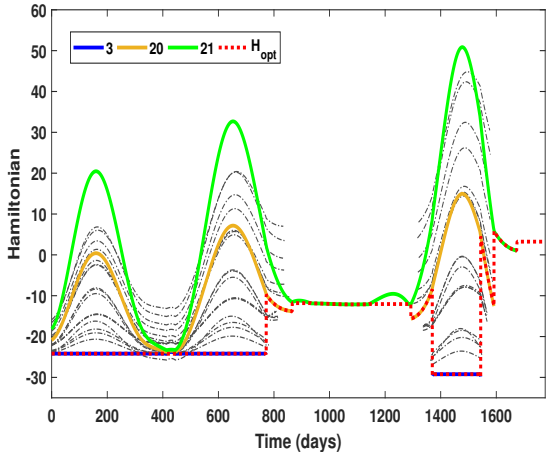
$N_{\text{sel}} = 2$	

Continued on next page

Table 3.15 – continued from previous page

Thrust profile, SF and g_p	Hamiltonian
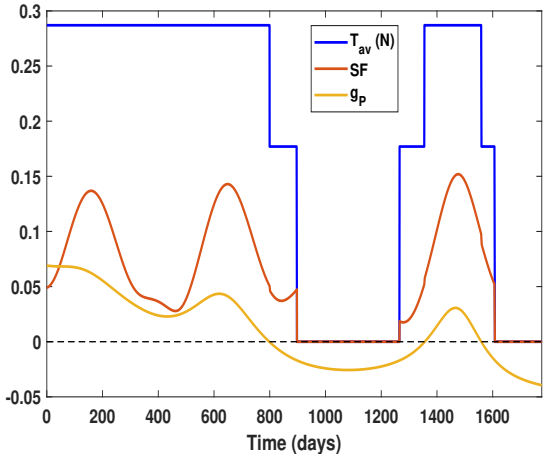	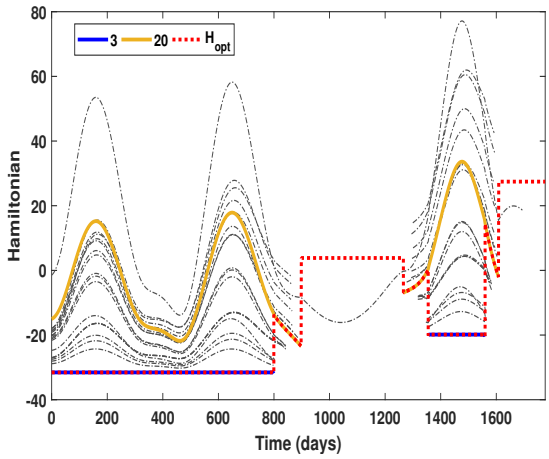
$N_{\text{sel}} = 1$	
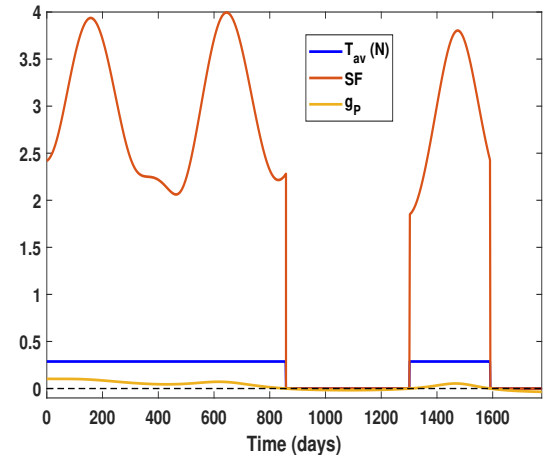	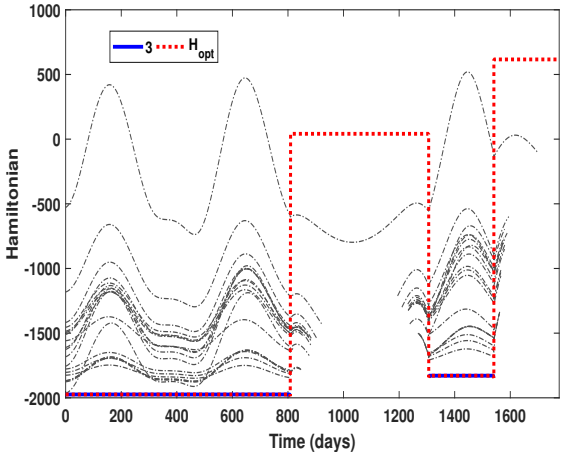

4. Guidance & Control[1]

In recent decades, aerospace vehicles' guidance and control problems for many space and aerial applications have been largely comprising of spacecraft and aircraft attitude regulation. Recent advances have opened up the arena for various other applications like Unmanned Aerial Vehicles (UAVs), Autonomous Underwater Vehicles (AUVs), miniaturized satellites like CubeSats, and close mapping of irregular asteroids [114] such that the requirement of the maneuver efficiency and the class of constraints associated with them have become challenging to accommodate and crucial to solve for successful operation. Apart from tracking challenges in proximity missions where stringent covariance constraints are imposed, the covariance study is also helpful in assessing the guidance policy in case of interplanetary maneuvers. Especially in case of use of multiple engines and gridded-ion engines with multiple modes of operation, the impact of various operation failures is crucial and lead to a portfolio of contingent trajectories.

4.1 Covariance Control

This section establishes a systematic methodology that delivers the weighting matrices of the LQR such that the specified covariance bounds are satisfied at each time. The work also allows to convert the output covariance assignment problem, from a generally very specialized solution framework into a very general and well-known LQR framework. Moreover, the traditional random guessing in the tuning of the constant weighting matrices in LQR is replaced by a systematic iterative process that yields time-varying $\boldsymbol{Q}$ or $\boldsymbol{R}$ matrices to satisfy a pre-specified time-varying covariance constraint on the system output. A finite-horizon optimal control problem is solved for a discrete linear time-varying system subject to a stochastic disturbance assuming fully observable states. The novelty of the method lies in finding judicious time-varying values of $\boldsymbol{Q}$ which deliver controls that satisfy tighter covariance bounds to suit the natural dynamics of the system in the

[1]Reprinted with permission from "Design of LQR Weighting Matrices for Time Varying Output Covariance Assignment" by Arya, Vishala and Goyal, Raman and Majji, Manoranjan and Junkins, John L, 2021. AAS Astrodynamics Specialist Conference at Big Sky, Montana (Virtual) 2021

presence of stochastic disturbance, with unbounded control inputs [115]. This is especially useful when higher precision is required in the maneuvers due to the enhanced capability of balancing feedback control effort with the desired covariance at any time instant. While the procedure does not explicitly enforce actuator limits, it implicitly minimizes the control effort by modulating the $\boldsymbol{Q}$ matrix. I believe it is the first time such a time-varying closed-loop covariance assignment technique for LTV systems has been proposed and demonstrated.

4.1.1 Bounded Output Covariance Assignment

4.1.1.1 Notation

We denote by $\mathbb{R}^n$ the set of n-dimensional real vectors. The matrices are defined by bold uppercase letters as $\boldsymbol{Y}$. The expectation operator is defined by $\mathbb{E}[\cdot]$ and $\mathcal{N}(\mu_x, \boldsymbol{Y})$ denotes the Gaussian distribution with mean μ_x and covariance $\boldsymbol{Y}$. The diagonal matrix generated from a vector $\boldsymbol{x}$ is denoted as $\textbf{diag}(\boldsymbol{x})$, the block diagonal matrix is denoted as $\textbf{blkdiag}(\boldsymbol{Y}_1, \boldsymbol{Y}_2, \cdots, \boldsymbol{Y}_3)$, and the transpose of a matrix $\boldsymbol{Y}$ is defined by $\boldsymbol{Y}^\top$. The symbol $\mathbf{0}$ defines a zero matrix with suitable dimensions. The notations $\boldsymbol{X} \succ 0$ and $\boldsymbol{Y} \succeq 0$ denote the symmetric positive definite ($\mathbb{S}_n^{++}$) and symmetric positive semidefinite ($\mathbb{S}_n^{+}$) matrices, respectively.

4.1.1.2 System Definition

A discrete-time linear time-varying system is described by the following state-space representation:

$$\boldsymbol{x}_{k+1} = \boldsymbol{A}_k \boldsymbol{x}_k + \boldsymbol{B}_k \boldsymbol{u}_k + \boldsymbol{D}_k \boldsymbol{\nu}_k, \tag{4.1}$$

$$\boldsymbol{y}_k = \boldsymbol{C}_k \boldsymbol{x}_k, \tag{4.2}$$

where $\boldsymbol{x}_k \in \mathbb{R}^n$ is the state of the system at time-step k, $\boldsymbol{u}_k \in \mathbb{R}^m$ is the control vector, $\boldsymbol{y}_k \in \mathbb{R}^p$ is the output of the system, and $k = \{0, 1, \cdots, N\}$. The noise in the system is added as process

noise $\boldsymbol{\nu}_k$ which is modeled as independent zero mean white noises with covariance $\mathbb{V} \in \mathbb{S}^{++}$, i.e.:

$$\mathbb{E}[\boldsymbol{\nu}] = \mathbf{0},\ \mathbb{E}[\boldsymbol{\nu}\boldsymbol{\nu}^\top] = \mathbb{V}, \tag{4.3}$$

where $\mathbb{E}[x]$ denotes the expected value of the random variable x. We assume the process noise covariance $\mathbb{V}$ to be known and fixed. Let us define the covariance of the state $\boldsymbol{x}_k$ and output $\boldsymbol{y}_k$ at any time step k as:

$$\boldsymbol{P}_k \triangleq \mathbb{E}[\boldsymbol{x}_k \boldsymbol{x}_k^\top], \tag{4.4}$$

$$\boldsymbol{Y}_k \triangleq \mathbb{E}[\boldsymbol{C}_k \boldsymbol{x}_k \boldsymbol{x}_k^\top \boldsymbol{C}_k^\top] = \boldsymbol{C}_k \boldsymbol{P}_k \boldsymbol{C}_k^\top. \tag{4.5}$$

4.1.1.3 Problem Statement

The final problem statement is to find the feedback control $u_k = \boldsymbol{K}_k x_k$, such that the output covariance at all times can be assigned as:

$$\boldsymbol{Y}_k = \boldsymbol{C}_k \boldsymbol{P}_k \boldsymbol{C}_k^\top = \bar{\boldsymbol{Y}}_k, \text{ for } k = 1, \cdots, N+1, \tag{4.6}$$

and the cost function J:

$$J = \mathbb{E}\left[\sum_{k=0}^{N} u_k^\top \boldsymbol{R}_k u_k\right], \tag{4.7}$$

is minimized for a given sequence of $\boldsymbol{R}_k$ and commanded covariance profile ($\bar{\boldsymbol{Y}}_k$).

4.1.2 Main Result and Algorithm

This section first provides the main theorem of the paper which results in an algorithm to calculate the gain matrix $\boldsymbol{K}_k$ to solve the above mentioned problem statement for some chosen values of Lagrange Multipliers $\boldsymbol{Q}_k$. It is further observed that the solution for the problem statement has the same formulation as that of Linear Quadratic Regulator (LQR) problem where weighting

matrix corresponding to state cost $\boldsymbol{Q}_k$ has taken the place of Lagrange Multipliers. The section further provides an iterative algorithm to calculate these weighting matrices $\boldsymbol{Q}_k$ to bound the output covariance while simultaneously minimizing the given cost function J.

Theorem: If there exists a feedback controller which minimizes the cost function:

$$J = \mathbb{E}\left[\sum_{k=0}^{N} u_k^\top \boldsymbol{R}_k u_k\right], \tag{4.8}$$

and satisfies the constraints given as: $\boldsymbol{C}_k \boldsymbol{P}_k \boldsymbol{C}_k^\top = \bar{\boldsymbol{Y}}_k,$ for $k = 1, \cdots, N+1$, for the discrete-time time-varying linear system described by the system equation (Eq. (4.1)) and the output equation ((Eq. (4.2)), then the solution for the time varying feedback gain is given by

$$\boldsymbol{K}_k = -\left(\boldsymbol{R}_k + \boldsymbol{B}_k^\top \boldsymbol{S}_{k+1} \boldsymbol{B}_k\right)^{-1} \boldsymbol{B}_k^\top \boldsymbol{S}_{k+1} \boldsymbol{A}_k. \tag{4.9}$$

and the discrete time Riccatti equation for some choice of Lagrange multipliers $\boldsymbol{Q}_k$ for $k = 1, 2, \cdots, N+1$ is given as:

$$\boldsymbol{S}_k = \boldsymbol{C}_k^\top \boldsymbol{Q}_k \boldsymbol{C}_k + \boldsymbol{A}_k^\top \left(\boldsymbol{S}_{k+1} - \boldsymbol{S}_{k+1} \boldsymbol{B}_k \left(\boldsymbol{R}_k + \boldsymbol{B}_k^\top \boldsymbol{S}_{k+1} \boldsymbol{B}_k\right)^{-1} \boldsymbol{B}_k^\top \boldsymbol{S}_{k+1}\right) \boldsymbol{A}_k, \tag{4.10}$$

with the terminal condition $\boldsymbol{S}_{N+1} = \boldsymbol{C}_{N+1}^\top \boldsymbol{Q}_{N+1} \boldsymbol{C}_{N+1}$.

Proof: Let us start by assuming the solution to be of the state-feedback form given as:

$$\boldsymbol{u}_k = \boldsymbol{K}_k \boldsymbol{x}_k. \tag{4.11}$$

The system dynamics equation for the above-mentioned control can be written as:

$$\boldsymbol{x}_{k+1} = (\boldsymbol{A}_k + \boldsymbol{B}_k \boldsymbol{K}_k)\boldsymbol{x}_k + \boldsymbol{D}_k \boldsymbol{\nu}_k, \tag{4.12}$$

and the corresponding covariance propagation equation for the state can be written as:

$$\boldsymbol{P}_{k+1} = \mathbb{E}[\boldsymbol{x}_{k+1}\boldsymbol{x}_{k+1}^{\top}], \tag{4.13}$$

$$\boldsymbol{P}_{k+1} = (\boldsymbol{A}_k + \boldsymbol{B}_k\boldsymbol{K}_k)\boldsymbol{P}_k(\boldsymbol{A}_k + \boldsymbol{B}_k\boldsymbol{K}_k)^{\top} + \boldsymbol{D}_k\mathbb{V}_k\boldsymbol{D}_k^{\top}, \tag{4.14}$$

Now, let us write the cost function J in terms of state covariance $\boldsymbol{P}_k$ as:

$$J = \mathbb{E}\left[\sum_{k=0}^{N}\boldsymbol{x}_k^{\top}\boldsymbol{K}_k^{\top}\boldsymbol{R}_k\boldsymbol{K}_k\boldsymbol{x}_k\right] = \sum_{k=0}^{N}\mathrm{Tr}\left(\mathbb{E}\left[\boldsymbol{K}_k\boldsymbol{x}_k\boldsymbol{x}_k^{\top}\boldsymbol{K}_k^{\top}\boldsymbol{R}_k\right]\right), \tag{4.15}$$

$$J = \sum_{k=0}^{N}\mathrm{Tr}\left(\boldsymbol{R}_k\boldsymbol{K}_k\boldsymbol{P}_k\boldsymbol{K}_k^{\top}\right), \tag{4.16}$$

where $\mathrm{Tr}(\cdot)$ is the trace operator. Using the cost function mentioned in Eq. (4.16), the augmented Lagrangian function corresponding to the constraint optimization problem can be written as:

$$\mathcal{L} = \sum_{k=0}^{N}\mathrm{Tr}\left(\boldsymbol{R}_k\boldsymbol{K}_k\boldsymbol{P}_k\boldsymbol{K}_k^{\top}\right) + \sum_{k=0}^{N}\mathrm{Tr}\left(\boldsymbol{S}_{k+1}(\hat{\boldsymbol{A}}_k\boldsymbol{P}_k\hat{\boldsymbol{A}}_k^{\top} + \boldsymbol{D}_k\mathbb{V}_k\boldsymbol{D}_k^{\top} - \boldsymbol{P}_{k+1})\right) + \sum_{k=1}^{N+1}\mathrm{Tr}\left(\boldsymbol{Q}_k(\boldsymbol{C}_k\boldsymbol{P}_k\boldsymbol{C}_k^{\top} - \bar{\boldsymbol{Y}}_k)\right), \tag{4.17}$$

where $\hat{\boldsymbol{A}}_k = \boldsymbol{A}_k + \boldsymbol{B}_k\boldsymbol{K}_k$, and $\boldsymbol{S}_{k+1}$ and $\boldsymbol{Q}_k$ are the Lagrange multipliers corresponding to satisfaction of the covariance propagation equation (Eq. (4.14)) and output covariance constraints (Eq. (4.6)).

Now, the partial of the Lagrange function w.r.t. $\boldsymbol{P}_{N+1}$ gives:

$$\frac{\partial\mathcal{L}}{\partial\boldsymbol{P}_{N+1}} = -\boldsymbol{S}_{N+1} + \boldsymbol{C}_{N+1}^{\top}\boldsymbol{Q}_{N+1}\boldsymbol{C}_{N+1}, \tag{4.18}$$

the partial of the Lagrange function w.r.t. $\boldsymbol{P}_k$ gives:

$$\frac{\partial\mathcal{L}}{\partial\boldsymbol{P}_k} = \boldsymbol{K}_k^{\top}\boldsymbol{R}_k\boldsymbol{K}_k + \hat{\boldsymbol{A}}_k^{\top}\boldsymbol{S}_{k+1}\hat{\boldsymbol{A}}_k - \boldsymbol{S}_k + \boldsymbol{C}_k^{\top}\boldsymbol{Q}_k\boldsymbol{C}_k, \tag{4.19}$$

and the partial of the Lagrange function w.r.t. $\boldsymbol{K}_k$ gives:

$$\frac{\partial \mathcal{L}}{\partial \boldsymbol{K}_k} = 2\boldsymbol{R}_k\boldsymbol{K}_k\boldsymbol{P}_k + 2\boldsymbol{B}_k^\top \boldsymbol{S}_{k+1}\boldsymbol{A}_k\boldsymbol{P}_k + 2\boldsymbol{B}_k^\top \boldsymbol{S}_{k+1}\boldsymbol{B}_k\boldsymbol{K}_k\boldsymbol{P}_k. \tag{4.20}$$

The partials w.r.t. the Lagrange multipliers $\boldsymbol{S}_{k+1}$ and $\boldsymbol{Q}_k$ gives back the covariance propagation equation (Eq. (4.14)) and output covariance constraints (Eq. (4.6)).

Now, using the following necessary conditions for the minimization of the Lagrange function:

$$\frac{\partial \mathcal{L}}{\partial \boldsymbol{P}_{N+1}} = \boldsymbol{0}, \;\; \frac{\partial \mathcal{L}}{\partial \boldsymbol{P}_k} = \boldsymbol{0}, \;\; \frac{\partial \mathcal{L}}{\partial \boldsymbol{K}_k} = \boldsymbol{0}, \tag{4.21}$$

we obtain:

$$\boldsymbol{S}_{N+1} = \boldsymbol{C}_{N+1}^\top \boldsymbol{Q}_{N+1}\boldsymbol{C}_{N+1}, \tag{4.22}$$

$$\boldsymbol{K}_k^\top \boldsymbol{R}_k\boldsymbol{K}_k + \hat{\boldsymbol{A}}_k^\top \boldsymbol{S}_{k+1}\hat{\boldsymbol{A}}_k + \boldsymbol{C}_k^\top \boldsymbol{Q}_k\boldsymbol{C}_k = \boldsymbol{S}_k, \tag{4.23}$$

and

$$\boldsymbol{R}_k\boldsymbol{K}_k\boldsymbol{P}_k + \boldsymbol{B}_k^\top \boldsymbol{S}_{k+1}\boldsymbol{B}_k\boldsymbol{K}_k\boldsymbol{P}_k = -\boldsymbol{B}_k^\top \boldsymbol{S}_{k+1}\boldsymbol{A}_k\boldsymbol{P}_k. \tag{4.24}$$

Ignoring the unlikely possibility that all columns of $\boldsymbol{P_k}$ lie in the null-space of Eq.(4.20), notice that the last equation can be used to solve for $\boldsymbol{K}_k$ in terms of $\boldsymbol{S}_{k+1}$ as:

$$\left(\boldsymbol{R}_k + \boldsymbol{B}_k^\top \boldsymbol{S}_{k+1}\boldsymbol{B}_k\right)\boldsymbol{K}_k = -\boldsymbol{B}_k^\top \boldsymbol{S}_{k+1}\boldsymbol{A}_k, \tag{4.25}$$

which yields the final equation (Eq. (4.9)) given in the theorem. Let us write Eq. (4.23) again as:

$$\boldsymbol{S}_k = \boldsymbol{A}_k^\top \boldsymbol{S}_{k+1}\boldsymbol{A}_k + \boldsymbol{K}_k^\top \left(\boldsymbol{R}_k + \boldsymbol{B}_k^\top \boldsymbol{S}_{k+1}\boldsymbol{B}_k\right)\boldsymbol{K}_k + \boldsymbol{A}_k^\top \boldsymbol{S}_{k+1}\boldsymbol{B}_k\boldsymbol{K}_k + \boldsymbol{K}_k^\top \boldsymbol{B}_k^\top \boldsymbol{S}_{k+1}\boldsymbol{A}_k + \boldsymbol{C}_k^\top \boldsymbol{Q}_k\boldsymbol{C}_k, \tag{4.26}$$

which after substitution for $\boldsymbol{K}_k$ from Eq. (4.9) in Eq. (4.23) gives:

$$\boldsymbol{S}_k = \boldsymbol{C}_k^\top \boldsymbol{Q}_k \boldsymbol{C}_k + \boldsymbol{A}_k^\top \boldsymbol{S}_{k+1} \boldsymbol{A}_k - \boldsymbol{A}_k^\top \boldsymbol{S}_{k+1} \boldsymbol{B}_k \left(\boldsymbol{R}_k + \boldsymbol{B}_k^\top \boldsymbol{S}_{k+1} \boldsymbol{B}_k \right)^{-1} \boldsymbol{B}_k^\top \boldsymbol{S}_{k+1} \boldsymbol{A}_k, \qquad (4.27)$$

which again can be written to solve as a backward-recursive equation given as Eq. (4.10) with terminal condition $\boldsymbol{S}_{N+1} = \boldsymbol{C}_{N+1}^\top \boldsymbol{Q}_{N+1} \boldsymbol{C}_{N+1}$. A variation of this theorem can also be proved using the continuous state dynamics as shown in the Appendix.

4.1.2.1 Remark: Relation with LQR

Notice that the feedback gain solution for the problem statement (Eq. (4.9) and Eq. (4.10)) with chosen Lagrange multipliers $\boldsymbol{Q}_k$ has the exact same solution form obtained for the LQR problem with chosen weighting matrices $\boldsymbol{Q}_k$. This suggests that the time-varying output covariance problem can be solved by a substitute LQR control problem which is well understood and have well established algorithms with an associated process to establish judicious choice of $\boldsymbol{Q}$ to enforce the prescribed covariance constraint. The following subsection gives an iterative algorithm we have established, to calculate the corresponding weighting matrices $\boldsymbol{Q}_k$.

4.1.2.2 CAWS : Covariance Assignment via Weight Selection Algorithm

The iterative algorithm used for training the weighting matrix $\boldsymbol{Q}$ is given in **Algorithm**:CAWS (see below). Assuming $\boldsymbol{R}_{0,..,N} = \boldsymbol{I}$ and $\boldsymbol{Q}^0_{1,..,N+1} = \boldsymbol{Q}^0 \; \forall \; k = 1, .., N+1$, where $\boldsymbol{Q}^0$ is a chosen diagonal matrix, the algorithm first evaluates the output covariance ($\boldsymbol{Y}_k^0$) by solving the Riccatti equation. The total number of violations (n_{viol}) over all time steps and states in a single iteration of CAWS are then calculated. For every iteration that carries a non-zero n_{viol} value, the algorithm alters all the elements of the $\boldsymbol{Q}$ matrix at all times as per their individual relative discrepancies expressed in terms of the ratio, $\boldsymbol{Y}_k^i / \bar{\boldsymbol{Y}}_k$. The algorithm continues until the weighting matrices $\boldsymbol{Q}^i_{1,..N+1}$ converges and the total number of violations go to zero.

The act of updating all elements of $\boldsymbol{Q}$ at all times in the i^{th} iteration ensures that any discrepancy in the covariance constraint at any time is collectively accredited by $\boldsymbol{Q}$ alterations throughout the trajectory. While no formal proof has been established, this procedure has been found to give a

Algorithm: Covariance Assignment via Weight Selection Algorithm (CAWS)

Result: $\boldsymbol{Q}_{1,..,N+1}$
initialize $i = 0, \boldsymbol{Q}^i_{1,..,N+1} = \boldsymbol{Q}^0_{1,..,N+1}$,
$n_{\text{viol}} = 1$
while $n_{viol} \geq 1$ **do**
  initialize $k = N$, $\boldsymbol{S}^i_{N+1} = \boldsymbol{C}^\top_{N+1} \boldsymbol{Q}^i_{N+1} \boldsymbol{C}_{N+1}$
  while $k \geq 1$ **do**
    $\boldsymbol{S}^i_k = \boldsymbol{C}^\top_k \boldsymbol{Q}^i_k \boldsymbol{C}_k + \boldsymbol{A}^\top_k \boldsymbol{S}^i_{k+1} \boldsymbol{A}_k - \boldsymbol{A}^\top_k \boldsymbol{S}^i_{k+1} \boldsymbol{B}_k \left(\boldsymbol{R}_k + \boldsymbol{B}^\top_k \boldsymbol{S}^i_{k+1} \boldsymbol{B}_k \right)^{-1} \boldsymbol{B}^\top_k \boldsymbol{S}^i_{k+1} \boldsymbol{A}_k$
    $\boldsymbol{K}^i_k = - \left(\boldsymbol{R}_k + \boldsymbol{B}^\top_k \boldsymbol{S}^i_{k+1} \boldsymbol{B}_k \right)^{-1} \boldsymbol{B}^\top_k \boldsymbol{S}^i_{k+1} \boldsymbol{A}_k$
    $k = k - 1$
  end
  $\boldsymbol{K}^i_0 = - \left(\boldsymbol{R}_0 + \boldsymbol{B}^\top_0 \boldsymbol{S}^i_1 \boldsymbol{B}_0 \right)^{-1} \boldsymbol{B}^\top_0 \boldsymbol{S}^i_1 \boldsymbol{A}_0$
  initialize $k = 0$, $\boldsymbol{P}^i_0 = \boldsymbol{P}_0$
  while $k \leq N$ **do**
    $\boldsymbol{P}^i_{k+1} = (\boldsymbol{A}_k + \boldsymbol{B}_k \boldsymbol{K}^i_k) \boldsymbol{P}^i_k (\boldsymbol{A}_k + \boldsymbol{B}_k \boldsymbol{K}^i_k)^\top + \boldsymbol{D}_k \mathbb{V}_k \boldsymbol{D}^\top_k$
    $\boldsymbol{Y}^i_k = \boldsymbol{C}_k \boldsymbol{P}^i_k \boldsymbol{C}^\top_k$
    $k = k + 1$
  end
  $\boldsymbol{Y}^i_{N+1} = \boldsymbol{C}_{N+1} \boldsymbol{P}^i_{N+1} \boldsymbol{C}^\top_{N+1}$
  $n_{\text{viol}} = \Sigma^N_k (\boldsymbol{Y}^i_k - \bar{\boldsymbol{Y}}_k \geq \epsilon)$
  if $n_{viol} \geq 1$ **then**
    initialize $k = 1$,
    while $k \leq N + 1$ **do**
      $Q^{i+1}_k = \frac{Q^i_k(k) \boldsymbol{Y}^i_k}{\bar{\boldsymbol{Y}}_k}$
      $k = k + 1$
    end
  end
  $i = i + 1$
end

near-unique $\boldsymbol{Q}$ profile for all its elements. In other words, if the elements of $\boldsymbol{Q}^0$ are selected sufficiently small such that there are at least some violations at the beginning of the training algorithm, it is observed numerically that the converged $\boldsymbol{Q}$ appears to be unique to within some tolerance. The training of $\boldsymbol{Q}$ in this fashion to satisfy the time-varying covariance constraint alters the gain, $\boldsymbol{K}_k$ and therefore the control input sequence. As with all LQR applications, the feasibility of the controls if one considers actuator saturation bounds is a practical issue one must address. In actual applications, the time-varying covariance commanded may not be physically realizable. For the case that this process control magnitude, $||\boldsymbol{u_k}||$ to exceed the maximum bound, insights can be obtained regarding choosing $\boldsymbol{P_k}$ to make $\boldsymbol{Y}_k - \bar{\boldsymbol{Y}}_k$ as small as possible while satisfying the control bounds.

4.1.3 Example Application

4.1.3.1 Attitude maneuver

Telemetry, tracking and control subsystem provides vital communication that facilitates observation of the spacecraft's state from the ground and transmission of commands from the ground control to the satellite for guidance or conducting particular science operations, etc. Telemetry relay satellites provide essential data like spacecraft's attitude, operational state, and navigational data as well as timely down-link collected scientific data. This requires these satellites to constantly point to the receiving ground station for transmitting and receiving data. Therefore, along with the requirement of very low maneuver errors at the end of the orientation change, the pointing maneuvers of these satellites have stringent constraints on the angular errors throughout the maneuver to ensure a high quality data transmission. In the case that the orbit is eccentric, it is obvious that the required covariance of pointing errors will necessarily be time varying. Therefore, the attitude control problem of such satellites provides a good example to demonstrate the capability of the proposed algorithm.

Attitude dynamics:

This sub-section establishes the attitude control dynamics of rigid spacecraft whose attitude is

described by the Classical Rodrigues Parameters (CRPs). The CRPs constitute a symmetric stereographic set that exhibits uniqueness and is quasi-linear for large angular motions [116], earning them the position of being one of the favorable sets of parameters for attitude dynamics. Unlike the transcendental expressions used in the case of Euler angles, CRPs provide purely algebraic expressions for the governing kinematic equations of motion. The domain of linearization and non-singular notion are also quite large as compared to the Euler angle parametrization [71]. The CRPs can be defined in terms of Euler's principal rotation axis ($\hat{\mathbf{e}}$) and the principal angle (Φ) through the relation [88]:

$$\boldsymbol{q} = \hat{\boldsymbol{e}} \tan\left(\frac{\Phi}{2}\right). \tag{4.28}$$

Therefore, the singularity condition in the CRPs is encountered only when the principal angle approaches 180 deg. The kinematic relations are then given by [116]:

$$\begin{aligned} \dot{\boldsymbol{q}} &= \boldsymbol{A}\boldsymbol{\omega}, \\ \boldsymbol{A} &= \frac{1}{2}\left(\boldsymbol{I}_{3\times 3} + [\tilde{\boldsymbol{q}}] + \boldsymbol{q}\boldsymbol{q}^{\top}\right), \end{aligned} \tag{4.29}$$

where, $\tilde{\boldsymbol{q}} = \begin{pmatrix} 0 & -q_3 & q_2 \\ q_3 & 0 & -q_1 \\ -q_2 & q_1 & 0 \end{pmatrix}$, $\boldsymbol{q} = [q_1, q_2, q_3]^{\top}$ and ω is the angular velocity of the rigid body which can be conveniently evaluated by inverting Eq. (4.29) as given in [116]:

$$\boldsymbol{\omega} = \boldsymbol{B}\dot{\boldsymbol{q}}, \tag{4.30a}$$

$$\boldsymbol{B} = \frac{2}{(1 + \boldsymbol{q}^{\top}\boldsymbol{q})}(\boldsymbol{I}_{3\times 3} - [\tilde{\boldsymbol{q}}]). \tag{4.30b}$$

Using Euler's equation for rigid body motion, the differential equation of angular velocity can be written as:

$$\dot{\boldsymbol{\omega}} = J_{\text{mat}}^{-1}(\boldsymbol{\omega} \times (J_{\text{mat}}\boldsymbol{\omega}) + \boldsymbol{u}), \tag{4.31}$$

where J_{mat} is a diagonal matrix (in the present example) with spacecraft's principal moment of inertia values (J_1, J_2, J_3) put as its diagonal entries. Therefore, the dynamics assumes a cascade form of system where the control, $\boldsymbol{u}$ drives the angular velocities which in turn control the orientation using the first kinematic equation (Eq. (4.29)). The system differential equations in the state space form can be expressed as:

$$\dot{\boldsymbol{x}} = \mathscr{F}(\boldsymbol{x}, \boldsymbol{u}, t) = \mathbb{A}(\boldsymbol{x}, t) + \mathbb{B}(\boldsymbol{x}, t)\boldsymbol{u}, \tag{4.32}$$

where

$$\mathbb{A} = \begin{bmatrix} \frac{1}{2}(1+q_1^2)\omega_1 + (q_1q_2 - q_3)\omega_2 + (q_1q_3 + q_2)\omega_3 \\ \frac{1}{2}(1+q_2^2)\omega_2 + (q_1q_2 + q_3)\omega_1 + (q_2q_3 - q_1)\omega_3 \\ \frac{1}{2}(1+q_3^2)\omega_3 + (q_3q_1 - q_2)\omega_1 + (q_3q_2 + q_1)\omega_2 \\ \frac{(J_2-J_3)}{J_1}\omega_2\omega_3 \\ \frac{(J_3-J_1)}{J_2}\omega_1\omega_3 \\ \frac{(J_1-J_2)}{J_3}\omega_1\omega_2 \end{bmatrix}, \quad \mathbb{B} = \begin{bmatrix} \mathbf{0}_{3\times 3} \\ J_{\text{mat}}^{-1} \end{bmatrix}.$$

and $\boldsymbol{x} = [q_1, q_2, q_3, \omega_1, \omega_2, \omega_3])$.

Design of the nominal trajectory using optimal control theory:

Considering a finite horizon problem, the nominal trajectory for the maneuver is evaluated using optimal control theory with an objective to minimize the control effort. Therefore, the optimal control problem (OCP) can be stated as

$$\begin{aligned} \text{Minimize } \ J &= \int_{t_0}^{t_f} \frac{1}{2}\boldsymbol{u}^\top \boldsymbol{u} dt, \\ \text{subject to :} \quad & \text{Equation (4.32)}, \\ & \boldsymbol{x}(t_f) - \tilde{\boldsymbol{x}}_d = \mathbf{0}, \\ & \boldsymbol{x}(t_0) = \boldsymbol{x}_0, \end{aligned} \tag{4.33}$$

where t_0 is the initial time, $\boldsymbol{x_0}$ are the the states at the initial time, t_f is the final time, $\Delta t = t_f - t_0$ is the time of flight, and $\tilde{\boldsymbol{x}}_d$ are the desired states at the final time.

The Hamiltonian associated with the defined OCP can be written as:

$$H = \frac{1}{2}\boldsymbol{u}^\top \boldsymbol{u} + \boldsymbol{\lambda}^\top \left(\mathbb{A}(\boldsymbol{x}, t) + \mathbb{B}(\boldsymbol{x}, t)\boldsymbol{u}\right), \tag{4.34}$$

where $\boldsymbol{\lambda} = [\lambda_{q_1}, \lambda_{q_2}, \lambda_{q_3}, \lambda_{w_1}, \lambda_{w_2}\lambda_{w_3}]^\top$ are the costate of the system. Since the control variable $\boldsymbol{u}$ is unbounded and appears non-linearly in the Hamiltonian, strong form of optimality can be used to give:

$$\boldsymbol{u} = -\mathbb{B}(\boldsymbol{x}, t)^\top \boldsymbol{\lambda}. \tag{4.35}$$

Here, the $\boldsymbol{u}$ is defined in the spacecraft's body frame. The co-states differential equation is derived using Euler-Lagrange equation,

$$\dot{\boldsymbol{\lambda}} = -\left[\frac{\partial H}{\partial \boldsymbol{x}}\right]^\top = \begin{bmatrix} \dot{\boldsymbol{\lambda}}_{\boldsymbol{q}} \\ \dot{\boldsymbol{\lambda}}_{\boldsymbol{\omega}} \end{bmatrix}. \tag{4.36}$$

Since the value of co-states at both initial and final boundary are unknown, TPBVP is solved to satisfy the boundary conditions defined in Eq. (4.33) using MATLAB's *fsolve* solver.

For conducting the linear covariance analysis for controller design, a linear discretized version of the system equations is obtained by piecewise linearizing about the nominal trajectory using the crude Euler's method with an integration step size of h seconds. Therefore, the resulting system matrices used for designing the controller are:

$$\begin{aligned} &\mathscr{A}_c = \left.\frac{\partial \mathscr{F}(\boldsymbol{x}, \boldsymbol{u}, t)}{\partial \boldsymbol{x}}\right|_{\bar{\boldsymbol{x}}_i, \bar{\boldsymbol{u}}_i}, \quad \mathscr{B}_c = \left.\frac{\partial \mathscr{F}(\boldsymbol{x}, \boldsymbol{u}, t)}{\partial \boldsymbol{u}}\right|_{\bar{\boldsymbol{x}}_i, \bar{\boldsymbol{u}}_i} \\ &\mathscr{A}_d = \boldsymbol{I}_{6\times 6} + h\mathscr{A}_c, \quad \mathscr{B}_d = h\mathscr{B}_c \end{aligned} \tag{4.37}$$

where, $\bar{\boldsymbol{x}}_i$ and $\bar{\boldsymbol{u}}_i$ are the state and controls on the nominal trajectory at the i^{th} time step and $[\cdot]_c$ and $[\cdot]_d$ are the linearized system matrices for continuous and discrete time dynamics equations.

4.1.3.2 Interplanetary maneuver

There is a significant economic impact of trajectory optimization on space missions. Specifically, with the advent of ion based electric propulsion, multi-year low thrust missions have emerged that are both challenging in terms of optimization as well as tracking. In this example, only the heliocentric phase of the trajectory where the motion is predominantly governed by the Sun's gravitational force is considered. As a consequence, weakly perturbed Keplerian motion is preserved.

Spacecraft dynamics:

The underlying dynamics, even when two body assumptions are made, is significantly more nonlinear than the attitude maneuver problem. To regularize the dynamics, additional normalization techniques are employed as well as a superior coordinate set of modified equinoctial elements is selected to describe the dynamics.

Nominal Open-loop Trajectory:

For generating the nominal trajectory, we optimize with respect to minimizing fuel consumption in place of maximizing the payload delivered, which should be chosen as an objective if a larger spacecraft design space is to be explored [43]. The resulting TPBVP is solved using the default settings of MATLAB's *fsolve* function which uses finite difference to evaluate the gradients.

4.1.4 Numerical Results

Using the algorithm explained in Section II and dynamics provided in Section III, we have solved two examples comprising of: 1) Attitude maneuver, and 2) Interplanetary maneuver.

4.1.4.1 Attitude maneuver

In this example, we solve a problem of orienting an asymmetric satellite from orientation $\mathring{A}$ to $\mathring{B}$ in fixed time. The boundary conditions of the maneuver are given in Table 4.1 where $\boldsymbol{x}_{\mathring{\boldsymbol{A}}}$ and $\boldsymbol{x}_{\mathring{\boldsymbol{B}}}$ define the states at orientation $\mathring{A}$ and $\mathring{B}$ respectively. Table 4.1 also lists the parameters used in the tracking problem where σ_0 defines the standard deviation of the uncertainty in the states at orientation A_0 and $\tilde{\sigma}$ sets the upper bound on the output state error which is used to provide the desired output covariance profile. The σ_0 and $\tilde{\sigma}$ values given in Table 4.1 are constants and are

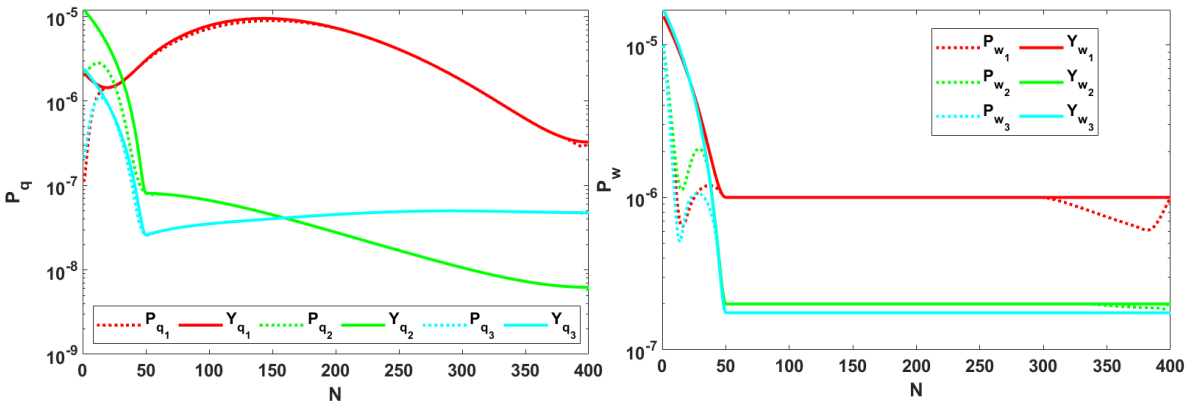

Figure 4.1: Time history of the diagonal entries of the output covariance for all states using the $\boldsymbol{Q}_d$ matrix designed by CAWS.

given in degrees which are accommodated and transformed into CRPs using the 3-2-1 Euler angle sequence rotation by angles θ_1, θ_2 and θ_3, respectively. The non-linear transformation required to transform CRPs into Euler angles is obtained by using the Cayley transform identity. The resulting direction cosine matrix used for this transformation is [**?**]:

$$\mathscr{C} = \frac{1}{(1+\boldsymbol{q}^\top\boldsymbol{q})}\left((1-\boldsymbol{q}^\top\boldsymbol{q})\boldsymbol{I}_{3\times3} + 2(\boldsymbol{q}\boldsymbol{q}^\top) - 2\tilde{\boldsymbol{q}}\right). \tag{4.38}$$

Table 4.1: Boundary conditions and parameters

$\boldsymbol{J}_{\text{mat}}$	diag([10,6,8])
$\boldsymbol{x}_{\mathring{\boldsymbol{A}}}$ (deg., rad/sec)	$[-10^o, 20^o, 8^o, 0.1, -0.0011, 0.01]$
$\boldsymbol{x}_{\mathring{\boldsymbol{B}}}$ (deg., rad/sec)	$[20^o, 5^o, 30^o, 0, 0, 0]$
t_f (sec)	40
N	400
σ_0 (deg, rad/sec)	$[2^o, 2^o, 2^o, 0.01, 0.01, 0.01]$
$\tilde{\sigma}$ (deg.,rad/sec)	$[0.5^o, 0.5^o, 0.5^o, 10^{-3}; 5\times10^{-4}; 5\times10^{-4}]$
$\mathbb{V}$ (N^2m^2)	$[0, 0, 0, 10^{-7}, 10^{-7}, 10^{-7}]$
$\boldsymbol{Q_0}$	$10^{-10}\boldsymbol{I}_{6\times6}$
$\boldsymbol{R}$	$\boldsymbol{I}_{6\times6}$

After performing the transformations discussed above at every discrete time step, the resulting covariance profiles (denoted by $\boldsymbol{Y}$) are plotted as solid lines in the left plot of Fig. 4.1. The actuators are assumed to generate continuous control profile like in the case of momentum wheels or gas jet actuators with pulse width pulse frequency modulators. As given in Table 4.1, the time of the maneuver is set as $t_f = 40$ seconds which is discretized into $N = 400$ steps making the bandwidth of the controller to be 10Hz. The uncertainty in the system dynamics is modeled via a zero-mean Gaussian white noise, $\boldsymbol{\nu} : \mathcal{N}(0, \mathbb{V}) \in \mathbb{R}^6$. Since the kinematic relation (given in Eq. (4.29)) is exact, no noise is assumed in the first three channels of the states as shown in Table 4.1.

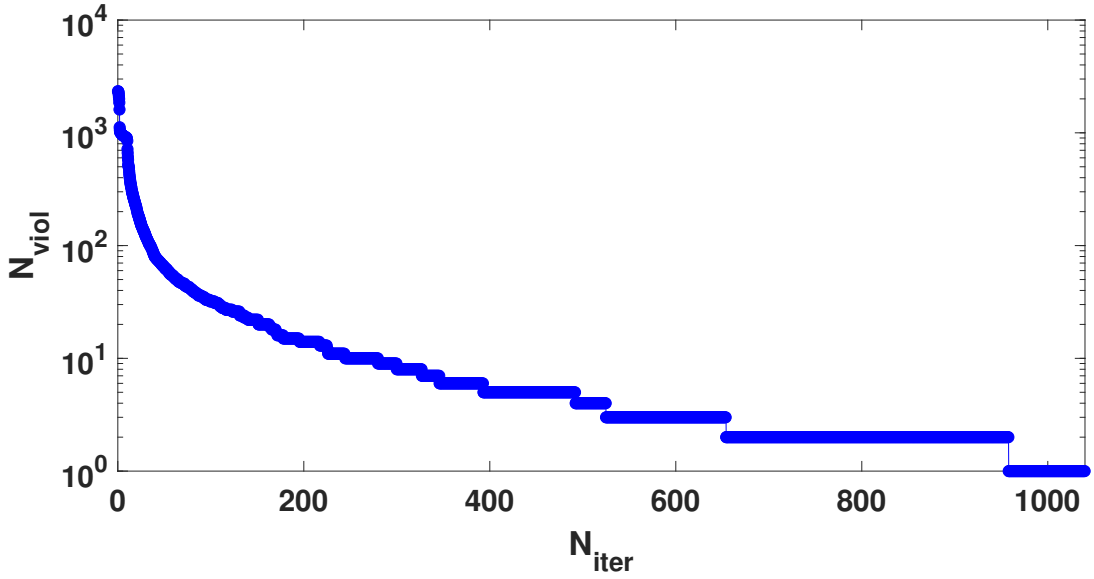

Figure 4.2: Rate of elimination of time points that violate the covariance bound constraint during CAWS.

The initial uncertainty and noise parameters used for training $\boldsymbol{Q}$ in CAWS are set to be a little higher than the one actually used in the non-linear simulation to design the feedback control on a more conservative system. Using the parameters for initial uncertainty and stochastic actuator errors defined in Table 4.1, CAWS algorithm is applied on the linearized system to obtain a time-

varying profile of $\boldsymbol{Q}$ iteratively (N_{iter} iterations). Starting from some initial number of covariance violations for each of the states, the violations decrease gradually to converge with no violations towards the end as shown in Fig. 4.2. As the number of violations decreases, the change in the magnitude of each of the diagonal entries of the $\boldsymbol{Q}$ matrix also converges as per the set tolerance. It is not necessary that the number of violations and the change in the norm of $\boldsymbol{Q}$ monotonically decreases throughout the training iterations as shown in Fig. 4.2.

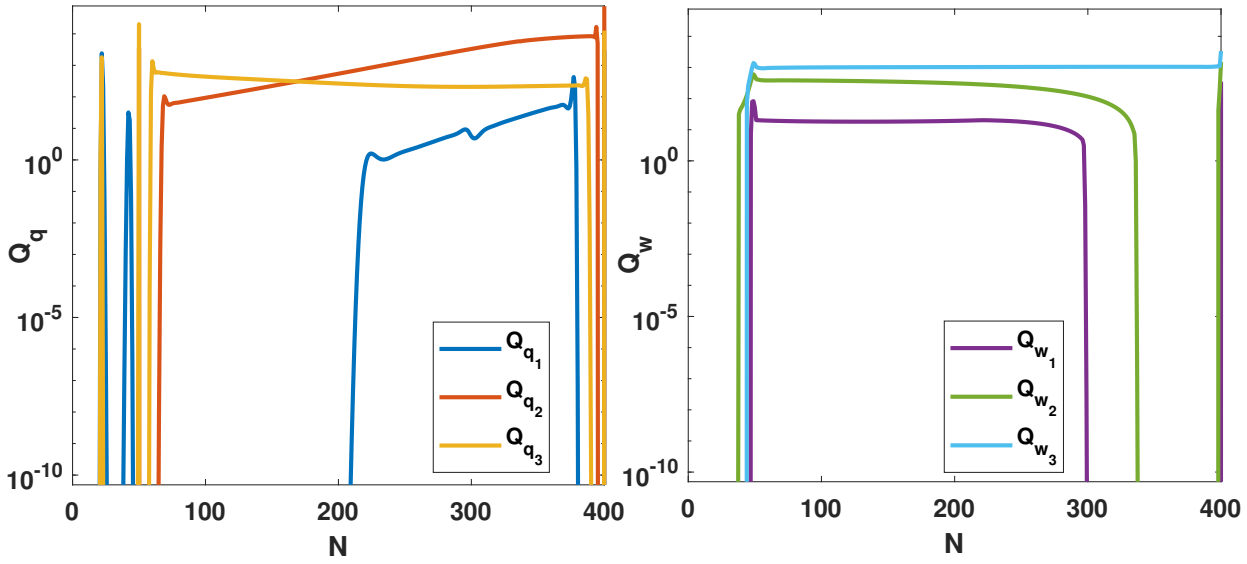

Figure 4.3: Diagonal entries for the designed $\boldsymbol{Q}_d$ matrix profile plotted against time-steps.

Fig. 4.1 shows the time history of the pre-specified covariance bounds and the diagonal entries of the achieved state covariance using the $\boldsymbol{Q}_d$ matrix designed by the iterative algorithm (CAWS). For the linearized system, one can observe that the actual covariances (solid lines) follow the specified covariance profile (dotted lines) in Fig. 4.1, exactly except for few short time periods where it stays below the hard limit of the set covariance bound. This is owing to the cross-coupling of states in the natural dynamics of the system. In other words, it is possible that in order to follow the covariance profile set for q_1, tighter bounds are required for q_2 as per the natural dynamics of the system. It also aids in conserving on the extra control effort that would have been required

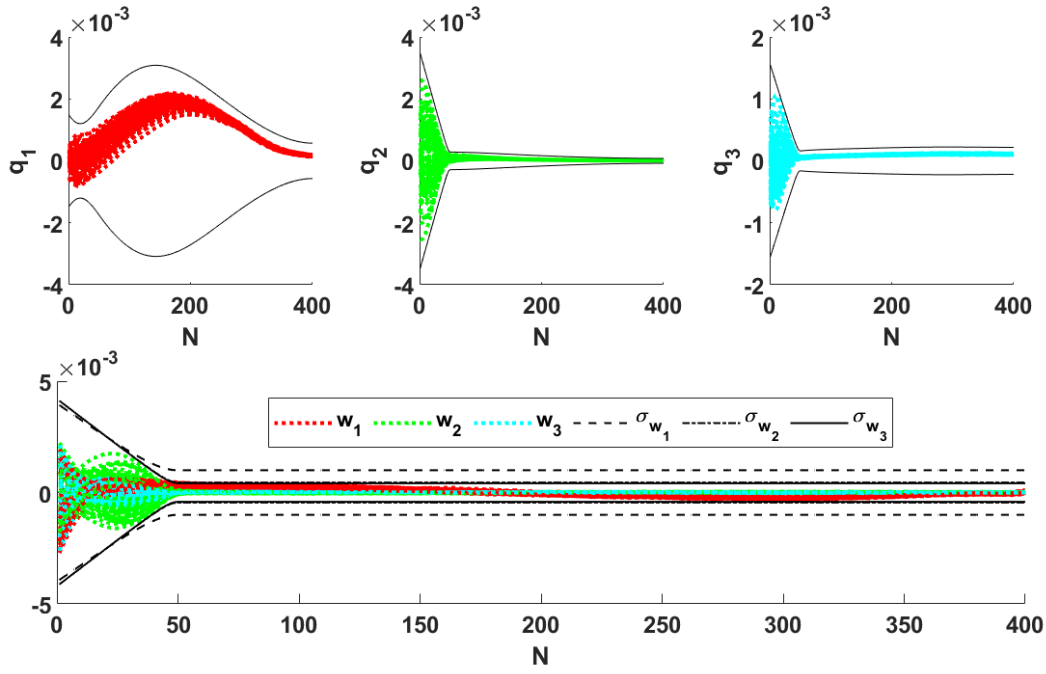

Figure 4.4: Time history of errors in CRPs and angular velocities plotted against time with the black lines (solid or dashed) denoting the set covariance bound for time varying $\boldsymbol{Q}$.

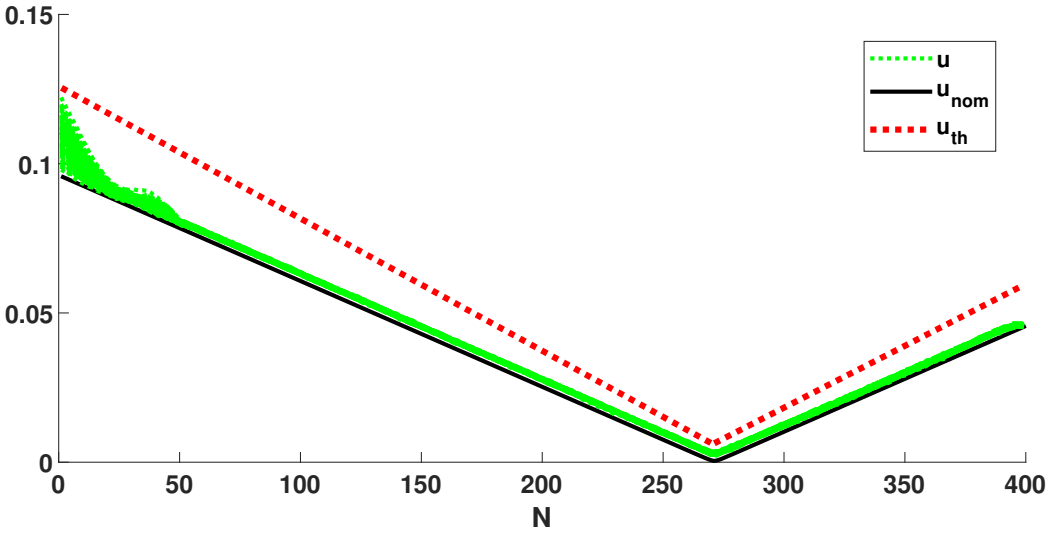

Figure 4.5: Time history of controls for 100 sample trajectories for time varying $\boldsymbol{Q}$.

to supersede the natural dynamics and match the covariance profile exactly. Fig. 4.3 provides the diagonal entries for $\boldsymbol{Q}_d$ matrix for both CRPs and angular velocity errors plotted against time. Here, the values of $\boldsymbol{Q}_d$ are truncated at 10^{-12} by considering it essentially as 0 as per machine precision.

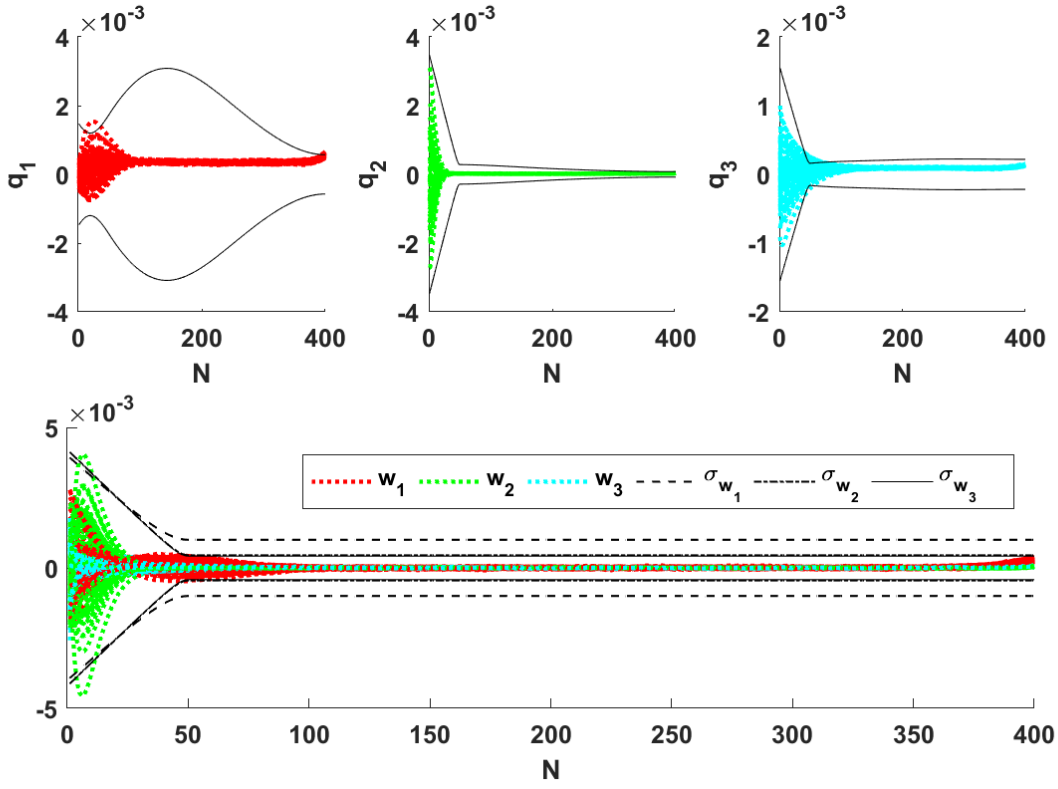

Figure 4.6: Time history of errors in CRPs and angular velocities plotted against time with the black lines (solid or dashed) denoting the prescribed covariance bound for constant $\boldsymbol{Q}_c$ case.

Post designing $\boldsymbol{Q}_d$ to solve the covariance assignment problem on the linearized system, the performance of the designed feedback control is illustrated using a small Monte Carlo analysis for 100 trajectories sampled from the initial distribution of process noise and initial covariance errors. Since the attitude dynamics, when designed using CRPs, is not highly non-linear, one can notice that the trajectories in Fig. 4.4 not only stay within the bounds (plotted as solid black lines) but the profile of the trajectories for the CRPs follow the shape of the covariance profile set in

the linearized system as shown in Fig. 4.1. Fig. 4.5 shows the time history of the magnitude of control torques applied for 100 sample trajectories. The black solid line featuring a very short "no control" arc near over the middle of the maneuver is the nominal control (u_{nom}) obtained using optimal control theory. The red dotted line denotes the upper bound (20% over the nominal value) on the total control effort allowed for the purpose of tracking the nominal trajectory. Even when no actuator constraints are formally imposed in our algorithm, Fig. 4.5 shows that the required feedback control does not violate the upper bound set over the nominal control.

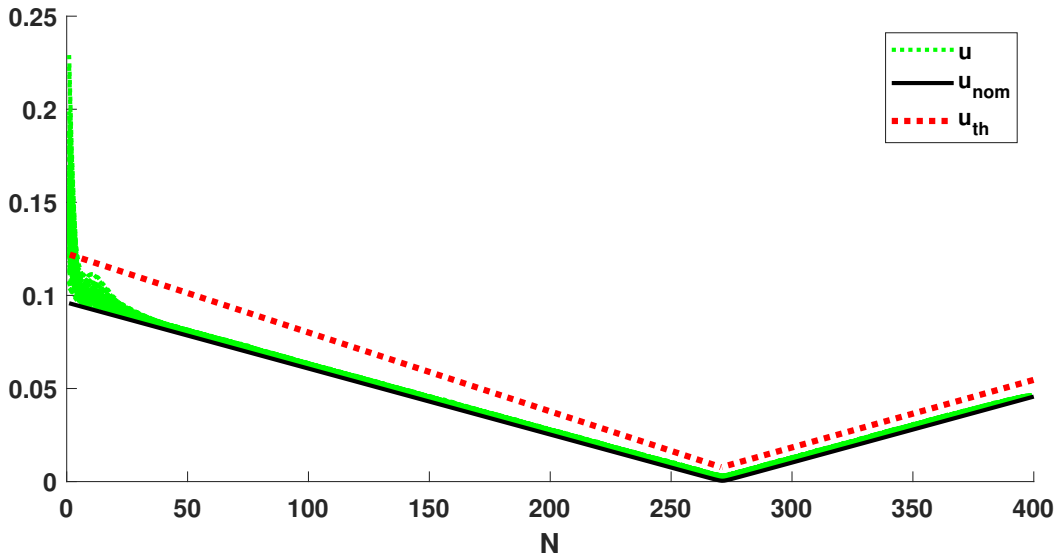

Figure 4.7: Time history of controls for 100 sample trajectories for constant $\boldsymbol{Q_c}$ case.

In order to demonstrate the advantage of our time-varying covariance constrained $\boldsymbol{Q}$ training algorithm over the classic constant $\boldsymbol{Q_c}$ strategy for solving traditional LQR, Monte Carlo runs for 100 trajectories are repeated keeping the $\boldsymbol{Q_c}$ values constant. The candidate values for the diagonal components of the constant $\boldsymbol{Q_c}$ is obtained by taking an average of the elements of $\boldsymbol{Q}_d$ profile such that:

$$\boldsymbol{Q_c} = [22, 2169, 332.3, 12.32, 210, 900].$$

The time history of state errors and actuator magnitude obtained from the Monte Carlo analysis is given in Figs. 4.6 and 4.7. The results, though inferior to the results obtained by using CAWS, feature few violations, mainly at the beginning of the maneuver and towards the end. Traditionally, the constant $\boldsymbol{Q_c}$ values are iteratively composed by utilizing the experience and time of the control designer. One possible application of the proposed method is to provide a better starting iteration for the designer if constant $\boldsymbol{Q_c}$ solutions are ultimately desired.

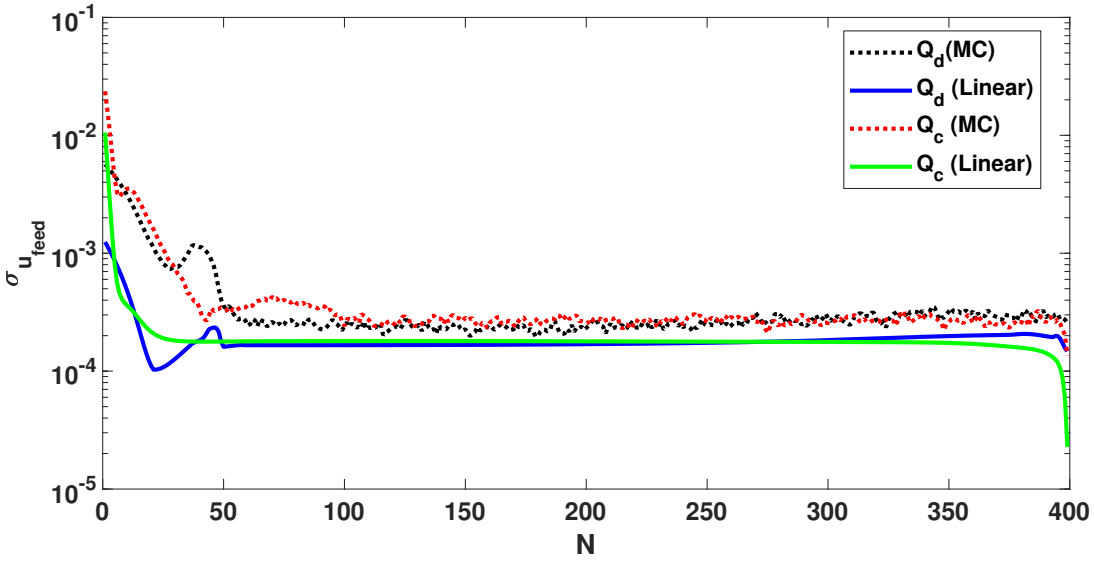

Figure 4.8: Comparison of standard deviation of feedback control history for designed $\boldsymbol{Q_d}$ and constant $\boldsymbol{Q_c}$ cases on linearized system and the non-linear Monte Carlo (MC) simulations.

The control effort required in the case of constant $\boldsymbol{Q_c}$ is almost twice the defined control threshold but only at the beginning of the maneuver as shown in Fig. 4.7. This high value of controls is probably attributed to controller's act of tracking the nominal while accounting for large initial uncertainties as they occur. This does not happen in the case of variable $\boldsymbol{Q_d}$ designed by CAWS due to the facility of effectively distributing the control effort throughout the maneuver to counter any tracking errors owing to either initial uncertainty or disturbances. Fig. 4.8 shows the standard deviation of feedback control efforts for constant $\boldsymbol{Q_c}$ and designed $\boldsymbol{Q_d}$ weighting matrices over the

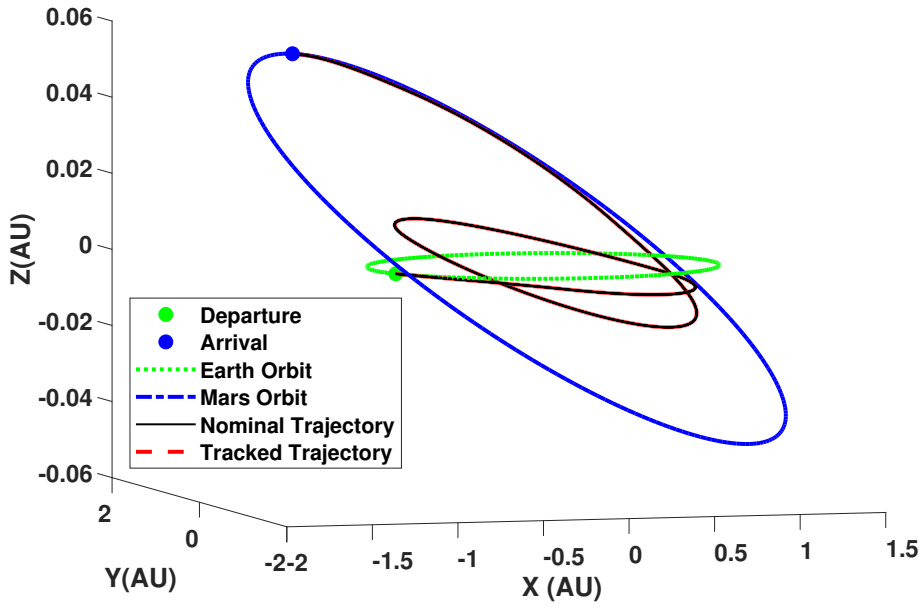

Figure 4.9: Nominal fuel optimal trajectory from Earth to Mars with dashed lines displaying tracked trajectories.

complete time horizon. The figure shows the standard deviation for the linearized and nonlinear cases where linearized control efforts are calculated using square root of $\mathrm{Tr}(\boldsymbol{U}_k) = \mathrm{Tr}\big(\boldsymbol{K}_k \boldsymbol{P}_k \boldsymbol{K}_k^\top\big)$ and the control efforts for the nonlinear case are calculated statistically by running 100 Monte Carlo simulations. Notice that the feedback control effort for the designed $\boldsymbol{Q_d}$ case is smaller than the constant $\boldsymbol{Q_c}$ case for the initial time-steps for both linear and nonlinear results owing to effectively distributing the control effort. Therefore, this example serves the purpose of effectively illustrating the proposed ideas. Another example involving a different physics is considered next.

4.1.4.2 Interplanetary maneuver

In this example, we have a powered orbit transfer from Earth to Mars with the spacecraft making a single en-route revolution around the Sun in a fixed time of 630 days, as shown in Fig.

4.9. The boundary conditions are:

$$\begin{aligned}
\boldsymbol{r}_0 =& [-140699693, -51614428, 980]^\top \text{km}, \\
\boldsymbol{v}_0 =& [\,9.774596, -28.07828, 4.337725 \times 10^{-4}]^\top \text{km/s}, \\
\tilde{\boldsymbol{r}} =& [-172682023, 176959469, 7948912]^\top \text{km}, \\
\tilde{\boldsymbol{v}} =& [-16.427384, -14.860506, 9.21486 \times 10^{-2}]^\top \text{km/s}.
\end{aligned}$$

For the normalization, we have adopted for our calculations canonical units for scaling the vari-

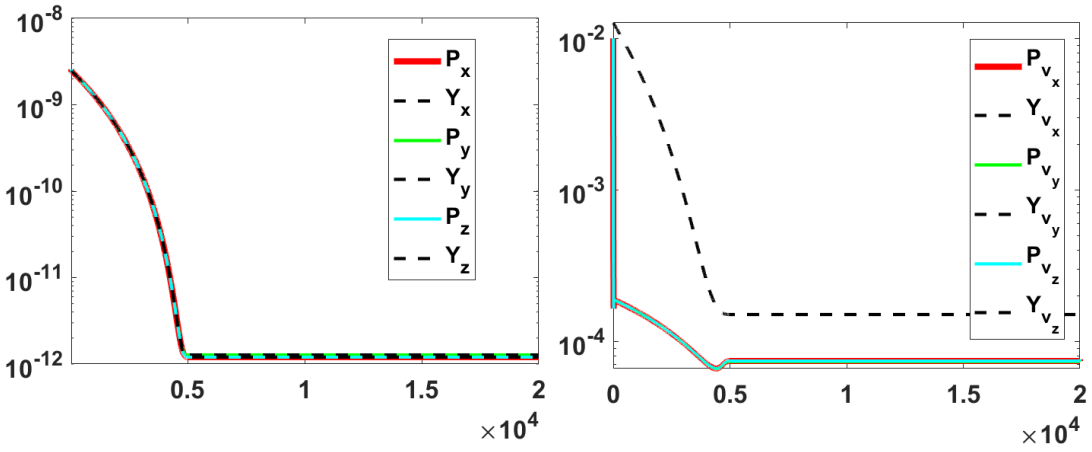

Figure 4.10: Time history of the diagonal entries of the output covariance for all states using the $\boldsymbol{Q}_d$ matrix designed by CAWS. The dashed black lines here are the set covariance bounds on the individual states.

ables such that one distance unit (DU) is equal to one astronomical unit (AU), and the Time Units (TU) is equal to $\frac{1}{2\pi}$ year. The parameters of the nuclear electric propulsion system used for the engine are extracted after the model of SPT-140 engine. Therefore, assuming an initial mass of the spacecraft as 1000kg, T = 0.264N, and Isp = 1645 s , are assumed. The optimal control problem in this case is solved using MEEs but the tracking algorithm is implemented using a Cartesian coordinate system. If you look carefully at the systems of the two examples (see Eqs.(4.32) & (2.5)),

the two differential equations in the second example are co-dependent unlike the cascade type system observed in the first example. Therefore, defining a covariance profile for the interplanetary maneuver for both position and velocity requires more care. In our case, the desired covariance profile is defined assuming a constant threshold for both position and velocity states throughout the maneuver as given in Table 4.2. The other settings like the initial covariance, σ_0, initial $\boldsymbol{Q}$ ($\boldsymbol{Q_0}$), $\boldsymbol{R}$ and noise covariance, $\mathbb{V}$ are also given in the same table. Since, the first relation in Eq. (2.5) is kinematic in nature, no noise is added in the first three equations corresponding to the position differential equation.

Table 4.2: Tracking parameters for interplanetary maneuver

N	20000
σ_0 (AU, VU)	$[5 \times 10^{-5}, 5 \times 10^{-3}]$
$\tilde{\sigma}$ (AU,VU)	$[5 \times 10^{-7}, 5 \times 10^{-4}]$
$\mathbb{V}$ (N^2/kg^2)	$10\%\ u_{nom}$
$\boldsymbol{Q_0}$	$10^{-10}\boldsymbol{I}_{6\times6}$
$\boldsymbol{R}$	$\boldsymbol{I}_{6\times6}$

In this example problem, the controller is again trained (using CAWS) assuming a conservative system with slightly higher initial covariances and noise parameters. As shown in Fig. 4.11, the total number of violations rapidly drop in the first 50 iterations, followed by a gradual convergence gradient to reach zero violations in ≈ 670 iterations. The converged $\boldsymbol{Q}$ matrices, $\boldsymbol{Q}_d$, are plotted in Fig. 4.12, where the values for $\boldsymbol{Q}_d$ matrices associated with position are $\mathbb{O}^8$ higher than the velocity values. One of the reasons for this stark difference in weighting is due to the normalization. Also, it can be observed from Fig. 4.10, how the linear covariance for position(P_x, P_y, P_z), match the desired covariance profile exactly while the linear covariance for velocity ($P_{v_x}, P_{v_y}, P_{v_z}$) remains below the desired velocity covariance threshold. This results in smaller values of $\boldsymbol{Q}_d$ associated with velocity, but not tending to zero because the errors in the velocity also feed into the position errors.

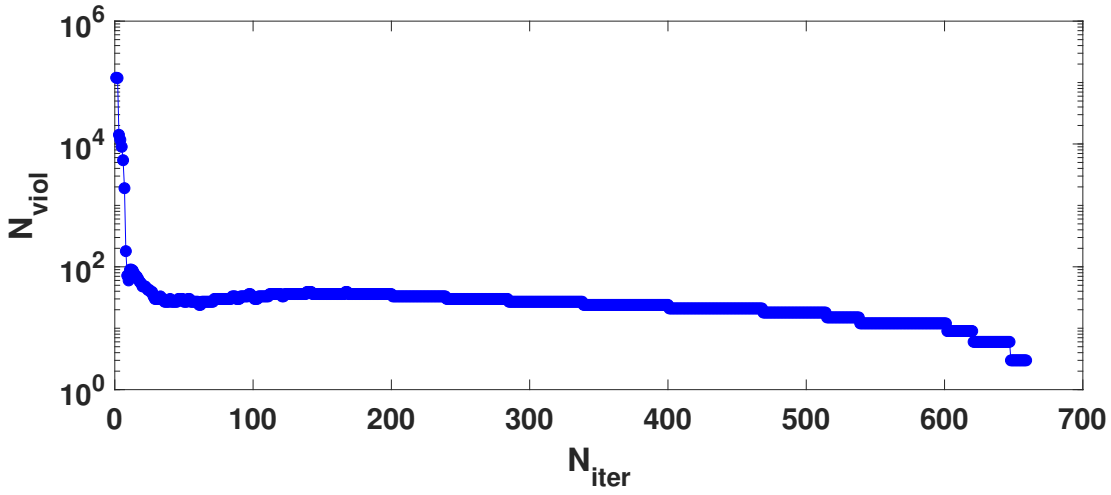

Figure 4.11: Rate of elimination of time points that violate the covariance bound constraint during CAWS.

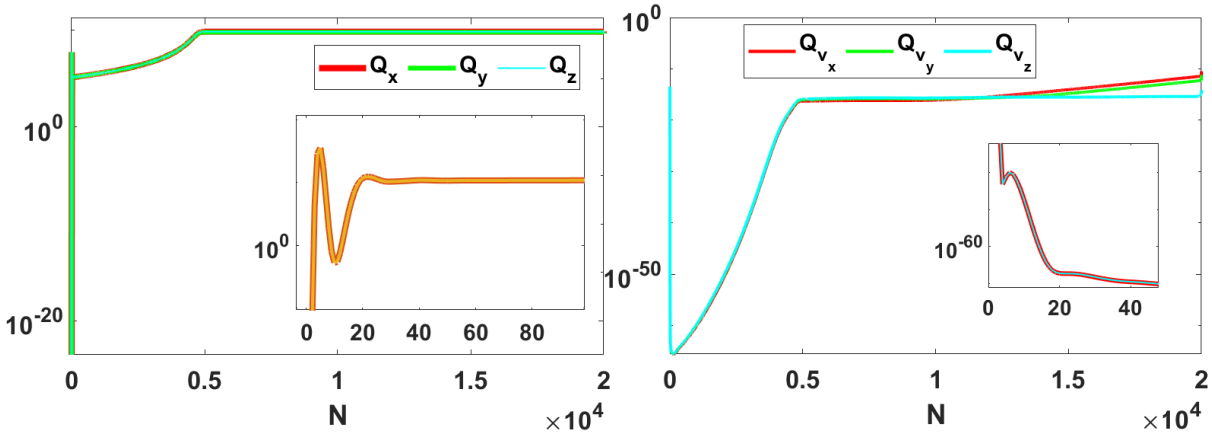

Figure 4.12: Diagonal entries for the designed Q_d matrix profile plotted against time-steps. Both figures are accompanied by a zoomed-in mini-plot to illustrate the fine variations in the profile at the initial time steps.

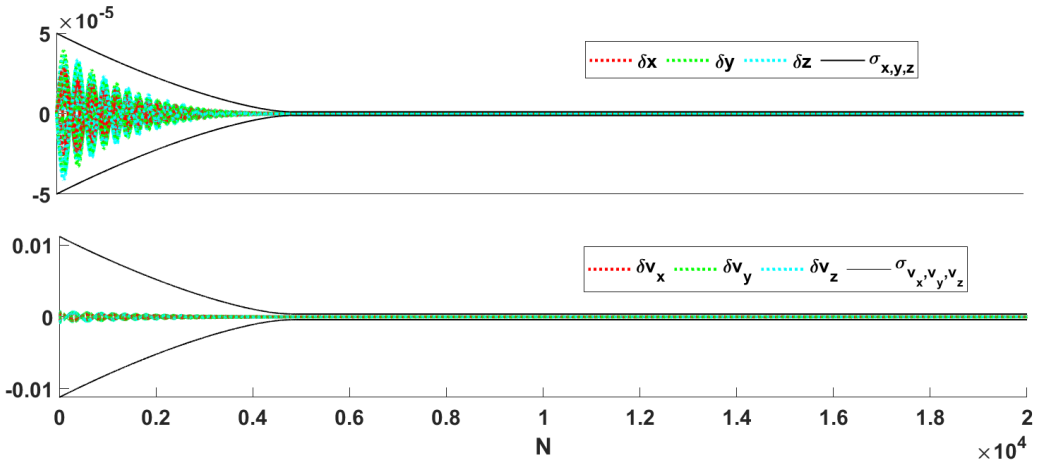

Figure 4.13: Time history of errors in position and velocity plotted against time with the solid black lines denoting the set covariance bound for time varying $\boldsymbol{Q}$. The large difference between the scaling of the two plots is due to the normalization scheme adopted.

Similar to the previous example of attitude maneuver, the control gain evaluated using the designed weights, $\boldsymbol{Q}_d$ are tested on the actual non-linear system perturbed by a Gaussian noise of covariance $\mathbb{V}$. We assume that the actuator error accommodates both the magnitude of the thrusting capacity of the engine as well as the pointing errors. The history of nominal control obtained from optimal control theory is approximated with the help of 6^{th} order polynomial in time to use in the Monte carlo runs. These sample 100 trajectories stay within the specified bounds as shown in Fig. 4.12. The initial errors in position are set to stay within 5×10^{-5}AU to gradually obtain the desired constant precision for the remaining 85% of the total maneuver. The feedback control effort required for all the 100 trajectories to adhere to the covariance constraint mostly stay within the threshold (u_{th}) which is fixed at 20% over the nominal control effort as plotted in Fig. 4.14.

It is just at the beginning of the maneuver that the control effort for a couple of trajectories among the 100 samples that violate the control constraint by a very small margin. Unlike the example of attitude manuever, there are three coast arcs in the nominal control profile in this case. For the coast arcs, the 20% threshold is not necessary to be applied since the controller is capable of providing more control effort over the nominal control in those regions. Note that if a variable covariance profile is designed, tighter tolerances during the coast periods could be enforced due

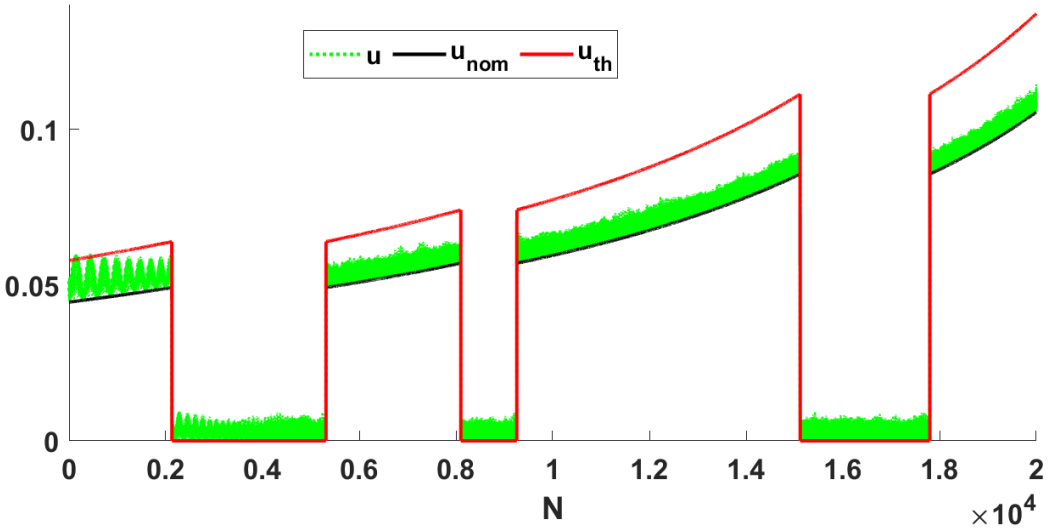

Figure 4.14: Time history of controls for 100 sample trajectories for time varying $\boldsymbol{Q}$.

to a higher capacity for feedback control available to achieve the set constraints. The tracked trajectories (100 runs) are also plotted in Fig. 4.9 which clearly track the nominal to graphical precision on a solar scale. In application, engines like SPT-140 feature multiple operating modes which can be used to realistically accommodate the feedback control into the preliminary analysis of this kind. This can provide any additional modes that are required for tracking the nominal over the modes already selected to form the nominal [91].

In this work, the mass consumption due to the feedback control is also factored into the differential equations of the Monte carlo runs. The instantaneous mass is approximately calculated using the mass differential equation(see Eq. (2.6)) with the thrust value evaluated as per the magnitude of the total control effort written as:

$$u = ||\boldsymbol{u_{nom}} + \boldsymbol{u_{feed}}||, \tag{4.39}$$

$$T = mu. \tag{4.40}$$

Using the above relations, the final mass for all 100 trajectories are plotted in Fig. 4.15 which comes out to be within 3% less than the optimal final mass. The optimal final mass of the spacecraft

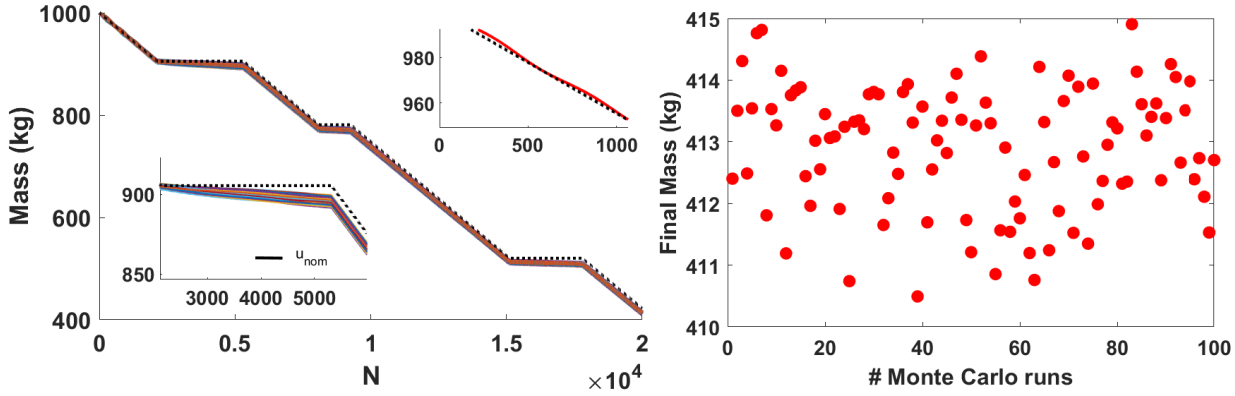

Figure 4.15: Mass history as well as final mass values for the 100 sample trajectories are plotted for time varying $\boldsymbol{Q}$. The dashed black lines in the left figure denote the mass history for the nominal trajectory and the embedded top and bottom mini-plots are the zoomed-in versions of the first encountered thrust and coast arcs respectively.

with respect to the nominal solution is 422.167kg. In Fig. 4.15, it can be observed how the mass consumption slope is non-zero for the disturbed trajectories compared to the nominal (denoted by black dashed line) for the period of the first coast arc. If zoomed in further (see Fig. 4.15), the actual control profiles are not straight lines for any of the thrust arcs as is observed in the case of the nominal trajectory without any feedback control. This is due to the constant mass flow rate assumed in the design of the nominal owing to a constant thrust, constant specific impulse type of actuator. In the case of tracked trajectories, the magnitude of thrust is evaluated using Eq.(4.40) which results in different mass flow rates which are piece-wise constant as per the discretization step.

Therefore, this section introduces a novel formulation and an associated algorithm that allows the control designer to assign a desired time-varying output covariance for a tracking or a guidance-type maneuver by systematically evaluating the time-varying weighting sequences in a simple and elegant LQR framework. The example of an attitude maneuver which has a large domain of linearization shows excellent tracking results where the non-linear error profiles in the Monte Carlo runs match the desired covariance profiles. The same problem when solved using the traditional

constant $\boldsymbol{Q_c}$ approach where the values of the constant $\boldsymbol{Q_c}$ are derived using the variable $\boldsymbol{Q_d}$ profile. The results obtained indicate the superiority of variable $\boldsymbol{Q_d}$ over the constant $\boldsymbol{Q_c}$ case as well as illustrates the usefulness of the proposed method as a potential starting point for iterating on the constant $\boldsymbol{Q}$'s diagonal entries. In case of a more non-linear system associated with interplanetary maneuvers, the utility of the method is demonstrated by how closely the trajectory is tracked while incurring $\approx 1\%$ extra fuel-mass consumption with respect to the initial mass. With only a constant error bound imposed on both position and velocity, it was observed that the errors in position and velocity couple with each other such that in order to obtain certain position error bound, velocity error bounds achievable are somewhat constrained as per the natural dynamics. It is not necessary to have $\boldsymbol{Q}$ as a diagonal matrix. In fact, the current algorithm can be expanded to use the full symmetric matrix $\boldsymbol{Q}$ to include the states cross-coupling weighting into the LQR formulation and this may offer additional advantages.

5. Conclusions & Future Work

This dissertation clearly enhances the class of optimal control problems that can be solved using calculus of variation. Indirect based methods wield Pontryagin's Minimum Principle (PMP) as a weapon that is the key to finding optimal control on the admissible set; be it discrete or discontinuous. A generalized invariant embedding approach is introduced in this work that embeds the Pontryagin necessary conditions into a smooth family (for discrete control, discrete events, discrete constraints) that can smoothly approach satisfaction of the exact necessary conditions with arbitrary precision.

The utility of the developed invariant embedding is displayed on various kind of maneuvers including impulsive, gravity assists and low thrust maneuvers. In case of impulsive, a heretofore unsolved problem of reliably providing optimal multi impulses ≈ 50 and ≈ 100 revolutions was achieved. Using a concept of *switching surfaces*, a class of engines are characterized to explore the engine design space for a fixed time rendezvous maneuver. This dissertation does not only provide mathematical constructs to include the operational aspects in the preliminary mission design but also introduces a framework of multi-disciplinary design optimization for co-optimization of trajectory, spacecraft sub-systems and propulsion system. This framework can be and will be inherited to include many other subsystems and spacecraft components like battery, sun-shield etc. in the future.

The covariance assignment problem solved in this dissertation allows to achieve desired tolerance at any time in the maneuver; therefore serving as an initiating step towards the goal of autonomy. Generally speaking, the future clearly lies in increased autonomy. In that regard, autonomous guidance especially for deep space missions using low thrust multi-mode solar electric propulsion systems is very challenging. To achieve this vision, it is not only crucial to design a nominal trajectory with operational limitations embedded into its framework but to accommodate several contingency in having the ability to re-plan in case of unforeseen failure.

If gridded-ion engines are considered, failures are not manifested only in terms of a com-

plete engine failures but failure of particular modes. This motivates a more directed study on the failure of particular modes or to analyze the robustness of a mission with regards to selecting a sub-optimal neighboring mode. Such actuator failures among other uncertainties are traditionally dealt with by introducing generous margins and conducting linear covariance analysis. These analyses often consider the closed loop guidance controller to provide continuous and unconstrained actuation which can lead to erroneous estimates of tracking robustness and stability. The future work belongs to combining the tracking stochastic control with the uncertain operation of multi-propulsion modes to provide a unified robust guidance scheme.

REFERENCES

[1] V. Petukhov and W. S. Wook, "Joint optimization of the trajectory and the main parameters of an electric propulsion system," *Procedia engineering*, vol. 185, pp. 312–318, 2017.

[2] T. Li and Y. Wang, Z.and Zhang, "Double-homotopy technique for fuel optimization of power-limited interplanetary trajectories.," *Astrophysics and Space Science*, vol. 364, no. 9, pp. 1–12, 2019.

[3] D. Manzella, *Performance Evaluation of the SPT-140*, vol. 206301. National Aeronautics and Space Administration, Lewis Research Center, 1997.

[4] J. T. Betts, "Survey of numerical methods for trajectory optimization," *Journal of guidance, control, and dynamics*, vol. 21, no. 2, pp. 193–207, 1998.

[5] J. T. Betts and S. O. Erb, "Optimal low thrust trajectories to the moon," *SIAM Journal on Applied Dynamical Systems*, vol. 2, no. 2, pp. 144–170, 2003.

[6] R. Bertrand and R. Epenoy, "New smoothing techniques for solving bang–bang optimal control problems—numerical results and statistical interpretation," *Optimal Control Applications and Methods*, vol. 23, no. 4, pp. 171–197, 2002.

[7] R. P. Russell, "Primer vector theory applied to global low-thrust trade studies," *Journal of Guidance, Control, and Dynamics*, vol. 30, no. 2, pp. 460–472, 2007.

[8] T. E. Carter, "Necessary and sufficient conditions for optimal impulsive rendezvous with linear equations of motion," *Dynamics and control*, vol. 10, no. 3, pp. 219–227, 2000.

[9] C. Wen, C. Peng, and Y. Gao, "Reachable domain for spacecraft with ellipsoidal delta-v distribution," *Astrodynamics*, vol. 2, no. 3, pp. 265–288, 2018.

[10] Z. Yang, Y.-Z. Luo, and J. Zhang, "Nonlinear semi-analytical uncertainty propagation of trajectory under impulsive maneuvers," *Astrodynamics*, vol. 3, no. 1, pp. 61–77, 2019.

[11] D. F. Lawden, *Optimal trajectories for space navigation*, vol. 3. Butterworths, 1963.

[12] T. Edelbaum, "How many impulses?," in *3rd and 4th Aerospace Sciences Meeting*, p. 7, 1967.

[13] T. Edelbaum, "Minimum impulse transfers in the near vicinity of a circular orbit," *Journal of the Astronautical Sciences*, vol. 14, p. 66, 1967.

[14] Y.-Z. Luo, J. Zhang, H.-y. Li, and G.-J. Tang, "Interactive optimization approach for optimal impulsive rendezvous using primer vector and evolutionary algorithms," *Acta Astronautica*, vol. 67, no. 3-4, pp. 396–405, 2010.

[15] K. A. Bokelmann and R. P. Russell, "Optimization of impulsive europa capture trajectories using primer vector theory," *The Journal of the Astronautical Sciences*, pp. 1–26, 2019.

[16] O. Abdelkhalik and D. Mortari, "N-impulse orbit transfer using genetic algorithms," *Journal of Spacecraft and Rockets*, vol. 44, no. 2, pp. 456–460, 2007.

[17] M. Pontani and B. A. Conway, "Particle swarm optimization applied to impulsive orbital transfers," *Acta Astronautica*, vol. 74, pp. 141–155, 2012.

[18] A. Shirazi, J. Ceberio, and J. A. Lozano, "An evolutionary discretized lambert approach for optimal long-range rendezvous considering impulse limit," *Aerospace Science and Technology*, vol. 94, p. 105400, 2019.

[19] S. P. Hughes, L. M. Mailhe, and J. J. Guzman, "A comparison of trajectory optimization methods for the impulsive minimum fuel rendezvous problem," *Advanced Astronautical Sciences*, vol. 113, no. 4, pp. 85–104, 2003.

[20] E. Taheri and J. L. Junkins, "How many impulses redux," *The Journal of the Astronautical Sciences*, pp. 1–78, 2019.

[21] T. Polsgrove, L. Kos, R. Hopkins, and T. Crane, "Comparison of performance predictions for new low-thrust trajectory tools," in *AIAA/AAS Astrodynamics Specialist Conference and Exhibit*, p. 6742, 2006.

[22] D. H. Ellison, B. A. Conway, J. A. Englander, and M. T. Ozimek, "Application and analysis of bounded-impulse trajectory models with analytic gradients," *Journal of Guidance, Control, and Dynamics*, pp. 1–15, 2018.

[23] M. D. Rayman, P. A. Chadbourne, J. S. Culwell, and S. N. Williams, "Mission design for deep space 1: a low-thrust technology validation mission," *Acta astronautica*, vol. 45, no. 4-9, pp. 381–388, 1999.

[24] M. D. Rayman, T. C. Fraschetti, C. A. Raymond, and C. T. Russell, "Dawn: A mission in development for exploration of main belt asteroids vesta and ceres," *Acta Astronautica*, vol. 58, no. 11, pp. 605–616, 2006.

[25] F. R. Chang-Diaz, E. Braden, I. Johnson, M. M. Hsu, and T. F. Yang, "Rapid mars transits with exhaust-modulated plasma propulsion," *NASA Technical Paper 3539, NASA*, 1995.

[26] J. A. Kechichian, "Optimal low-thrust transfer using variable bounded thrust," *Acta Astronautica*, vol. 36, no. 7, pp. 357–365, 1995.

[27] H. Seywald, C. M. Roithmayr, and P. Troutman, "Fuel-optimal orbital transfers for variable specific impulse powered spacecraft.," *Advances in the Astronautical Sciences*, vol. 114, p. 20, 2003.

[28] L. Casalino and G. Colasurdo, "Optimization of variable-specific-impulse interplanetary trajectories," *Journal of guidance, control, and dynamics*, vol. 27, no. 4, pp. 678–684, 2004.

[29] G. Mengali and A. A. Quarta, "Fuel-optimal, power-limited rendezvous with variable thruster efficiency," *Journal of Guidance, Control, and Dynamics*, vol. 28, no. 6, pp. 1194–1199, 2005.

[30] E. Taheri, J. L. Junkins, I. Kolmanovsky, and A. Girard, "A novel approach for optimal trajectory design with multiple operation modes of propulsion system, part 1," *Acta Astronautica*, vol. 172, pp. 151–165, 2020.

[31] E. Taheri, J. L. Junkins, I. Kolmanovsky, and A. Girard, "A novel approach for optimal trajectory design with multiple operation modes of propulsion system, part 2," *Acta Astronautica*, vol. 172, pp. 166–179, 2020.

[32] C. Russell and C. Raymond, *The Dawn Mission to Minor Planets 4 Vesta and 1 Ceres*. Springer Science & Business Media, 2012.

[33] D. Y. Oh, S. Collins, T. Drain, W. Hart, T. Imken, K. Larson, D. Marsh, D. Muthulingam, J. Snyder, G. Whiffen, *et al.*, "Development of the psyche mission for nasa's discovery program," in *The 35th International Electric Propulsion Conference, Georgia Institute of Technology, USA*, 2017.

[34] W. Hart, G. M. Brown, S. M. Collins, M. D. S.-S. Pich, P. Fieseler, D. Goebel, D. Marsh, D. Y. Oh, S. Snyder, N. Warner, *et al.*, "Overview of the spacecraft design for the psyche mission concept," in *2018 IEEE Aerospace Conference*, pp. 1–20, IEEE, 2018.

[35] J. E. Polk, D. Brinza, R. Y. Kakuda, J. R. Brophy, I. Katz, J. R. Anderson, and J. Hamley, "Demonstration of the nstar ion propulsion system on the deep space one mission," *27th International Electric Propulsion Conference, 2001.*

[36] M. D. Rayman and S. N. Williams, "Design of the first interplanetary solar electric propulsion mission," *Journal of Spacecraft and Rockets*, vol. 39, no. 4, pp. 589–595, 2002.

[37] A. A. Quarta and G. Mengali, "Minimum-time space missions with solar electric propulsion," *Aerospace Science and Technology*, vol. 15, no. 5, pp. 381–392, 2011.

[38] J. Knittel, J. A. Englander, M. T. Ozimek, J. Atchison, and J. Gould, "Improved propulsion modeling for low-thrust trajectory optimization," *2017 AAS/AIAA Space Flight Mechanics Meeting, San Antonio, Texas*, February 2017.

[39] E. Taheri, "Low-thrust trajectory design using multi-mode propulsion systems: A grid-based thruster model," in *AIAA Scitech 2020 Forum*, p. 2183, 2020.

[40] R. Chertovskih, D. Karamzin, N. T. Khalil, and F. L. Pereira, "An indirect method for regular state-constrained optimal control problems in flow fields," *IEEE Transactions on Automatic Control*, 2020.

[41] J. D. Aziz, *Low-Thrust Many-Revolution Trajectory Optimization*. PhD thesis, University of Colorado at Boulder, 2018.

[42] V. Arya, E. Taheri, and J. L. Junkins, "Low-thrust gravity-assist trajectory design using optimal multimode propulsion models," *Journal of Guidance, Control, and Dynamics*, vol. 44, no. 7, pp. 1280–1294, 2021.

[43] V. Arya, E. Taheri, and J. L. Junkins, "A composite framework for co-optimization of spacecraft trajectory and propulsion system," *Acta Astronautica*, vol. 178, pp. 773–782, 2021.

[44] M. Vavrina, J. Englander, and A. Ghosh, "Coupled low-thrust trajectory and systems optimization via multi-objective hybrid optimal control," *AAS/AIAA Space Flight Mechanics Meeting, Williamsburg, VA*, 2015.

[45] J. Sims, P. Finlayson, E. Rinderle, M. Vavrina, and T. Kowalkowski, "Implementation of a low-thrust trajectory optimization algorithm for preliminary design," in *AIAA/AAS Astrodynamics specialist conference and exhibit*, p. 6746, 2006.

[46] J. T. Hwang, D. Y. Lee, J. W. Cutler, and J. R. Martins, "Large-scale multidisciplinary optimization of a small satellite's design and operation," *Journal of Spacecraft and Rockets*, vol. 51, no. 5, pp. 1648–1663, 2014.

[47] J. R. Martins and A. B. Lambe, "Multidisciplinary design optimization: a survey of architectures," *AIAA journal*, vol. 51, no. 9, pp. 2049–2075, 2013.

[48] H. Zhang, B. Song, F. Li, and J. Xuan, "Multidisciplinary design optimization of an electric propulsion system of a hybrid uav considering wind disturbance rejection capability in the quadrotor mode," *Aerospace Science and Technology, 2020*.

[49] H. Ma and S. Xu, "Optimization of bounded low-thrust rendezvous with terminal constraints by interval analysis," *Aerospace Science and Technology*, vol. 79, pp. 58–69, 2018.

[50] A. Shirazi, J. Ceberio, and J. A. Lozano, "Spacecraft trajectory optimization: A review of models, objectives, approaches and solutions," *Progress in Aerospace Sciences*, vol. 102, pp. 76–98, 2018.

[51] E. Taheri and J. L. Junkins, "Generic smoothing for optimal bang-off-bang spacecraft maneuvers," *Journal of Guidance, Control, and Dynamics*, vol. 41, no. 11, pp. 2470–2475, 2018.

[52] V. Arya, E. Taheri, and J. L. Junkins, "Spacecraft payload maximization using realistic multi-mode models of electric propulsion systems," *American Control Conference*, 2021.

[53] F. E. Laipert and J. M. Longuski, "Automated missed-thrust propellant margin analysis for low-thrust trajectories," *Journal of Spacecraft and Rockets*, vol. 52, no. 4, pp. 1135–1143, 2015.

[54] N. Ozaki, S. Campagnola, and R. Funase, "Tube stochastic optimal control for nonlinear constrained trajectory optimization problems," *Journal of Guidance, Control, and Dynamics*, vol. 43, no. 4, pp. 645–655, 2020.

[55] J. T. Olympio and C. H. Yam, "Deterministic method for space trajectory design with mission margin constraints," in *61st International Astronautical Congress*, International Astronautical Federation Prague, 2010.

[56] J. T. Olympio, "Designing robust low-thrust interplanetary trajectories subject to one temporary engine failure," in *Proceedings of the 20th AAS/AIAA Space Flight Meeting*, pp. 10–171, 2010.

[57] J. L. Crassidis and F. L. Markley, "Sliding mode control using modified rodrigues parameters," *Journal of Guidance, Control, and Dynamics*, vol. 19, no. 6, pp. 1381–1383, 1996.

[58] H. Schaub, M. R. Akella, and J. L. Junkins, "Adaptive control of nonlinear attitude motions realizing linear closed loop dynamics," *Journal of Guidance, Control, and Dynamics*, vol. 24, no. 1, pp. 95–100, 2001.

[59] G. Lymperopoulos and P. Ioannou, "Adaptive aircraft control in the presence of unstructured dynamic uncertainties," *Journal of Guidance, Control, and Dynamics*, vol. 42, no. 1, pp. 153–162, 2019.

[60] R. S. Christensen and D. Geller, "Linear covariance techniques for closed-loop guidance navigation and control system design and analysis," *Proceedings of the Institution of Mechanical Engineers, Part G: Journal of Aerospace Engineering*, vol. 228, no. 1, pp. 44–65, 2014.

[61] R. Goyal, M. Majji, and R. E. Skelton, "Integrating structure, information architecture and control design: Application to tensegrity systems," *Mechanical Systems and Signal Processing*, vol. 161, p. 107913, 2021.

[62] E. Collins and R. Skelton, "A theory of state covariance assignment for discrete systems," *IEEE Transactions on Automatic Control*, vol. 32, no. 1, pp. 35–41, 1987.

[63] A. Hotz and R. E. Skelton, "Covariance control theory," *International Journal of Control*, vol. 46, no. 1, pp. 13–32, 1987.

[64] R. E. Skelton, T. Iwasaki, and K. Grigoriadis, *A Unified Algebraic Approach to Control Design.* Taylor & Francis, London, UK, 1998.

[65] C. Hsieh and R. E. Skelton, "All covariance controllers for linear discrete-time systems," *IEEE transactions on automatic control*, vol. 35, no. 8, pp. 908–915, 1990.

[66] K. Okamoto and P. Tsiotras, "Input hard constrained optimal covariance steering," in *2019 IEEE 58th Conference on Decision and Control (CDC)*, pp. 3497–3502, IEEE, 2019.

[67] J. Ridderhof and P. Tsiotras, "Minimum-fuel powered descent in the presence of random disturbances," in *AIAA Scitech 2019 Forum*, p. 0646, 2019.

[68] J. Ridderhof, K. Okamoto, and P. Tsiotras, "Nonlinear uncertainty control with iterative covariance steering," in *2019 IEEE 58th Conference on Decision and Control (CDC)*, pp. 3484–3490, IEEE, 2019.

[69] K. Okamoto and P. Tsiotras, "Optimal stochastic vehicle path planning using covariance steering," *IEEE Robotics and Automation Letters*, vol. 4, no. 3, pp. 2276–2281, 2019.

[70] L. Blackmore, H. Li, and B. Williams, "A probabilistic approach to optimal robust path planning with obstacles," in *2006 American Control Conference*, pp. 7–pp, IEEE, 2006.

[71] J. L. Junkins and P. Singla, "How nonlinear is it? a tutorial on nonlinearity of orbit and attitude dynamics," *The Journal of the Astronautical Sciences*, vol. 52, no. 1, pp. 7–60, 2004.

[72] J. L. Junkins and E. Taheri, "Exploration of alternative state vector choices for low-thrust trajectory optimization," *Journal of Guidance, Control, and Dynamics*, vol. 42, no. 1, pp. 47–64, 2018.

[73] E. Taheri, V. Arya, and J. L. Junkins, "Costate mapping for indirect trajectory optimization," *Astrodynamics*, vol. 5, no. 4, pp. 359–371, 2021.

[74] T. Haberkorn, P. Martinon, and J. Gergaud, "Low thrust minimum-fuel orbital transfer: a homotopic approach," *Journal of Guidance, Control, and Dynamics*, vol. 27, no. 6, pp. 1046–1060, 2004.

[75] E. Taheri, I. Kolmanovsky, and E. Atkins, "Enhanced smoothing technique for indirect optimization of minimum-fuel low-thrust trajectories," *Journal of Guidance, Control, and Dynamics*, vol. 39, no. 11, pp. 2500–2511, 2016.

[76] V. Arya, E. Taheri, and J. Junkins, "Hyperbolic tangent-based smoothing with state transition matrix implementation for generating fuel-optimal trajectories," *29th AAS/AIAA Space Flight Mechanics Meeting, Maui, HI, 2019*, 2019.

[77] E. Taheri, V. Arya, and J. L. Junkins, "Costate transformation for indirect trajectory optimization," *31st AAS/AIAA Space Flight Mechanics Meeting, Virtual, February 1-February 3, 2021*.

[78] A. Bryson and Y.-C. Ho, "Applied optimal control: Optimization, estimation, and control (revised edition)," *Levittown, Pennsylvania: Taylor & Francis*, 1975.

[79] Y. Gao and C. Kluever, "Low-thrust interplanetary orbit transfers using hybrid trajectory optimization method with multiple shooting," in *AIAA/AAS Astrodynamics Specialist Conference and Exhibit*, p. 5088, 2004.

[80] J. E. Prussing, "Illustration of the primer vector in time-fixed, orbit transfer.," *AIAA Journal*, vol. 7, no. 6, pp. 1167–1168, 1969.

[81] S. Wagner and B. Wie, "Hybrid algorithm for multiple gravity-assist and impulsive delta-v maneuvers," *Journal of Guidance, Control, and Dynamics*, vol. 38, no. 11, pp. 2096–2107, 2015.

[82] J. Shimoun, E. Taheri, I. Kolmanovsky, and A. Girard, "A study on gpu-enabled lambert's problem solution for space targeting missions," in *2018 Annual American Control Conference (ACC)*, pp. 664–669, IEEE, 2018.

[83] H.-X. Shen, L. Casalino, and Y.-Z. Luo, "Global search capabilities of indirect methods for impulsive transfers," *The Journal of the Astronautical Sciences*, vol. 62, no. 3, pp. 212–232, 2015.

[84] E. Taheri, V. Arya, and J. L. Junkins, "Acceleration-based indirect method for continuous and impulsive trajectory design," *31st AAS/AIAA Space Flight Mechanics Meeting, Virtual, February 1-February 3, 2021*.

[85] D. J. Jezewski and H. L. Rozendaal, "An efficient method for calculating optimal free-space n-impulse trajectories.," *AIAA journal*, vol. 6, no. 11, pp. 2160–2165, 1968.

[86] P. Lion and M. Handelsman, "Primer vector on fixed-time impulsive trajectories.," *AIAA Journal*, vol. 6, no. 1, pp. 127–132, 1968.

[87] J. E. Prussing, "Primer vector theory and applications," *Spacecraft trajectory optimization*, vol. 29, p. 16, 2010.

[88] J. L. Junkins and H. Schaub, *Analytical mechanics of space systems*. American Institute of Aeronautics and Astronautics, 2009.

[89] C. G. Marirrodriga, A. Pacros, S. Strandmoe, M. Arcioni, A. Arts, C. Ashcroft, L. Ayache, Y. Bonnefous, N. Brahimi, F. Cipriani, *et al.*, "Solar orbiter: Mission and spacecraft design," *Astronomy & Astrophysics*, vol. 646, p. A121, 2021.

[90] V. Arya, E. Taheri, and J. Junkins, "A composite framework for joint optimization of trajectory and propulsion design," *AAS Guidance, Navigation and Control Conference,Breckenridge, Colorado.*, 2020.

[91] V. Arya, E. Taheri, and J. Junkins, "Electric thruster mode-pruning strategies for trajectory-propulsion co-optimization," *Aerospace Science and Technology*, vol. 116, p. 106828, 2021.

[92] J. A. Kechichian, "Orbit raising with low thrust tangential acceleration in the presence of earth shadow," 1991.

[93] J. T. Betts, "Optimal low–thrust orbit transfers with eclipsing," *Optimal Control Applications and Methods*, vol. 36, no. 2, pp. 218–240, 2015.

[94] C. Ferrier and R. EPENOY, "Optimal control for engines with electro-ionic propulsion under constraint of eclipse," *Acta Astronautica*, vol. 48, no. 4, pp. 181–192, 2001.

[95] R. Woollands and E. Taheri, "Optimal low-thrust gravity perturbed orbit transfers with shadow constraints," in *The 2019 AAS/AIAA Astrodynamics Specialist Conference*, 2019.

[96] C. A. Kluever and S. R. Oleson, "Direct approach for computing near-optimal low-thrust earth-orbit transfers," *Journal of Spacecraft and Rockets*, vol. 35, no. 4, pp. 509–515, 1998.

[97] G. Yang, "Direct optimization of low-thrust many-revolution earth-orbit transfers," *Chinese Journal of Aeronautics*, vol. 22, no. 4, pp. 426–433, 2009.

[98] B. Neta and D. Vallado, "On satellite umbra/penumbra entry and exit positions," *The Journal of the astronautical sciences*, vol. 46, no. 1, pp. 91–103, 1998.

[99] K. F. Graham and A. V. Rao, "Minimum-time trajectory optimization of low-thrust earth-orbit transfers with eclipsing," *Journal of Spacecraft and Rockets*, vol. 53, no. 2, pp. 289–303, 2016.

[100] E. Taheri, "Optimization of many-revolution minimum-time low-thrust trajectories using sundman transformation," in *AIAA Scitech 2021 Forum*, p. 1343, 2021.

[101] B. Pan, Y. Ma, and Y. Ni, "A new fractional homotopy method for solving nonlinear optimal control problems," *Acta Astronautica*, vol. 161, pp. 12–23, 2019.

[102] R. H. Battin, *An introduction to the mathematics and methods of astrodynamics*. AIAA, 1999.

[103] G. Whiffen, "Mystic: Implementation of the static dynamic optimal control algorithm for high-fidelity, low-thrust trajectory design," in *AIAA/AAS Astrodynamics Specialist Conference and Exhibit*, p. 6741, 2006.

[104] J. P. Gutkowski, T. F. Dawn, and R. M. Jedrey, "Trajectory design analysis over the lunar nodal cycle for the multi-purpose crew vehicle (mpcv) exploration mission 2 (em-2)," *Advances in the Astronautical Sciences: Guidance, Navigation and Control*, vol. 151, pp. 14–096, 2014.

[105] V. Arya, E. Taheri, R. Woollands, and J. Junkins, "Gravity-assist fuel-optimal low-thrust trajectory design using hybrid optimization techniques," *70th International Astronautical Congress (IAC), Washington D.C., United States.*, 2019.

[106] S. Cheng, H. Lu, X. Lei, and Y. Shi, "A quarter century of particle swarm optimization," *Complex & Intelligent Systems*, vol. 4, no. 3, pp. 227–239, 2018.

[107] J. A. Englander, B. A. Conway, and T. Williams, "Automated mission planning via evolutionary algorithms," *Journal of Guidance, Control, and Dynamics*, vol. 35, no. 6, pp. 1878–1887, 2012.

[108] J. A. Sims and S. N. Flanagan, "Preliminary design of low-thrust interplanetary missions," in *AAS/AIAA Astrodynamics Specialist Conference, AAS Paper 99-338, Girdwood, Alaska,*, Aug. 1997.

[109] S. N. Williams and V. Coverstone-Carroll, "Mars missions using solar electric propulsion," *Journal of Spacecraft and Rockets*, vol. 37, no. 1, pp. 71–77, 2000.

[110] A. E. Petropoulos and J. M. Longuski, "Shape-based algorithm for automated design of low-thrust, gravity-assist trajectories," *Journal of Spacecraft and Rockets*, vol. 41, no. 5, pp. 787–796, 2004.

[111] L. Watson, F. C., and P. P., "Multidisciplinary design optimization," *Encyclopedia of Optimization, 2008.*

[112] Z. Chi, F. Jiang, and G. Tang, "Optimization of variable-specific-impulse gravity-assist trajectories via optimality-preserving transformation," *Aerospace Science and Technology, 2020*, vol. 101.

[113] M. Trisolini, H. G. Lewis, and C. Colombo, "Spacecraft design optimisation for demise and survivability," *Aerospace Science and Technology*, vol. 77, pp. 638–657, 2018.

[114] X. Li, R. R. Warier, A. K. Sanyal, and D. Qiao, "Trajectory tracking near small bodies using only attitude control," *Journal of Guidance, Control, and Dynamics*, vol. 42, no. 1, pp. 109–122, 2019.

[115] V. Arya, R. Goyal, M. Majji, and J. L. Junkins, "Design of lqr weighting matrices for time varying output covariance assignment," *AAS Astrodynamics Specialist Conference at Big Sky, Montana, 2021*.

[116] H. Schaub, J. L. Junkins, *et al.*, "Stereographic orientation parameters for attitude dynamics: A generalization of the rodrigues parameters," *Journal of the Astronautical Sciences*, vol. 44, no. 1, pp. 1–19, 1996.